7.051
PN-ABM 788
79968

Asian Institute of Technology
Bangkok Thailand

WELDED WIRE WALL AND EMBANKMENT SYSTEM WITH COHESIVE BACKFILL ON SOFT CLAY

Fourth Progress Report for the
Period Ending January 31, 1990

Submitted to: U.S. Agency for International Development
Science and Technology Division
Office of Technical Resources
USAID Thailand, 37 Soi Somprasong
Petchburi Road, Bangkok

Submitted by

Dr. Dennes T. Bergado, Principal Investigator
Mr. Casan L. Sampaco, Research Associate
Mr. Marolo C. Alfaro, Research Associate
Mr. Ramaiah Shivashankar, Doctoral Candidate
and
Prof. A.S. Balasubramaniam, Co-Principal Investigator

Division of Geotechnical and Transportation Engineering
Asian Institute of Technology
G.P.O. Box 2754,
Bangkok, Thailand

Rec'd in SCI APR 19 1990

March, 1990

PN-ABM-788
-79962

WELDED WIRE WALL AND EMBANKMENT SYSTEM WITH POOR QUALITY COHESIVE BACKFILL ON SOFT CLAY

Fourth Progress Report for the
Period Ending January 31, 1990

Submitted by:

DR. DENNES T. BERGADO, Principal Investigator

MR. CASAN L. SAMPACO, Research Associate

MR. MAROLO C. ALFARO, Research Associate

MR. RAMAIAH SHIVASHANKAR, Doctoral Candidate

and

PROF. A.S. BALASUBRAMANIAM, Co-Principal Investigator

Division of Geotechnical and Transportation Engineering
Asian Institute of Technology
G. P. O. Box 2754
Bangkok, Thailand

March, 1990

TABLE OF CONTENTS

		Page No.
	SUMMARY	1
I.	RESEARCH PERSONNEL	2
II.	PUBLICATIONS	3
III.	RESEARCH COLLABORATION	3
IV.	PLANS FOR THE NEXT SUCCEEDING REPORTS	4
V.	ADDITIONAL EQUIPMENTS ACQUIRED BY THE PROJECT	4
VI.	TENSILE STRENGTH TESTS OF W4.5 STEEL BARS	5
VII.	SYSTEM MODIFICATION FOR PULLOUT TEST	6
VIII.	LABORATORY PULLOUT TESTS	7
	Weathered Clay Backfill	7
	Lateritic Residual Soil	9
	Clayey Sand Backfill	10
IX.	FIELD PULLOUT TESTS ON REINFORCED SOIL SYSTEMS	11
	Review of Past Works	11
	Field Pullout Tests at USAID Experimental Wall	13
X.	FIELD BEHAVIOR OF THE USAID WELDED WIRE WALL	17
	Lateral Movements	17
	Settlements	17
	Excess Pore Pressures	18
	Earth Pressure Variations and Effect on Strains	19
	Reinforcement Stresses and Maximum Tension Line	22

		Page No.
XI.	NUMERICAL MODELING OF REINFORCED SOIL SYSTEMS	24
	Introduction	24
	Finite Element Analysis of Reinforced Soil Systems	25
	Discrete Material Approach	25
	Composite Material Approach	25
	Modeling of Material Behavior	26
	Soil Stress-Strain Relation	26
	Tangent Modulus	28
	Bulk Modulus	29
	Tangent Poisson's Ratio	30
	Analytical Method for Soil-Geogrid Interaction	32
	The Concept of Grid Junctions	32
	Finite Element Implementation	33
XII.	COMPUTER PROGRAM NON LIN 1	35
	Element Types	35
	Material Nonlinearities	36
	Elastic-Plastic Material Models	36
	Tension Cut-off Model	36
	Nonlinear Joint Model	37
XIII.	COMPUTER PROGRAM REA (REINFORCED EARTH ANALYSIS)	37
	Background	37
	General Features	37
	Incremental Iterative Analysis	37
	Material Models	37
	Modeling the Foundation Material	38
	Slippage Model	38
	Edge Effects	39
	Finite Element Implementation	40
	Modifications Made on the REA Program	41
	Material Model	41
	Equivalent Friction Coefficient	42
XIV.	REFERENCES	43
	TABLES	46
	FIGURES	51

WELDED WIRE WALL AND EMBANKMENT SYSTEM WITH POOR QUALITY COHESIVE BACKFILL ON SOFT CLAY

SUMMARY

For the past seven months since the submission of the last report, the USAID project team was able to continue the monitoring programs of the welded wire experimental wall which primarily consist of settlement and pore pressure measurements, lateral deformations, strain measurements in the reinforcing mats, and earth pressure readings at the base of the wall. It was found that the wall had suffered severe lateral and vertical deformations due to the consolidation of the soft clay foundation. Because of these movements, the variations of earth pressures at the base of the wall was found to shift with time and was found to influence significantly the magnitude and variation of strains in the reinforcing mats.

Modifications made on the pullout test apparatus by incorporating the load cell to measure the load, and the electro-hydraulic systems of the 50,000-lb capacity pullout jack to control the pulling rate, had been a remarkable improvement to the pullout testing program, both in the laboratory and in the field. A total of 132 pullout tests were conducted in the laboratory using the 3 backfill materials and steel reinforcements of varying geometry. In the field, 15 dummy mats located at different levels in the wall were also pulled out. Typical results of these tests are discussed in this report.

A review of the finite element modeling of soil-reinforcement interaction and reinforced earth wall behavior is also presented. Currently available finite element computer programs applicable to the purposes of the project are discussed and their significant features are emphasized.

I. RESEARCH PERSONNEL

Presently, the USAID research project personnel comprises of 2 research associates, 2 doctoral students, and 3 master's students. One of the doctoral students had been working on his dissertation on the project for almost two years now, and is expected to complete his program this year. The other doctoral student has just started his program last September, 1989 and will soon be joining the project after completing the course work requirements this term.

The three master's students have joined the project last September, 1989. One of them is studying the mechanism of interaction between the welded wire reinforcement and the poor quality backfill by conducting field pullout tests and compare the results to the output of a finite element computer model. He is also expected to carry out 3 constant stress pullout tests on different levels of reinforcements embedded in the welded wire wall. Another master's student is engaged in monitoring the behavior of the welded wire wall, and had already conducted laboratory pullout tests on weathered clay backfill using 1/2" and 1/4" diameter bars on a 6"x9" mesh and 3 different moisture contents (dry, optimum, wet). This laboratory pullout testing program for weathered clay backfill is an extension to the work of Cisneros (1989) whose data had been presented in the last report (Bergado et al, 1989). In addition, the effect of reinforcement on the stress distribution within the reinforced embankment will be investigated by conducting plate load and screw plate tests. The third master's student extends the previous work of Amin (1989) for lateritic residual backfill by employing higher vertical overburden pressures ranging from 1 to 13 t/m^3. Three different sizes of wires (1/4",3/8",1/2") with grid openings of 6"x6" and 6"x9" is used. These master's students are expected to complete their research works this coming April, 1990, after which, it is possible that a new batch of thesis students will be joining the project for the next academic year. Finally, two temporary workers for physical assistance in the pullout tests and monitoring activities are presently being retained by the project.

II. PUBLICATIONS

In addition to the three publications mentioned in the previous progress report concerning the results and analysis of this project, the following papers have been submitted and accepted for publication:

(a) Bergado, D. T., Sampaco, C. L., Alfaro, M.C., Shivashankar, R. and Balasubramaniam, A.S. (1989). "Mechanically stabilized earth (MSE) and other ground improvement techniques for infrastructure constructions on soft and subsiding ground." Proc. Symp. on Underground Excavations in Soils and Rocks, Including Earth Pressure Theories, Buried Structures, and Tunnels, Bangkok, Thailand, 27-29 November, 1989.

(b) Bergado, D.T., Balasubramaniam, A.S., Alfaro, M.C. and Sampaco, C.L. (1990). "Ground improvement techniques for approach road embankments to bridges and viaducts in the soft and subsiding ground." Proc. 8th Conf. of ASEAN Federation of Eng'g. Organizations (CAFEO), Penang, Malaysia, 12-14 February, 1990.

(c) Bergado, D.T., Sampaco, C.L., Shivashankar, R., Alfaro, M.C., Anderson, L.R. and Balasubramaniam, A.S. (1990). "Interaction of welded wire reinforcement with poor quality backfill." Proc. 10th Southeast Asian Geotechnical Conf., Taipei, 16-20 April, 1990.

(d) Bergado, D.T., Cisneros, C.B., Sampaco, C.L., Alfaro, M.C. and Shivashankar, R. (1990). "Effects of compaction moisture contents on pullout resistance of steel geogrids with weathered clay backfill." Proc. 4th Intl. Conf. on Geotextiles and Geomembranes, The Hague, Netherlands, May 27-June 1, 1990.

III. RESEARCH COLLABORATION

Last August 1-2, 1989, Dr. Dennes T. Bergado attended the Symposium on the Application of Geosynthetic and Geofibre in Southeast Asia which was organized by the Geotechnical Engineering Technical Division of the Institution of Engineers in Malaysia in collaboration with the Southeast Asian Geotechnical Society and the International Geotextile Society (Southeast Asian Chapter). He presented the paper on the results gathered in this project concerning the laboratory pullout tests on weathered clay backfill. The conference was held in Petaling Jaya, Selangor Darul Ehsan, Malaysia.

Another symposium was held in Bangkok, Thailand, last November 27-29, 1989 concerning underground excavation in soils and rocks, including earth pressure theories, buried structures, and tunnels, which was organized by the Southeast Asian Geotechnical Society. A paper which includes a part of the data and analyses obtained from this project was also presented by Dr. Bergado.

IV. PLANS FOR THE NEXT SUCCEEDING REPORTS

For the next succeeding months, pullout tests using the three different backfills will be conducted. The months of March and April, 1990 will be devoted to pullout tests on clayey sand backfill. Detailed analyses of the results on laterite and weathered clay will also be made as soon as sufficient amount of data will be achieved to at least establish a definite consistency and a decisive conclusion. Results of the constant stress pullout tests carried out both in the field and in the laboratory will be reported. Since this report reviews all the available materials needed for the numerical modeling of the wall behavior as well as the soil-reinforcement interaction from field and laboratory data, the results of these analyses will be presented in the next succeeding reports.

V. ADDITIONAL EQUIPMENTS ACQUIRED BY THE PROJECT

(1) Wooden platform for constant strain pullout test in the field

Since the field pullout testing is to be conducted on dummy reinforcements embedded at different elevations of the welded wire wall, it was necessary to design a platform with an adjustable height to mount the hydraulic cylinder and other accessories needed in running the pullout test. Consequently, a wooden platform with three removable disk components and a wooden staircase was constructed at the Physical Plant Division of AIT. It has a maximum height of 4.50 m but can be adjusted for different locations in the wall by varying the combination of mounting the three desks. Figures 1 to 4 illustrate the details of the platform used in the constant strain pullout test in the field. Photographs showing these platforms are given in Figs. 58 and 59.

(2) Wooden platform for constant stress pullout test in the field

It is also planned to conduct pullout tests in the field by holding the pullout load constant at a specified interval of time while observing the strain changes in the reinforcement. As the test is to be carried out on 3 dummy reinforcements embedded at 3 different levels of the welded wire wall, a wooden frame, attached with a 6" diameter pulley and a 3/8" diameter flexible cable tied to a load hanger, was designed and constructed. Figures 5 to 8 show the different views of the frame. For higher reinforcement levels, the frame can be mounted on any of the 3 desks designed for the constant strain pullout test, as previously described.

(3) Steel reaction frame for the field pullout test

A steel built-up frame to provide the pullout reaction against the wall facing was also constructed. The frame was made up of steel channels and rolled H and I beams built up together as shown in Fig. 9. Figures 61 to 63 show the photographs of the steel reaction frame during field pullout test.

VI. TENSILE STRENGTH TESTS OF W4.5 STEEL BARS

In order to establish the stress-strain curve of the wire sizes used in the welded wire wall, tensile strength tests were performed on W4.5 steel bars bonded with strain gages at conditions which simulate those for the instrumented wire mats reinforcing the wall. The test having the localized zone of fracture closest to the strain gage location was then chosen and modeled by a bilinear stress-strain curve as plotted in Fig. 10. Accordingly, the modulus of elasticity was found to be 25,556,100 psi while the yield strain was estimated at 0.37%. The bar failed by tension at a measured strain of 2.25%. The tension in the wires for W4.5 bars can then be calculated from the axial strains measured by the 21X micrologger using the following equations:

$$T = 1{,}191{,}379 * \varepsilon \qquad \text{For } \varepsilon \leq \varepsilon_y = 0.0037 \qquad (1)$$

$$T = 4{,}309 + 20{,}730 * \varepsilon \qquad \text{For } \varepsilon > \varepsilon_y = 0.0037 \qquad (2)$$

where T is the tension in pounds and ε is the axial strain expressed as a decimal.

VII. SYSTEM MODIFICATION FOR PULLOUT TEST

The present system of running the pullout test has gone through remarkable improvements since the incorporation of the SR-4 load cell and the Vicker's electronic control components which combine to form an electro-hydraulic control systems.

The load cell enables the measurement of the pullout load at a specified execution interval of the 21X datalogger by translating the changes in force into changes in voltage. Since the load cell is bonded with special strain gages which are electrically connected to form a balanced Wheatstone bridge, a constant voltage is then applied across the opposite corners of the bridge using the 21X datalogger Instruction 4, so that a change in force of the cell, changing the resistance of the gage, will produce a change in the output voltage. The measured change in the output voltage is then converted into units of force by using the calibration curve of the load cell such as that shown in Fig. 11. Figure 12 shows the photograph of the load cell (green) mounted on a steel frame with an adjustable height, and a curve-shaped surface, smoothened with grease to eliminate frictional effects as the steel grid is pulled out. Both the front and rear ends of the load cell is threaded with a well-designed connection to the clamping apparatus of the mat, leading to the 50,000-lb capacity hydraulic cylinder which provides the pullout load.

The electro-hydraulic control systems used in running the pullout test consist of a power supply (EMRS-A-11) and an amplifier module (EM-D-20) which provide the means of supplying the proper input to the electro-hydraulic, flapper nozzle piloted servo valve (SM4-20). The servo valve, in turn, provides the flow modulation, reversibility, and fast response for precise control of velocity, position, or force supplied by the hydraulic cylinder. The integral power packages which include the dual voltage Lincoln 7.5-hp motor, variable displacement in-line type piston pump, valving, hydraulic oil reservoir, and oil filters (high pressure and return line) are self-contained power sources used as main hydraulic systems.

Due to the inavailability of the Temposonics analog output module with a velocity output (the project has a linear displacement output module), an open loop control circuit with linear displacement feedback is presently adopted. The rate of pulling is controlled by interfacing the electronic control components with a potentiometer pot which manually regulates the input signal to the servo valve, thus allowing changes in velocity and direction of the hydraulic cylinder. The rate is controllable by manual adjustments of the potentiometer in accordance with the dial gage reading and clock timer to attain the desired strain rate. The typical set-up of the pullout test

in the laboratory is given in Fig. 13. The electronic control components with the interfaced potentiometer pot is shown in Fig. 14 together with the 21X datalogger and AM416 relay multiplexer.

VIII. LABORATORY PULLOUT TESTS

For the past seven months since the submission of the 3rd Progress Report, a total of 132 pullout tests were conducted at the laboratory using 3 types of backfill materials and using steel grids of different bar sizes and mat configurations. The results are discussed and presented in the following sections including the comparison with previous data reported.

A. Weathered Clay Backfill

For the weathered clay backfill, a total of 54 tests were conducted using 1/2" and 1/4" diameter bars on a 6"x9" mesh and 3 different compaction moisture conditions of the backfill (dry side, optimum, wet side) at 95% relative compaction density. The result forms a part of the extension to the previously reported data (Bergado et al, 1989b; Cisneros, 1989). The tests were conducted in such a way that for a given mat geometry, bar size, and compaction condition of the backfill, the overburden pressures were overlapped, forming a series consisting of 3 test set-ups, each set-up having 3 applied normal pressures as follows:

Test Set-Up Number	Overburden Pressure (t/m^2)
1	1, 3, 5
2	5, 7, 9
3	9, 11, 13

This procedure provides a means of checking the strain dependency of the backfill material (although it is unlikely possible to exactly duplicate the test condition in every set-up) by comparing the pullout capacities at normal pressures of 5 and 9 t/m^2. Several tests have also undergone weld failures such that the results were rendered unreliable. For 1/4" diameter bars, tension failures were observed for normal pressures of 5 t/m^2 and higher. A summary of the results gathered in these tests are given in Table 1.

The load-displacement curves for the tests performed on dry, optimum, and wet side compactions using 1/4" and 1/2" diameter bars are, respectively, shown in Figs. 15 to 20. As in the previous results reported earlier (Bergado et al, 1989b), the load-displacement curves also displayed yield points wherein the curve flattens out such that any further increase in displacement

of the mat does not cause significant increase in the load. These yield points exhibit well-defined locations for higher normal pressures. Smooth curves with no well-defined yield points were observed for lower overburden pressures, and occasionally, for the first run of a test set-up. More test is needed to look into the factors influencing the shapes and magnitudes of the pullout curves to arrive at a decisive conclusion. The yield pullout strength occurred at relatively small displacements of 4 to 6 mm for dry side and optimum compactions, and even smaller displacements at 2 to 4 mm for the wet side compaction.

Figures 21 and 22 show the plots of maximum pullout resistance with overburden pressures for 1/4" and 1/2" diameter bars, respectively. It seems that for the same size of bars (1/4" or 1/2") and overburden pressure, the dry side compacted sample yielded the highest pullout capacity, while the sample compacted on the wet side of optimum gave a comparatively very low pullout resistance. The plots evidently show the influence of compaction water contents on the pullout resistance of the mat. These curves were rearranged to provide the comparison on the effect of bar sizes as shown in Figs. 23, 24, and 25. In all of the plots, the maximum pullout resistance is found to increase with the increasing diameter of the reinforcement.

With regards to strains, more test is needed to yield at least a consistent trend as it seems that the workability of the poor quality backfill material, especially during compaction, strongly influence the performance of the strain gages attached to the mat. Figures 26 to 31 show the axial strains plotted against the mat displacement for different bar sizes and overburden pressures. The relative locations of strain gages L1, L2, L3, and T are given in Fig. 26. Figure 32 shows the typical variation of strains with distance from the point of application of the load for 1/2" diameter bars and different backfill conditions (optimum and wet side). Most of the results exhibited a decreasing magnitude of strains with distance from the face of the box.

These results are then compared to the data presented earlier (Cisneros, 1989; Bergado et al, 1989b) for 1/4" diameter bars and 2 compaction conditions (dry and wet) as shown in Figs. 33 and 34. The recent results obtained using the modified system of running the pullout test are consistently higher than the previous data due perhaps to the increased accuracy of the new pullout testing system.

B. Lateritic Residual Soil

The additional tests involving lateritic soil is an extension of the work of Amin (1989) who conducted laboratory pullout tests on lateritic soil at low normal pressures. A total of 162 additional tests were conducted by employing higher overburden pressures ranging from 1 to 13 t/m^2 and 3 different backfill conditions (dry, optimum, wet). Three different sizes of wires consisting of 1/4", 3/8", and 1/2" were adopted using grid openings of 6"x6" and 6"x9". However, as of the time of writing this report, a total of 72 tests were conducted and will be discussed in the following section. It is estimated that all the 162 tests will be completed in the first week of March, 1990.

Similar set-ups as that used for weathered clay backfill was adopted. Table 2 summarizes the result of pullout tests on lateritic residual soil. It can be seen that an initial comparison can only be possibly made for those tests conducted on the dry side compacted specimen with 6" x 9" mesh and 3 bar sizes (1/4", 3/8", 1/2").

Figures 35, 36, and 37 show the load-displacement curves for 1/4", 3/8", and 1/2" bar sizes, respectively. Similar shapes of the curve as that observed for weathered clay, can be inferred, except that the yield strength occurs at higher displacements of 6 to 8 mm. These plots are presented in a different form as shown in Fig. 38 which show the influence of the bar size on the pullout resistance.

Figures 39, 40, and 41 show the typical plots of the strains L1, L2, and L3 (refer to Fig. 26 for relative locations in the mat) with horizontal displacements using 1/2" diameter bar for different values of normal pressures. The shapes and yield points of these curves are consistent with the corresponding load-displacement curves as given in Fig. 37. Typical variation of these strains with distance from the face is depicted in Fig. 42 for different values of overburden pressures. As in the weathered clay backfill, the strains were found to decrease approximately linearly with distance from the face of the box.

Combining the results with that of Amin (1989) who conducted tests on the same backfill material but at lower normal pressures ranging from 0.2 to 1.8 t/m^2, it is seen that a bilinear plot can be deduced, with the lower normal pressures displaying steeper slopes than higher normal pressures (Figs. 43 to 45). This observation seems to support the particle breakage phenomena inherent to lateritic residual soils (Bergado et al, 1988c) which was also reported by Amin (1989) from the results of direct shear tests on the same backfill material. It also seems that the recent data yielded higher magnitudes of pullout resistance than that obtained by Amin (1989).

C. Clayey Sand Backfill

The soil specimen is a brownish clayey sand with 45% passing the U.S. standard sieve No. 200. The optimum moisture content is 14% at a corresponding maximum dry density of 1.73 t/m^3. The shear strength parameters of the 95% dry compacted specimen obtained from triaxial tests indicated a UU strength of $c = 4.2\ t/m^2$ and $\phi = 23.5^o$ and CIU strengths of $c = 3.2\ t/m^2$, $\phi = 18.2^o$ (total stress) and $c = 2.5\ t/m^2$, $\phi = 24^o$ (effective stress). Direct shear test results also indicated values of $c = 3.8\ t/m^2$ and $\phi = 26.8^o$. The complete data for this backfill material was given by Bergado et al (1989a,b).

Eighteen laboratory pullout tests using clayey sand backfill were carried out using W4.5 x W3.5 wires with 6"x9" mesh openings. The tests were conducted on normal pressures ranging from 1 to 13 t/m^2 at 95% dry side compacted density. As in the weathered clay and lateritic residual soil, it was planned to investigate the effects of bar sizes, mesh configurations, compaction density, moisture content, and overburden pressure on the pullout resistance using clayey sand backfill. In addition, the friction component of the pullout resistance was evaluated by running pullout tests on mats without transverse members. Furthermore, the results obtained from the field pullout tests was compared to the data gathered from the laboratory using the same backfill.

The same procedure of pullout testing as that adopted for weathered clay and lateritic residual soil was used. The pullout test result is summarized in Table 3. Figures 46 and 47 show the load-displacement curves for W4.5 x W3.5 mats having mesh sizes of 6" x 9" and 6" x 18", respectively, and conducted with moisture contents within the dry side of optimum. Figure 48 shows the load-displacement curves for W4.5 longitudinal bars pulled out to investigate the frictional component of pullout resistance. The corresponding strain-displacement plots are depicted in Figs. 49 to 52. As there are still very few tests conducted so far, it is quite early and unlikely to make any inference and comparison.

IX. FIELD PULLOUT TESTS ON REINFORCED SOIL SYSTEMS

Field pullout tests are usually conducted in conjunction with laboratory pullout tests to investigate the pullout resistance of reinforcements embedded at representative overburden and field moisture and density conditions. Dummy bar mats of different configurations are installed during construction at different levels in the wall. In this manner, the pullout resistance can be verified for actual conditions using full scale field prototypes.

A. Review of Past Works

Hannon and Forsyth (1984) made a preliminary evaluation of 4 mechanically stabilized embankment-retaining wall systems constructed on Interstate 80 at Baxter, California using low quality backfill materials. Two of these walls were instrumented to monitor the performance over a 3-year period. Dummy bar mats were installed at five levels between stations 398+97 and 399+22. The dummy bar-mat configurations consisted of three longitudinal bars and one, two, or three transverse bars to form a 6 x 24 in. grid. The outer 6 ft. 2 in. of the longitudinal bars was equipped with greased sleeves to prevent soil bond. The mats extended a maximum of 10 ft. 8 in. back from the front concrete face panels of the wall with overburden heights of 4,6,8,10, and 12 ft. for each of the three bar-mat configurations. During the pullout test these mats were loaded until 8 in. of extension or failure occurred. The primary objective was to develop pullout information on the relative effect of individual transverse bars at various overburden pressures and then relate it to laboratory pullout test results. Comparison of test results for 10 ft. overburden height was reported as shown in Fig. 53 with one, two, and three transverse bars. The results were reported to confirm previously reported laboratory tests that suggest the dominant role of the transverse bars in mobilizing the total pullout resistance of grid-type reinforcements. Comparison of field pullout resistance for the five different overburden heights was also presented as shown in Fig. 54 for the dummy bar-mats with three transverse bars. The result suggests that the peak pullout loads were quite variable and were not consistent with the theory that pullout capacity increases with increased overburden. It was then construed that this inconsistency is partially due to the strength variability of the low quality backfill resulting from the moisture regime within the reinforced mass.

The comparison of laboratory and field pullout test was also presented as depicted in Fig. 55. In all cases, the field tests provided pullout capacities in excess of those provided in the laboratory under the same backfill conditions. The lower values obtained in the laboratory were partially attributed to the free

face test condition as opposed to the restraint provided by the concrete face panels in the field test. It was then conclusively reported that laboratory pullout test results are conservative for use in design.

Anderson et al (1986) also carried out both field and laboratory pullout tests to investigate the apparent friction coefficients of reinforcing bars and soils embedded on a 17 ft high experimental tie-back, timber-faced, anchor retaining wall constructed in Centerville, Utah in 1985. The anchor system consisted of an angle section (2"x2"x1/4"), tied to the wall face with No. 4 or No. 5 reinforcing bars having 2 ft. horizontal and vertical spacings. Two different sections of the wall were constructed and instrumented. Section 1 (east half) consisted of a quality backfill material (well-graded pit gravel with < 5% passing No. 100 sieve). Section 2 in the west half was constructed with a lower quality backfill material (sandy silt), obtained from several sources with 40 to 85% passing the No. 200 sieve. There were six layers of reinforcement instrumented at each section as shown in Fig. 56. The dummy anchors used for field pullout tests consisted of both single rebars as shown in Fig. 57a and rebar-angle anchor systems (three rebars attached to one angle) as shown in Fig. 57b. The latter (rebar-angle anchor system) was used to investigate the lateral bearing capacity of the embedded angles while the former (single rebars) were used to measure the frictional component of anchor resistance. Selected anchors (both single bars and anchor systems) were instrumented with strain gages to measure the distribution of the anchor resistance along the length of the tie rod.

Pullout tests conducted in the laboratory test cell indicated that the pullout resistance is a function of the angle size and orientation and the horizontal spacing of the tie rods. For closely-spaced tie rods and high moment capacity angles, the pullout resistance per unit width was computed as:

$$F_t/w = \sigma_v \, (d) \, N_q \qquad \ldots\ldots\ldots\ldots\ldots\ldots \qquad (3)$$

where: F_t/w = pullout resistance per unit length
σ_v = vertical soil stress (overburden pressure)
d = height of angle normal to the tie rods
N_q = bearing capacity factor that is a function of the shear strength of the soil.

It was reported that the back-calculated values of N_q ranged from 11 to 26 for the experimental wall. It is also interesting to note that the same range was obtained from the laboratory test cell. The variability of N_q was attributed to the larger particle size of the soil compared to the size of the embedded angle.

On the other hand, the back-calculated value of the coefficient of friction, tan δ, from single bars that were pulled from the experimental wall varied from 0.60 to 11.0, which was said to be much higher than would be expected for a straight bar being pulled through soil. It was collated that the high measured values were partly caused by not pulling along the alignment of the rod, from bonding of the rod as it was pulled through holes in the face of the wall, from a wedge of soil being "piled up" against the face, or from using deformed rods. Based on the equation:

$$F = f\ A\ \sigma_v \quad \ldots\ldots\ldots\ldots\ldots\ldots\ldots\ldots \quad (4)$$

where: F = peak pullout force from load-displacement curves;
σ_v = overburden pressure;
f = apparent friction coefficient; and
A = contact area = circumference x bar length,

Liu (1988) reported that the values of the apparent friction coefficients calculated for the Syro wall field pullout tests decrease with the increasing overburden pressure which agreed well with the observation published by Schlosser and Elias (1978). The decrease in apparent friction coefficient with increasing overburden pressure was attributed to suppressed dilatancy at high normal pressures, leading to the crushing of soil particles instead of rolling over each other during the process of shearing.

B. Field Pullout Tests at USAID Welded Wire Experimental Wall

The months of December 1989 to January 1990 was devoted to field pullout testing at the USAID welded wire experimental site. A total of 15 dummy mats of different sizes and configurations, and located at different levels in the wall were pulled out using the same strain rate (1 mm/min) and test procedure as adopted in the laboratory pullout tests. Photographs showing the test set-up and views of the tests at different levels in the wall are given in Figs. 58 to 65. Figure 66 depicts the front section of the welded wire wall showing the locations of the dummy mats. Also shown in the figure are the relative locations L1, L2, and L3 of the strain gages in the dummy mats.

Field pullout tests were conducted for varying overburden pressures and bar sizes as can be seen in Table 4 and plotted in Figs. 67 to 85. Three of the mats tested had no transverse bars (only 4 longitudinal bars of size W4.5), and would therefore measure only the frictional resistance. The rest of the mats were of 6" X 9" mesh size, with 5 to 6 transverse bars. These dummy mats were supplied by the Hilfiker Co. of Eureka, California. Some of them were galvanized. Two mats in each of the

three backfills were instrumented. All the mats were pulled out up to displacements of about 5 inches. The average lengths of embedment of all the mats were around 2 meters.

The field pullout (friction) tests conducted with no transverse bars, one in each of the three backfills, had about the same overburden height of 3.75 to 3.8 meters. The frictional resistances obtained in these three different soils were nearly the same. These values will be clarified from the results of laboratory pullout (friction) tests with the same diameter and number of longitudinal bars and similar overburden pressures as in the field. The friction coefficients obtained in the laboratory and the field will be compared. Furthermore, the laboratory pullout tests (for friction) will be conducted for different sizes of bars and for varying overburden pressures in order to study the variation of friction coefficient with these factors and will be correlated back to the field performance.

In all the three friction tests performed in the field, it was observed that after reaching a peak value and holding on to this peak value for a while, the maximum pullout (frictional) resistance decreased with further displacement. The value of the frictional resistance, and thereby, the friction coefficient obtained with laterite may not be truly representative (as when the embankment was resting on an unyielding foundation, or as is the case with weathered clay or clayey sand in the same embankment as the present one) due to the contradicting (with theoretical) behavior of laterite, as discussed in the following paragraphs. Hence, more laboratory friction tests will have to be conducted in order to arrive at a more decisive conclusion. The friction coefficient in the longitudinal member obtained in each of the three backfills was around 2.45.

In the case of weathered clay and clayey sand, it was observed that overburden pressures, bar sizes, and number of transverse bars definitely affected the total pullout resistances, confirming with theoretical expectations. It was observed that sizes of less than W12 X W5 could be more efficiently and economically employed to reinforce such poor-quality or marginal-quality backfills.

Comparing dummy nos. 26 (Fig. 67) and 8 (Fig. 73), both in weathered clay, of bar sizes W7 X W4.5 and mesh size 6" X 9" with same number of transverse bars and about the same lengths of embedment, but with overburden heights of 0.6 and 3.93 m, respectively, the peak pullout resistances obtained were, respectively, 3.839 and 6.428 tons. Again comparing dummy nos. 26 (Fig. 67) and 22 (Fig. 69), both in weathered clay, even though the bar sizes decreased but due to increased overburden pressure, there was a considerable increase in the maximum pullout resistances obtained. Comparing dummy no. 22 in weathered clay

(Fig. 69) and dummy no. 20 in clayey sand (Fig. 81), in the case of weathered clay, a peak value was reached at about 100 mm displacement and, thereafter, the total pullout resistance decreased. But in the case of clayey sand, the maximum pullout resistance was still increasing at about 60 mm displacement, but then had already attained the tension capacity of the reinforcement. The reinforcing mat failed bv tension simultaneously in the middle two longitudinal bars, some distance behind the grips, and outside the face of the welded-wire wall. This proves the superiority of clayey sand as a backfill material, in comparison with the other two backfills used in this context. Comparing dummy nos. 22 (Fig. 69) and 17 (Fig. 71), both in weathered clay, the sizes of bars are increased considerably in the case of the latter and also the number of transverse bars are increased to 6, but the increase in maximum pullout resistance is not very much. Comparing dummy no. 8 in weathered clay (Fig. 73) and dummy no. 7 in clayey sand (Fig. 85), it can be seen that with the same size of bars and mesh and nearly the same overburden pressures, the maximum pullout resistance in case of clayey sand is considerably higher, again proving clayey sand as a better backfill material. Dummy nos. 9 and 7 in clayey sand (Figs. 84 and 85) can also be taken to illustrate that in case of clayey sand, the maximum pullout resistance increases with overburden pressure. Also, even though the bar sizes have decreased, there is an increase in the maximum pullout resistance which can be attributed to the increased normal stress.

On the contrary, lateritic backfill shows a decrease in maximum pullout resistances with increase in the overburden pressures. The maximum pullout resistances of dummy nos. 23 and 12 in Table 4 are self explanatory. The maximum pullout resistance has reduced to about 50% of the former. Again comparing dummy nos. 21 (Fig. 75) and 15 (Fig. 76), in the case of the latter the bar sizes have increased and also the number of transverse bars are increased to 6, but still then there is a decrease in the maximum pullout resistance. To find out the exact cause of this behavior needs more investigative study. Maybe it could be due to the very high subsoil settlements beneath the lateritic backfill at the center, which must have caused the laterite in the embankment especially at the lower depths to loosen and decrease its degree of compaction due to arching effects. Another reason could be that laterite is liable to particle crushing under high normal stresses. But this seems to be less probable as to cause such drastic reduction in the pullout capacities. The other reason could be the strength variability of low quality backfill resulting from moisture regime within the reinforced mass (Hannon and Forsyth, 1984). But the probability of the influence of moisture regime also

seems to be less, since weathered clay which is also a poor quality backfill material, rather poorer than laterite, has consistently proved increased maximum pullout resistances with increase in overburden pressures and bar sizes, in conformance with the theory.

More laboratory pullout tests on laterite and a more careful study of the settlements, vertical pressures beneath the embankment, and lateral movements of the embankment and the subsoil might throw some light in this aspect. If the laboratory tests with laterite also prove to be consistent with the theoretical expectations, then the behavior of laterite as observed in the field will have to be attributed to the (soft clay) subsoil deformations and its subsequent effect on the backfill material in causing arching effects.

As regarding the strains, it was observed that the axial strains in the longitudinal bars decrease with increasing distance from the face of the wall. Comparing dummy no. 20 in clayey sand (Fig. 82) and dummy no. 22 in weathered clay (Fig. 70), it can be observed that the axial strains near the face and up to the location of the strain gauge L3 are considerably higher in the case of clayey sand than that of weathered clay. Beyond L3, the strains are nearly similar in both clayey sand and weathered clay. In the case of clayey sand dummy no. 20, there was a tension failure near the face. From the tension tests performed in the laboratory (as discussed earlier) on bars of size W4.5, the axial strain obtained at failure was about 2.25% while the yield strain was about 0.4%. Thus, with W4.5 bars it can be observed that the stresses near the face are beyond the yield point i.e., would have crossed the elastic limit, especially with clayey sand backfill. With W7 size bars the strains are well below the elastic limit.

X. FIELD BEHAVIOR OF THE USAID WELDED WIRE WALL

Periodic monitoring of the welded wire wall is continually carried out to evaluate the long term performance of both the wall and the soft subsoil. The monitoring program consists of settlement measurements, pore pressure monitoring, lateral movement monitoring, measurements of the pressure at the base of the wall, and tension measurements along the longitudinal wires. The purpose, scope, and description of the monitoring program were already described in detail in the Third Progress Report. The instrumentation plan for the monitoring program is shown in Fig. 86.

A. Lateral Movements

The plots of depth/height versus lateral movements for each of the five inclinometer casings are shown in Figs. 87 to 91 indicating continuous outward lateral movement of the wall face and the squeezing out of the subsoil beneath the embankment, but were found to be decreasing with time. After 228 days from the end of construction, the maximum outward lateral movement of the wall face is about 30 cm located at the top. The maximum lateral movement in the subsoil, in the order of 11 cm, occurs at about 3 m depth, which is along the soft clay layer (see Figs. 87 to 89). The rate of maximum lateral movement in the subsoil, however, was observed to be decreasing with time as shown in Fig. 92. Figures 93 to 95 show the vertical movement at different depths plotted against the corresponding lateral movement in the subsoil based from I1 to I3, respectively. Indicating a more stable behavior, the slopes generally decreased at the later stage after 30 days (starting from 23/06/89 onwards) as compared to the corresponding slope for a period of one month after construction (24/05/89 to 23/06/89).

B. Settlements

Surface and subsurface settlement-time relationships at different sections of the embankments are shown in Figs. 96 to 101, indicating continued settlements with time. The surface settlements at the front along the longitudinal section, near the face of the wall (S1, S2, S3) have been almost identical (see Figs. 102 and 103). The reason for the nearly identical surface settlement at the front may be attributed to the interconnection of the reinforcement at the face of the wall. The subsurface settlements at 6.0 m depth at the front along the longitudinal section have been also nearly identical (Figs. 104 and 105). However, at 3.0 m depth of the same longitudinal section, settlement plate SS4 was observed to be much lower than its adjacent settlement plate locations SS2 and SS6. This may be

caused by the squeezing out of the soft clay from beneath the center of the embankment pushing settlement plate SS4 upwards. At the back of the same longitudinal section, settlement plate S8, which is located at the lateritic soil section, settled more compared to the adjacent locations S7 and S9, installed at the clayey sand and weathered clay sections, respectively (Figs. 106 and 107). In Fig. 97, the surface settlements at the clayey sand and weathered clay sections (S1, S4, S7 and S3, S6, S9, respectively) are compared and they indicate a similarity in behavior, with larger settlement at the front, and decreasing as we go towards the back. At the lateritic soil section (S2, S5, S8), the center plate S5 is the maximum followed by the front plate S2, then the back plate S8 (Fig. 98). The subsurface settlements at 3.0 m depth along the lateritic soil section (SS4, SS8, SS10) followed the same trend as with the corresponding surface settlement behavior (Fig. 101). Figures 102 to 103 show the maximum surface settlement profiles at different sections of the embankment which indicate a dish-like deformation of the surface beneath the embankment.

C. Excess Pore Pressures

Excess pore pressure monitoring results measured from hydraulic and pneumatic piezometers installed at different depths and locations beneath the embankment, are plotted in Figs. 108 to 113. Only five hydraulic piezometer readings are presented as the other one was damaged shortly after it was activated. Also, as indicated in the Third Progress Report, three out of four pneumatic piezometers were damaged during construction, probably due to excessive settlements. As shown in the above-mentioned figures, the porewater pressures continued to decline although at a very slow rate. The porewater pressure coefficient, r_u, which is defined as the ratio of the porewater pressure at any depth to the corresponding increase in vertical stress, can be seen to be also declining. This indicated an improved stability in the long term, resulted from the dissipation of excess porewater pressure with time.

D. Earth Pressure Variations and Effect on Strains

The variation in vertical pressures beneath the embankment at different stages of construction and subsequently, after the end of construction, are shown in Figs. 114 to 123. Three earth pressure cells were placed in the center section below the lateritic soil backfill, one (E1) near the face at 0.5 m behind the face, the second (E2) at the center (3 m from the face), and the third (E3) at the back (5.5 m from the face), all below the reinforced section. The instrumentation plan is shown in Fig. 86. The summary of earth pressure readings at the base of the mechanically stabilized embankment are shown in Figs. 114 and 115.

As can be seen in Fig. 116 during the first 4 lifts (i.e. embankment at 1.35 m above the general ground level), the base pressure at the face (E1) was high and increasing, while at E2 and E3, very small pressures of about 0.1 t/m^2 were recorded. This may be due to the soft clay being squeezed out at the center (below E2 and E3) beneath the embankment out from the front, i.e. away from the vertical face. This soft clay that is being squeezed out from below the center tends to exert an upward pressure at the face as it moves out. This must have caused the center of pressure to be located near the face. Figure 117 shows the variation of these base pressures from lifts V to VIII (i.e. embankment at 3.15 m above the general ground level) (also Fig. 125). At this stage the center of pressure must have shifted backwards from near the vertical face, due to the increase in the weight of the embankment, and with it, the increase in the surface settlements at the center near E2, i.e. S5. There was a substantial increase in the values of E2 and little increase in the values of E3 while E1 remains nearly constant in this period. By the end of the twelfth lift (i.e. embankment at 4.95 m above the general ground level), the base pressures recorded in all the three cells, E1 to E3, are nearly the same (Fig. 118). The surface settlements near these points are also about the same (Fig. 126). But towards the end of construction (i.e. embankment at about 5.7 m above the general ground level) base pressure E2 is greater than E1 and far greater than E3 (Fig. 119). At this instance, the surface settlement S5 (near E2) had increased well beyond the surface settlements near the face (S2) and at the back (S8) (Fig. 127).

It has been observed throughout the post-construction phase that any abrupt increase in E2 is followed by a release of pressure at E1. This is because the centroid/center of pressure being located near E2, would cause a higher rate of lateral displacement of the soft clay subsoil below it, and also higher settlements at S5. Also here at the center, the reinforcements at different layers being independent of each other, can sink/settle more easily. But at the face, all the reinforcement layers are connected together by the facing mesh to the full height of the

wall which prevents the immediate response (in terms of settlement) of the toe of the embankment whenever there is a large settlement occurring at the center (arching effects).

This time lag in the settlement response at the toe or below the vertical face withdraws the contact between the bottom of the embankment/reinforcement and the subsoil immediately below it. This causes a release in the base pressure E1 (many a time E1 is also reduced to zero) whenever there is an abrupt increase in the value of base pressure at the center (E2). This is clearly depicted in Fig. 128 and also in Figs. 119 to 123. In Fig. 119, it can be seen that at the end of 8 days after construction, there is a considerable release or decrease in the value of E1. This release in E1 is continuing even up to 22 days after construction, when the value of E1 is reduced to zero (Fig. 120). Pressure cell E3 is more or less constant in this period. After 26 days and up to 89 days after construction (Fig. 121), when sufficient settlements would have taken place at the toe (and also at the center) for the bottom layer of the reinforcement/embankment below the vertical face to get into firm contact with the subsoil again, E1 starts picking up (increasing) again along with E2 and E3. Also, the soft clay beneath the vertical face seems to be moving upwards and pushing the weathered clay crust upwards and helping to bring back the contact between the bottom of the embankment and the weathered clay immediately below it. This is also substantiated by the observations of the subsurface settlements at 3 m depth. The lateral movement of the soft clay is found to be maximum around the same 3 m depth. At 3 m depth in the center row (i.e. 3 m behind the vertical face), the subsurface settlements are very high; but at the same 3 m depth below the vertical face, these subsurface settlements are far lower. Also at the center of the center row (below laterite) at 3 m depth, the subsurface settlement is maximum and is lesser on either side, i.e. below clayey sand and weathered clay. On the contrary, in the front row at the center below laterite, the subsurface settlement at 3 m depth is a minimum and is much higher on either side, i.e. below clayey sand and weathered clay (refer to Fig. 106). This proves the point that the soft clay beneath laterite at 3 m depth is being squeezed out from below the center and could be pushing the subsurface settlement plate near the face at 3 m depth upwards. Therefore, after the withholding forces at the face and at different reinforcement layers are being released, the weight of the embankment pushes the subsurface settlement plate at 3 m depth below laterite at face downwards and the soft clay beneath tends to push it upwards and the net result is that we have a lesser settlement at the face than at the center row. At the center row (3 m behind the face), especially at the center, there are no such opposing upward forces by way of upward movement of the soft clay and to some extent, at center-left below the weathered clay and at center-right below the clayey sand.

When E1 starts increasing from its reduced/lowest value, there will be at first a slight release in the value of E2, and thereafter E2 again starts increasing gradually at first for a while and then at some stage, there will be an abrupt increase and the whole process (of release in E1, surface settlements at the face, and also at the center and back, contact between the base of the embankment at the face and the subsoil, increase in E1, some release in E2, gradual increase in both E1 and E2, abrupt increase in E2, etc.) repeats. This process should continue until there is no more lateral movement of the subsoil, and until the process of consolidation of the subsoil is complete.

The value of E1 immediately at the end of construction was about 6.2 t/m^2. But during the entire post-construction phase until now, this value of E1 has never been able to raise beyond 1.9 t/m^2. This could mean that the contact between the toe below the vertical face and the soil immediately below it, has not been as firm as it was immediately after construction due to the arching effects caused by the facing mesh. The rate of lateral movement of the subsoil up to about 100 days after construction was still high (Fig. 92). At the end of 203 days after construction (Fig. 122, also Figs. 123 and 128), there is again an abrupt increase in the value of E2, followed by a decrease in the value of E1 to nearly zero at the end of 243 days.

Any abrupt increase in the value of E2 coupled with large settlements therein at the center, is also reflected by a sharp increase in the porewater pressures at the center as recorded in the piezometers (see Figs. 111 to 112). The rate of lateral movement of the subsoil had decreased remarkably after 100 days after construction, which means that the stability of the embankment should be improving thereafter.

The above cyclic process of variation in the base pressures due to the presence of the soft clay beneath the embankment with a vertical face have also been affecting the strains in the reinforcements in all the layers. Whenever there is an abrupt increase in the value of E2 followed by a release in the value of E1, the maximum tension at some distance behind the face and the tension near the face both increased (refer to Figs. 129 to 134). But as E1 starts picking up, followed by a slight release in the value of E2, the strains (usually tensile) in the reinforcements also show a decrease. The variation in the values of the maximum tension (the location of this maximum tension being more or less stable) and also the tension near the face, especially in the lower layers seems to be in complete conformation with the continuous variation in the base pressures. The variation in the

base pressures due to the movements of the soft clay subsoil, combined with some other physical factors could also be the cause for the compressive strains recorded in some of the reinforcement layers (Shen et al, 1976).

E. Reinforcement Stresses and Maximum Tension Line

The variation of the axial tension in the reinforcement during construction was shown for different heights of fill in the Third Progress Report, and it was discussed that the stresses measured were quite high which yielded higher values of the lateral earth pressure coefficient K. An additional analyses made in this report revealed that the magnitude of the strains in the reinforcing mats are strongly influenced by the variation of the earth pressures at the bottom of the wall as discussed in the preceding section. This is particularly true for the middle section (laterite) where the three earth pressure cells were installed. However, the response of the outer sections (clayey sand and weathered clay) were also found to be comparable to the behavior of the middle section due to their interconnections at the facing of the wall.

Figures 129 to 131 show the reinforcement tensions after 4, 8, and 12 layers of fill, respectively. The corresponding pressures at the base of the middle section are depicted in Figs. 116 to 118. It seems that the variation of the strains are in close conformity with the earth pressure variations at the wall base, particularly for the bottom 4 instrumented mats. The reinforcement tensions after construction are shown in Figs. 132, 135, and 138, respectively, for laterite, clayey sand, and weathered clay sections. The corresponding earth pressures at the base of the middle section for this stage are shown in Fig. 119. It can be seen that the bottom 4 instrumented mat layers have been affected the most by this response, and seems to display a similar trend with that of the other sections (clayey sand and weathered clay). After 26 days (from the end of construction), the strains are plotted as shown in Figs. 133, 136, and 139, for laterite, clayey sand, and weathered clay, respectively. Figure 120 shows the corresponding earth pressures at the wall base. It is believed that the abrupt change in the earth pressure near the face (E1) to almost a zero value, with E2 and E3, retaining almost the same condition as it was, immediately after construction, is the cause of the compressive strains (negative) observed in the reinforcing mats for the three sections of the wall. After 93 days, the earth pressures at 3 locations were found to increase drastically at almost the same rate as shown in Fig. 121. This resulted to very high stresses recorded for all the layers in the 3 backfills as depicted in Figs. 134, 137, and 140.

The response generated by the wall due to foundation compressibility creates a unique situation wherein existing theories on earth pressures may not be directly applicable. One possible inference is the location of the maximum tension line which is believed to define the failure surface or wedge of a Coulomb/Rankine type failure plane, or maybe the reinforced earth bilinear failure plane (see Figs. 132 to 140), or the log spiral failure plane. These theories were derived primarily for those cases wherein the wall foundation is rigid, causing the wall to possibly rotate about the toe. The resulting base pressure for such a case maybe uniform, trapezoidal, or triangular, with the maximum below the wall face. The plots of maximum tension observed in the USAID welded wire wall was found to closely conform to the log spiral failure plane (farther from the face than Coulomb failure plane) at lower half of wall, and conform to the reinforced earth failure plane (closer to the face than the Coulomb failure plane) for upper half of the wall. For subsequent analyses, finite element models will be used. This is especially true for the middle section wherein the settlement profile indicates maximum settlement at the center (Fig. 103). For the outer sections wherein the settlement profiles were almost identical, with maximum at the face, conformity with existing theories maybe possible.

XI. NUMERICAL MODELING OF REINFORCED SOIL SYSTEMS

A. Introduction

In the recent years, the finite element method has become an effective and established tool in the solutions of static and dynamic analysis of complex earth and rock engineering problems. The method has the advantage that distributions of stresses and displacements can be obtained both in the subsoil and in the structure itself. It has also other unique capabilities of incorporating problems which involve material non-homogeneity, nonlinear stress-strain behavior of the soil, complex boundary conditions, incremental loading sequence, etc.

Finite element techniques have also been, and are being, used in the analysis of many reinforced/mechanically stabilized earth structures. Finite element techniques can also be used to determine the pullout resistance of the reinforcements. The successful application of the method in the field of geotechnical engineering depends to a large extent upon the use of appropriate geomechanical models for a given type of situation which involves determination of representative material parameters. When the stress-strain relationship is inelastic, it is generally known as material nonlinearity, whereas when the strain-displacement relationship is nonlinear, it is known as geometric nonlinearity. Nonlinear problems are being solved by either the variable stiffness method or the initial stiffness method. In nonlinear analysis, loads will have to be applied incrementally. With nonlinear stress-strain laws, the stiffness is not constant but is dependent on the stress or strain. In the variable stiffness method, the elasticity matrix is adjusted. The other techniques use a constant value of the elasticity matrix and adjustments are done for the initial strain or initial stress. The former is called the "initial strain" approach, and the latter is called the "initial stress" approach. The initial stress approach involves a number of iterations for each load increment until convergence is attained. The method is applicable to all cases such as strain hardening, perfectly plastic materials, and cyclic loadings. In the case of strain softening, the convergence is very slow and some accelerator techniques are used.

Various shapes of finite elements are used in the finite element analysis. Some of the shapes represent a number of different types, depending on the degrees of freedom at each node. Higher order elements with more than one midside node are also available. For geotechnical problems, triangular elements applied in a plane strain analysis are most commonly used. In the finite element analysis of reinforced soil systems, the slippage between the soil and the reinforcement is of prime concern. The adequate modeling of the soil-reinforcement interaction requires

the use of appropriate interface elements which are capable of expressing the behavior of discontinuous plane between grid reinforcement and soil with a peculiar friction. Joint elements have been used to represent the interface conditions such as the joints in rocks. Goodman et al (1968) originally developed the stiffness matrix of a two-dimensional joint element with four nodes of a length L and zero thickness.

B. Finite Element Analysis of Reinforced Soil Systems

There are two general approaches to FEM analysis of reinforced soil systems involving, respectively, discrete and composite representations of the constituents (Hermann and Al-Yassin, 1978) as discussed below.

Discrete Material Approach

In a discrete representation (Clough and Tsui, 1974; Al-Hussaini and Johnson, 1977), the reinforced system is modeled as distinct materials that interact with each other. The soil is usually represented by an array of continuum elements and each and every reinforcement is represented by either an array of continuum elements or a one-dimensional string of bending elements. The advantage of the approach which renders it preferable is that the properties and responses of the soil-reinforcement interfaces are directly quantifiable. The chief disadvantage, however, is the excessive computational cost (computer capacity and analysis time) for those configurations containing large numbers (possibly hundreds) of reinforcing members.

Composite Material Approach

The composite model concept (Romstad et al, 1976) is developed by consideration of a small unit of the material as a fundamental building block called the "unit cell" or "representative volume." The composite properties defining the stress-strain relationships are predicted by considering a number of simple composite stress-strain states and approximately determining the response of the unit cell. The basis for such a representation involves extending the continuum concept to a larger level of observation. When performing a finite element analysis of a composite representation of a reinforced material, the body is represented by an array of continuum elements whose boundaries need bear no spatial relationship to the geometric arrangement of the reinforcing members. The "composite" material properties assigned to the continuum elements reflect the properties of the matrix material and the reinforcing members,

and their composite interaction. The advantage of a composite representation is the economy of analysis achieved by not having to discretely represent each and every reinforcing member. The disadvantage is that the analysis does not directly yield detailed information about the stress and strain states at the interfaces of the soil and the reinforcing members nor about localized deformations near the edges of the reinforced mass.

Both approaches described above have been used successfully to predict stresses in uncompacted full-scale structures (Hermann and Al-Yassin, 1978; Al-Hussaini and Johnson, 1978; Clough and Tsui, 1974; Chang and Forsyth, 1977; Liu, 1988). However, recent evidence suggests that construction operations have a significant effect on stresses and deformations in reinforced soil walls (Ingold, 1983; Collin, 1986; Seed and Duncan, 1986; Schmertmann et al, 1989). A discrete finite element analysis which explicitly accounts for construction compaction operations has therefore emerged recently as the preferred method of analysis (Schmertmann et al, 1989).

C. Modeling of Material Behavior

Soil Stress-Strain Relation

The successful application of the finite element method in the analysis of reinforced soil systems depends to a large extent upon the use of appropriate geomechanical models for its constitutive behavior which is known to be nonlinear, inelastic, and highly stress dependent. Unfortunately, no complete satisfactory model has as yet been proposed and accepted. The most commonly used and implemented model in today's FEM computer programs is the nonlinear elastic (with inelastic unloading) model proposed by Duncan (Duncan and Chang, 1970; Wong and Duncan, 1974). In this model, the soil is usually represented by a constant-strain triangular or quadrilateral elements. In each increment of the analysis, the stress-strain behavior of the soil is treated as homogeneous, isotropic, and piecewise linear and the relationship between stress and strain is assumed to be governed by the generalized Hooke's law of elastic deformations, which may be expressed for conditions of plane strain as:

$$\begin{Bmatrix} \Delta\sigma_x \\ \Delta\sigma_y \\ \Delta\tau_{xy} \end{Bmatrix} = \frac{E_t}{(1+\nu_t)(1-2\nu_t)} \begin{bmatrix} (1-\nu_t) & \nu_t & 0 \\ \nu_t & (1-\nu_t) & 0 \\ 0 & 0 & (0.5-\nu_t) \end{bmatrix} \begin{Bmatrix} \Delta\varepsilon_x \\ \Delta\varepsilon_y \\ \Delta\gamma_{xy} \end{Bmatrix} \quad (5)$$

in which:

$\Delta\sigma_x$ and $\Delta\sigma_y$: normal stress increment in x and y directions, respectively;
$\Delta\tau_{xy}$: shear stress increment;
$\Delta\varepsilon_x$ and $\Delta\varepsilon_y$: normal strain increment in x and y directions, respectively;
$\Delta\gamma_{xy}$: shear strain increment;
E_t : tangent Young's modulus; and
ν_t : tangent Poisson's ratio.

The instantaneous values of the Young's modulus (E_t) and Poisson's ratio (ν_t) in each element is changed during each increment of loading in accordance with the calculated stresses in every element in order to account for the important soil characteristics (i.e. nonlinearity, stress-dependency, and inelasticity).

It was subsequently shown (Duncan et al, 1980) that the volume change behavior of most soils can be modeled with equal accuracy by assuming that the bulk modulus of the soil varies with confining pressure and is independent of the percentage of strength mobilized. This assumption yields a more reasonable means of representing the mechanical properties of soils at high stress levels. Employing this assumption, the above equation can be expressed in the following manner:

$$\begin{Bmatrix} \Delta\sigma_x \\ \Delta\sigma_y \\ \Delta\tau_{xy} \end{Bmatrix} = \frac{3M_b}{(9M_b-E_t)} \begin{bmatrix} (3M_b+E_t) & (3M_b-E_t) & 0 \\ (3M_b-E_t) & (3M_b-E_t) & 0 \\ 0 & 0 & E_t \end{bmatrix} \begin{Bmatrix} \Delta\varepsilon_x \\ \Delta\varepsilon_y \\ \Delta\gamma_{xy} \end{Bmatrix} \qquad (6)$$

where M_b represents the bulk modulus of the soil.

After numerous laboratory tests and in-depth research, Duncan et al (1980) conclusively reported that the tangent values of Young's modulus (E_t) vary with the confining pressure and the percentage of strength mobilized. Furthermore it was construed that the values of bulk modulus (M_b) vary with confining pressure and are independent of the percentage of strength mobilized.

Tangent Modulus (E_t)

The hyperbolic description of stress-strain curves (Fig. 141) developed by Kondner (1963) has been found to be a convenient and useful means of representing the nonlinearity of the stress-strain behavior of the backfill materials. The hyperbolic formulation of the stress-strain curves can be represented by an equation of the form:

$$(\sigma_1 - \sigma_3) = \frac{\varepsilon}{(1/E_i) + [\varepsilon/(\sigma_1-\sigma_3)_{ult}]} \quad \ldots\ldots\ldots\ldots (7)$$

where:
E_i = initial Young's modulus;
ε = strain;
$(\sigma_1-\sigma_3)$ = deviator stress; and
$(\sigma_1-\sigma_3)_{ult}$ = the asymptotic values of stress difference which is close to the strength of the soil.

Transforming the hyperbolic equation (Eq. 7), we obtain the following linear relationship between $\varepsilon/(\sigma_1-\sigma_3)$ and ε which can be used to obtain the values of E_i and $(\sigma_1-\sigma_3)_{ult}$ at a specific confining pressure σ_3:

$$\frac{\varepsilon}{(\sigma_1-\sigma_3)} = \frac{1}{E_i} + \frac{\varepsilon}{(\sigma_1-\sigma_3)_{ult}} \quad \ldots\ldots\ldots\ldots (8)$$

Using the empirical equations suggested by Janbu (1963), the variation of E_i with confining pressure (σ_3) may be taken into account from:

$$E_i = K*P_a*(\sigma_3/P_a)^n \quad \ldots\ldots\ldots\ldots\ldots\ldots (9)$$

where: K = modulus number;
P_a = atmospheric pressure; and
n = modulus exponent.

The compressive strength or stress difference at failure, $(\sigma_1-\sigma_3)_f$ as shown in Fig. 141 can be related to $(\sigma_1-\sigma_3)_{ult}$ by:

$$(\sigma_1-\sigma_3)_f = R_f*(\sigma_1-\sigma_3)_{ult} \quad \ldots\ldots\ldots\ldots\ldots (10)$$

in which R_f is the failure ratio which varies from 0.50 to 0.90 for most soils. The variation of $(\sigma_1-\sigma_3)_f$ with σ_3 is represented

by the Mohr-Coulomb strength relationship, which can be expressed as follows:

$$(\sigma_1-\sigma_3)_f = (2c*\cos\phi + 2\sigma_3*\sin\phi)/(1-\sin\phi) \quad \ldots\ldots\ldots \quad (11)$$

in which c and ϕ are the cohesion intercept and friction angle of the soil, respectively.

The instantaneous Young's modulus, E_t, for primary loading (values of the main shear stress larger than any previous value for the element) can then be found by differentiating Eq. 8 with respect to ε and substituting the expressions of Eqs. 9, 10 and 11 into the resulting expression to yield:

$$E_t = \left[1 - \frac{R_f*(1-\sin\phi)*(\sigma_1-\sigma_3)}{2c*\cos\phi + 2\sigma_3*\sin\phi}\right]^2 K*P_a*(\sigma_3/P_a)^n \quad \ldots\ldots \quad (12)$$

The above equation (Eq. 12) can be used to calculate the appropriate value of tangent modulus for any stress conditions σ_3 and $(\sigma_1-\sigma_3)$ given the other parameters. Parameters K, n, R_f, c, and ϕ are determined from the results of triaxial or plane strain compression tests performed on specimens of the backfill material (Wong and Duncan, 1974; Duncan et al, 1980).

Bulk Modulus (M_b)

The bulk modulus was previously assumed to be a constant for a given minor principal stress, but was later found to vary with minor principal stress in the same manner as the initial tangent modulus and the unloading-reloading modulus (Clough and Duncan, 1971). The equation employed to calculate the bulk modulus was:

$$M_b = \frac{0.50*E}{(1+\nu)(1-2\nu)} \quad \ldots\ldots\ldots\ldots\ldots\ldots \quad (13)$$

in which $E=E_i$ during loading and $E=E_{ur}$ during unloading and reloading. The value of the bulk modulus can also be defined by:

$$M_b = (\Delta\sigma_1 + \Delta\sigma_2 + \Delta\sigma_3)/(3\Delta\varepsilon_v) \quad \ldots\ldots\ldots\ldots\ldots \quad (14)$$

in which M_b is the bulk modulus, $\Delta\sigma_{1,2,3}$ are the changes in the values of the principal stresses, and $\Delta\varepsilon_v$ is the corresponding change in volumetric strain. Duncan et al (1980) found that most soils exhibit nonlinear and stress-dependent volume change characteristics as illustrated in Fig. 142. For a conventional triaxial test in which the deviator stress $(\sigma_1-\sigma_3)$ increases

while the confining pressure is held constant, Eq. 14 can be expressed as:

$$M_b = (\sigma_1 - \sigma_3)/(3*\varepsilon_v) \quad \ldots\ldots\ldots\ldots\ldots\ldots \quad (15)$$

It was also suggested that the bulk modulus can be calculated from the following procedure:

(a) If the volume change curve does not read a horizontal tangent prior to the stage at which 70% of the strength is mobilized, use the points on the stress-strain and volume change curves which correspond to a stress level of 70%.

(b) If the volume change curve does reach a horizontal tangent prior to the stage at which 70% of the strength is mobilized, use the point in the volume change curve at which it becomes horizontal and the corresponding point on the stress-strain curve.

It was further inferred that the bulk modulus may be found by an empirical equation if the same soil is tested at various confining pressures as depicted in Fig. 143, i.e.

$$M_b = K_b*P_a*(\sigma_3/P_a)^m \quad \ldots\ldots\ldots\ldots\ldots\ldots \quad (16)$$

in which K_b is the bulk modulus number, m is the bulk modulus exponent, and P_a is the atmospheric pressure expressed in the same units as σ_3 and M_b.

Tangent Poisson's Ratio

The tangent Poisson's ratio (ν_t) maybe related to the soil bulk modulus M_b using the following equation:

$$\nu_t = 0.50 - \frac{E_t}{6M_b} \quad \ldots\ldots\ldots\ldots\ldots\ldots \quad (17)$$

Using the above expression, Hermann (1978) limited the values of ν_t for mechanically stabilized retaining walls to avoid numerical problems to $0 \leq \nu_t \leq 0.49$. Thus, if the above equation (Eq. 17) is adopted, the following condition must be imposed when too high or too low bulk modulus values M_b are generated in Eq. 17:

$$17*E_t \geq M_b \geq E_t/3 \quad \ldots\ldots\ldots\ldots\ldots\ldots \quad (18)$$

An expression for the tangent Poisson's ratio was also developed by Kulhawy et al (1969) in the following form:

$$\nu_t = \frac{H - F*\log(\sigma_3/P_a)}{1 - \dfrac{d*(\sigma_1-\sigma_3)}{K*P_a*(\sigma_3/P_a)^n\left[1 - \dfrac{R_f*(1-\sin\phi)(\sigma_1-\sigma_3)}{2c*\cos\phi + 2\sigma_3*\sin\phi}\right]^2}} \qquad (19)$$

where G, F, and d are material parameters.

In general, the friction angle (ϕ) is not constant but decreases with increasing stress level as follows:

$$\phi = \phi_1 - \delta\phi*\log(\sigma_3/P_a) \quad \ldots\ldots\ldots\ldots\ldots\ldots \quad (20)$$

in which ϕ_1 is the value of the friction angle at a confining stress of one atmosphere and $\delta\phi$ is the reduction in friction angle for a ten-fold increase in confining stress.

The Duncan model described above provides an option wherein an equation for Poisson's ratio is replaced by the one expressed in terms of Duncan's variable value for E and a constant value for the bulk modulus. This alternative formulation assures that mass will be conserved for near failure states (Hermann and Al-Yassin, 1978).

A strain compatibility design approach for reinforced soil walls with metallic reinforcements had recently been presented by Juran and Chen (1989). The design approach which satisfy the soil-reinforcement strain compatibility requirements was fundamentally based on the analogy between the plane strain shear mechanism which develops along a potential failure surface in the actual structure and the response of the reinforced soil material to direct shearing. The assumptions were verified by comparing the numerical simulations of construction process with the experimental results obtained on both reduced scale model walls and full scale structures.

D. Analytical Method for Soil-Geogrid Interaction

The Concept of Grid Junctions

Most of the design methods for reinforced soil structures currently being employed are based on the theory of rigid-plasticity which takes no account of displacement and deformation of reinforcing material in the soil. Specifically, these design methods do not properly account for the realistic stress-strain properties of the reinforcement and the soil, which can significantly affect the tension forces in the inclusions of actual reinforced earth structures. The rapidly increasing use of a large variety of extensible and inextensible reinforcements requires appropriate strain compatibility design methods to predict tension strains and stresses in the inclusions under expected working loads. Ochiai and Sakai (1987) conducted experimental studies using pullout shear box apparatus and have emphasized the important role of grid junctions in the pullout resistance (Ochiai et al, 1988a). The pullout behavior of polymer geogrid was observed visually by using a soil box with transparent plastic plate. The plastic plate was marked by vertical red lines and the marker rubber membrane strips were pasted with silicone grease on the plate to make clear the displacement of each grid. Applying a constant confining pressure, the grid was pulled out with constant speed. It was found that an elliptic slip field is formed in front of each grid junction and expanded with increasing displacement level of the grid junction. When the displacement reaches some large value, adjacent slip fields interact each other so that the pullout resistance acting on each junction decreases and reaches the residual state.

Figure 144 shows an example of the results obtained from a series of pullout tests in a soil box on geogrids by Ochiai and Sakai (1987), in which the pullout resistance mobilized on each grid junction is plotted against the displacement of junction at a given pullout force, F. The resistance force changes with the displacement of junction in a shape of convex distribution, and two limit curves, upper and lower, can be drawn along the group of distribution curves. In the initial stages of displacement under small pulling forces, the resistance mobilized on the junctions along the forefront side approaches the lower limit curve. On the other hand, the resistance acting on the subsequent junction comes nearer to the upper limit curve. It was implied that for either limit curve, there is a kind of friction law expressed by the following equation which is expressed as a function of the displacement of the grid junction:

$$S = C_o + f_o N \quad \ldots\ldots\ldots\ldots\ldots\ldots\ldots \quad (21)$$

where S and N are, respectively, the pullout resistance and the vertical force per unit width, and C_o and f_o are coefficients corresponding to cohesion and friction components of the pullout resistance, respectively.

As the polymer grid in the soil is subjected to a pulling force, the pullout resistance is mobilized on both the grid junctions and ribs of the polymer grid (Fig. 145a). Since the soil on either side of the grid is partially continuous, the resistance effect of the rib at right angle with the direction of pulling is assumed to be transferred to the grid junctions in a concentrated manner as shown in Fig. 145b. The pullout force, F_t, exerted in front of the geogrid produces a displacement, X_i, at each grid junctions which can be measured in a pullout test under a condition of constant vertical stress (Fig. 145c). The strain, ε_{ij}, of the geogrid between junctions is calculated by:

$$\varepsilon_{ij} = (X_i - X_j)/a \quad \ldots\ldots\ldots\ldots\ldots\ldots \quad (22)$$

where a is the distance between each grid junction. Figure 145d shows the strains plotted against the junction number. The pulling force (F_i) betwen each grid junction that correspond to the strain, ε_{ij}, is determined using standard stress-strain curves of the geogrids (e.g. Netlon, 1984). The plot (Fig. 145e) of the pulling force (F_i-F_j) represents the pullout resistance, T_i, mobilized on the grid junction. The distribution of the pullout resistance acting on the geogrid is not always uniform even at the same level of vertical stress but varies with the displacement of grid junctions in the soil. The shear stiffness, K_s, can be obtained from the plot of T_i versus the displacement of grid junction, u, by the following expression:

$$2*\tau = 2*K_s*u \quad \ldots\ldots\ldots\ldots\ldots\ldots \quad (23)$$

$$2*\tau = T_i/(\text{length of ribs}) \quad \ldots\ldots\ldots\ldots\ldots \quad (24)$$

where τ is the shear resistance.

Finite Element Implementation

Using the analytical method described above for the interaction of soil-geogrid systems, the FEM model transform this system into a combination of the joint element which expresses the property of a discontinuous plane (interface with the soil), and a truss element which is assumed to transmit axial force only as shown in Fig. 146. The grid is modeled by a truss element whose ends are connected by the pin joint. Using the joint element, the mechanism of pullout resistance of the geogrids in soils can be treated as a nonlinearity of the element. Considering the possibility of expressing the change of

coefficients of pullout resistance with the shear displacement, the nonlinear behavior of the joint element can be evaluated by introducing the dependence of shear displacement into a shear stiffness.

The joint element has two unit stiffnesses, namely: a normal stiffness, K_n, and a shear stiffness, K_s. The former expresses a transmission of axial forces only, while the latter describes the sliding against a shear displacement. The shear stiffness can be determined from laboratory pullout tests based on the analytical procedure outlined previously. The value of the normal stiffness, K_n, is found to be constant for working stresses. In soil-structure interaction problems, it is usually assumed that the structural and the soil medium may not penetrate each other and, hence, during the translational and shear model, the value of the normal stiffness, K_n, is assumed to be very high, of the order of 10^8-10^{12} (F/L^3) (Desai, 1981). Recently, Kennedy et al (1988) reported that large changes in the value of K_n were found to have negligible effects on the results.

The relationship between shear displacement $\{u\}_{s,n}$ of the joint element (length=L) and the incremental loading $\{F\}_{s,n}$ is given by the following expression:

$$\{F\}_{s,n} = [K]_{s,n} \{u\}_{s,n} \quad \ldots\ldots\ldots\ldots\ldots\ldots \quad (25)$$

where the local stiffness matrix of the joint element, $[K]_{s,n}$ is expressed by:

$$[K]_{s,n} = L/4 \begin{bmatrix} K_s & 0 & K_s & 0 & -K_s & 0 & -K_s & 0 \\ 0 & 2K_n & 0 & 0 & 0 & 0 & 0 & -2K_n \\ K_s & 0 & K_s & 0 & -K_s & 0 & -K_s & 0 \\ 0 & 0 & 0 & 2K_n & 0 & -2K_n & 0 & 0 \\ -K_s & 0 & -K_s & 0 & K_s & 0 & K_s & 0 \\ 0 & 0 & 0 & -2K_n & 0 & 2K_n & 0 & 0 \\ -K_s & 0 & -K_s & 0 & K_s & 0 & K_s & 0 \\ 0 & -2K_n & 0 & 0 & 0 & 0 & 0 & 2K_n \end{bmatrix} \quad (26)$$

The above FEM model have been successfully employed to analyze the settlement of an actual box culvert and sewage pipeline construction with reinforced foundation (Bergado et al, 1988a;1988b) and the behavior of polymer grid reinforcement retaining walls (Ochiai and Sakai, 1987; Ochiai et al, 1988a,1988b; Ogisako et al, 1988).

XII. COMPUTER PROGRAM NON LIN 1

The Non Lin 1 program combines the joint element expressing the property of the discontinuous plane with the bar element transmitting axial force only. The program was based on the analytical method suggested by Ochiai and Sakai (1987) and was developed to solve various nonlinear problems in structural mechanics and geomechanics. Material nonlinearity is included and uses "initial stress" iterative technique. The program is useful in modelling the soil-reinforcement interaction in a pullout test and can be used to predict the pullout resistance of the reinforcement of given geometry.

A. Element Types

1. One-dimensional bar element in two-dimensional space to model reinforcing bars. Only axial stresses are allowed. The element can have either 2 or 3 nodes to represent linear or quadratic variation of displacements.

2. Two-dimensional isoparametric plane stress or plane strain element are used to model the continuum problems. The shape of the element can be triangle or general quadrilateral. Triangular element has either 3 or 6 nodes to represent linear or quadratic variation of displacements. Six noded element can be of curved shape. Quadrilateral element with 4 or 8 nodes can also be used to represent linear or quadratic variation of displacements. Eight-noded element can be of curved shape.

3. Two-dimensional joint element are used to express the property of the discontinuous plane or any interface conditions. It can have normal and shear stresses. The element has either 4 or 6 nodes to be compatible with continuum element of 4 or 8 nodes. The joint element expresses a transmission of compressive force and a sliding against shear displacement. The relationship between shear displacement $\{u\}_{s,n}$ of the joint element of length L, and incremental loading $\{F\}_{s,n}$ is given in Eqs. 25 and 26.

B. Material Nonlinearities

The following discusses the types of material nonlinearities which have been included in the program.

Elastic-Plastic Material Models

(a) Von-Mises Yield Criterion

In this criterion, the material can be assumed as work hardening or perfectly elastic. The yield criterion is given by:

$$F = J_2^{0.50} \quad \ldots\ldots\ldots\ldots\ldots\ldots \quad (27)$$

where F is the yield function. The parameter J_2 is the second stress invariant given as:

$$J_2 = I_1^2/3 - I_2 \quad \ldots\ldots\ldots\ldots\ldots\ldots \quad (28)$$

or

$$J_2 = (1/6)[(\sigma_x-\sigma_y)^2+(\sigma_y-\sigma_z)^2+(\sigma_z-\sigma_x)^2]+\tau_{xy}^2+\tau_{yz}^2+\tau_{zx}^2 \quad (29)$$

(b) Drucker-Prager Yield Criterion (Extended Von-Mises Criterion)

This criterion is suitable for cohesion-friction materials and is based on the Mohr-Coulomb hypothesis. The material is assumed to be elastic-perfectly plastic. Plane strain condition is assumed. The yield criterion is given by:

$$F = \alpha J_1 + J_2^{0.50} - K \quad \ldots\ldots\ldots\ldots\ldots\ldots \quad (30)$$

$$\alpha = \tan\phi/(9 + 12*\tan^2\phi)^{0.50} \quad \ldots\ldots\ldots\ldots \quad (31)$$

$$K = 3c/(9+12*\tan^2\phi)^{0.50} \quad \ldots\ldots\ldots\ldots\ldots\ldots \quad (32)$$

where c is the cohesion and ϕ is the angle of internal friction of the soil.

Tension Cut-off Model

This model can be used where tensile stresses cannot exceed the tensile strength of the material. As a result, the excess tensile stress at any location is redistributed to the other parts of the continuum.

Nonlinear Joint Model

In this model, the normal stress for a joint element can be only compressive. If they are tensile, tension cut-off criterion is then applied. The shear stress can only be within the shear strength. If the strength is exceeded, the excess stresses are redistributed using initial stress technique.

XIII. COMPUTER PROGRAM REA (REINFORCED EARTH ANALYSIS)

A. Background

The REA program developed by Hermann (1978a) was specifically designed to analyze Reinforced Earth Walls (e.g. Chang and Forsyth, 1977). The program assumes plane strain condition and implements the composite material approach to model the reinforced soil systems. Liu (1988) reported that from the theoretical basis, the program will overestimate the displacement at the edge of a reinforced body (see Fig. 147) which consequently lead to a generation of larger force in the reinforcement than actually occurs.

B. General Features

Incremental Iterative Analysis

The behavior of soil is in general nonlinear inelastic and the slippage process is very strongly nonlinear and inelastic. To account for these phenomena, the REA program utilizes an incremental-iterative solution procedure.

Material Models

The nonlinear elastic (with inelastic unloading) model proposed by Duncan and Chang (1970) and Wong and Duncan (1974) has been used in the program to model the constitutive behavior of the backfill material. An option has been provided wherein the equation for Poisson's ratio given by Duncan is replaced by the one expressed in terms of the variable E and a constant value for the bulk modulus.

For metal reinforcing material, an elastic-plastic, isotropic strain hardening model with rupture determined by a maximum strain criterion is used. For the purposes of determining when yielding or rupture occurs, it is assumed that the axial force is dominant; hence, shear and moments are considered not to contribute to the onset of these phenomena and, in addition, in the plastic range the incremental bending stiffness is based on the incremental plastic modulus. In the case of the facing plates which may buckle at stress levels much lower than the yield value, the pre- and post-buckling behaviors are modeled by the elastic-plastic model; with the yield stress being set equal to the buckling stress.

Modeling the Foundation Material

The program provides three different methods for modelling the foundation material upon which a reinforced soil structure rests i.e., (a) Represent all parts of the foundation by finite elements, (b) Model the constraints, on the soil mass of interest, by boundary springs, (c) Model the interface by a frictional-cohesional law as described by Hermann (1978b). This procedure is particularly well-suited for a configuration where the interface between the soil mass being analyzed and the surrounding soil or rock is sharply defined.

Slippage Model

One of the critical aspects of composite behavior for reinforced materials is the possible breakdown of the bond between the constituent materials and subsequent slippage of the reinforcement (Hermann, 1977). This phenomenon has been regarded important for reinforced soil where the bond is primarily the result of friction and hence is relatively weak.

The force slip relationship observed in "pullout" tests is modeled by introducing artificial bond links or spring between the reinforcement and the soil and selecting the nonlinear stiffness characteristics of the tangential bond springs. The usual procedure is to place a pair of nodes at the same initial geometric location, one attached to the reinforcement and the other to the soil and link them with a pair of nonlinear springs normal and tangential to the reinforcement. The principal advantages of the procedure are the relatively accurate bond stress predictions and the straightforward manner in which slippage is introduced. The procedure, however, has two disadvantages. The normal link

introduces an additional global unknown (relative normal displacement) which is of little practical significance (unless actual separation occurs in the system being analyzed). Secondly, the description of the nonlinear stiffness for the tangential link, for systems above the primary mechanism for developing bond stress is friction, is difficult.

Figure 148 illustrates the idealized model of bond between reinforcement and soil. The soil and reinforcement experience the same normal displacements u_n; however, the tangential displacements u_t differ by the relative movement δ. In the case when the attainable bond stress has been fully mobilized (denoted by ISPRG=0), the relative movement δ is the resulting slippage. When the bond has not broken down (denoted by ISPRG=1), relative movement δ is resisted by the fictitious, uniformly distributed bond springs. If the stiffness K of the fictitious springs is made very large, the relative movement can be made effectively zero. The logic for determining the values of ISPRG (i.e., whether or not slippage occurs) and τ_{max} is described by Hermann (1977). When the maximum attainable bond stress τ_{max} is exceeded, slippage is resisted by τ_{max} applied as loads to the soil and the reinforcement. It is assumed that the maximum bond stress is determined by a Coulomb law, i.e., $\tau_{max}=c-f\sigma_n$. It is further assumed that even though slippage has taken place, that cohesion is maintained; the analysis can be modified to account for cases where cohesion vanishes (or is reduced) once slippage occurs. The procedure can also be modified to treat nonlinear Mohr envelope representations of bond strength.

Edge Effects

For sparsely reinforced systems, such as the case of a reinforced soil, characterization of edge effects plays a very important role. Hermann (1977) reported that the neglecting of the edge effects in the analysis may give a distorted view of the effectiveness of the reinforcement near the boundaries of the body.

The predicted deflection and stress distribution for a free edge of a loaded reinforced soil wall are shown in Fig. 147a,b. Because the edge is free, the edge stress distribution must yield a zero resultant, i.e., F_c is the integral of $\sigma_x(y)$. Figure 147b shows the actual deflection and stress distribution. In this figure, the facing plate is assumed to be extremely flexible and merely serves to

restrain the soil from "falling out" of the wall. The free edge distribution as shown in Fig. 147a is obtained in case where the facing plate is infinitely stiff in bending, thus, preventing all edge effects.

Due to the edge effect, there is a local displacement of the reinforcement relative to the average displacement of the composite system, i.e. $\delta = u_c - u_r$ (Fig. 147). This displacement (edge effect) is modeled by the relative movement between soil and reinforcement, which results from the presence of the fictitious bond springs as part of the reinforcement slippage model. The analysis for determining the spring coefficient assumes the soil to be isotropic; thus it is required to define an equivalent isotropic incremental soil shear modulus if a nonlinear inelastic characterization were to be used for the soil (includes damage-induced anisotropy).

C. Finite Element Implementation

The first step in the FEM implementation of the REA program is to express orthotropic composite material properties as functions of the properties of the individual constituent materials and their geometric arrangement. Structural analysis are then performed by utilizing the composite properties in conventional numerical analysis programs applicable to orthotropic bodies. An alternative procedure is used to account for the composite nature of the system by directly combining the element stiffness matrices of the constituents.

The finite element analysis is performed by subdividing the structure to be analyzed into a large number of regularly shaped elements; within each element simple functions are used to approximate the solution. The procedure adopted for developing the element stiffness matrix for reinforced soil is to successively apply the approximate displacement field to each of the several constituents of the composite and to sum the results. The constituents comprise of the soil, the M reinforcement systems, and the M systems of bond springs linking the reinforcement and the soil. Denoting the element stiffness and load matrices for the composite as $[K]_c$ and $[L]_c$, respectively, the composite behavior of reinforced soil yields (because of the

low volume fraction of reinforcement the several constituents are treated as coexistent):

$$[K]_c = [K]_s + \sum_{m=1}^{M} \{ [K]_{rm} + [K]_{\delta m} * ISPRG_m \} \quad . . . . . (33)$$

$$[L]_c = [L]_s + \sum_{m=1}^{M} [L]_{\lambda m} \quad . . . . . (34)$$

The respective contributions of the soil, reinforcement, and bond springs are subscripted S, r_m and δ_m. The code $ISPRG_m$ as discussed in the previous section (Fig. 148) denotes whether or not the bond springs are present. When slippage occurs, the applied bond stress τ_{max} (Fig. 148) contributes to the load matrices for both the soil and the reinforcement.

D. Modifications Made on the REA Program

Material Model

Liu (1988) modified the code of REA according to the newer Duncan's soil model (Duncan et al, 1980) as given in Eq. 6. Reinforcement tensile stresses and vertical soil pressures at three locations (bottom, middle height, top) of the WES wall (Al-Hussaini and Johnson, 1978) and the Rainier Avenue wall (Anderson et al, 1988) upon completion of the construction were then compared using the older soil model (Duncan and Chang, 1970; Wong and Duncan, 1974). It was concluded that the resulting reinforcement and soil stress distribution patterns using the 1974 and 1980 soil models are basically similar to each other in shape. Furthermore, it was reported that except for reinforcement stress curve at the middle height in the WES wall, all curves show a tendency that the 1974 soil model results in slightly higher vertical soil pressures and reinforcement stresses than that of the 1980 soil model.

Equivalent Friction Coefficient

Since the REA program was developed for the analysis of Reinforced Earth wall which utilizes steel strips as reinforcing material in the retaining wall, it naturally does not apply to other types of mechanically stabilized retaining walls such as the welded wire wall where the anchoring effect of the transverse members must be considered. In order to match the REA input format, Liu (1988) transformed the tie-back anchor wall (Syro wall) and the welded wire wall (Rainier Avenue) into a Reinforced Earth wall by using high equivalent friction coefficient as respectively shown in Figs. 149 and 150 to simulate the high pullout resistant force provided by the transverse wires. In mechanically stabilized retaining walls, the friction force between the soils and the reinforcement can be obtained by:

$$F = f * N = f * A * \sigma_v \quad \ldots\ldots\ldots\ldots\ldots\ldots \quad (35)$$

where A is the contact surface area of the reinforcement with soil, and σ_v is the vertical soil pressure.

By transforming the REA inputs from flat steel strips to round bars comprising the longitudinal members of the welded wire wall, the average soil pressure was calculated from:

$$\sigma_{ave} = 0.50(\sigma_v + \sigma_h) = 0.50(\sigma_v + K_o*\sigma_v)$$

$$= 0.50(\sigma_v + 0.50\sigma_v) = 0.75\sigma_v \quad \ldots\ldots\ldots\ldots \quad (36)$$

and substituting into Eq. 35:

$$F = f * A * 0.75\sigma_v = (0.75f)*A*\sigma_v = f'*A*\sigma_v \quad \ldots\ldots \quad (37)$$

in which $f'=0.75f$ is termed the equivalent friction coefficient in the REA inputs for round bars and for longitudinal reinforcement.

For the transverse members, an expression of the passive resistance contribution was derived from the pullout test results and was equated to the friction force of a transformed strip (Eq. 37) to obtain the equivalent friction coefficient, f', as a function of the size and geometry of the wires.

XIV. REFERENCES

Al-Hussaini, M.M. and Johnson, L.D. (1978). "Numerical analysis of a reinforced earth wall." Proc. ASCE Symp. on Earth Reinforcement, Pittsburgh, Pennsylvania, pp. 98-126.

Amin, N.U. (1989). "Direct shear and pullout tests on lateritic soil at low pressure." M. Eng. Thesis No. GT-88-4, Asian Institute of Technology, Bangkok, Thailand.

Anderson, L.R., Liu, J. and Bay, J.A. (1986). "Experimental evaluation and design recommendations for Syro anchored retaining wall system." Report Submitted to the Syro Steel Company. Utah State University, Logan, Utah, U.S.A.

Anderson, L.R., Sharp, K.D. and Harding, O.T. (1987). "Performance of a 50-foot high welded wire wall." Soil Improvement - A Ten Year Update, pp. 280-308.

Bergado, D.T., Sampaco, C.L., Miura, N. and Onitsuka, K. (1988a). "Interaction of geogrid reinforcement with gravel and decomposed granite backfill with applications." Proc. 2nd Intl. Conf. on Geomech. of Tropical Soils, Singapore, pp. 351-358.

Bergado, D.T., Sampaco, C.L., Miura, N. and Sakai, A. (1988b). "Reinforced gravel foundations for box culvert and sewage pipeline constructions on soft and subsiding ground." Proc. 1st Indian Geotextiles Conf., Bombay, India.

Bergado, D.T., Sampaco, C.L. and Lekhak, B.M. (1988c). "Welded wire reinforced earth (mechanically stabilized) embankments with cohesive backfill on soft clay." First Progress Report Submitted to the U.S. Agency for Intl. Development, Bangkok, Thailand, 137 pp.

Bergado, D.T., Sampaco, C.L., Alfaro, M.C. and Balasubramaniam, A.S. (1989a). "Welded wire wall and embankment system with cohesive backfill on soft clay." Second Progress Report Submitted to the U.S. Agency for Intl. Development, Bangkok, Thailand.

Bergado, D.T., Sampaco, C.L., Alfaro, M.C., Shivashankar, R. and Balasubramaniam, A.S. (1989b). "Welded wire wall and embankment system with cohesive backfill on soft clay." Third Progress Report Submitted to the U.S. Agency for Intl. Development, Bangkok, Thailand.

Chang, J.C. and Forsyth, R.A. (1977). "Finite element analysis of reinforced earth wall." J. of Geotech. Eng'g. Div., ASCE, Vol. 103, No. GT7, pp. 711-724.

Cisneros, C.B. (1989). "Pullout resistance of steel grids with weathered clay as backfill material." M. Eng. Thesis No. GT-88-7, Asian Institute of Technology, Bangkok, Thailand.

Clough, G.W. and Duncan, J.M. (1971). "Finite element analysis of retaining wall behavior." J. Soil Mech. and Found. Eng'g., ASCE, Vol. 97, No. SM12, pp. 1657-1673.

Clough, G.W. and Tsui, Y. (1974). "Performance of tied-back walls in clay." J. of Geotech. Eng'g. Div., ASCE, Vol. 100, No. GT12, pp. 1259-1273.

Collin, J.G. (1986). "Earth wall design," thesis presented to the University of California, Berkeley, in partial fulfillment of the requirements for the degree of Doctor of Philisophy.

Desai, C.S. (1981). "Behavior of interfaces between structural and geologic media." Proc. Intl. Conf. Recent Advances in Geotech. Earthquake Eng'g. and Soil Dynamics, St. Louis, Vol. 2, pp. 619-638.

Duncan, J.M., Byrne, P., Wong, K.S. and Mabry, P. (1980). "Strength, stress-strain and bulk modulus parameters for finite element analysis of stresses and movements in soil masses." Report No. UCB/GT/80-01, University of California, Berkeley, California, U.S.A., 70 pp.

Duncan, J.M. and Chang, C.Y. (1970). "Nonlinear analysis of stress and strain in soils." J. of Soil Mech. Found. Div., ASCE, Vol. 96, No. SM5, pp. 1624-1653.

Duncan, J.M. and Seed, R.B. (1986). "Compaction-induced earth pressures under K_o-conditions." J. Geotech. Eng'g. Div., ASCE, Vol. 112, No. 1, pp. 1-22.

Hannon, J.B. and Forsyth, R.A. (1984). "Performance of an earthwork reinforcement system constructed with low quality backfill." Transportation Research Record 965.

Hardiyatimo, H.C. (1990). "Behavior of mechanically stabilized embankment on soft Bangkok clay." M. Eng. Thesis, Asian Institute of Technology, Bangkok, Thailand.

Hermann, L.R. (1977). "Nonlinear finite element analysis of frictional systems." Proc. Intl. Conf. Finite Elements in Nonlinear Solids and Struct. Mech., Vol. 2, Geilo, Norway.

Hermann, L.R. (1978a). "User's manual for REA: A general two-dimensional soils and reinforced earth analysis program." University of California, Davis, California, U.S.A. 122 pp.

Hermann, L.R. (1978b). "Solution of contact problems in Civil Eng'g.," Dept. of Civil Eng'g., Report No. 78-2, Univ. of California, Davis, California, U.S.A.

Hermann, L.R. and Al-Yassin, Z. (1978). "Numerical analyses of reinforced soil system." Proc. ASCE Symp. on Earth Reinforcement, Pittsburgh, Pennsylvania, pp. 428-457.

Ingold, T.S. (1983). "The design of reinforced soil walls by compaction theory." The Structural Engineer, Vol. 61A, No. 7, pp. 205-211.

Janbu, N. (1963). "Soil compressibility as determined by oedometer and triaxial tests." Proc. European Conf. Soil Mech. Found. Eng'g., Wissbaden, Germany, Vol. 1, pp. 19-25.

Juran, I. and Chen, C.L. (1989). "Strain compatibility design method for reinforced earth walls." J. of Geotech. Eng'g. Div., ASCE, Vol. 115, No. 4, pp. 435-456.

Kennedy, J.B., Laba, J.T. and Shaheen, H. (1988). "Reinforced soil-metal structures." J. Struct. Eng'g. Div., ASCE, Vol. 114, No. 6, pp. 1372-1389.

Kondner, R.L. (1963). "Hyperbolic stress-strain response: cohesive soils." J. of Soil Mech. and Found. Division, ASCE, Vol. 89, No. SM1, pp. 115-143.

Kulhawy, F.H., Duncan, J.M. and Seed, H.B. (1969). "Finite element analysis of stresses and movements in embankments during construction." Geotechnical Eng'g. Report No. TE-69-4, University of California, Berkeley, California, U. S. A.

Liu, J.S. (1988). "Analysis of mechanically stabilized retaining walls," dissertation presented to Utah State University, Logan, Utah, in partial fulfillment of the requirements for the degree of Doctor of Philosophy.

Macatol, K.C.B. (1990). "Interaction of laterite backfill and steel grid reinforcements at high vertical stresses using pullout tests." M. Eng. Thesis, Asian Institute of Technology, Bangkok, Thailand.

Netlon, Ltd. (1984). "Techniques and design philosophy for utilizing Tensar grids in the reinforcing of soil structures." Technical Guideline of Netlon, Ltd., England.

Ochiai, H. and Sakai, A. (1987). "Analytical method for geogrid-reinforced soil structures." Proc. 8th Asian Reg. Conf. on Soil Eng'g., Kyoto, Japan, pp. 483-486.

Ochiai, H., Hayashi, S., Ogisako, E. and Sakai, A. (1988a). "Analysis of polymer grid reinforced soil retaining wall." Proc. 6th Intl. Conf. on Num. Meth. in Geomech., Innsbruck.

Ochiai, H., Hayashi, S., Otani, J., Umezaki, T. and Ogisako, E. (1988b). "Field pullout test of polymer grid in embankment." Proc. Intl. Geotech. Symp. on Theory and Practice of Earth Reinf., Fukuoka, Japan, pp. 147-151.

Ogisako, E., Ochiai, H., Hayashi, S. and Sakai, A. (1988). "FEM analysis of polymer grid-reinforced soil retaining walls and its application to the design method." Proc. Intl. Geotech. Symp. Theory and Prac. of Earth Reinf., Fukuoka, Japan, pp. 559-564.

Romstad, K.M., Hermann, L.R. and Shen, C.K. (1976). "Integrated study of reinforced earth - I: Theoretical Formulation." J. Geotech. Eng'g. Div., ASCE, Vol. 102, No. GT5, pp. 457-471.

Schlosser, F. and Elias, V. (1978). "Friction in reinforced earth." Proc. ASCE Symp. on Earth Reinforcement, Pittsburgh, Pennsylvania.

Schmertmann, G.R., Chew, S.H. and Mitchell, J.K. (1989). "Finite element modeling of reinforced soil wall behavior." Geotechnical Eng'g. Report No. UCB/GT/89-01, Univ. of Calif., Berkeley, California, U.S.A.

Seed, R.B. and Duncan, J.M. (1986). "FE analyses: Compaction-induced stresses and deformations." J. Geotech. Eng'g. Div., ASCE, Vol. 112, No. 1, pp. 23-43.

Wong, K.S. and Duncan, J.M. (1974). "Hyperbolic stress-strain parameters for nonlinear finite element analysis of stresses and movements in soil masses." Geotechnical Eng'g. Report No. TE-74-3, University of California, Berkeley, California, U.S.A.

TABLES

Table 1. Summary of Laboratory Pullout Tests on Weathered Clay Backfill

Test No.	Bar Size (inches)	Mesh Size (in.xin.)	Overburden Pressure (tsm)	Wet, Dry, or Optimum	Embedment Length (inches)	Number of Transverse Bars	Maximum Pullout Resistance (tons)			Maximum Strains (%)											
										L1			L2			L3			T		
							1	2	3	1	2	3	1	2	3	1	2	3	1	2	3
CQNAX	1/4	6" x 9"	1	Dry	38.5	6	3.37			0.198			0.161			*			-0.35		
			3		37.5	6		3.65			0.29			0.165			*			0.066	
			5		36.5	6			4.11			-0.165			0.170			*			*
CQNBX	1/4	6" x 9"	3	Dry	38.5	6	4.03			0.157			0.130			0.06			0.030		
			5		37.5	6		3.71			0.03			0.140			0.050			0.050	
			7		36.5	6			4.91			0.040			0.030			0.099			0.040
CQNCX	1/4	6" x 9"	5	Dry	38.5	6	4.356			0.195			0.150			0.03			0.034		
			7		37.5	6		4.93			*			0.450			0.019			0.050	
			9		36.5	6			5.32			*			0.200			0.050			0.040
CQNAY	1/4	6" x 9"	1	Opt	38.5	6	3.080			0.062			0.161			*			-0.366		
			3		37.5	6		3.590			0.390			0.160			0.039			*	
			5		36.5	6			4.170			*			0.136			0.086			*
CQNBY	1/4	6" x 9"	3	Opt	38.5	6	3.65			0.084			0.070			0.027			0.097		
			5		37.5	6		3.470			0.450			0.073			-0.028			0.498	
			7		36.5	6			3.980			*			0.082			-0.063			*
CQNCY	1/4	6" x 9"	5	Opt	38.5	6	3.720			0.220			0.165			*			0.097		
			7		37.5	6		3.890			*			0.720			*			0.153	
			9		36.5	6			3.710			*			0.400			*			0.112
CQNAZ	1/4	6" x 9"	1	Wet	38.5	6	2.290			0.086			0.105			0.028			-0.002		
			3		37.5	6		2.630			0.194			0.105			0.030			*	
			5		36.5	6			2.990			*			0.130			0.035			*
CQNBZ	1/4	6" x 9"	3	Wet	38.5	6	2.290			0.094			0.124			0.022			-0.260		
			5		37.5	6		2.96			0.156			0.119			0.029			*	
			7		36.5	6			3.140			*			0.154			0.045			*
CQNCZ	1/4	6" x 9"	5	Wet	38.5	6	2.970			0.092			*			0.025			0.126		
			7		37.5	6		3.35			*			0.110			0.030			0.62	
			9		36.5	6			3.700			*			*			0.025			0.610
CHNAX	1/2	6" x 9"	1	Dry	38.5	6	3.21			0.011			0.085			0.015			0.048		
			3		37.5	6		4.00			0.014			0.005			0.012			0.029	
			5		36.5	6			4.680			0.025			0.096			0.540			0.025
CHNBX	1/2	6" x 9"	5	Dry	38.5	6	5.184			0.044			-0.080			-0.350			0.056		
			7		37.5	6		6.34			0.530			0.055			0.019			0.003	
			9		36.5	6			6.990			-0.23			0.060			0.020			-0.024

Cont. Table 1 ....

Test No.	Bar Size (inches)	Mesh Size (in.xin.)	Overburden Pressure (tsm)	Wet, Dry, or Optimum	Embedment Length (inches)	Number of Transverse Bars	Maximum Pullout Resistance (tons)			Maximum Strains (%)											
										L1			L2			L3			T		
							1	2	3	1	2	3	1	2	3	1	2	3	1	2	3
CHNCX	1/2	6" x 9"	9	Dry	38.5	6	8.460			*			0.103			0.028			-0.007		
			11		37.5	6		9.480			0.139			0.098			*			-0.001	
			13		36.5	6			10.00			0.113			-0.126			*			0.001
CHNAY	1/2	6" x 9"	1	Opt	38.5	6	4.26			0.111			*			0.011			0.002		
			3		37.5	6		5.05			0.013			0.052			0.011			0.0006	
			5		36.5				5.99			0.149			0.088			0.017			0.001
CHNBY	1/2	6" x 9"	5	Opt	38.5	6	3.60			-0.045			0.116			-0.012			0.009		
			7		37.5	6		4.250			0.009			0.070			0.009			0.036	
			9		36.5	6			5.23			0.212			0.012			0.009			-0.011
CHNCY	1/2	6" x 9"	9	Opt	38.5	6	8.46			*			0.103			0.028			-0.008		
			11		37.5	6		9.48			0.139			0.098			*			-0.00	
			13		36.5	6			10.00			0.113			0.103			*			0.002
CHNAZ	1/2	6" x 9"	1	Wet	38.5	6	3.73			0.155			0.047			0.009			0.034		
			3		37.5	6		4.27			-0.44			-0.19			0.010			-0.043	
			5		36.5	6			4.66			*			0.137			0.164			
CHNBZ	1/2	6" x 9"	5	Wet	38.5	6	2.226			0.086			0.024			0.004			-0.028		
			7		37.5	6		2.56			0.053			0.048			0.007			0.0002	
			9		36.5	6			2.70			0.136			0.032			0.014			0.001
CHNCZ	1/2	6" x 9"	9	Wet	38.5	6	2.44			0.027			0.020			0.001			0.089		
			11		37.5	6		2.75			0.036			0.028			0.005			-0.057	
			13		36.5	6			2.92			0.013			0.031			0.015			0.002

Table 2. Summary of Laboratory Pullout Tests on Laterite Backfill

Test No.	Bar Size (inches)	Mesh Size (in.xin.)	Overburden Pressure (tsm)	Wet, Dry, or Optimum	Embedment Length (inches)	Number of Transverse Bars	Maximum Pullout Resistance (tons)			Maximum Strains (%)											
										L1			L2			L3			T		
							1	2	3	1	2	3	1	2	3	1	2	3	1	2	3
LQNAX	1/4	6" x 9"	1	Dry	38.5	6	5.675			0.232			*			0.053			0.034		
			3		37.5	6		6.914			0.759			*			0.715			0.16	
			5		36.5	6			7.2377			*			*			0.057			0.062
LQNBX	1/4	6" x 9"	5	Dry	38.5	6	6.5302			*			0.1945			0.039			0.132		
LQNCX	1/4	6" x 9"	3	Dry	38.5	6	5.9529			0.422			0.2432			0.041			0.154		
			7		37.5	6		6.752			*			0.214			*			0.102	
LHNAX	1/2	6" x 9"	1	Dry	38.5	6	5.758			0.069			0.058			*			0.025		
			3		37.5	6		6.203			0.057			0.05			*			0.105	
			5		36.5	6			6.906			0.083			0.075			*			0.062
LHNBX	1/2	6" x 9"	5	Dry	38.5	6	7.054			0.072			0.075			0.016			*		
			7		37.5	6		6.716			0.063			0.064			0.013			0.004	
			9		36.5	6			6.397			0.049			0.052			0.013			0.005
LHNCX	1/2	6" x 9"	9	Dry	38.5	6	9.702			0.095			0.085			0.028			*		
			11		37.5	6		10.79			0.101			0.092			0.029			*	
			13		36.5	6			11.339			0.124			0.113			0.064			*
LTNAX	3/8	6" x 9"	1	Dry	38.5	6	6.262			1.328			0.094			0.007			0.0022		
			3		37.5	6		7.608			*			0.111			0.070			0.12	
			5		36.5	6			8.517			*			0.696			0.073			*
LTNBX	3/8	6" x 9"	5	Dry	36.5	6	7.841			*			0.086			0.034			0.006		
			7		37.5	6		8.991			*			*			0.036			0.011	
			9		36.5	6			9.7781			*			0.4448			0.033			0.051
LTNCX	3/8	6" x 9"	9	Dry	38.5	6	8.442			1.135			0.119			0.023			0.008		
			11		37.5	6		9.397			*			0.136			0.032			0.027	
			13		36.5	6			7.388			*			*			0.035			0.034
LHSAX	1/2	6" x 6"	1	Dry	38.5	8															
			3		37.5	8															
			5		36.5	8															
LHSBX	1/2	6" x 6"	5	Dry	38.5	8	9.787			0.103			0.342			*			*		
			7		37.5	8		10.97			0.125			0.128			*			*	
			9		36.5	8			11.62			0.106			0.304			*			*
LHSCX	1/2	6" x 6"	9	Dry	38.5	8	10.69			*			0.077			*			*		
			11		37.5	8		12.09			*			0.087			*			*	
			13		36.5	8			12.96			*			*			*			*

Cont. Table 2 ....

Test No.	Bar Size (inches)	Mesh Size (in.xin.)	Overburden Pressure (tsm)	Wet, Dry, or Optimum	Embedment Length (inches)	Number of Transverse Bars	Maximum Pullout Resistance (tons)			Maximum Strains (%)											
										L1			L2			L3			T		
							1	2	3	1	2	3	1	2	3	1	2	3	1	2	3
LQNAY	1/4	6" x 9"	1	Opt	38.5	6	4.956			0.171			0.179			0.043			0.005		
			3		37.5	6		5.736			*			1.306			0.037			0.010	
LQNBY	1/4	6" x 9"	5	Opt	38.5	6	5.251			0.349			0.168			0.046			0.015		
			7		37.5	6		5.660			0.047			0.0003			0.0459			0.042	
LQNCY	1/4	6" x 9"	3	Opt	38.5	6	5.199			1.515			0.169			0.036			*		
			7		37.5	6		5.690			*			0.731			0.171			*	
LTNAY	3/8	6" x 9"	1	Opt	38.5	6	4.964			0.076			0.061			0.029			0.002		
			[illegible]		37.5	6		5.996			0.041			0.037			0.011			0.0003	
			5		36.5	6			6.697			0.064			*			0.027			0.006
LTNBY	3/8	6" x 9"	5	Opt	38.5	6	8.289			0.485			0.129			0.034			*		
			7		37.5	6		9.450			*			0.588			0.022			0.005	
			9		36.5	6			9.866			*			0.126			0.138			0.032
LTNCY	3/8	6" x 9"	9	Opt	38.5	6	9.225			0.151			0.132			0.031			*		
			11		37.5	6		10.336			*			0.077			0.035			*	
			13		36.5	6			11.124			*			0.101			0.035			*

Table 3. Summary of Laboratory Pullout Tests on Clayey Sand Backfill

Test No.	Bar Size (inches)	Mesh Size (in.xin.)	Overburden Pressure (tsm)	Wet, Dry, or Optimum	Embedment Length (inches)	Number of Transverse Bars	Maximum Pullout Resistance (tons)			Maximum Strains (%)											
										L1			L2			L3			T		
							1	2	3	1	2	3	1	2	3	1	2	3	1	2	3
LQSAY	1/4	6" x 6"	1	Opt	39	7	4.310			0.165			0.189			0.066			-0.0022		
			3		38	7		5.305			0.174			0.108			0.062			0.002	
			5		37	7			5.660			-0.211	-		0.122			0.068			0.003
SFNAX	W4.5 x W3.5	6" x 9"	1	Dry	41	5	4.096			0.194			0.159			0.034			0.132		
			9		40	5		6.277			0.444			0.277			*			0.213	
			13		39	5			6.339			0.423			0.098			*			*
SFNBX	W4.5 x W3.5	6" x 9"	5	Dry	41	5	5.459			0.220			0.397			0.028			-0.82		
			13		40	5		7.06			0.912			0.464			0.026			*	
SFEAX	W4.5 x W3.5	6" x 18"	1	Dry	41	3	2.982			0.106			*						-0.313		
			9		40	3		5.185			0.215			*						0.141	
			13		39	3			6.142			0.229			*						0.181
SFEBX	W4.5 x W3.5	6" x 18"	5	Dry	41	3	5.108			0.237			0.172						0.153		
			13		40	3		5.199			0.214			*						0.035	
SFLABX	W4.5	6" x --	1	Dry	41	-	1.834														
			5		40	-		2.057													
			9		39	-			2.064												

Table 4. Summary of Field Pullout Tests on USAID Welded Wire Wall

FIELD PULLOUT TESTING

TESTED ON JULIAN DAY	DUMMY NO. (REFER FIG. NO.)	NO. OF TRANS-VERSE BARS	GALVA-NISED/ INSTRU-MENTED	BAR SIZES	AVERAGE LENGTH OF EMBED-MENT (Metres)	HEIGHT OF OVER-BURDEN (Metres)	PULLOUT (Cms)	MAXIMUM PULLOUT RESIST-ANCE in (Tons)	MAXIMUM AXIAL STRAINS L1% BACK	L2% MIDDLE	L3% FRONT
WEATHERED CLAY											
362	26	5	G-I	W7 XW4.5	2.046	0.60	12.550	3.839	0.036	0.094	0.166
9	22	5	G-I	W4.5XW3.5	2.043	2.35	13.230	6.015	0.080	0.258	0.337
2	17	6	B-NI	W12 X W5	2.116	3.27	13.820	7.806	-	-	-
4	13	0	G-NI	W4.5=4Nos	2.047	3.80	12.530	2.389	-	-	-
3	8	5	G-NI	W7 XW4.5	2.041	3.93	13.600	6.428	-	-	-
LATERITE											
12	23	5	B-NI	W12 X W5	2.117	1.50	13.670	10.983	-	-	-
10	21	5	G-I	W4.5XW3.5	2.035	2.40	14.750	5.713	Strains recorded not good		
11	15	6	G-I	W7 XW4.5	2.037	3.33	14.430	4.055	0.007	0.086	0.094
5	12	5	B-NI	W12 X W5	2.046	3.80	12.600	5.482	-	-	-
6	11	0	G-NI	W4.5=4Nos	2.045	3.80	12.670	2.537	-	-	-
CLAYEY SAND											
354	24	5	G-I	W7 XW4.5	2.091 2.086	0.60	3.625 4.600	* 2.366#	not realistic-due to slippage		
356	20	5	G-I	W4.5XW3.5	2.085 2.078	2.40	4.730 6.150	5.650# 7.382@	0.069 0.102	0.163 0.216	0.242 0.510
8	10	0	G-NI	W4.5=4Nos	2.045	3.75	12.700	2.466	-	-	-
360	9	5	B-NI	W12 X W5	2.046	3.90	12.600	9.400	-	-	-
359	7	5	G-NI	W7 XW4.5	2.045	4.23	12.750	10.352	-	-	-

Note : All mats except 10,11,13 are of 6"X9" mesh size

* no peak
\# not peak value
@ tension failure

FIGURES

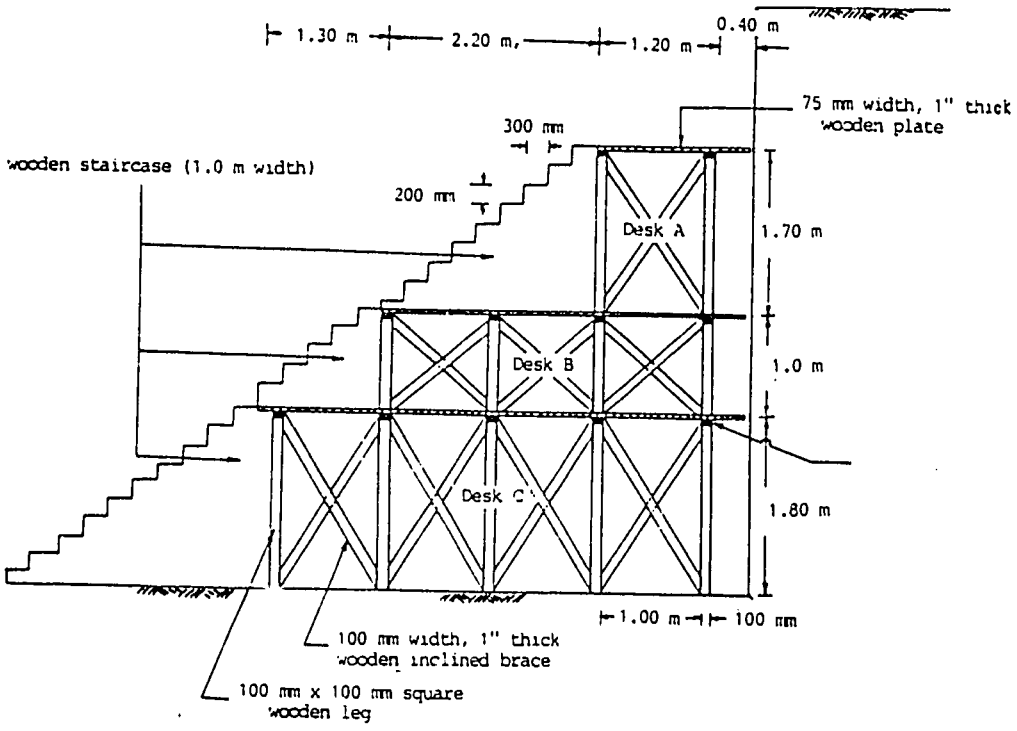

Fig. 1 Elevation View of Wooden Platform Used in Field Pullout Tests.

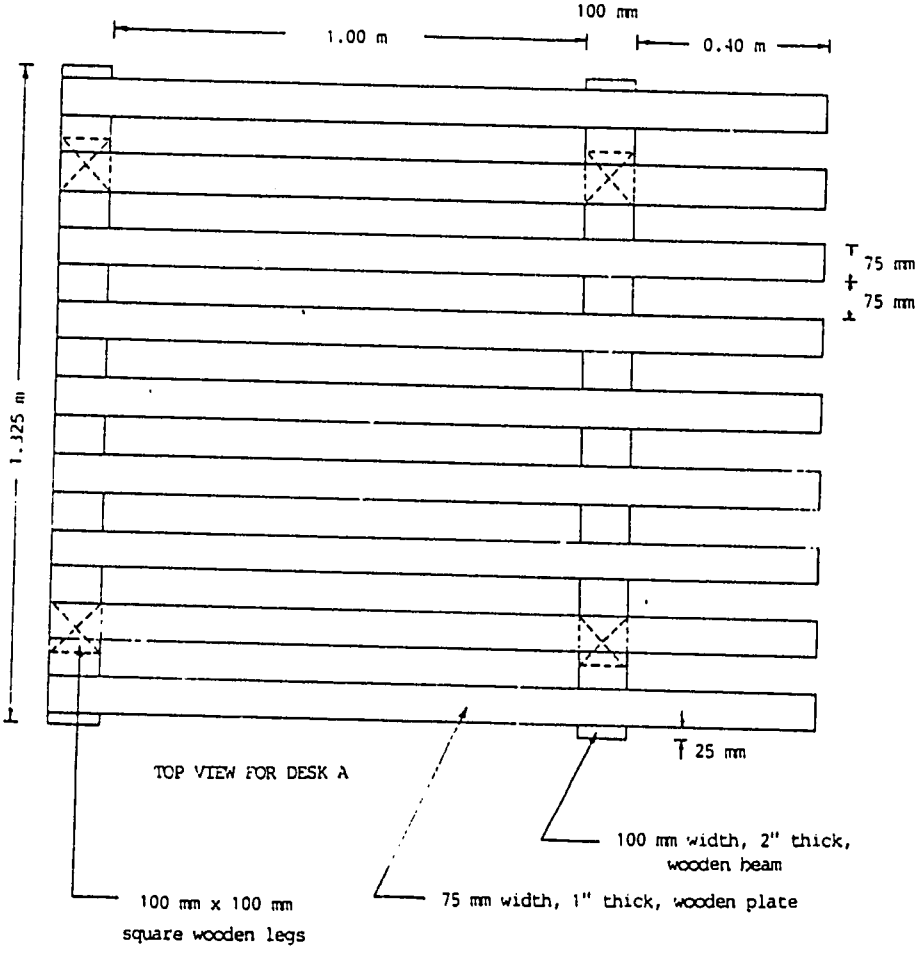

Fig. 2 Top View of Platform (DESK A) Used in Field Pullout Tests.

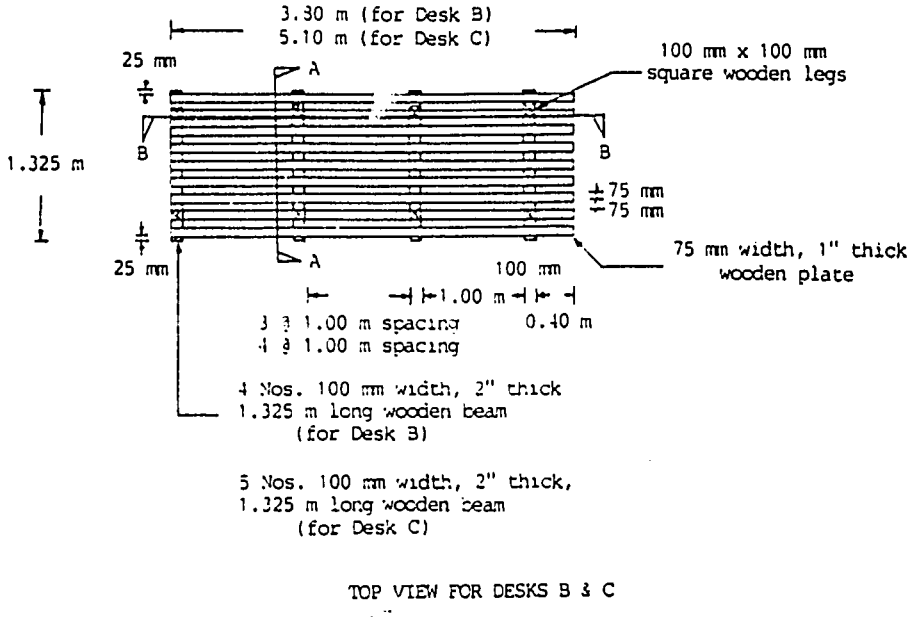

Fig. 3 Top View of Platform (DESKS A and B) Used in Field Pullout Test.

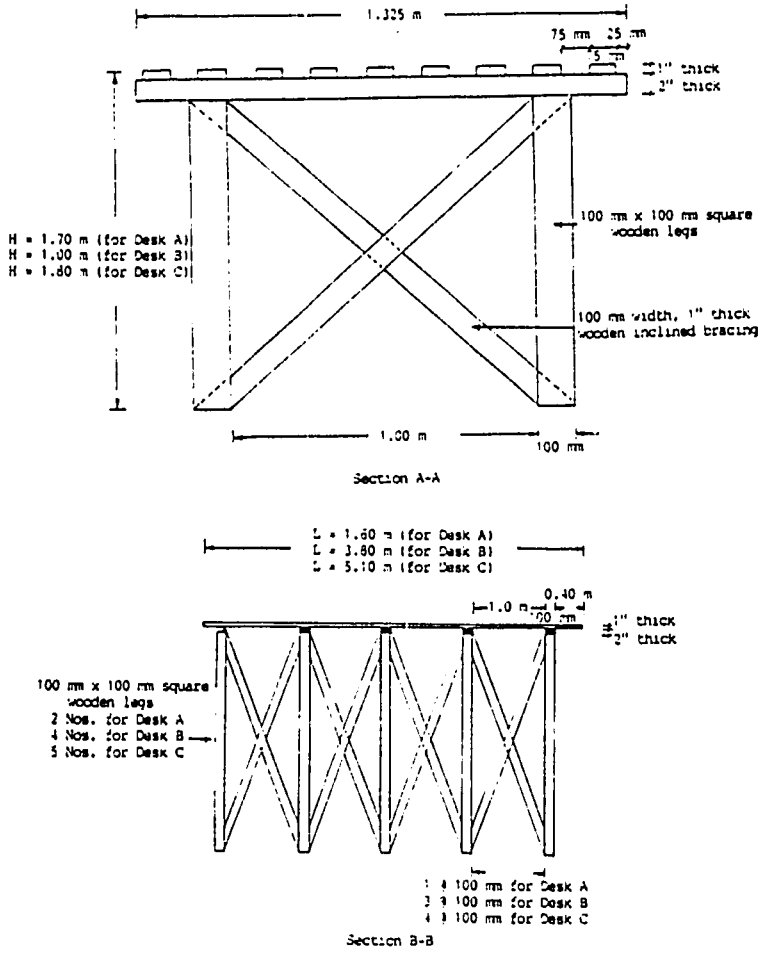

Fig. 4 Section Views of Platform Along A-A and B-B, respectively.

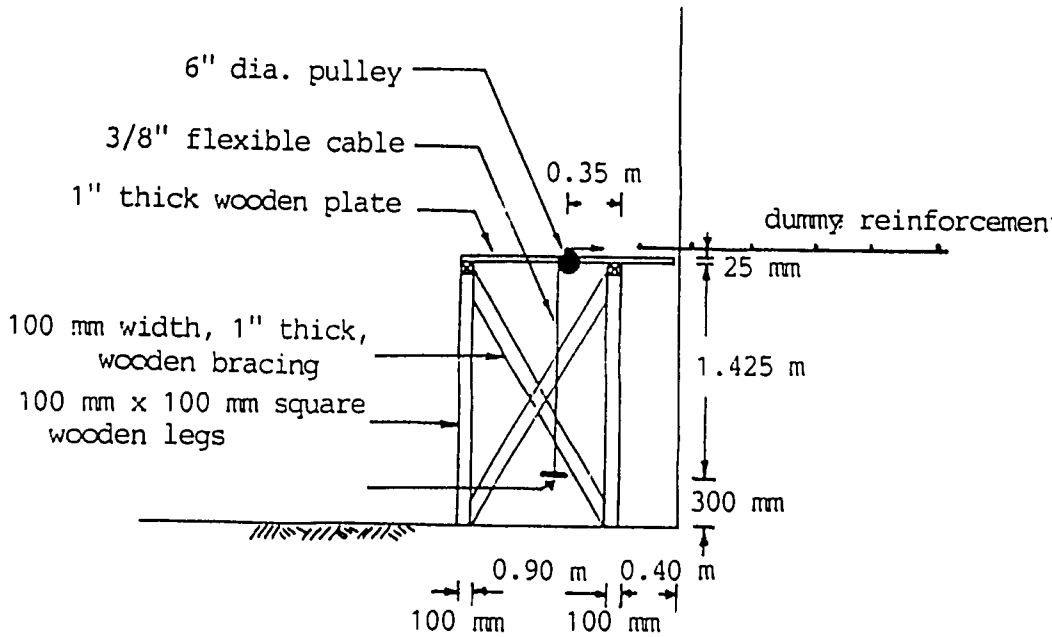

ELEVATION

Fig. 5 Elevation View of Wooden Platform Used in Constant Stress Pullout Tests in the Field.

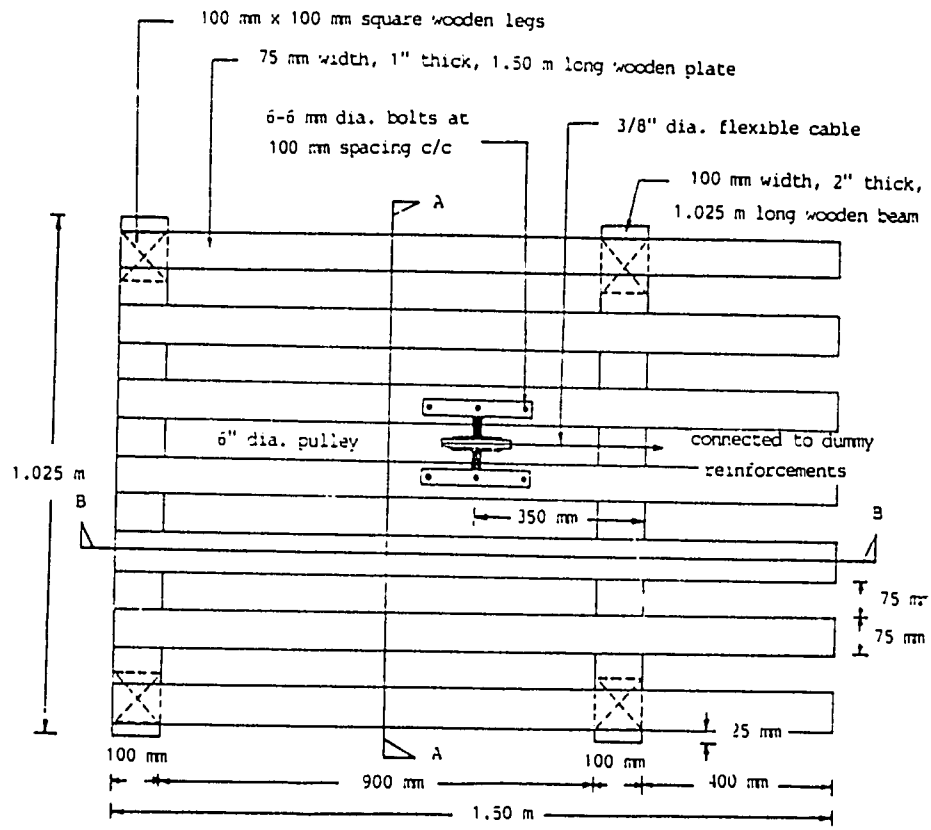

TOP VIEW

Fig. 6 Top View of Wooden Platform Used in Constant Stress Pullout Tests in the Field.

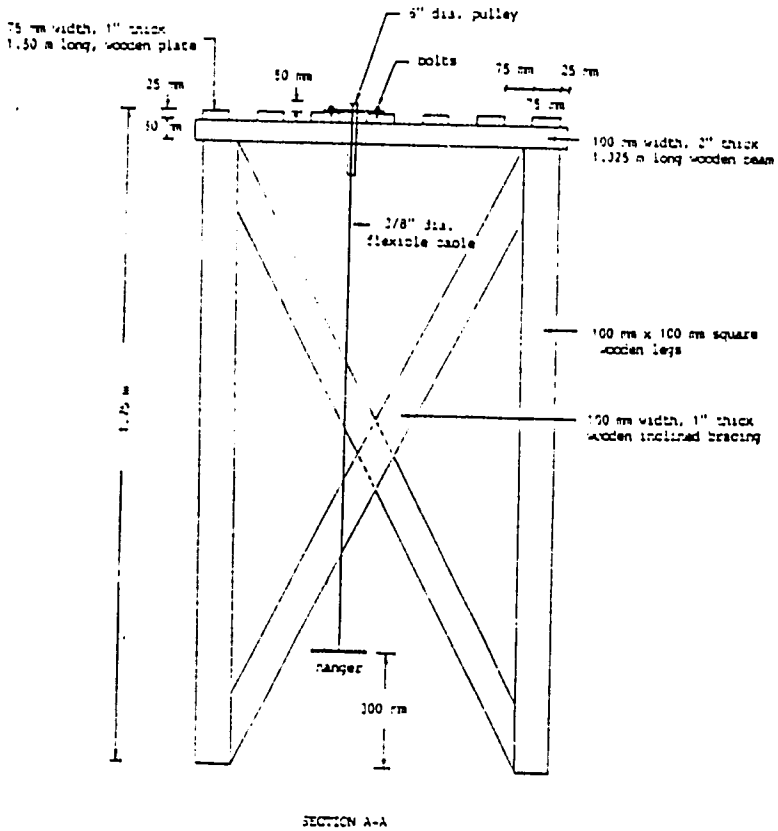

Fig. 7 Section View of Wooden Platform Used in Constant Stress Pullout Tests in the Field (along A-A).

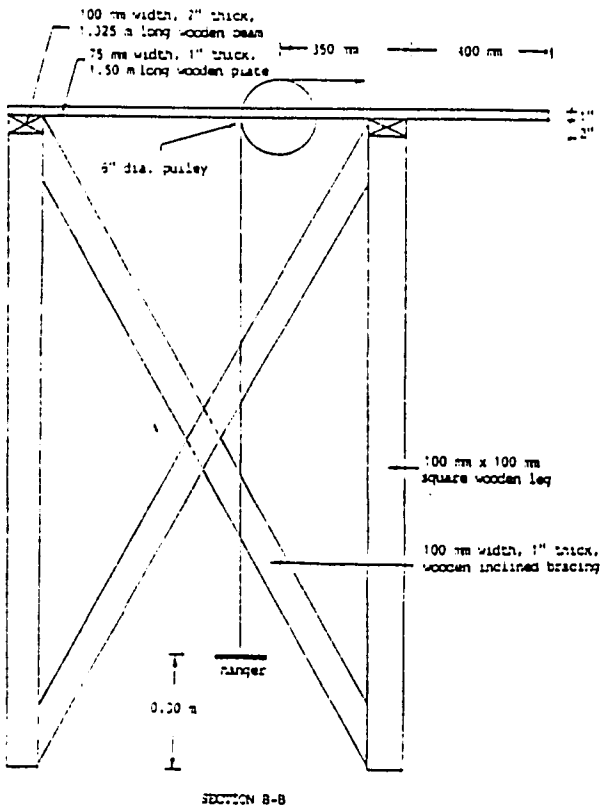

Fig. 8 Section View of Wooden Platform Used in Constant Stress Pullout Tests in the Field (along B-B).

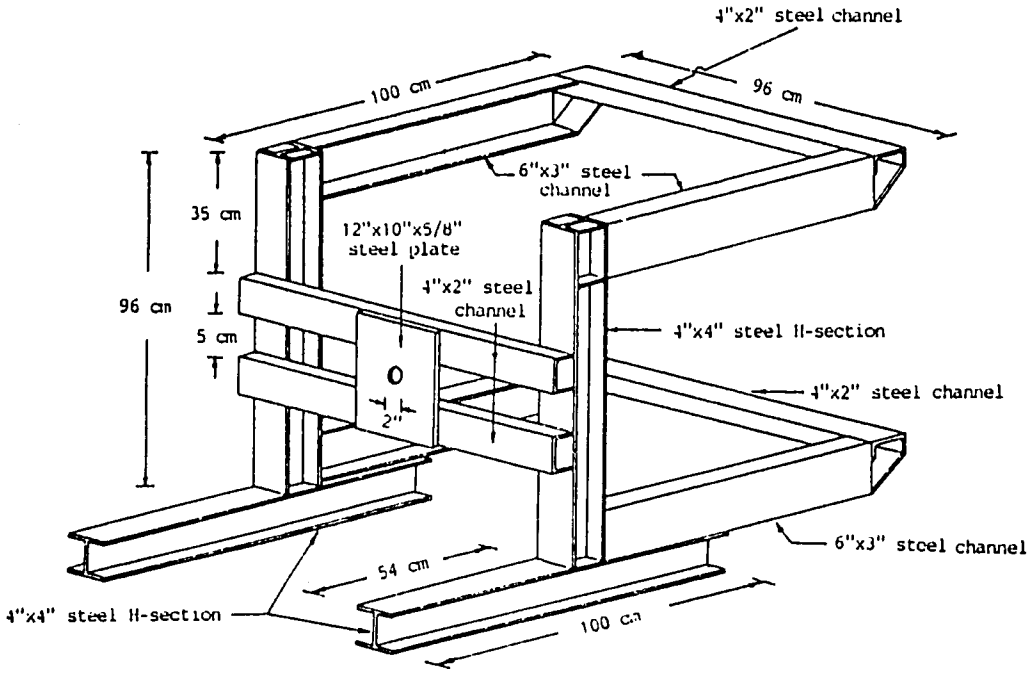

Fig. 9 Steel Reaction Frame Used in Field Pullout Tests.

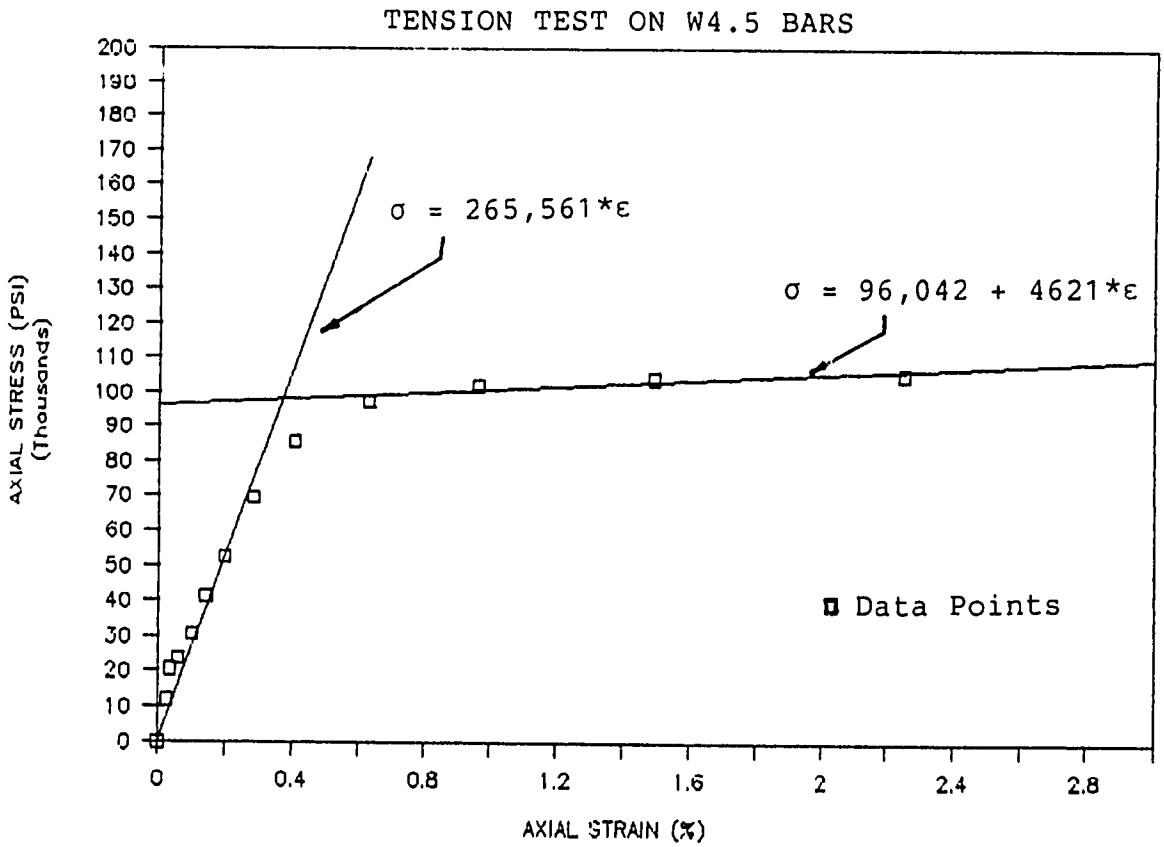

Fig. 10 Bilinear Stress-strain Plot of W4.5 Bars from Tension Test.

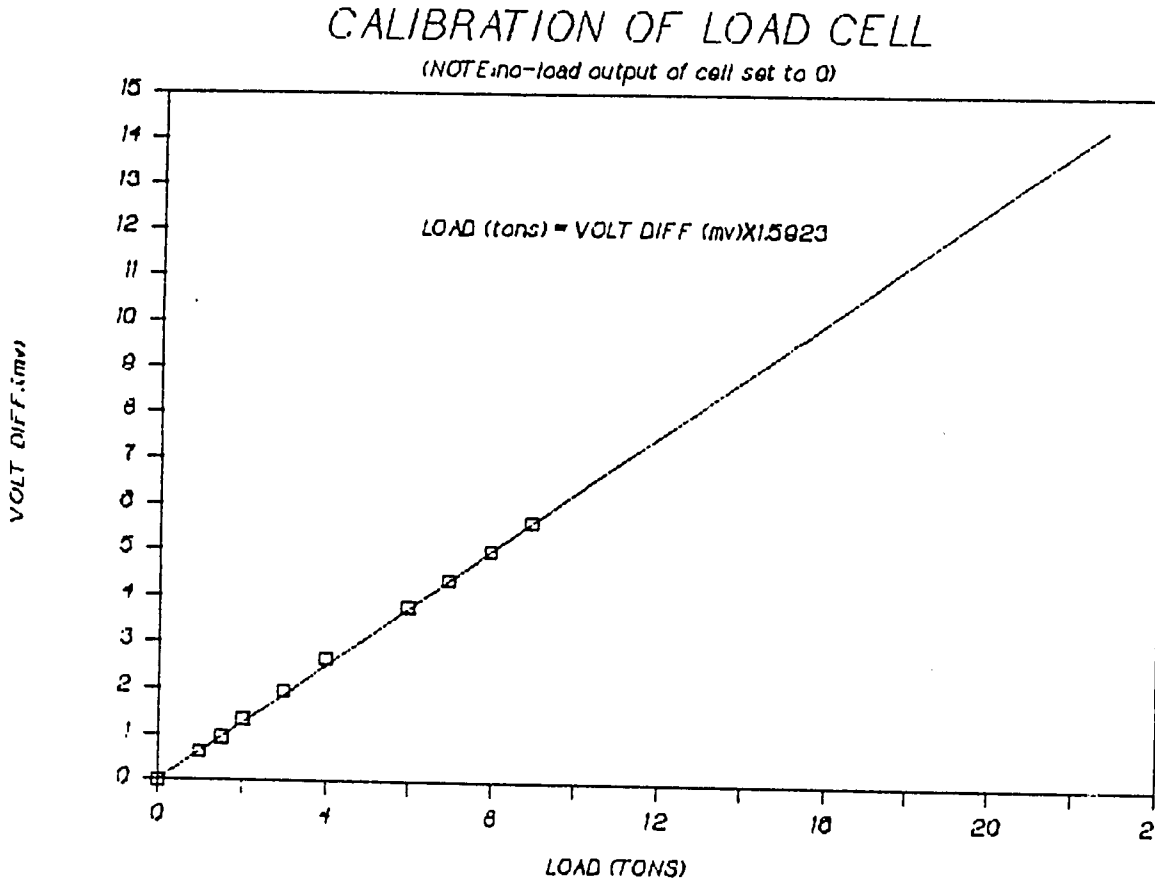

Fig. 11 Calibration Data of the SR-4 Load Cell.

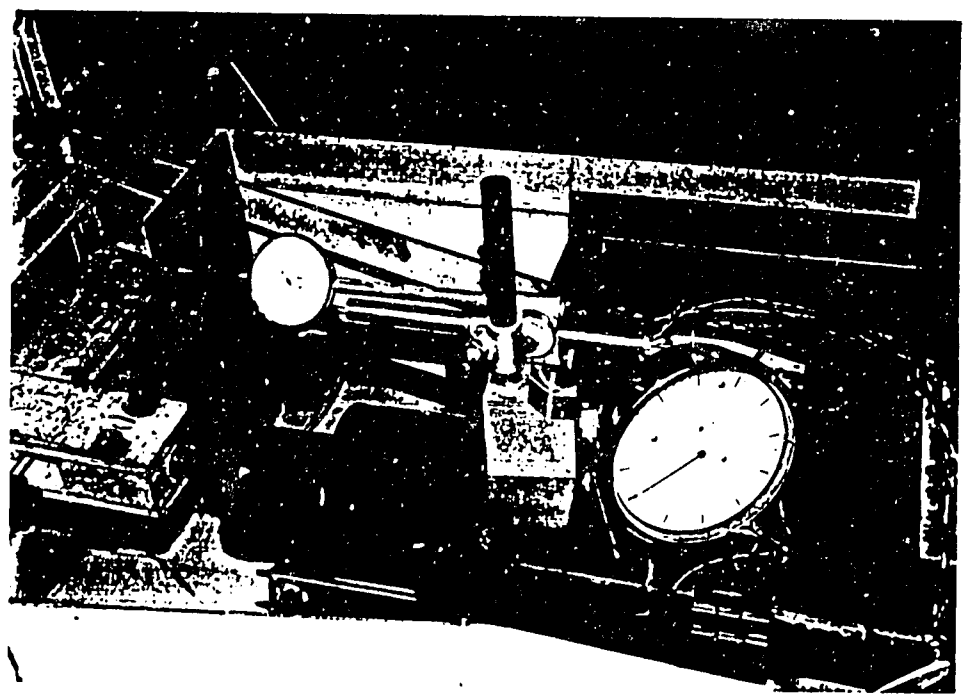

Fig. 12 Photograph of SR-4 Load Cell and Steel Frame Mounting.

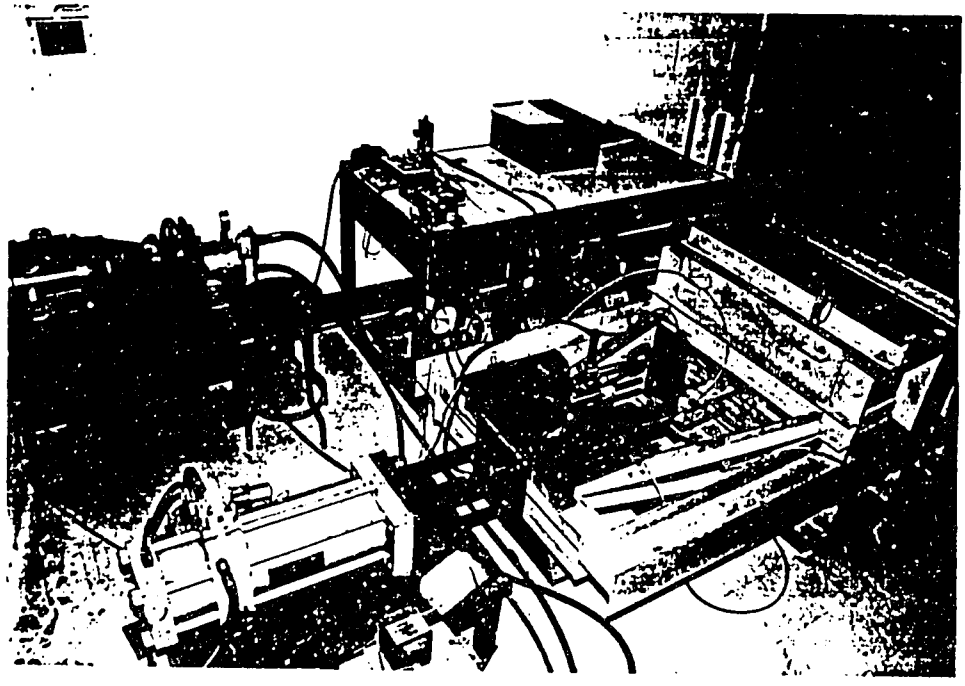

Fig. 13 Typical Set-up of Laboratory Pullout Test after System Modification.

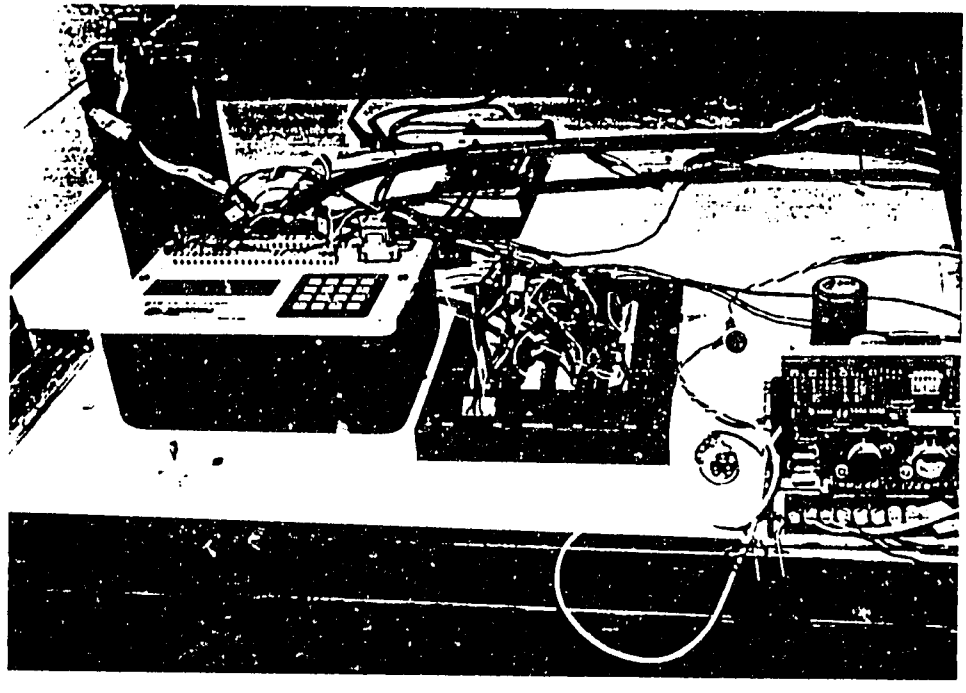

Fig. 14 Photograph Showing Electronic Controls (EMRS-A-11 and EM-D-20 Interfaced with Potentiometer Pot Adjustment).

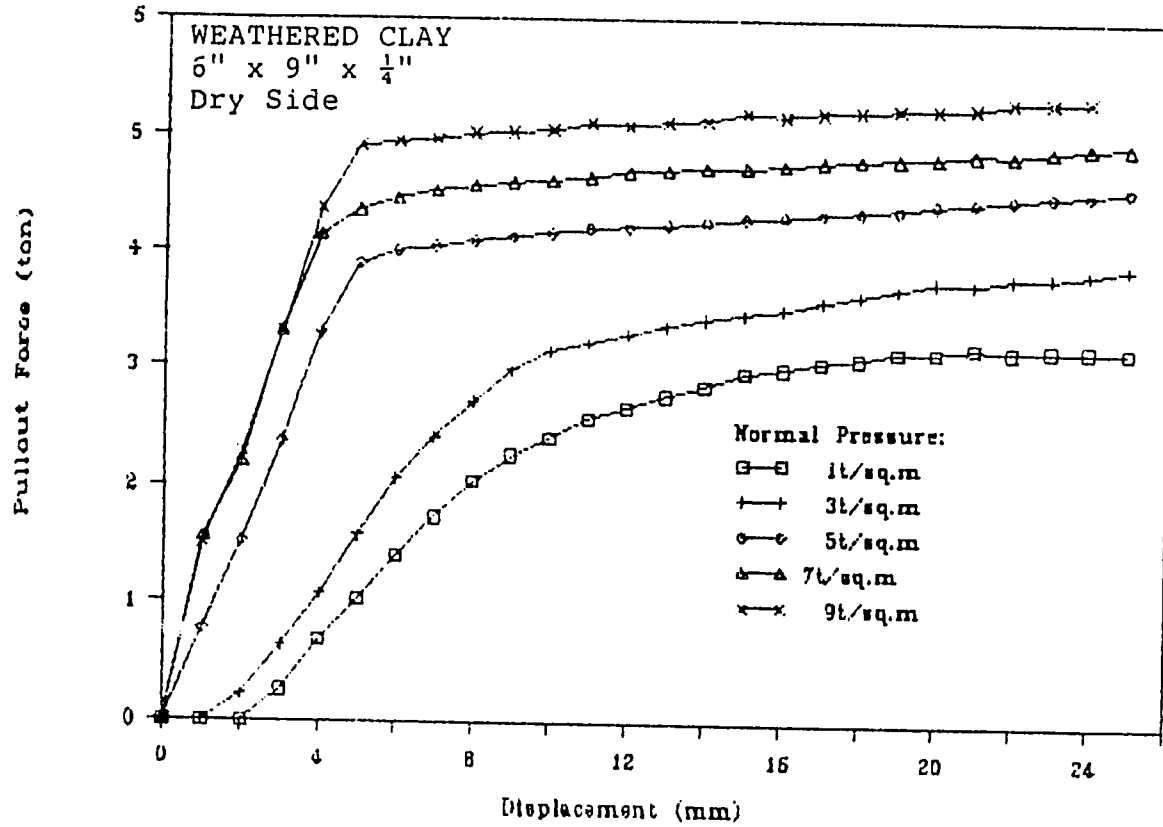

Fig. 15 Load-displacement Curves for 1/4" Diameter Bars with Weathered Clay Backfill Compacted at the Dry Side of Optimum.

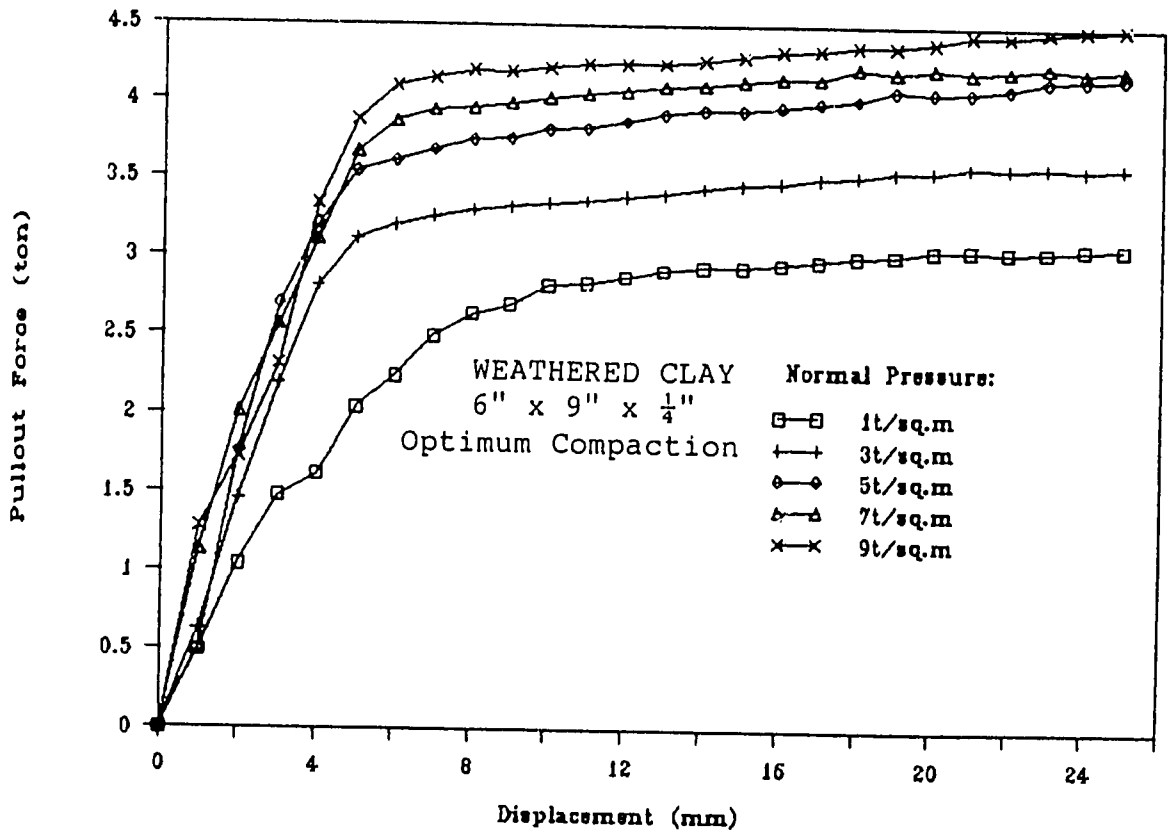

Fig. 16 Load-displacement Curves for 1/4" Diameter Bars with Weathered Clay Backfill Compacted at Optimum Water Content.

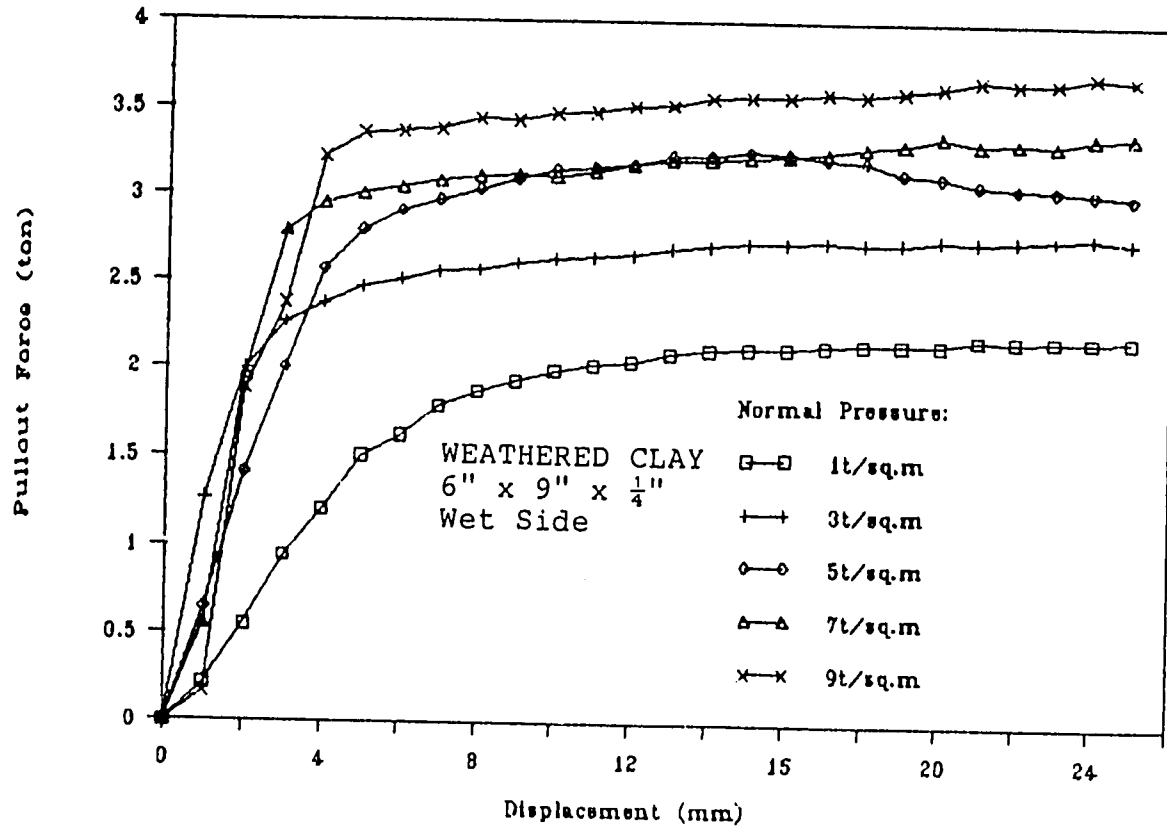

Fig. 17 Load-displacement Curves for 1/4" Diameter Bars with Weathered Clay Backfill Compacted at the Wet Side of Optimum.

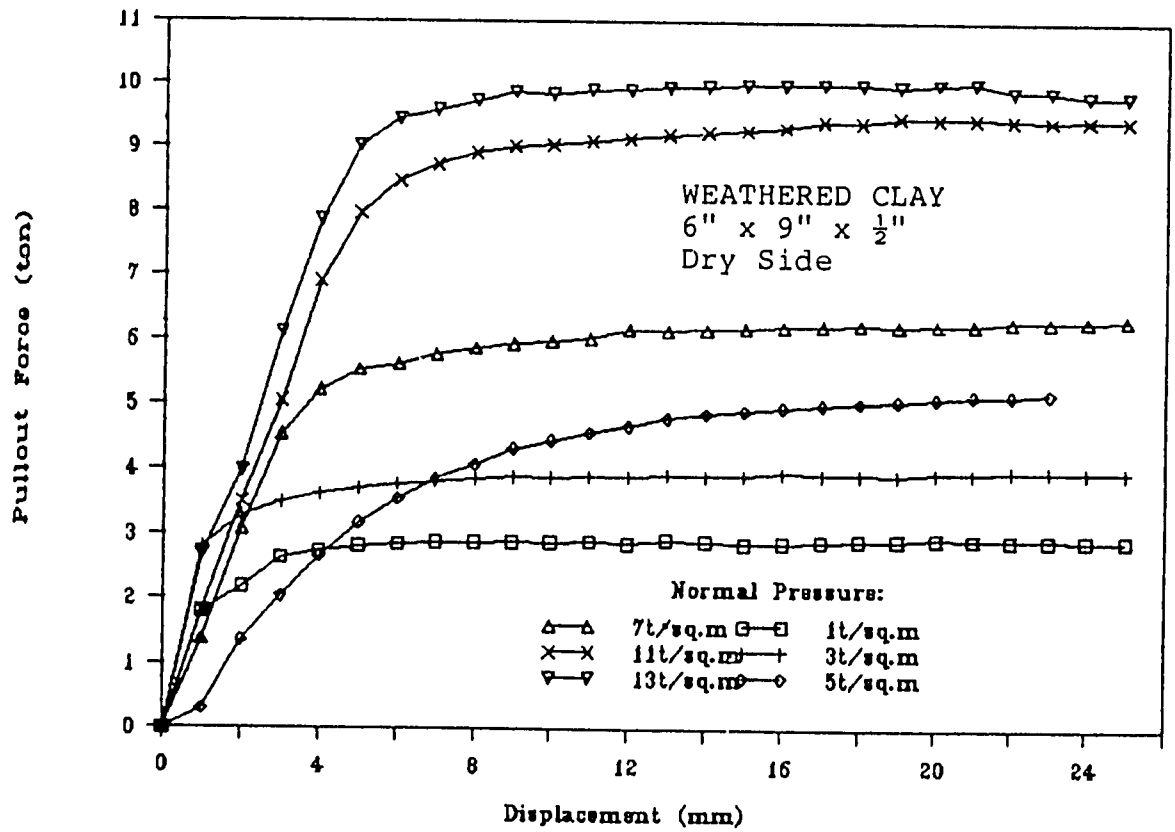

Fig. 18 Load-displacement Curves for 1/2" Diameter Bars with Weathered Clay Backfill Compacted at the Dry Side of Optimum.

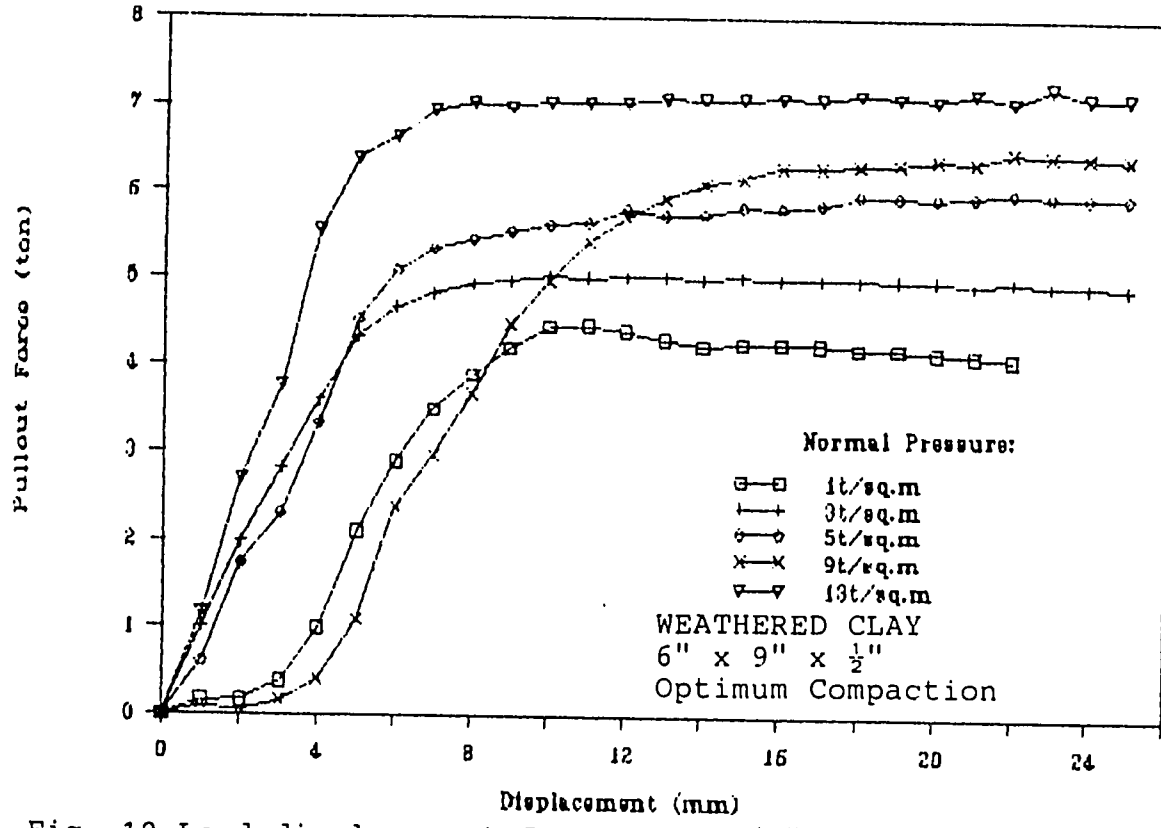

Fig. 19 Load-displacement Curves for 1/2" Diameter Bars with Weathered Clay Backfill Compacted at Optimum Water Content.

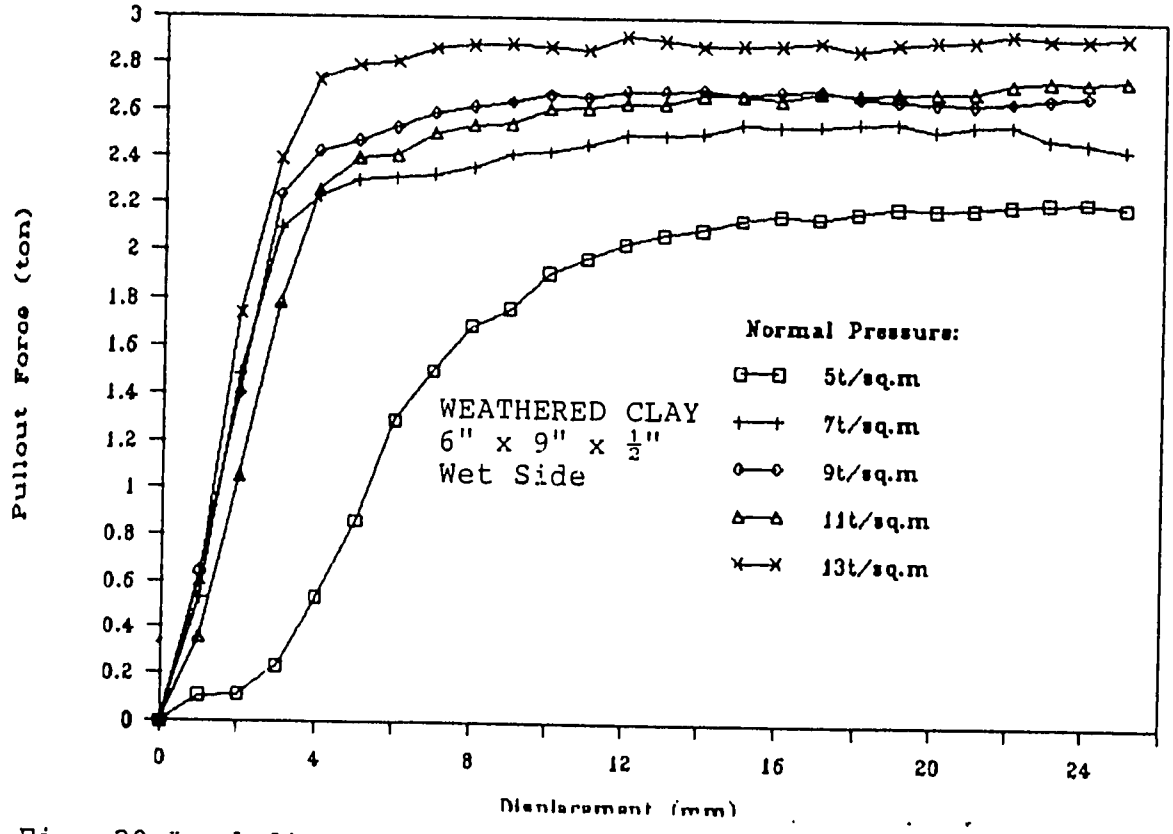

Fig. 20 Load-displacement Curves for 1/2" Diameter Bars with Weathered Clay Backfill Compacted at the Wet Side of Optimum.

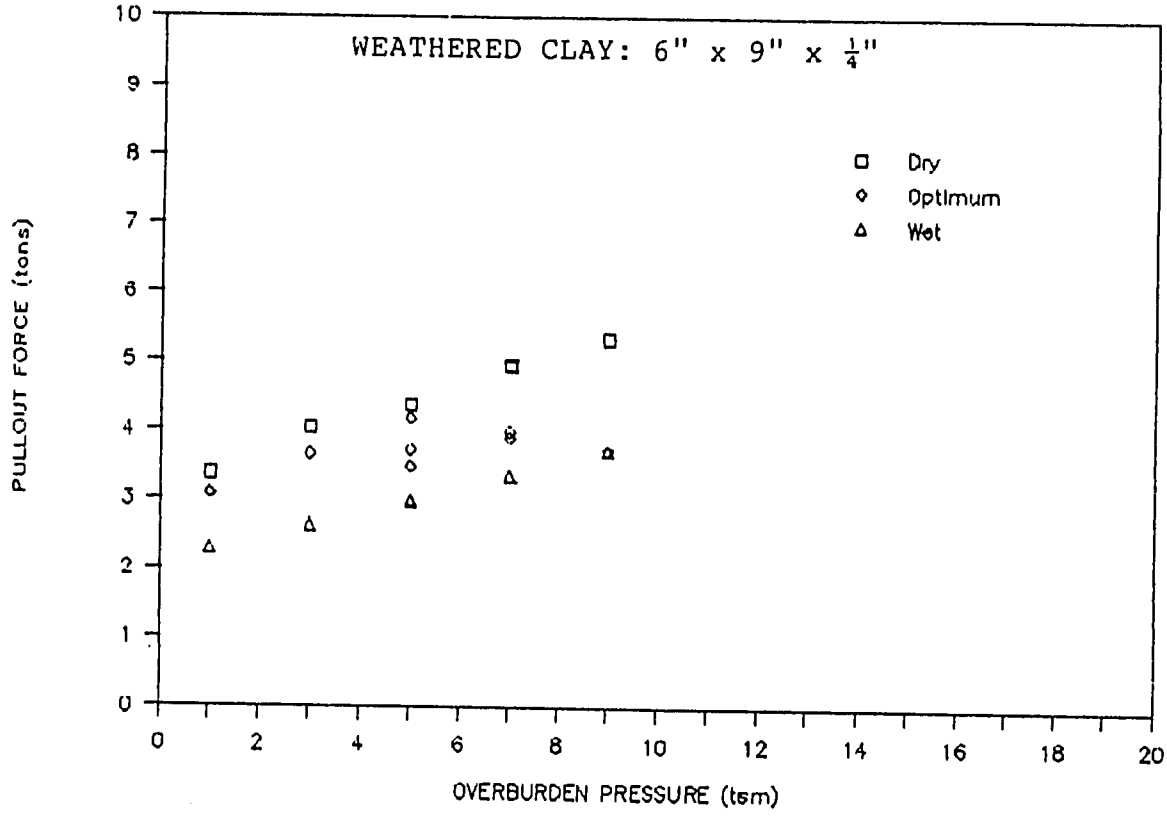

Fig. 21 Plots of Maximum Pullout Resistance Versus the Overburden Pressure Using Weathered Clay Backfill at Different Compaction Moisture Contents (1/4" diameter bar).

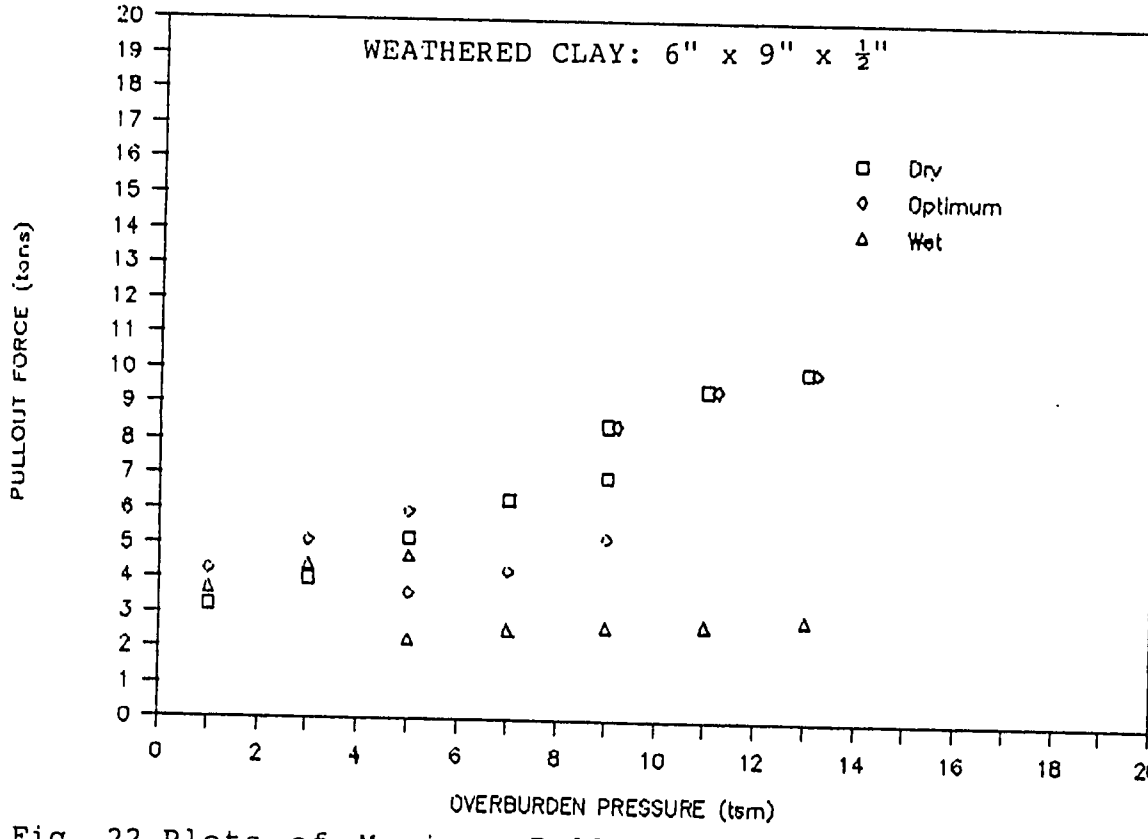

Fig. 22 Plots of Maximum Pullout Resistance Versus the Overburden Pressure Using Weathered Clay Backfill at Different Compaction Moisture Contents (1/2" diameter bar).

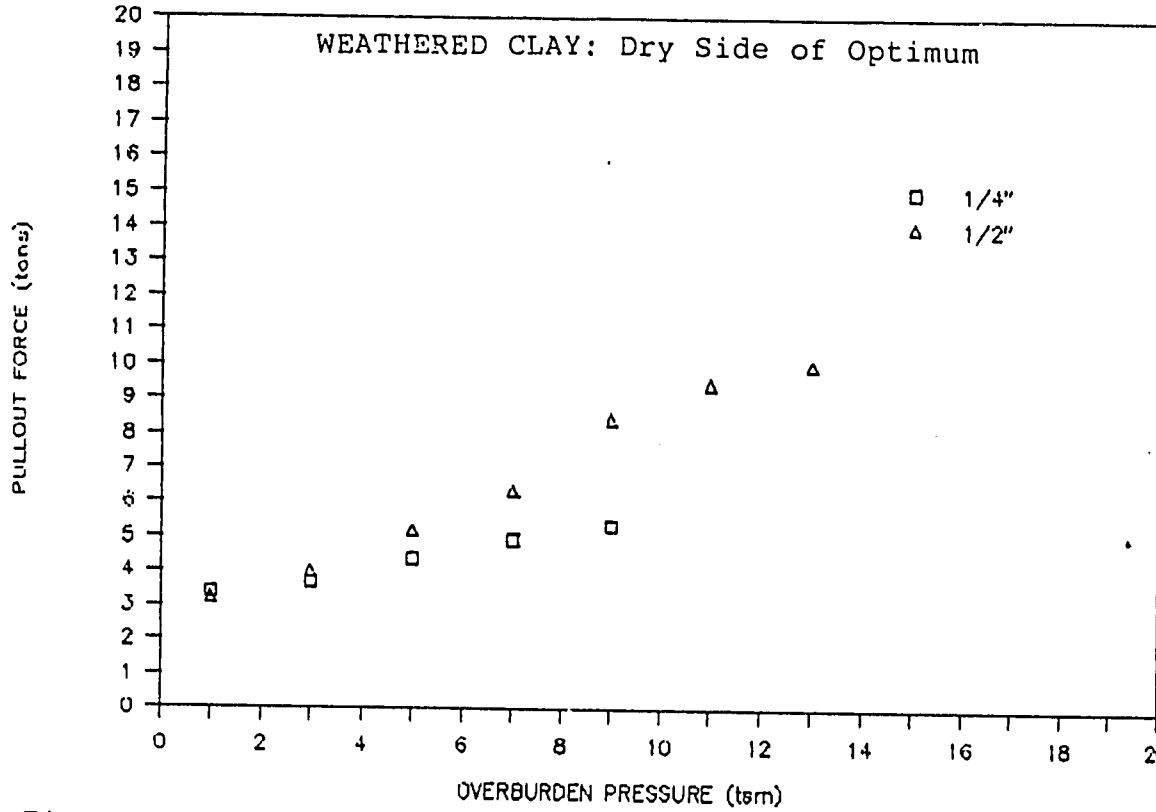

Fig. 23 Plots of Maximum Pullout Resistance Versus the Overburden Pressure Using Weathered Clay Backfill at Dry Side of Optimum and for Different Bar Sizes (6"x9" mesh).

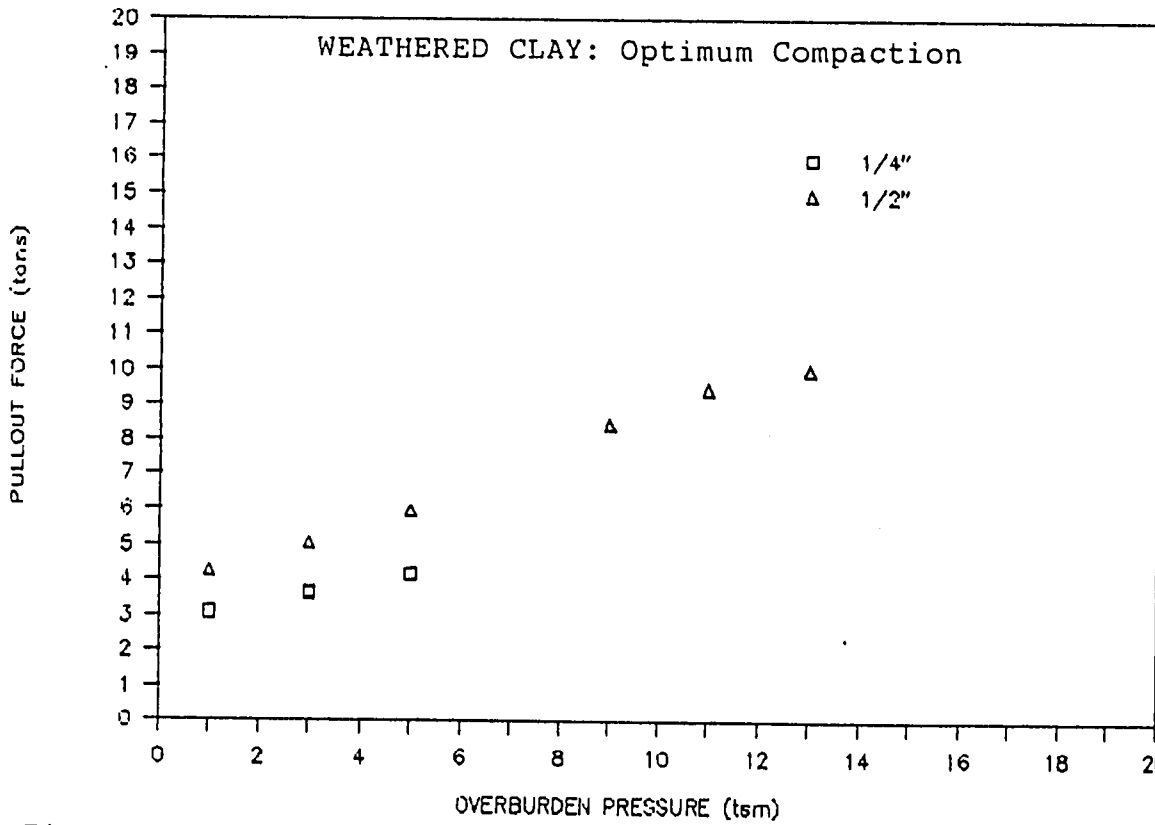

Fig. 24 Plots of Maximum Pullout Resistance Versus the Overburden Pressure Using Weathered Clay Backfill at Optimum Moisture Content and for Different Bar Sizes (6"x9" mesh).

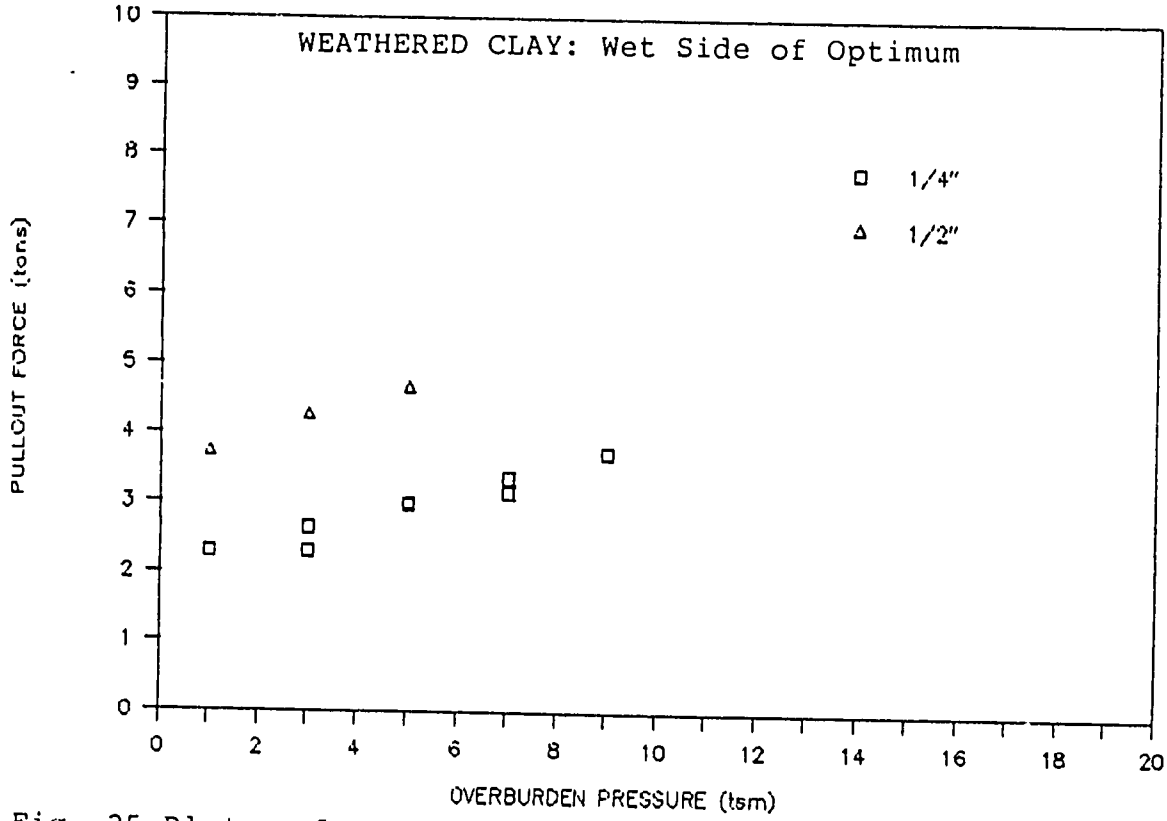

Fig. 25 Plots of Maximum Pullout Resistance Versus the Overburden Pressure Using Weathered Clay Backfill at Wet Side of Optimum and for Different Bar Sizes (6"x9" mesh).

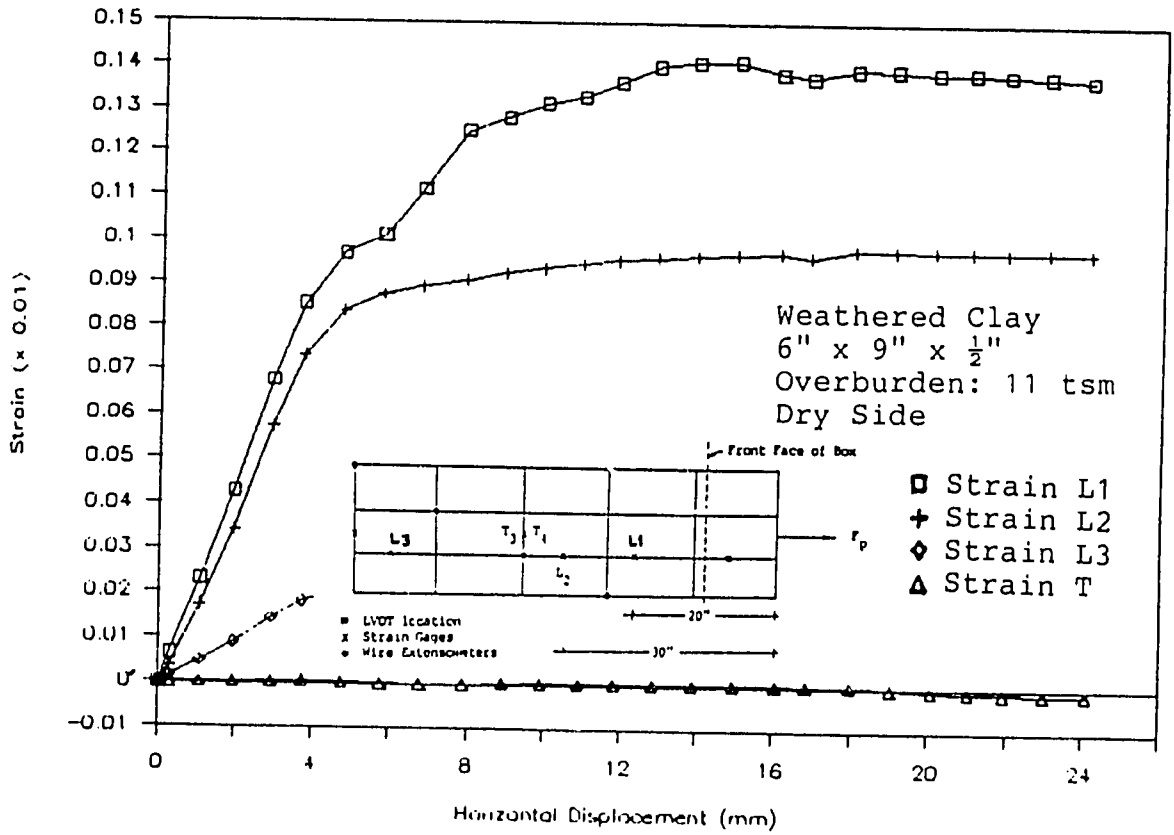

Fig. 26 Typical Plots of Axial Strain in the Longitudinal Bars Versus Horizontal Displacement for Different Strain Gage Locations (6"x9"x1/2", Dry Side).

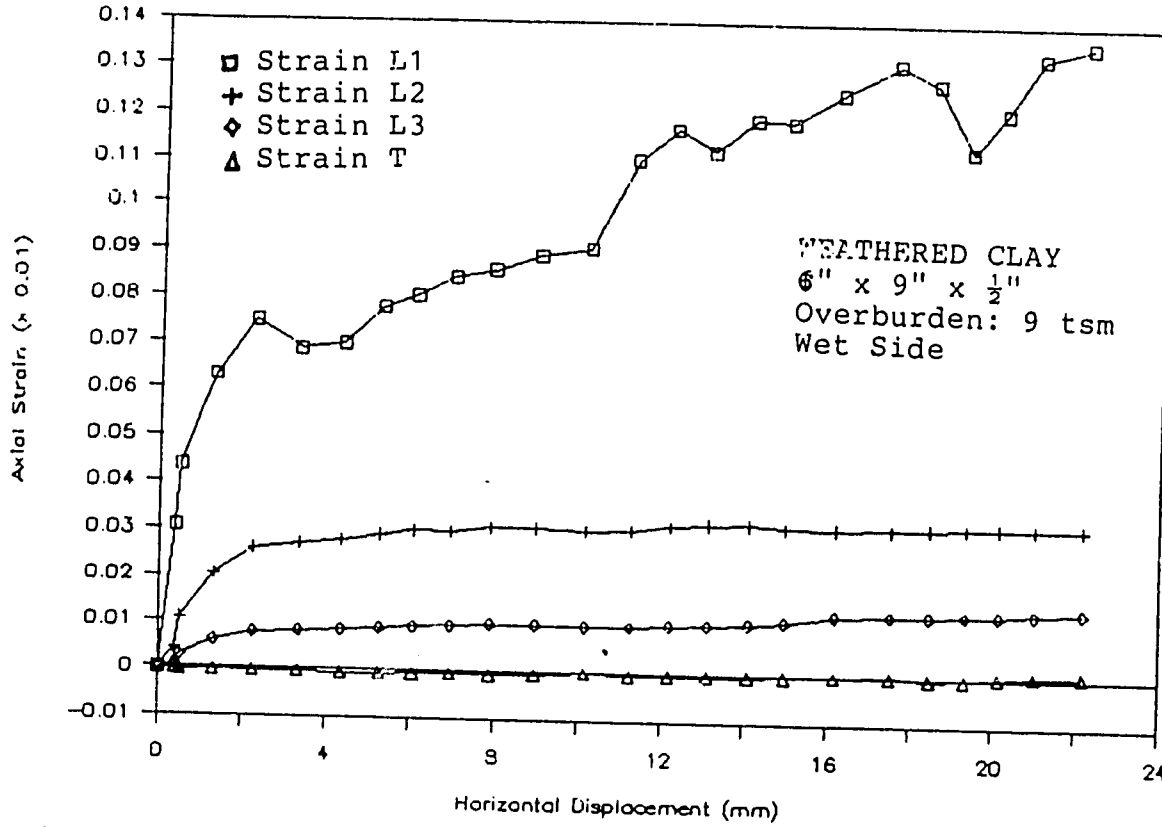

Fig. 27 Typical Plots of Axial Strain in the Longitudinal Bars Versus Horizontal Displacement for Different Strain Gage Locations (6"x9"x1/2", Wet Side).

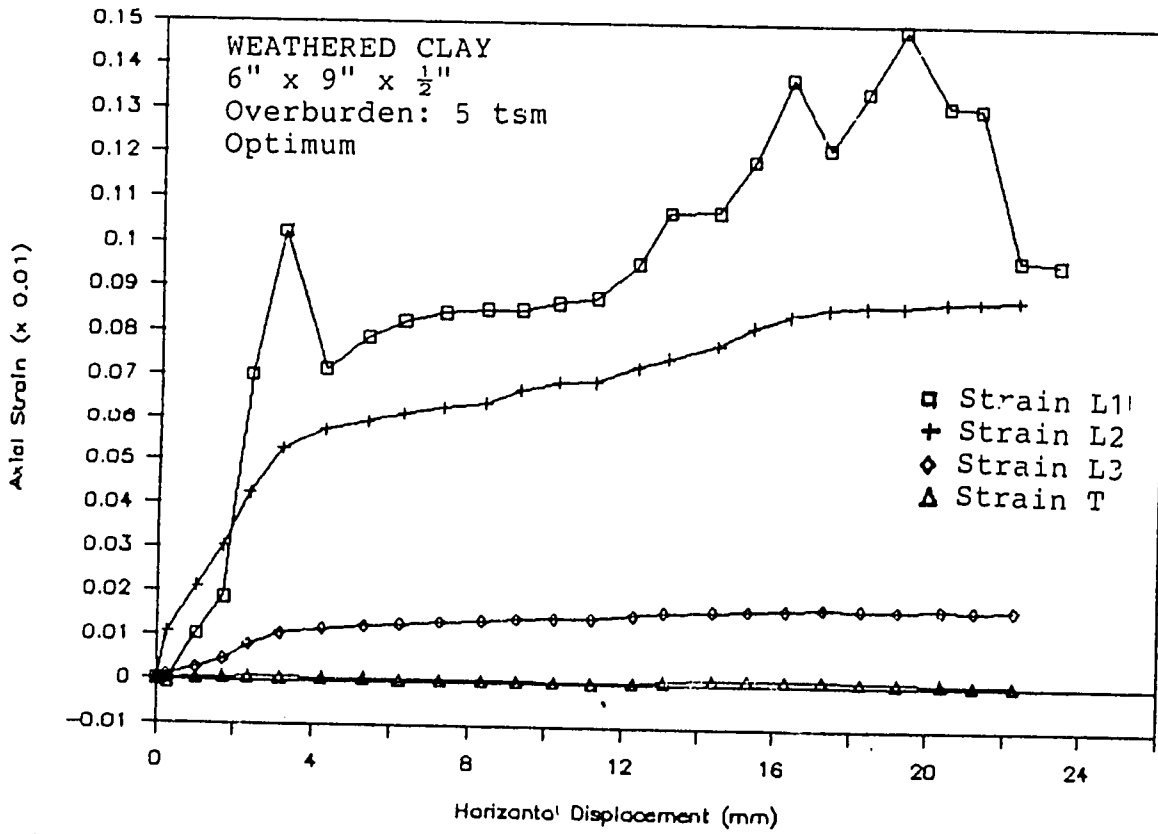

Fig. 28 Typical Plots of Axial Strain in the Longitudinal Bars Versus Horizontal Displacement for Different Strain Gage Locations (6"x9"x1/2", Optimum).

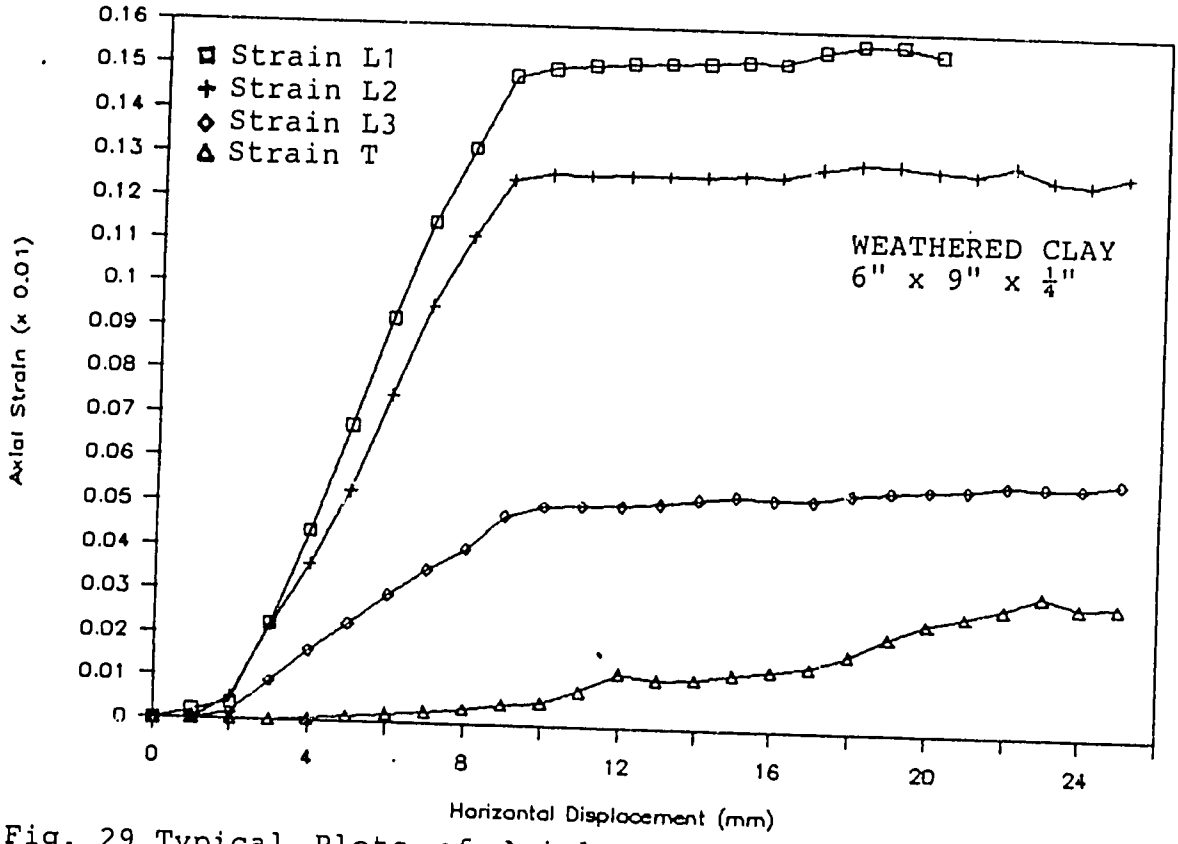

Fig. 29 Typical Plots of Axial Strain in the Longitudinal Bars Versus Horizontal Displacement for Different Strain Gage Locations (6"x9"x1/4", Dry Side).

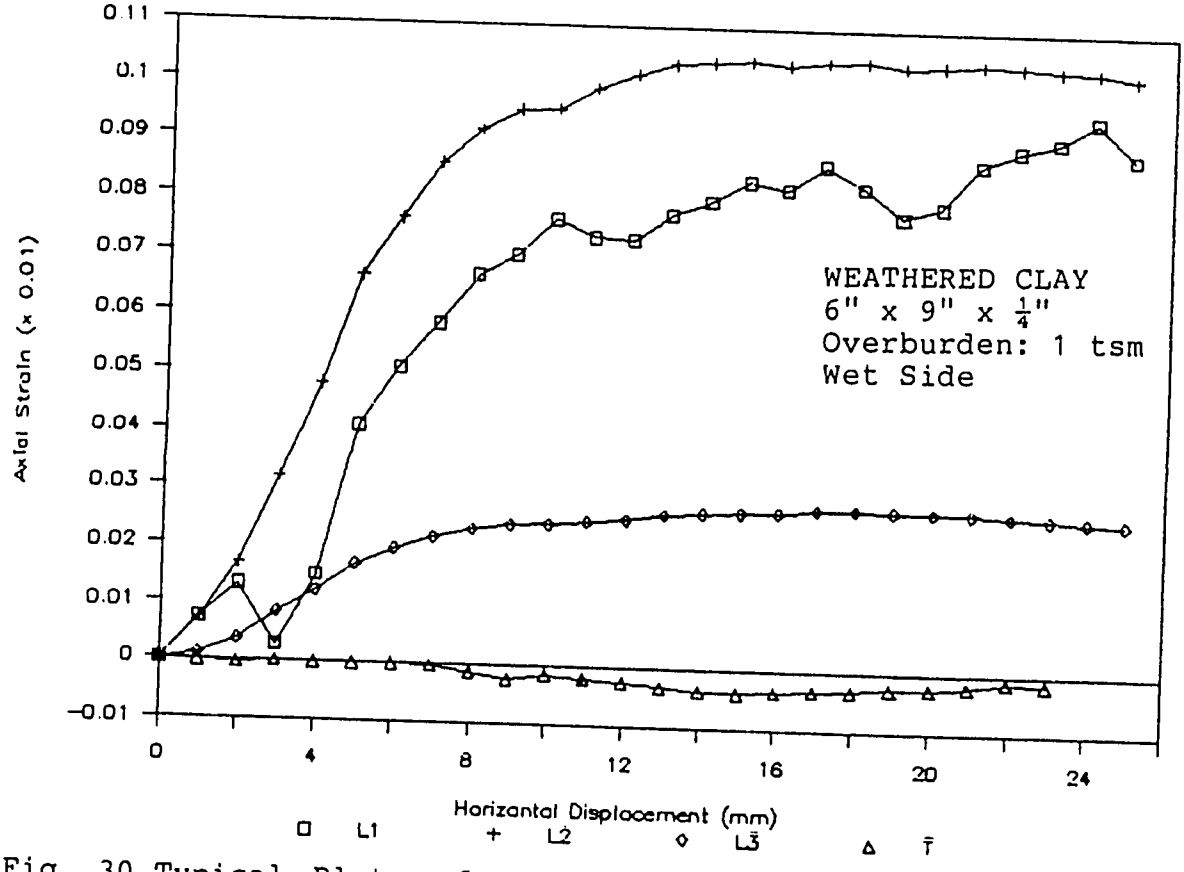

Fig. 30 Typical Plots of Axial Strain in the Longitudinal Bars Versus Horizontal Displacement for Different Strain Gage Locations (6"x9"x1/4", Wet Side).

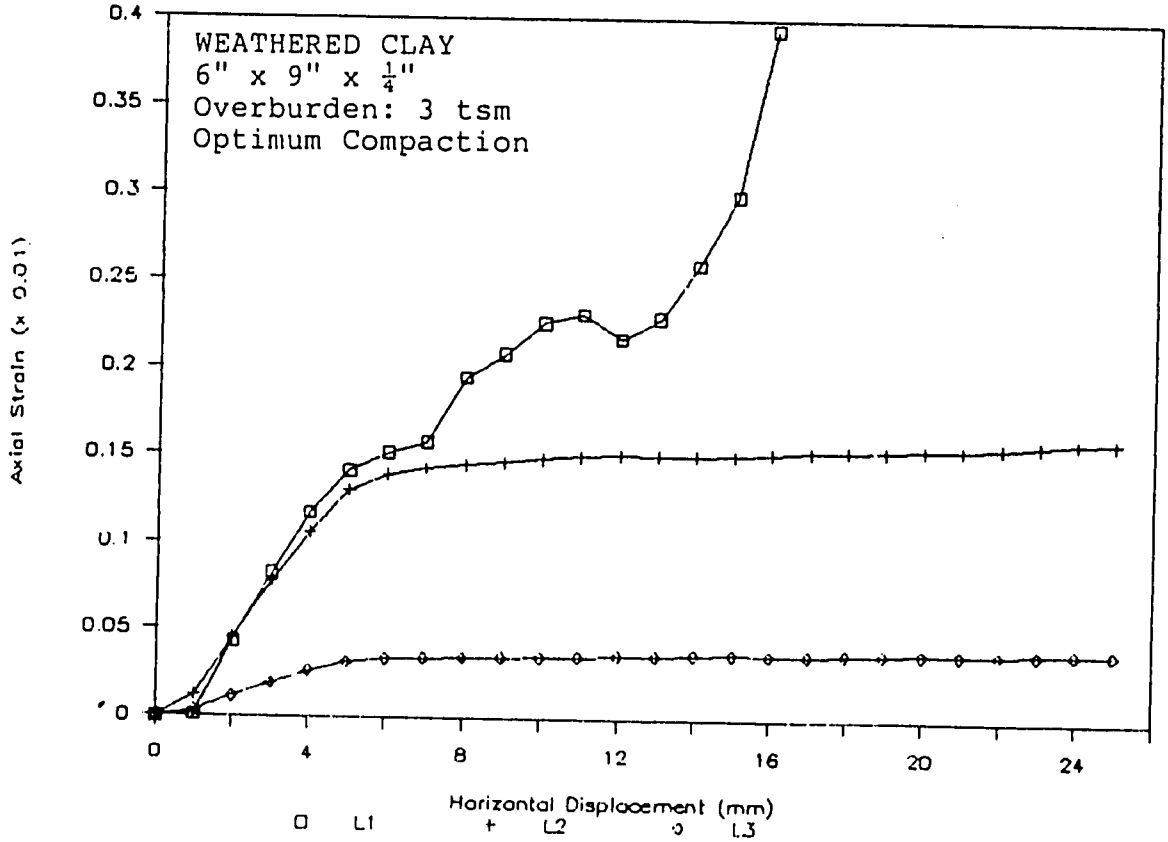

Fig. 31 Typical Plots of Axial Strain in the Longitudinal Bars Versus Horizontal Displacement for Different Strain Gage Locations (6"x9"x1/4", Optimum).

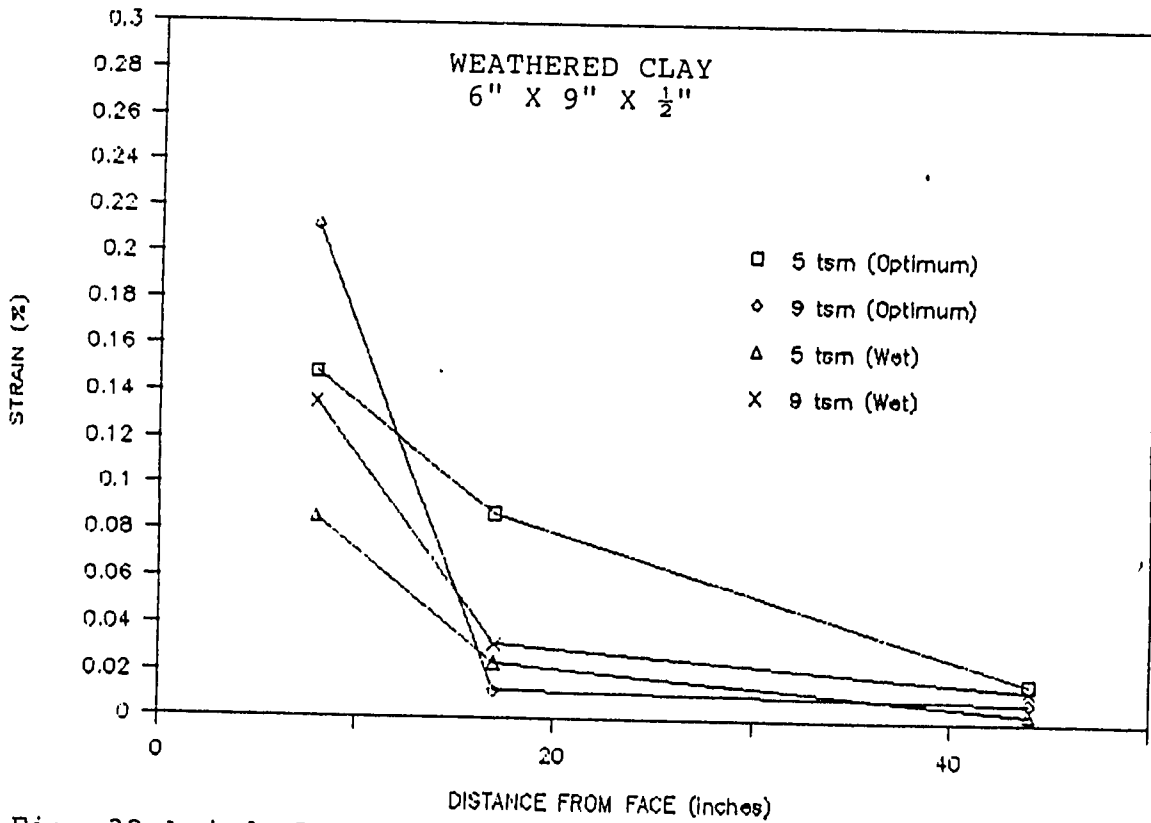

Fig. 32 Axial Strains in the Longitudinal Bars Plotted against Distance from the Point of Application of the Pullout Load for Different Overburden Pressures and Compaction Moisture Contents.

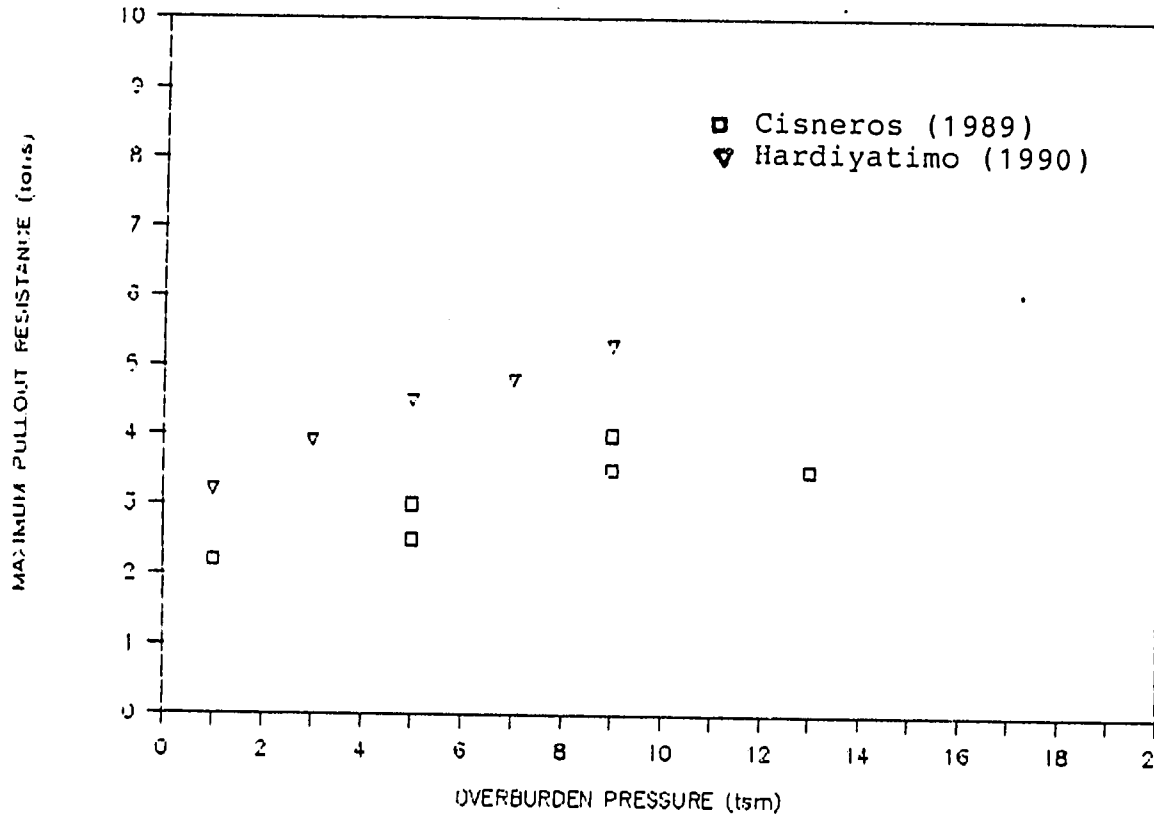

Fig. 33 Comparison of the Recent Data Obtained for Weathered Clay Compacted at the Dry Side of Optimum with Data Previously Reported (1/4" diameter bars).

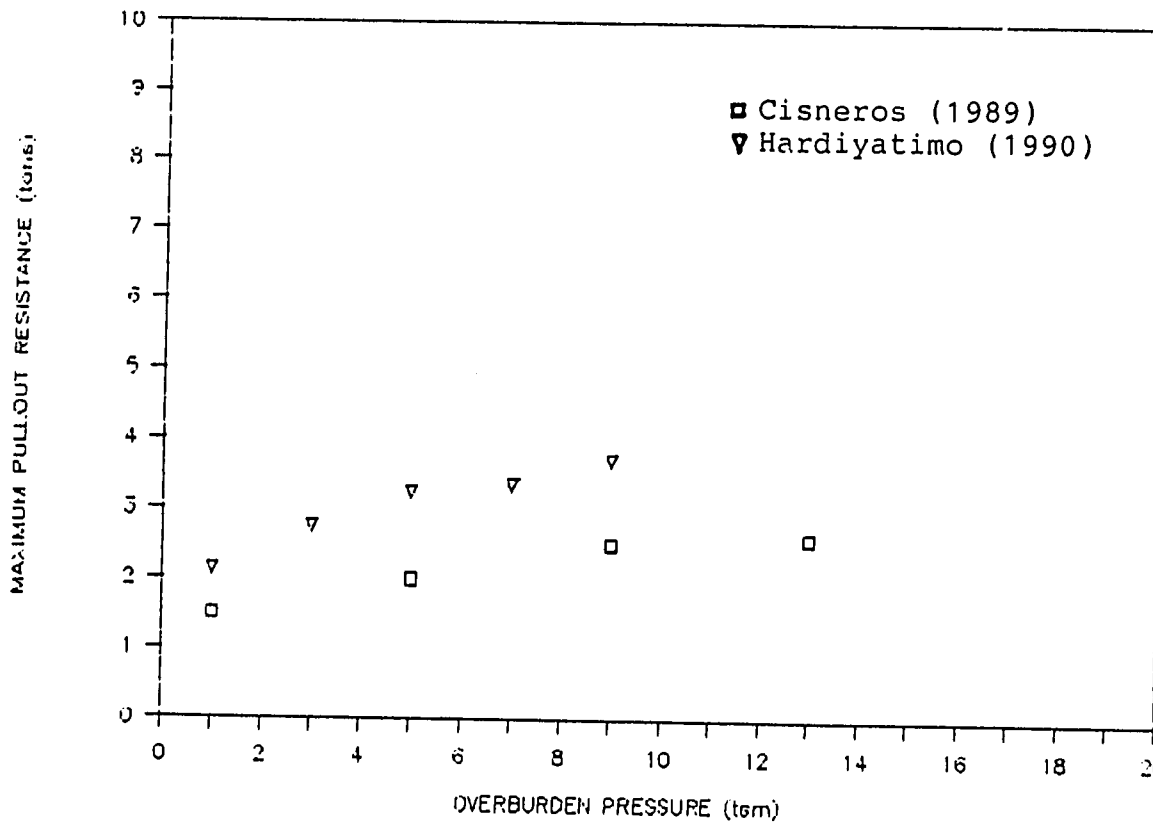

Fig. 34 Comparison of the Recent Data Obtained for Weathered Clay Compacted at the Wet Side of Optimum with Data Previously Reported (1/4" diameter bars).

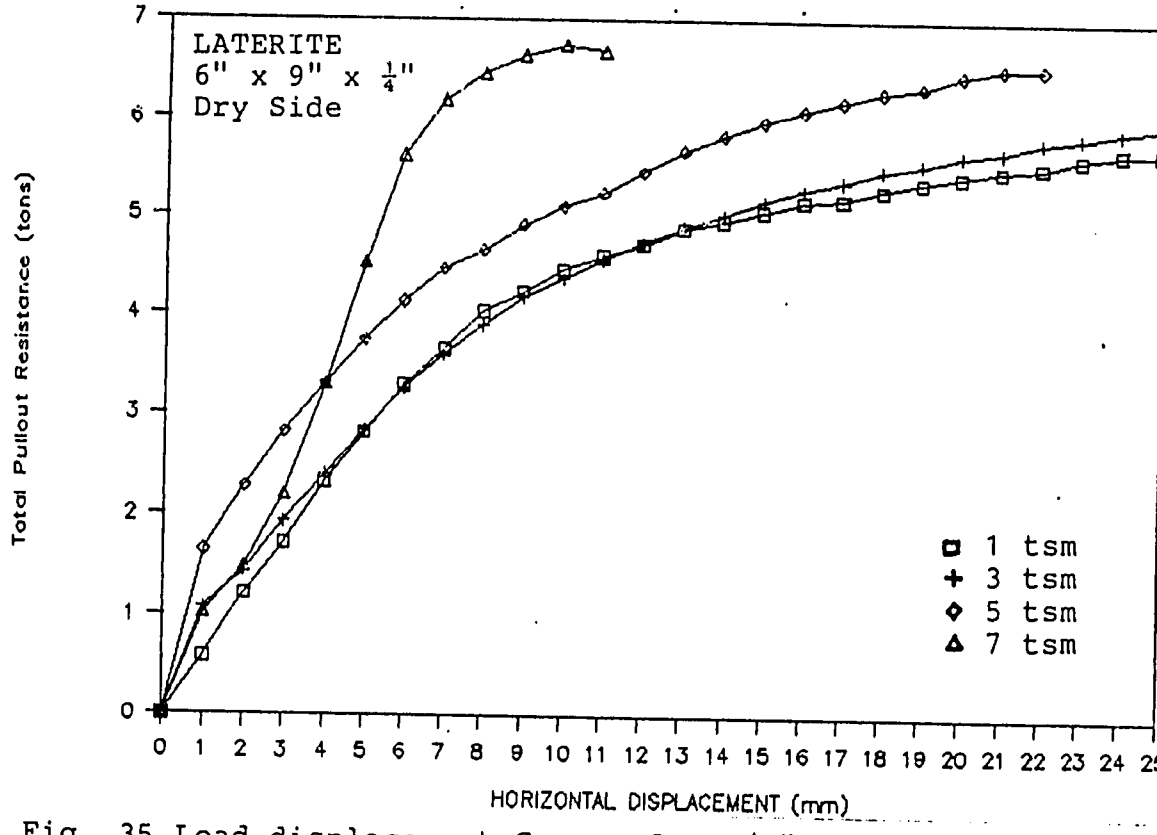

Fig. 35 Load-displacement Curves for 1/4" Diameter Bars with Lateritic Backfill Compacted at the Dry Side of Optimum (6"x9" mesh).

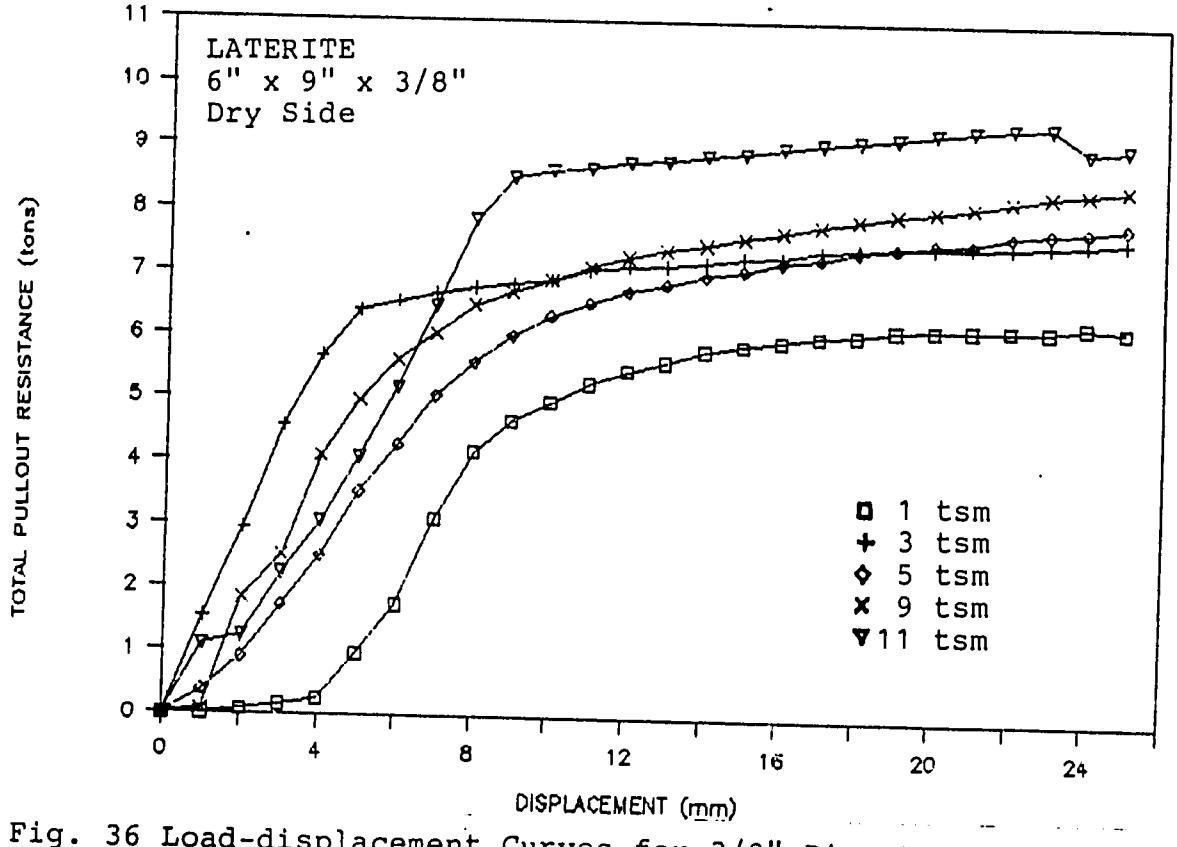

Fig. 36 Load-displacement Curves for 3/8" Diameter Bars with Lateritic Backfill Compacted at the Dry Side of Optimum (6"x9" mesh).

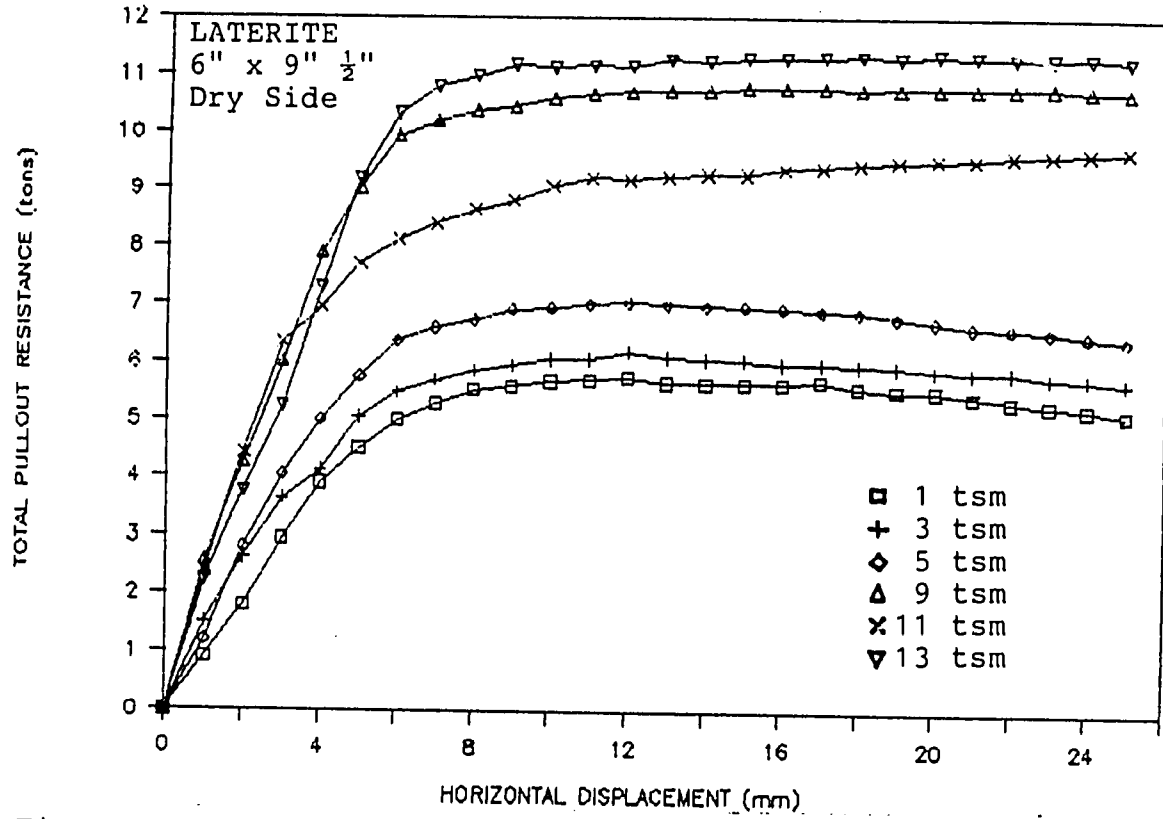

Fig. 37 Load-displacement Curves for 1/2" Diameter Bars with Lateritic Backfill Compacted at the Dry Side of Optimum (6"x9" mesh).

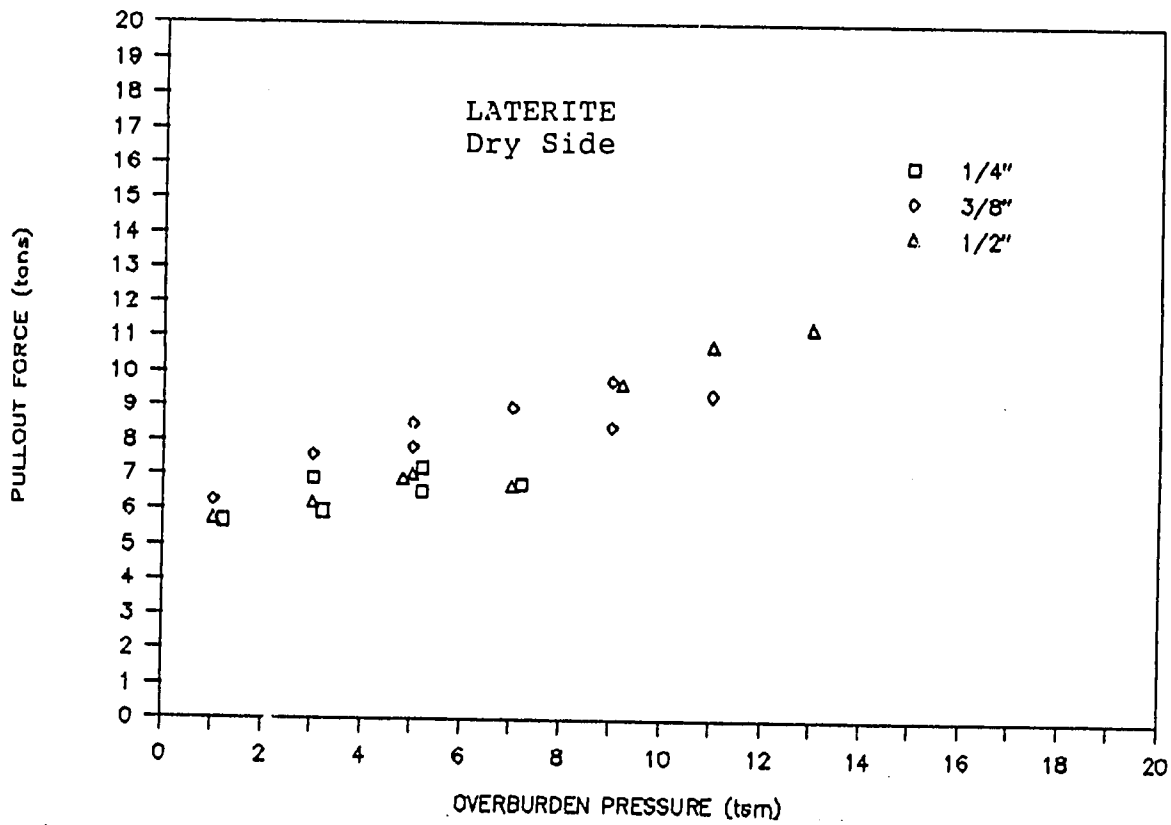

Fig. 38 Plots of Maximum Pullout Resistance Versus the Overburden Pressure Using Lateritic Backfill Compacted at the Dry Side of Optimum and for Different Bar Sizes (6"x9" mesh).

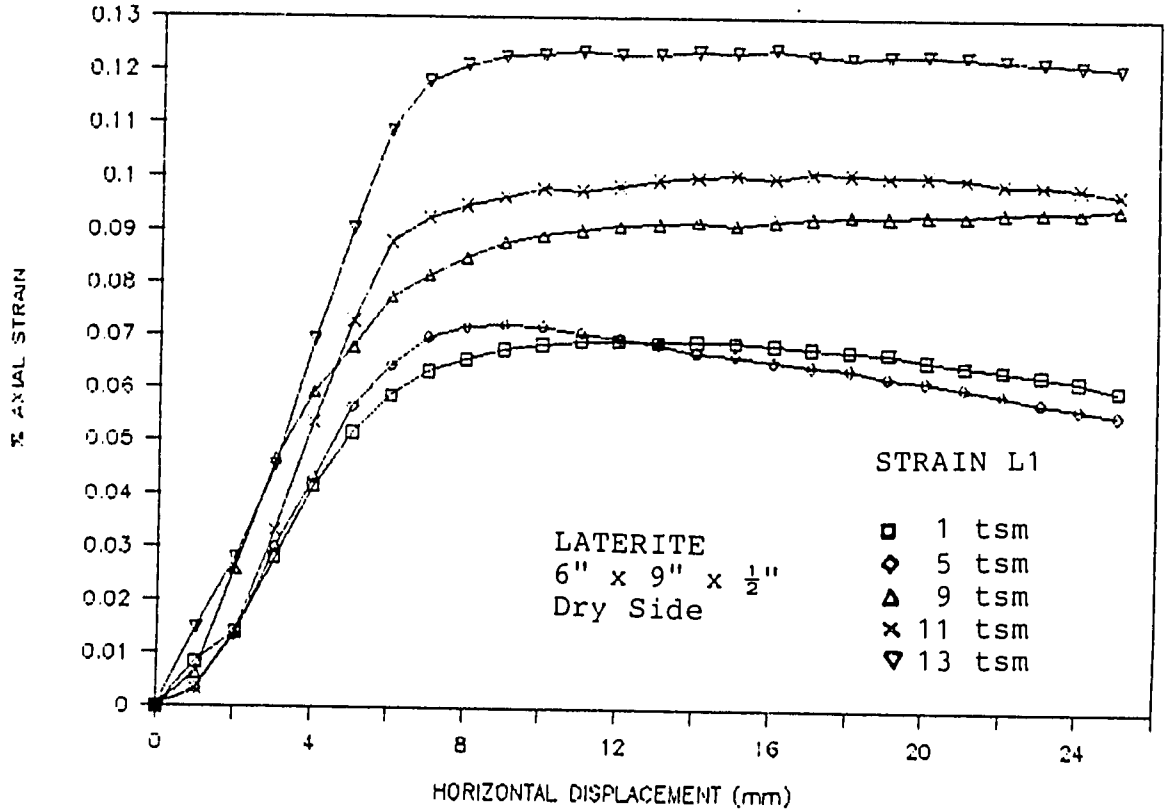

Fig. 39 Plots of Axial Strain at Location L1 Versus Horizontal Mat Displacement for Different Overburden Pressures (1/2" diameter bar).

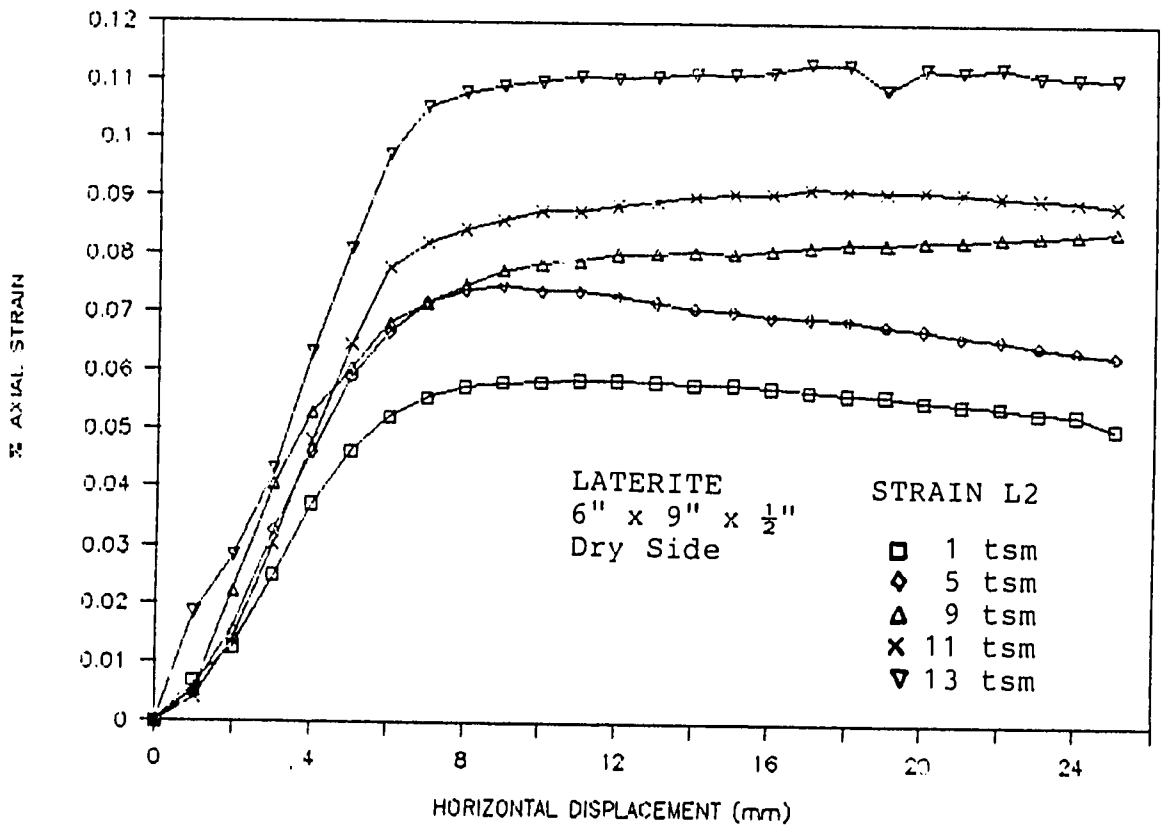

Fig. 40 Plots of Axial Strain at Location L2 Versus Horizontal Mat Displacement for Different Overburden Pressures (1/2" diameter bar).

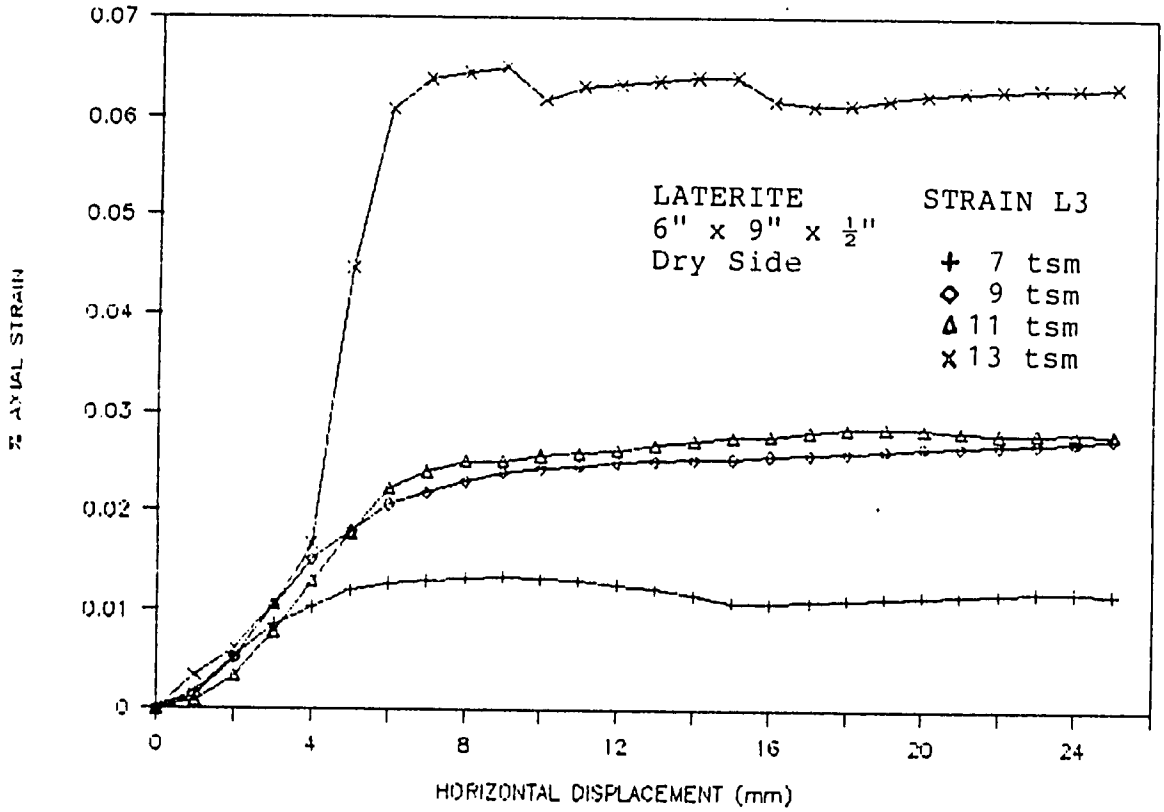

Fig. 41 Plots of Axial Strain at Location L3 Versus Horizontal Mat Displacement for Different Overburden Pressures (1/2" diameter bar).

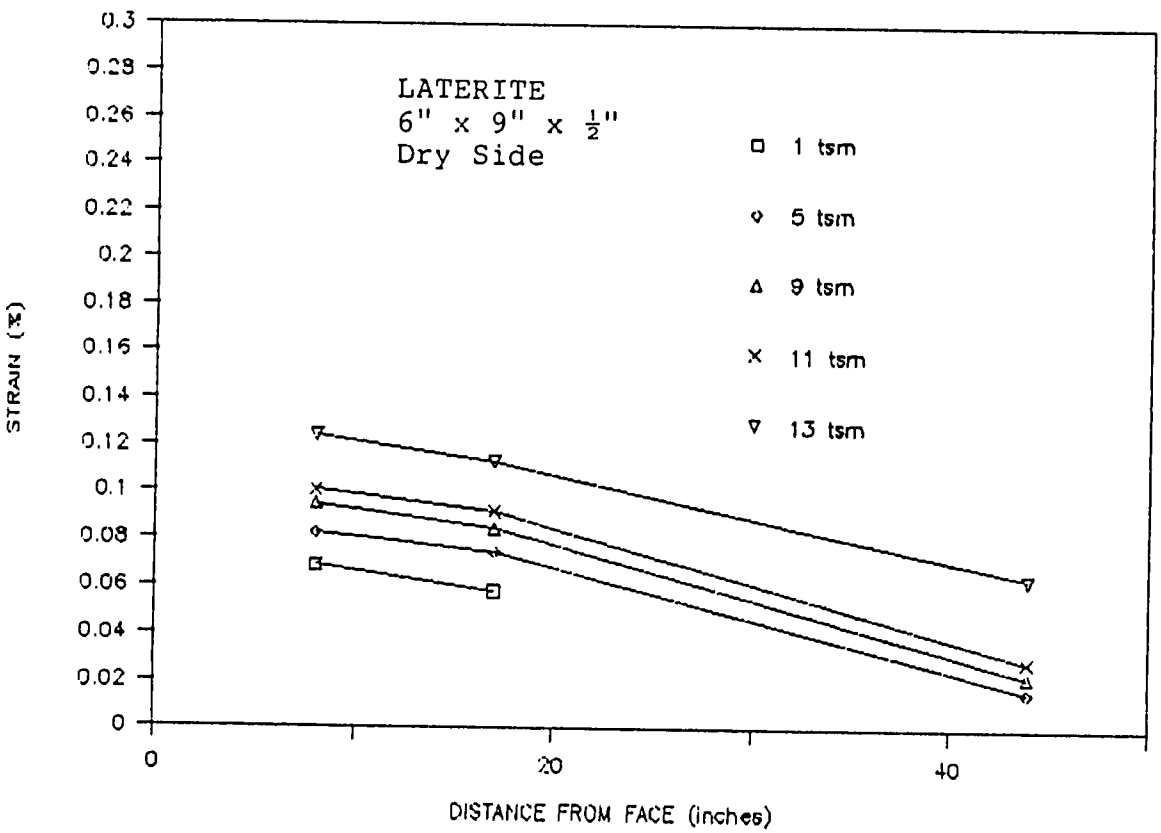

Fig. 42 Typical Plots of Axial Strain in the Longitudinal Bars against Distance from the Point of Application of the Load and for Different Normal Pressures (1/2" diameter bar).

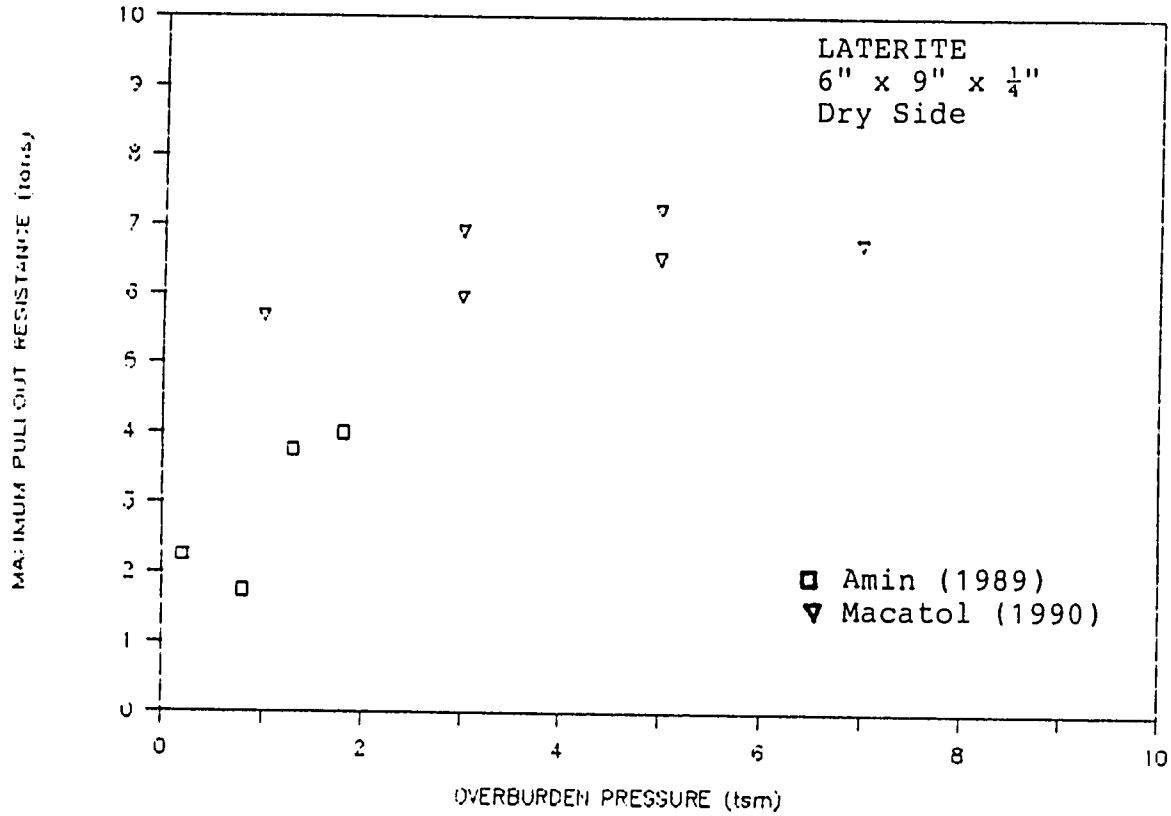

Fig. 43 Comparison of the Recent Data Obtained for Lateritic Residual Soil Compacted at the Dry Side of Optimum with Data Previously Reported (1/4" diameter bars).

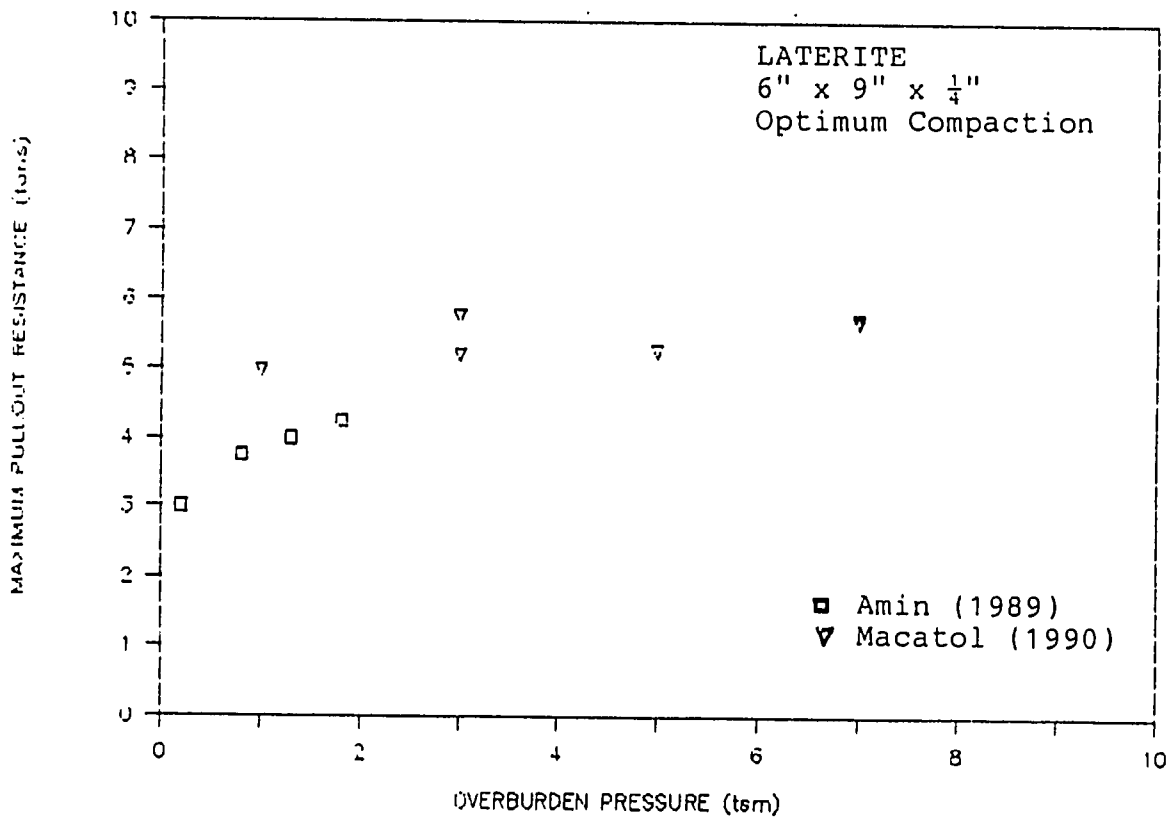

Fig. 44 Comparison of the Recent Data Obtained for Lateritic Residual Soil Compacted at Optimum Water Content with Data Previously Reported (1/4" diameter bars).

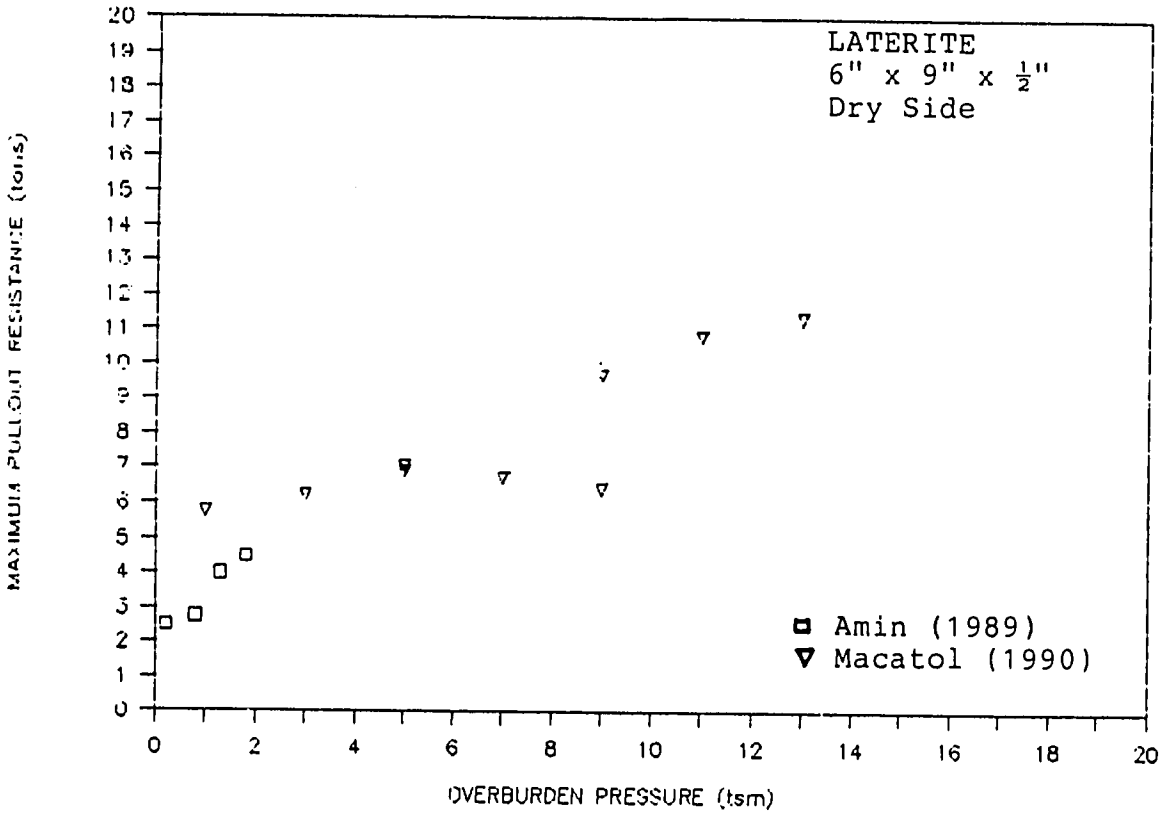

Fig. 45 Comparison of the Recent Data Obtained for Lateritic Residual Soil Compacted at the Dry Side of Optimum with Data Previously Reported (1/2" diameter bars).

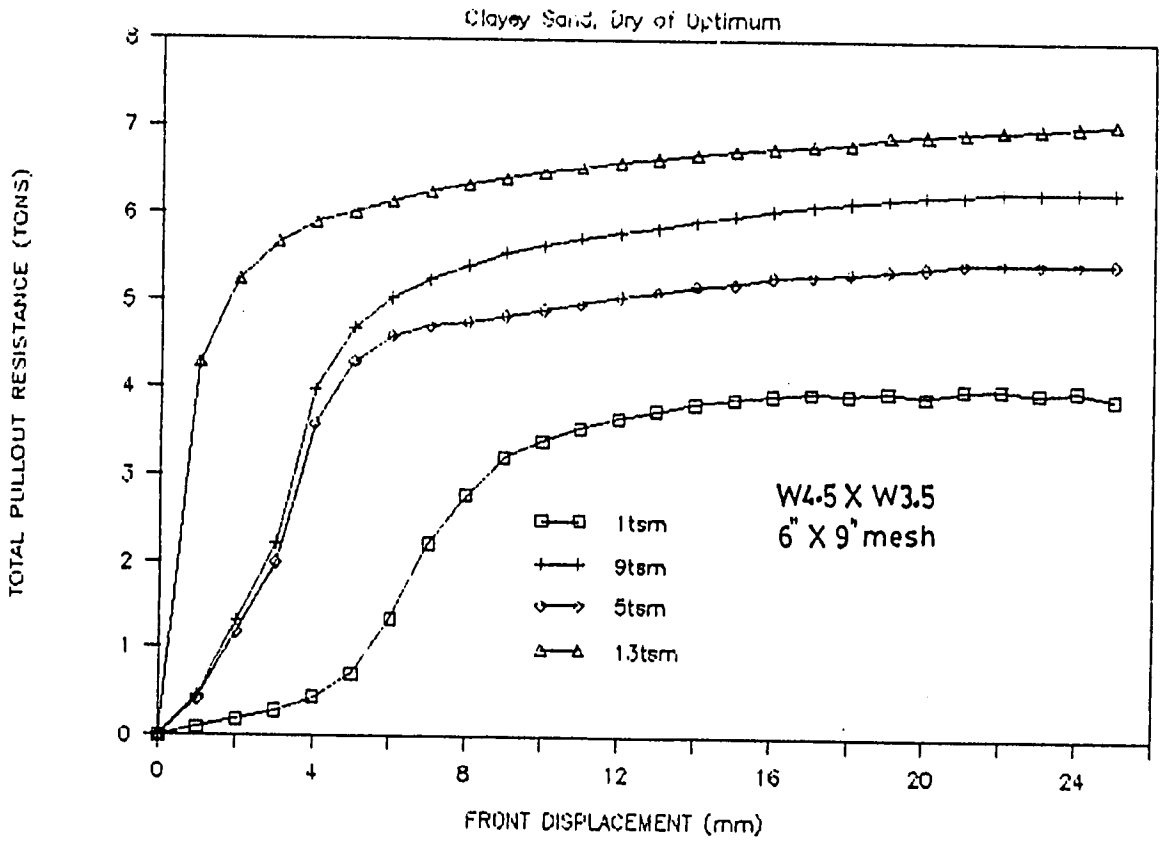

Fig. 46 Load-displacement Curves for W4.5xW3.5 Mats with Clayey Sand Backfill Compacted at the Dry Side of Optimum (6"x9" mesh).

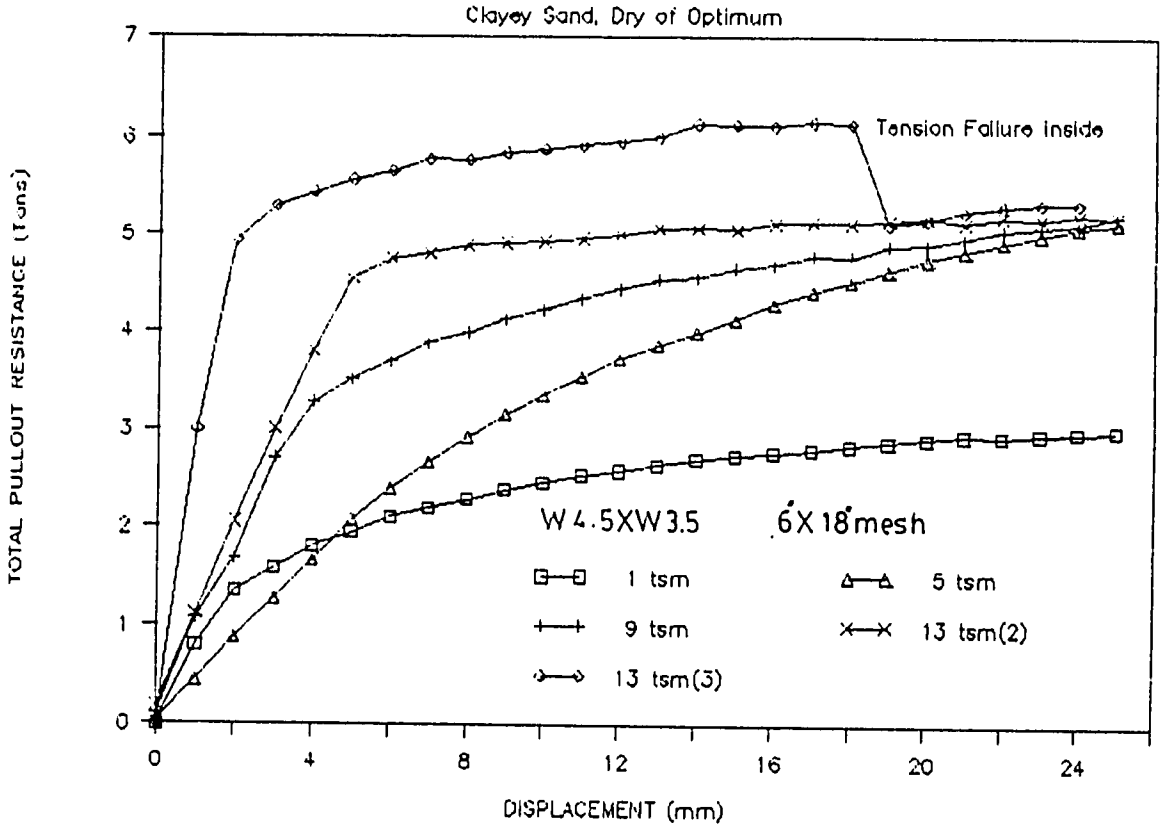

Fig. 47 Load-displacement Curves for W4.5xW3.5 Mats with Clayey Sand Backfill Compacted at the Dry Side of Optimum (6"x18" mesh).

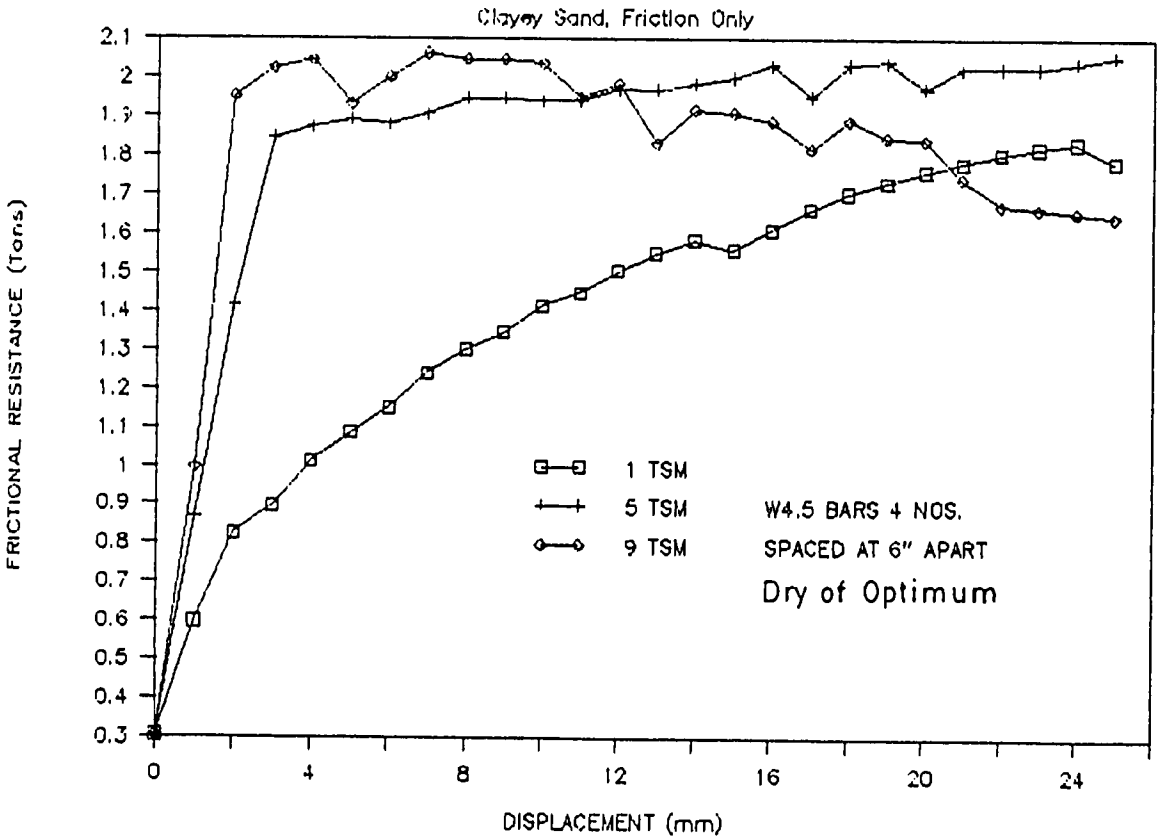

Fig. 48 Load-displacement Curves for W4.5 bars with Clayey Sand Backfill Compacted at the Dry Side of Optimum to Measure Frictional Resistance.

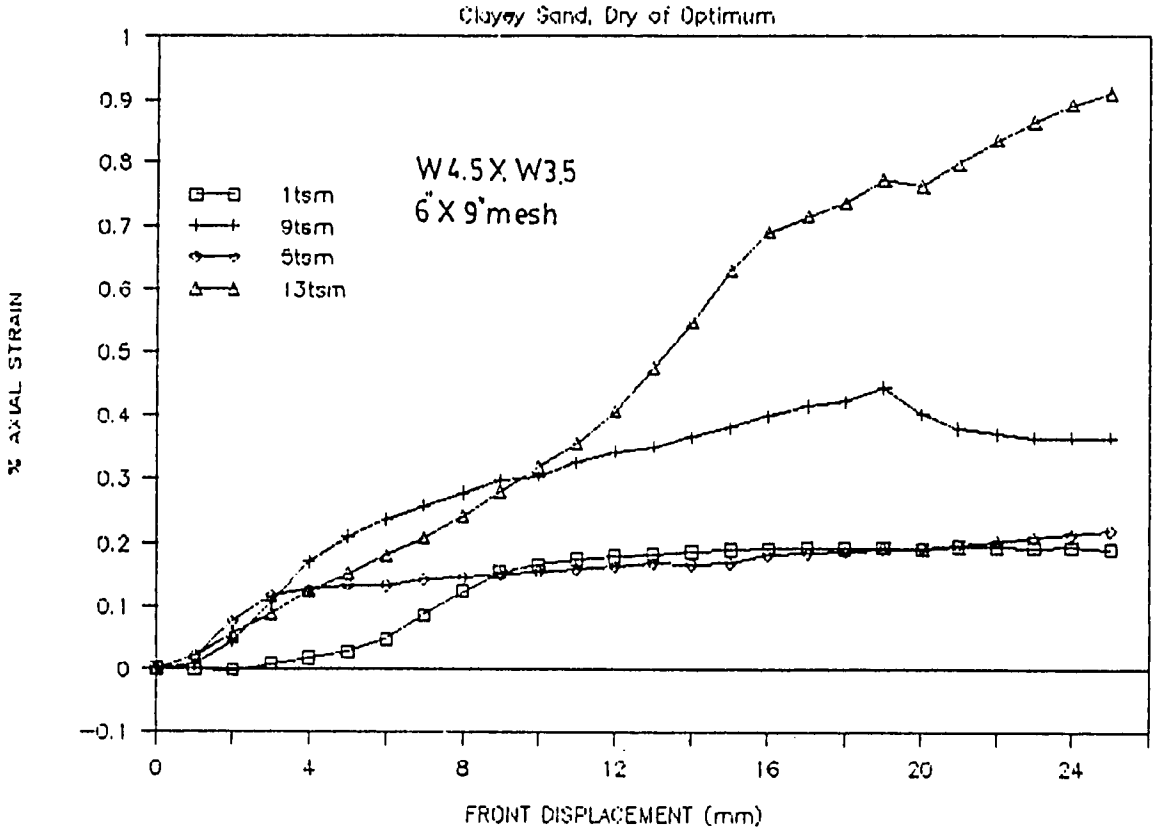

Fig. 49 Plots of Axial Strain at Location L1 Versus the Horizontal Mat Displacement for Different Normal Pressures Using Clayey Sand Backfill Compacted at the Dry Side of Optimum (W4.5xW3.5, 6"x9" mesh).

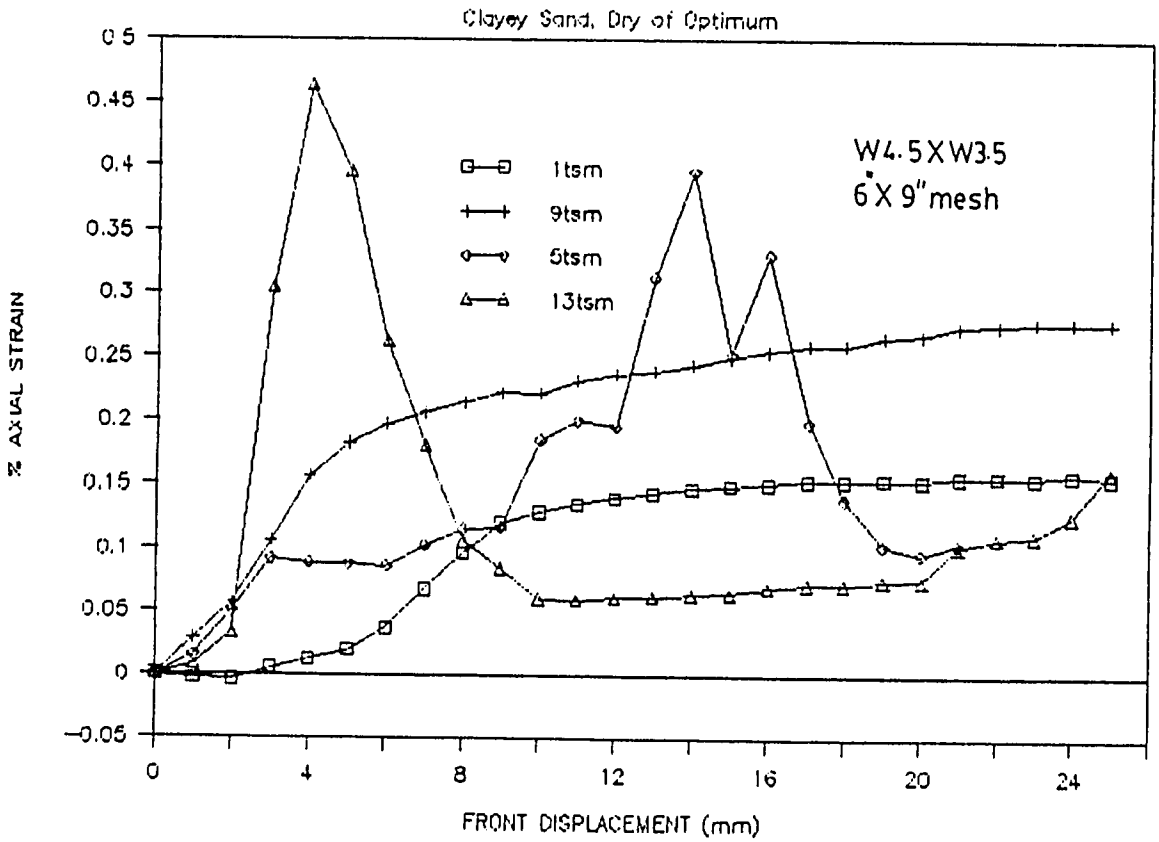

Fig. 50 Plots of Axial Strain at Location L2 Versus the Horizontal Mat Displacement for Different Normal Pressures Using Clayey Sand Backfill Compacted at the Dry Side of Optimum (W4.5xW3.5, 6"x9" mesh).

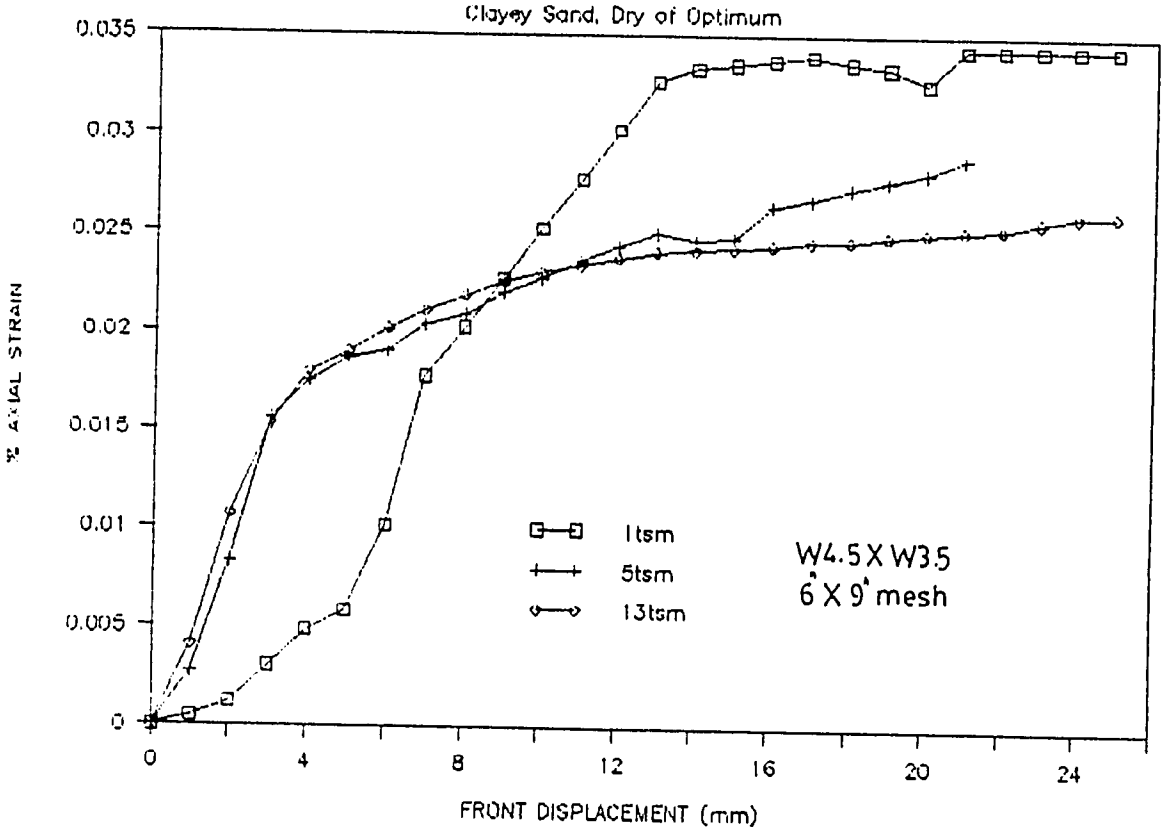

Fig. 51 Plots of Axial Strain at Location L3 Versus the Horizontal Mat Displacement for Different Normal Pressures Using Clayey Sand Backfill Compacted at the Dry Side of Optimum (W4.5xW3.5, 6"x9" mesh).

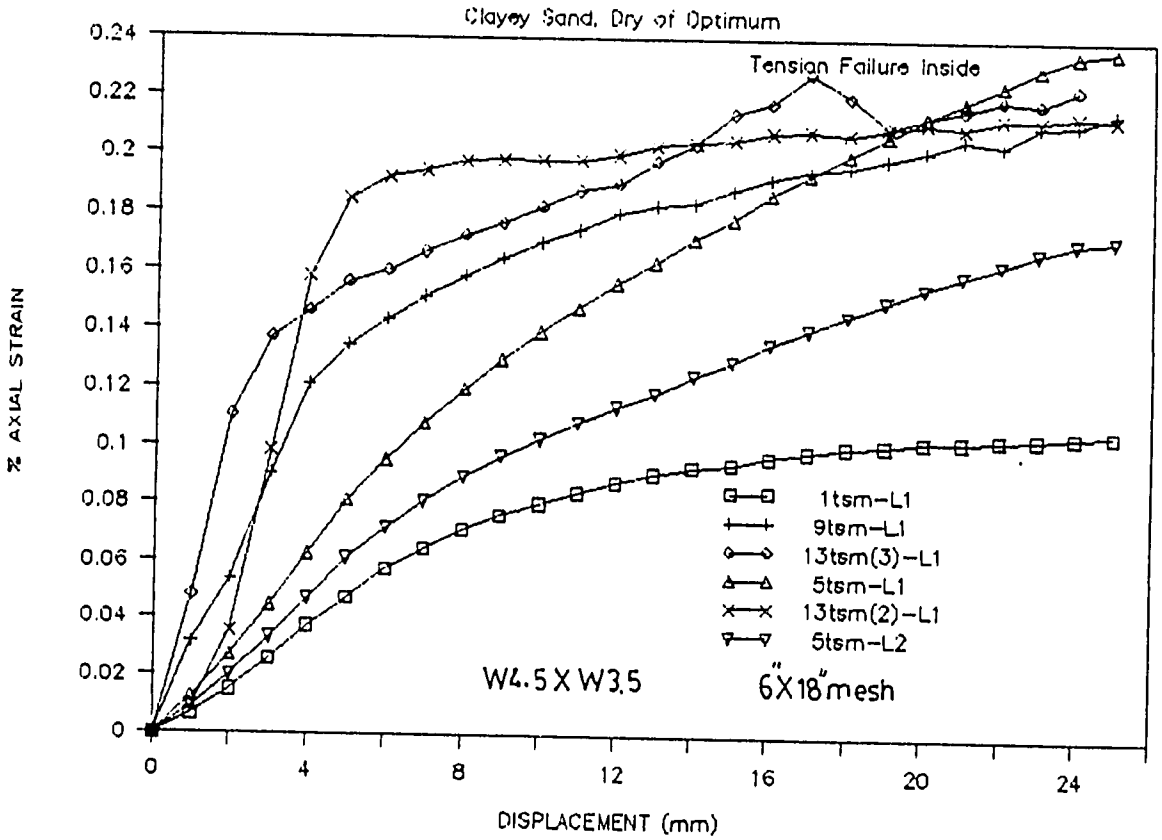

Fig. 52 Plots of Axial Strain at Locations L1 and L2 Versus the Horizontal Mat Displacement for Different Normal Pressures Using Clayey Sand Backfill Compacted at the Dry Side of Optimum (W4.5xW3.5, 6"x18" mesh).

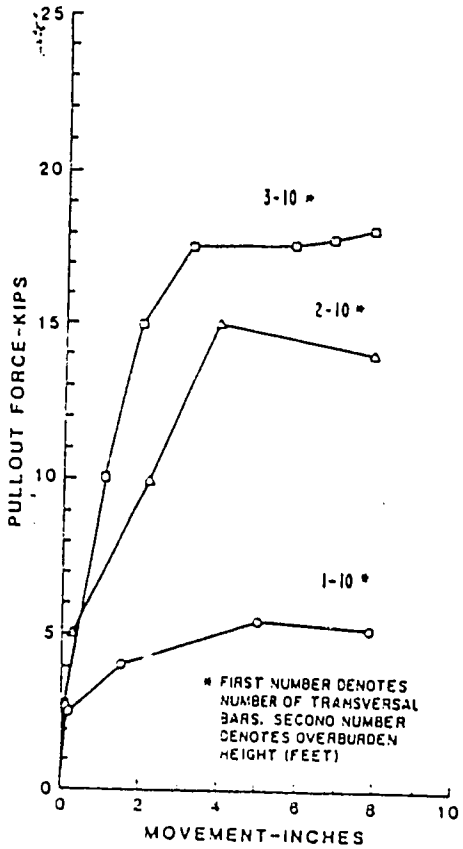

Fig. 53 Field Pullout Resistance of Dummy Bar-Mats at 10 ft. Overburden (after Hannon and Forsyth, 1984).

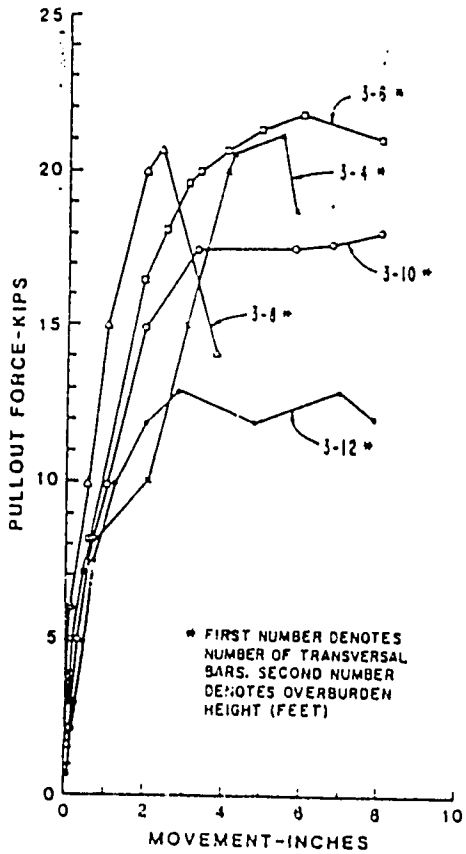

Fig. 54 Field Pullout Resistance of Dummy Bar-mats with Variable Overburden (after Hannon and Forsyth, 1984).

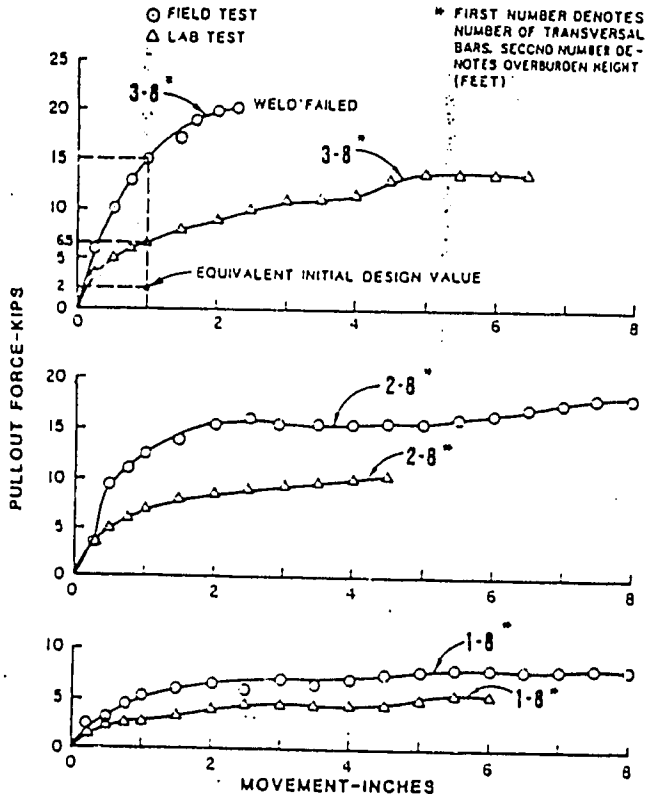

Fig. 55 Comparison of Laboratory and Field Pullout Tests with One, Two and Three Transverse Bars (after Hannon and Forsyth, 1984).

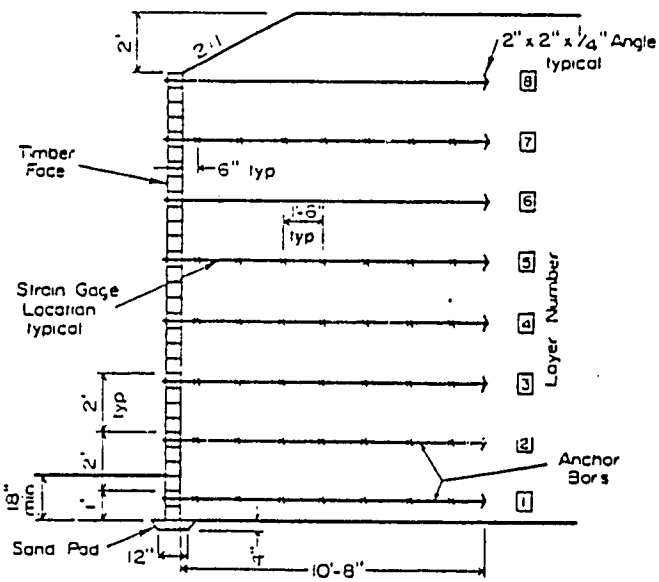

Fig. 56 Section of Syro Anchored Retaining Wall Showing Instrumentation Points (after Anderson et al, 1986).

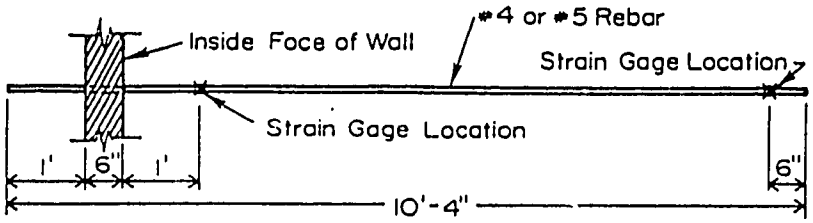

Fig. 57 (a) Single Instrumented Rebar Used for Pullout Testing in the Syro Experimental Wall to Measure Frictional Resistance (after Anderson et al, 1986).

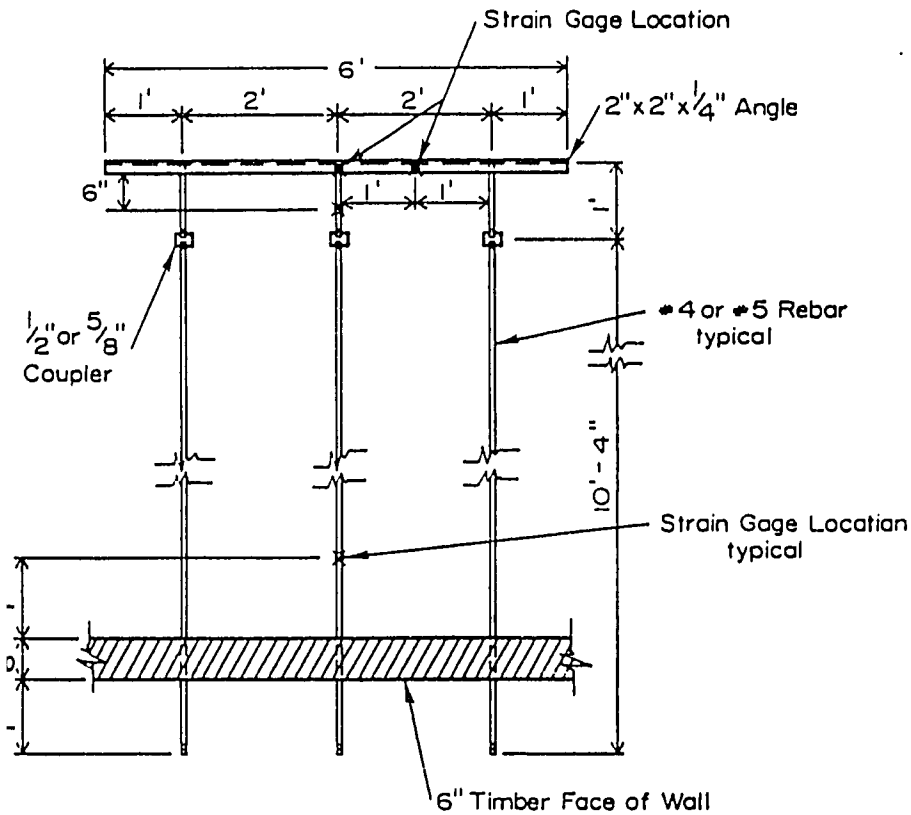

Fig. 57 (b) Instrumented Rebar-angle Anchor Used for Pullout Testing in the Syro Experimental Wall (after Anderson et al, 1986).

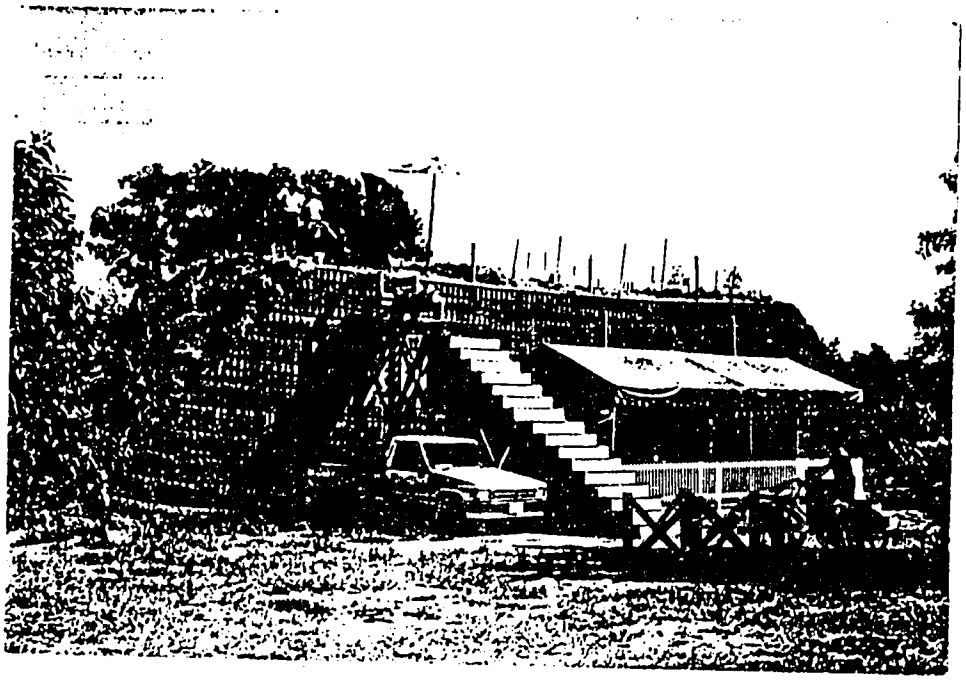

Fig. 58 Photograph Showing the Typical Set-up of the Field Pullout Test at the USAID Wire Wall for Highest Level Dummy Mat.

Fig. 59 A Closer View of the Typical Field Pullout Test for Highest Level Dummy Mat.

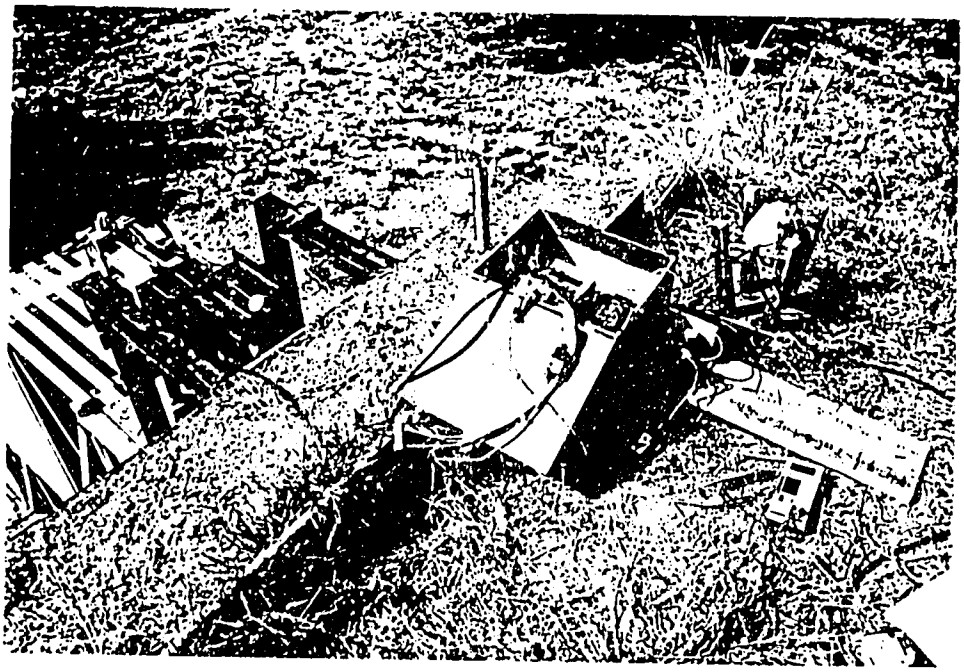

Fig. 60 Typical Field Pullout Test Set-up for Higher Level Mat and its Control Viewed from the Top of the Wall.

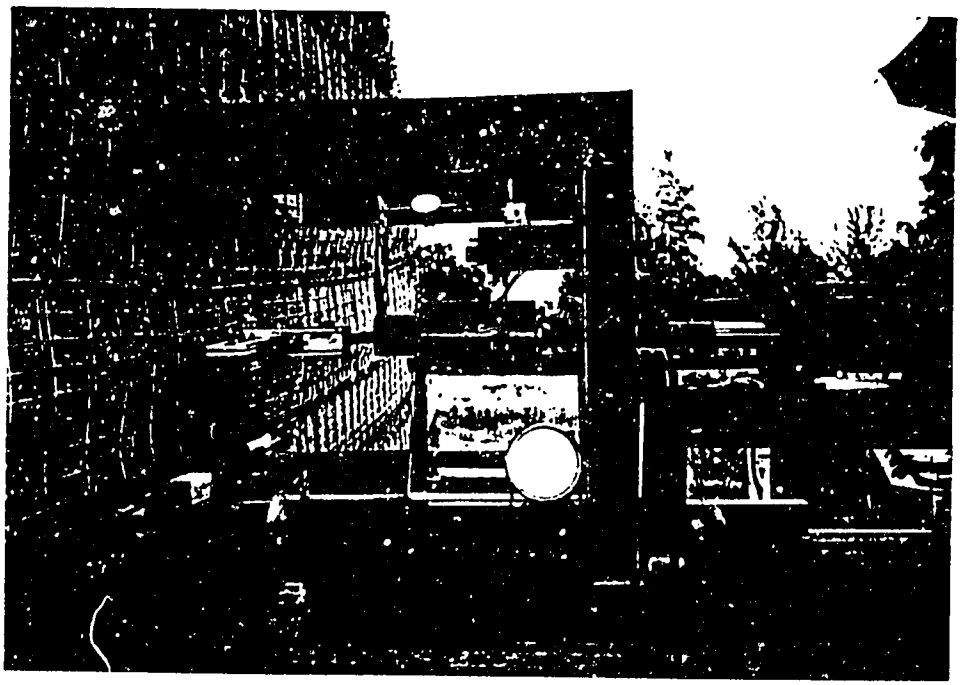

Fig. 61 Photograph Showing the Typical Field Pullout Test Set-up for Intermediate Level Dummy Bar-mat (Side View).

Fig. 62 Photograph Showing the Typical Field Pullout Test Set-up for Intermediate Level Dummy Bar-mat (Front View).

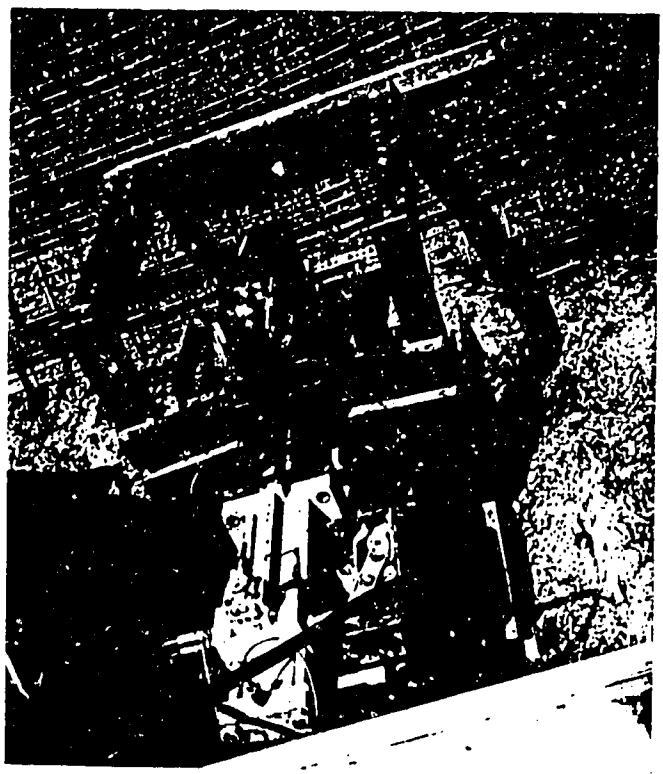

Fig. 63 Typical Field Pullout Test Set-up for Lowest Level Dummy Bar-mat.

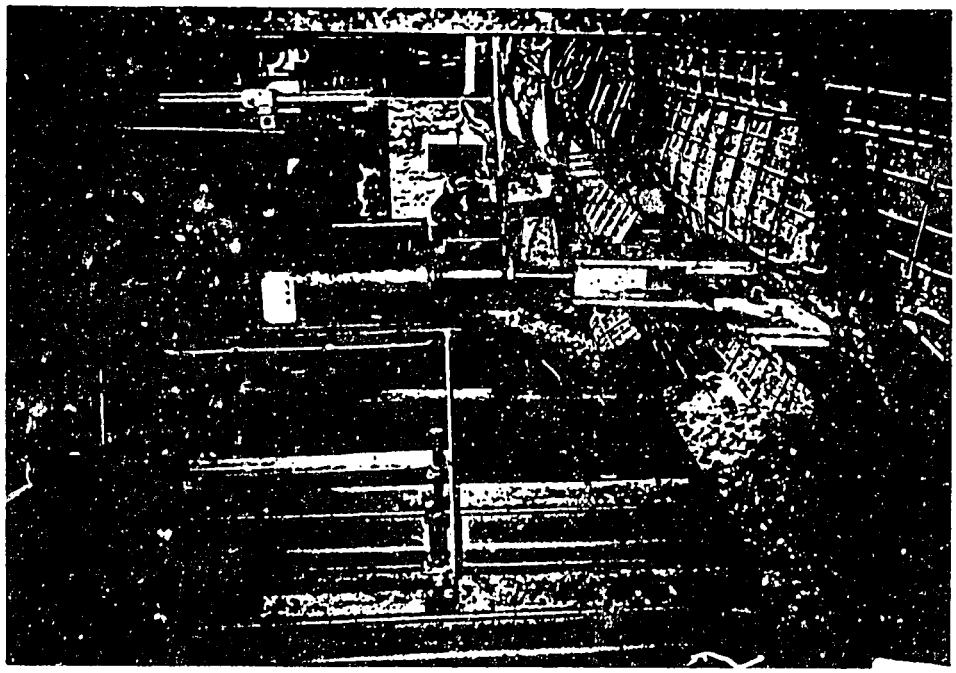

Fig. 64 Closer View of Typical Field Pullout Test Set-up for Lowest Level Dummy Bar-mat.

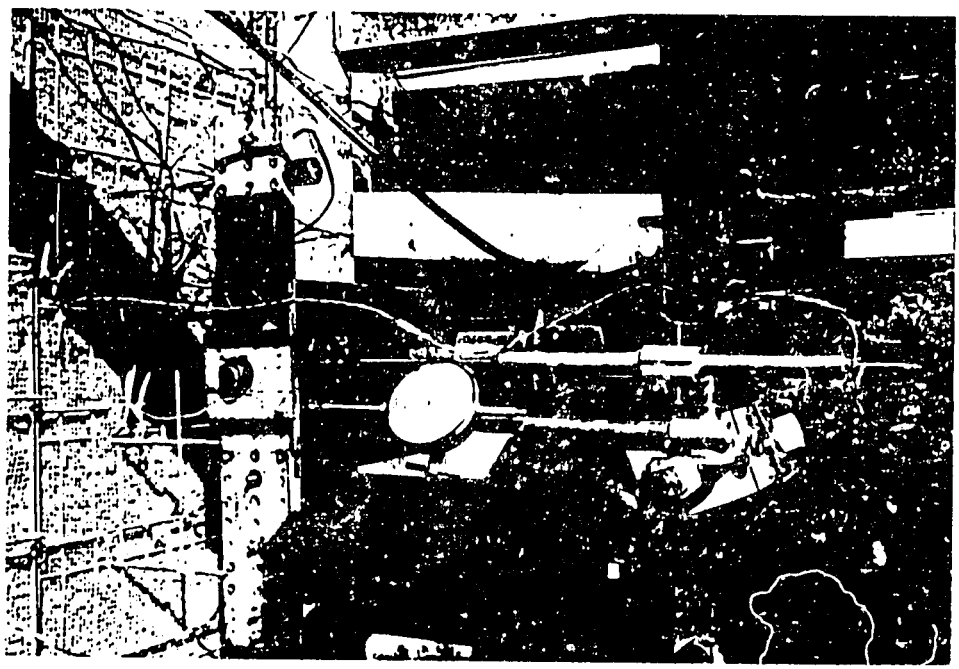

Fig. 65 Close-up View of the Set-up Adopted in the Field Pullout Test.

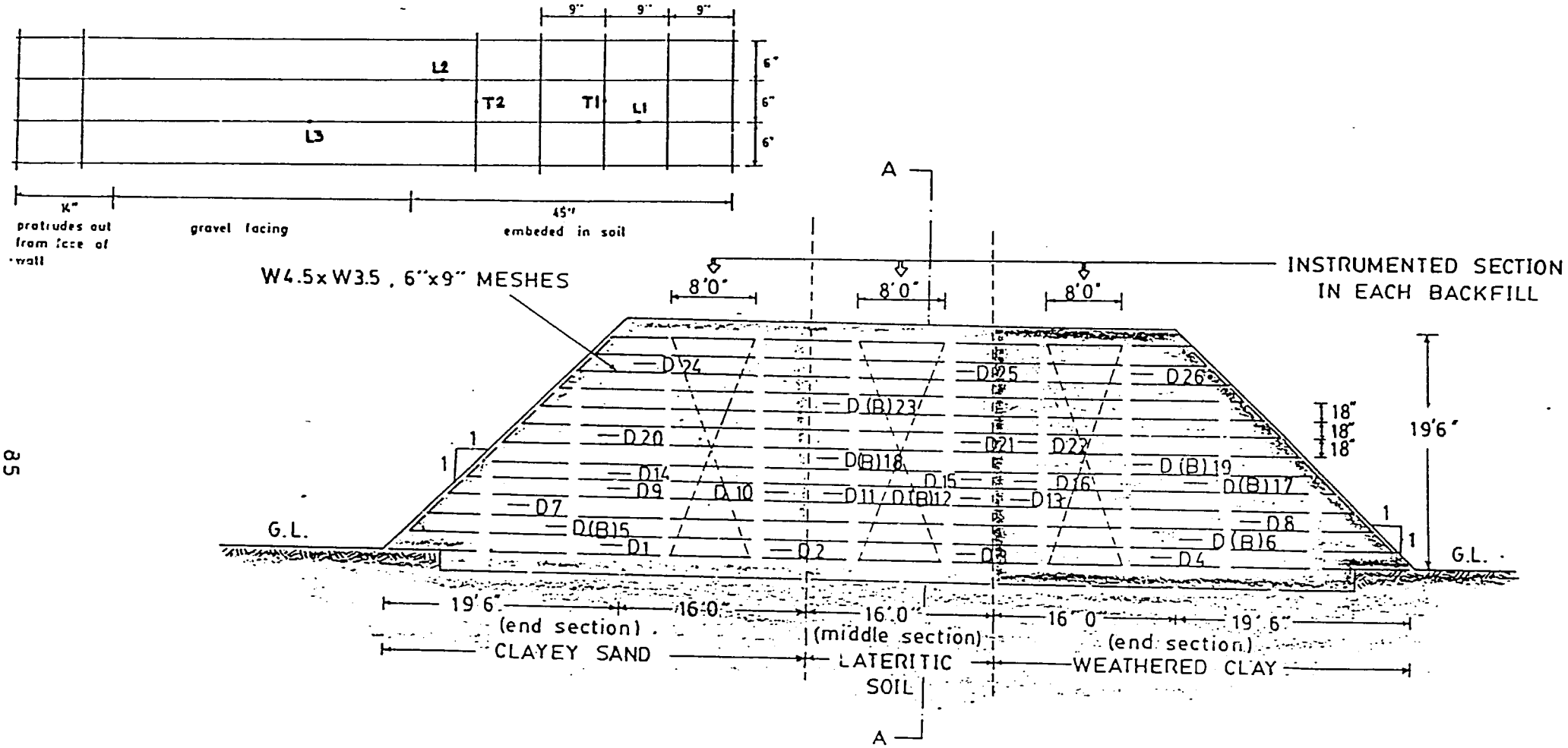

Fig. 66 Front Section of the Welded Wire Wall Showing Locations of Dummy Bar-mats for Field Pullout Tests.

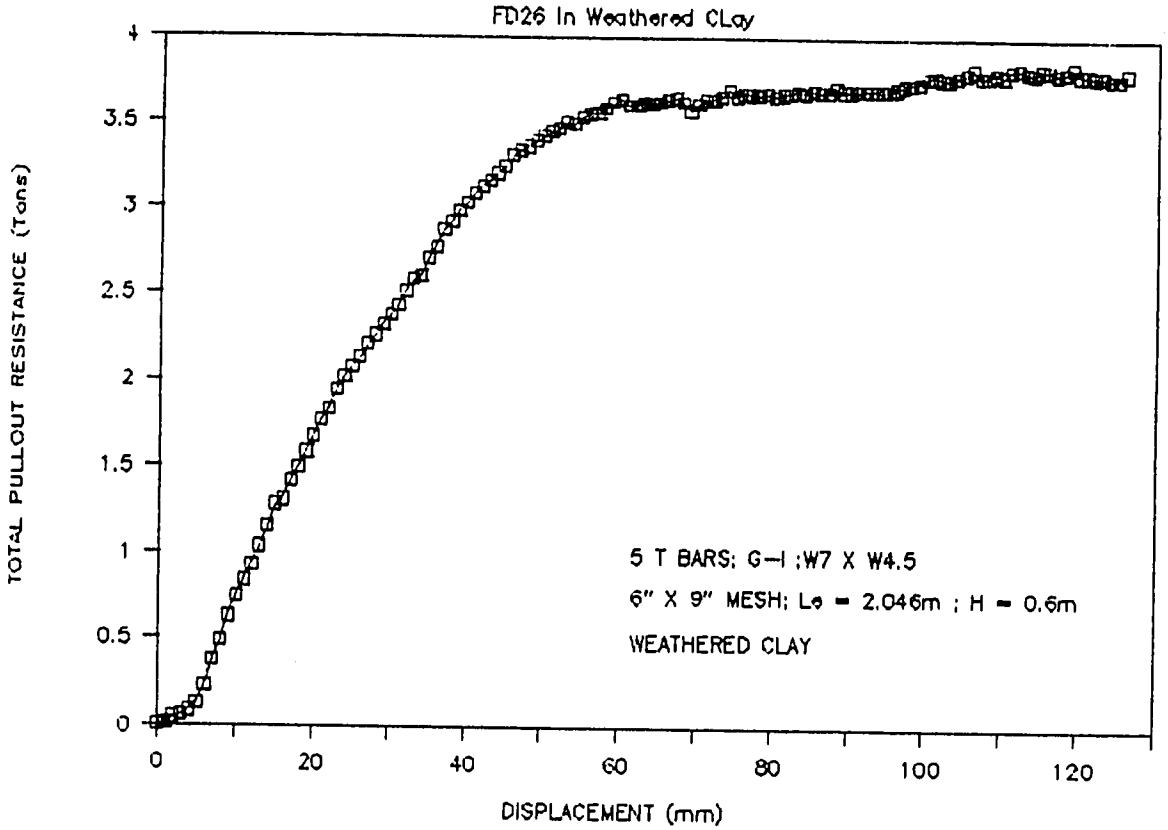

Fig. 67 Field Pullout Resistance of Dummy Bar-mat FD26 in Weathered Clay.

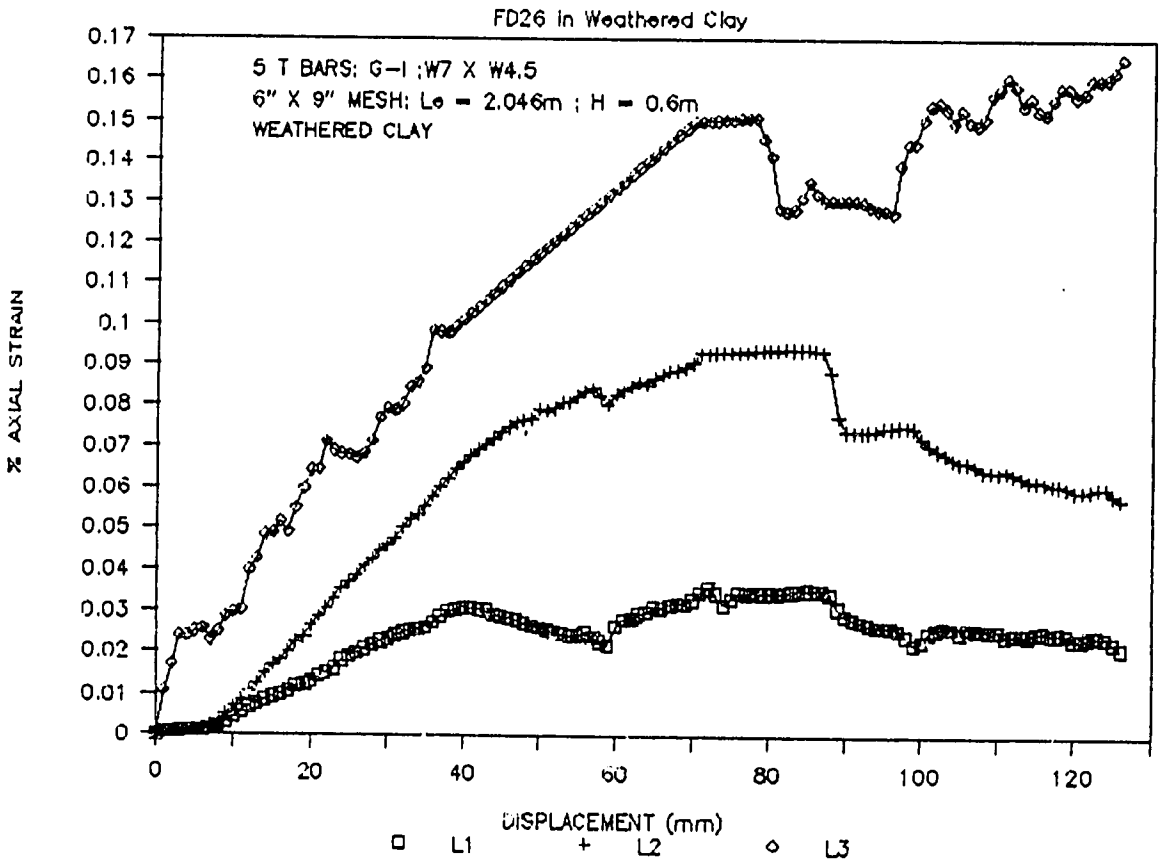

Fig. 68 Plots of Axial Strains Versus Horizontal Mat Displacements for Dummy Bar-mat FD26 in Weathered Clay.

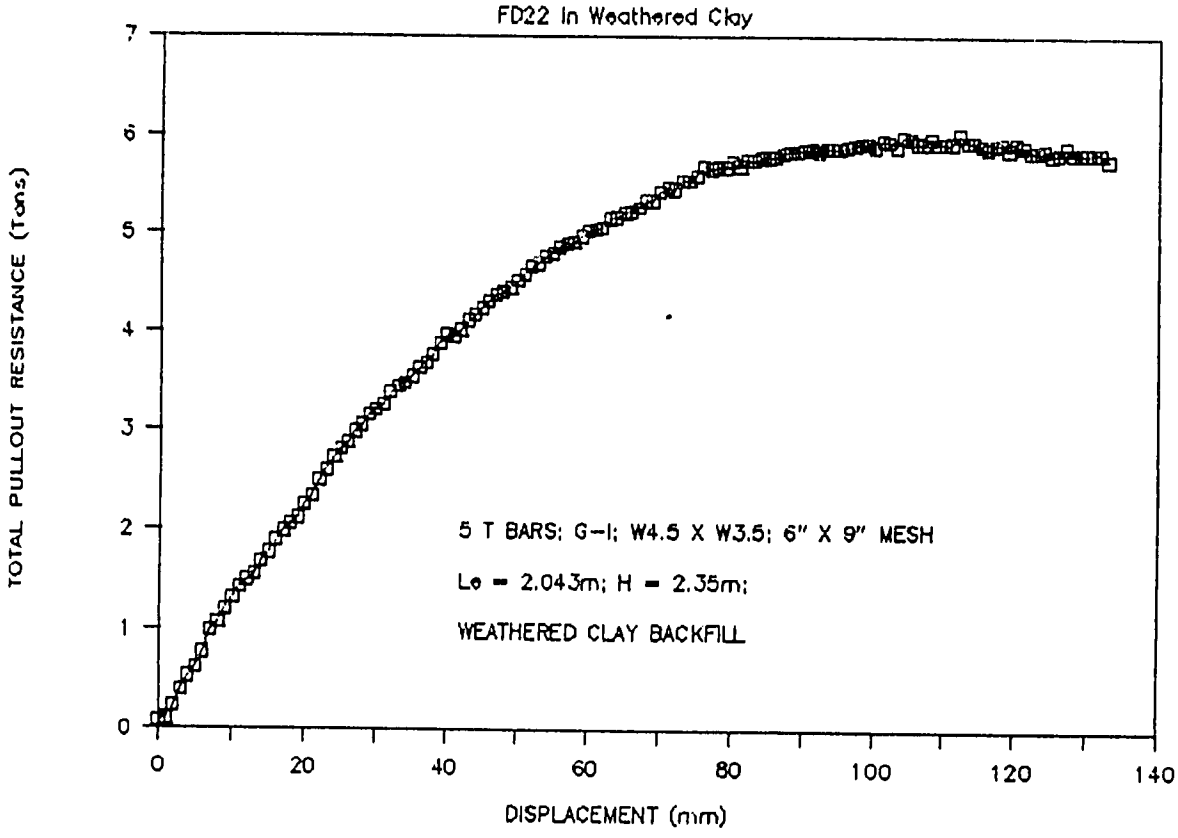

Fig. 69 Field Pullout Resistance of Dummy Bar-mat FD22 in Weathered Clay.

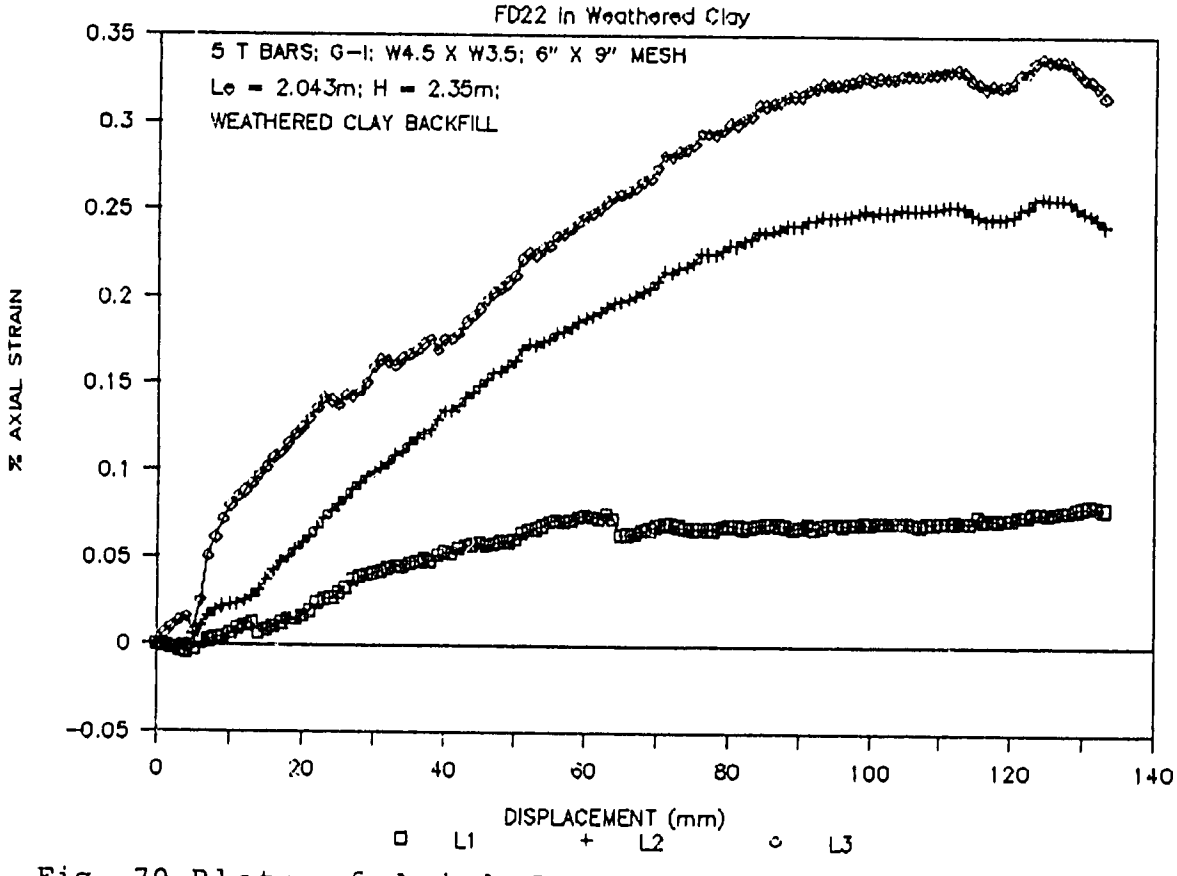

Fig. 70 Plots of Axial Strains Versus Horizontal Mat Displacements for Dummy Bar-mat FD22 in Weathered Clay.

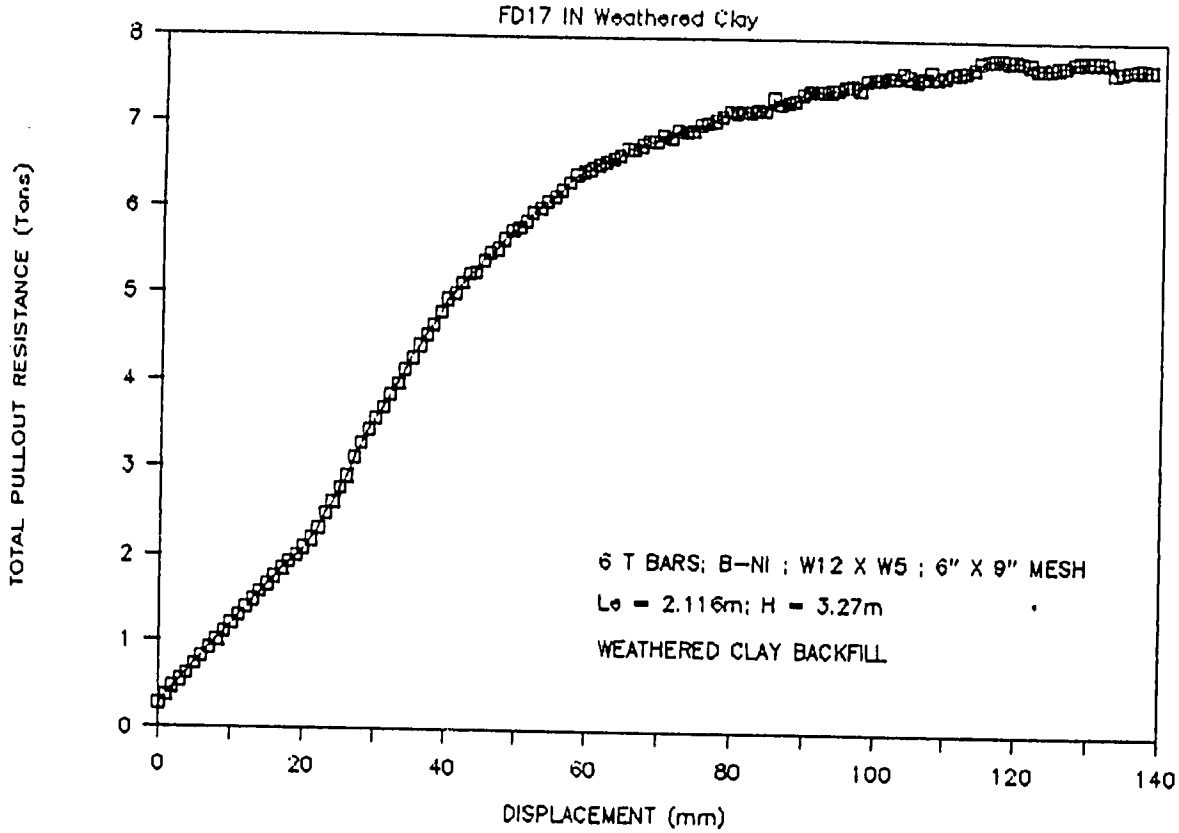

Fig. 71 Field Pullout Resistance of Dummy Bar-mat FD17 in Weathered Clay.

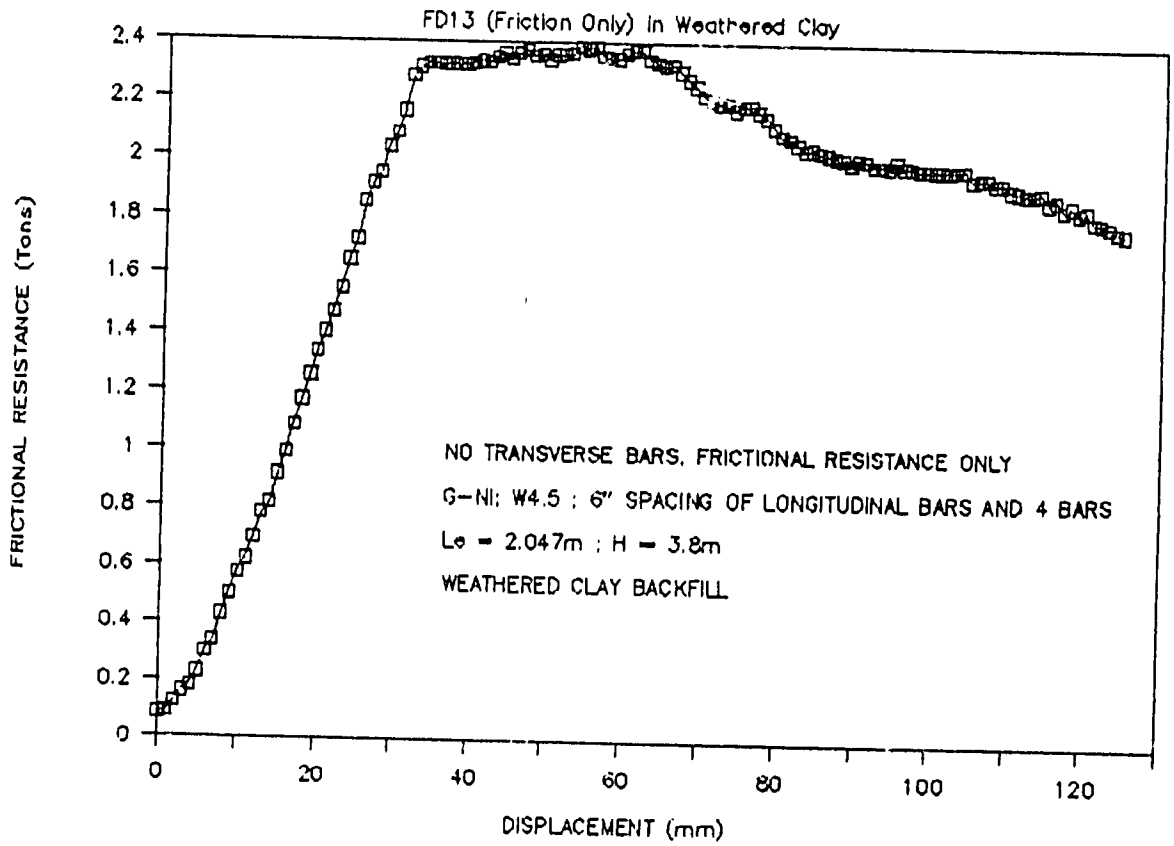

Fig. 72 Field Pullout Resistance of Dummy Bar-mat FD13 in Weathered Clay.

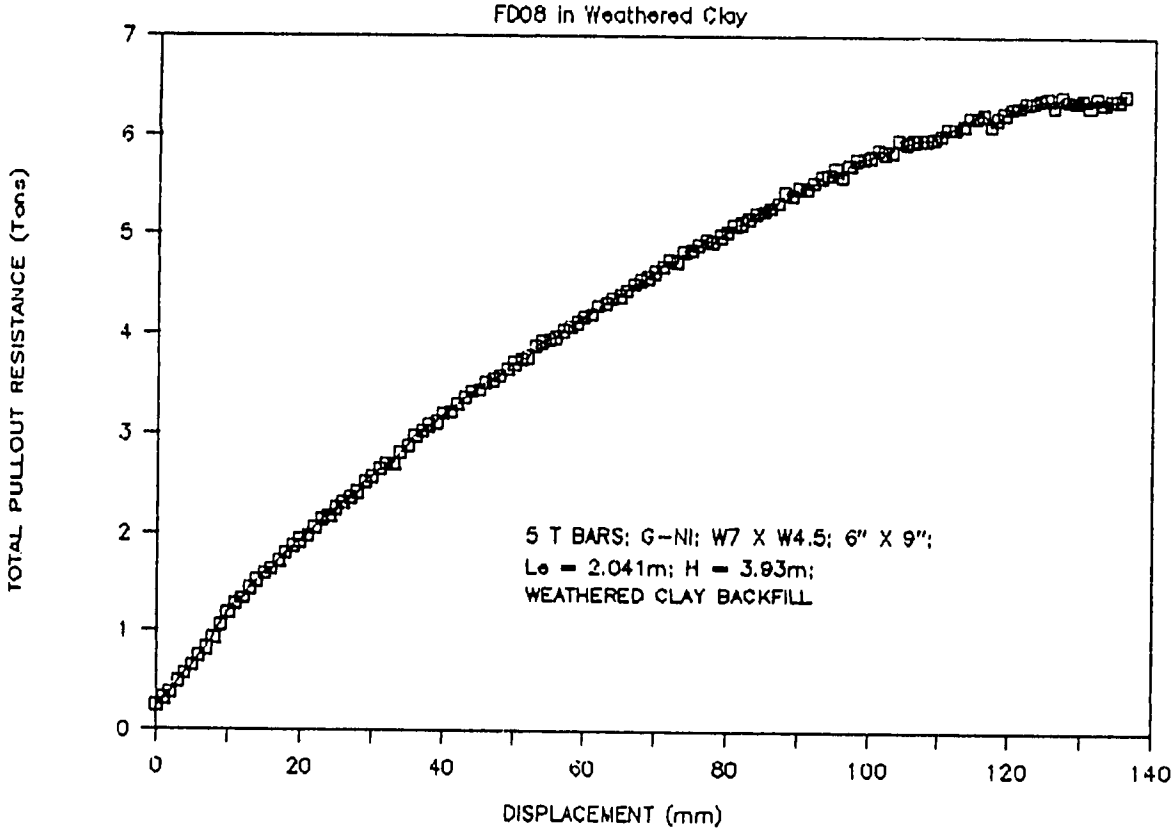

Fig. 73 Field Pullout Resistance of Dummy Bar-mat FD08 in Weathered Clay.

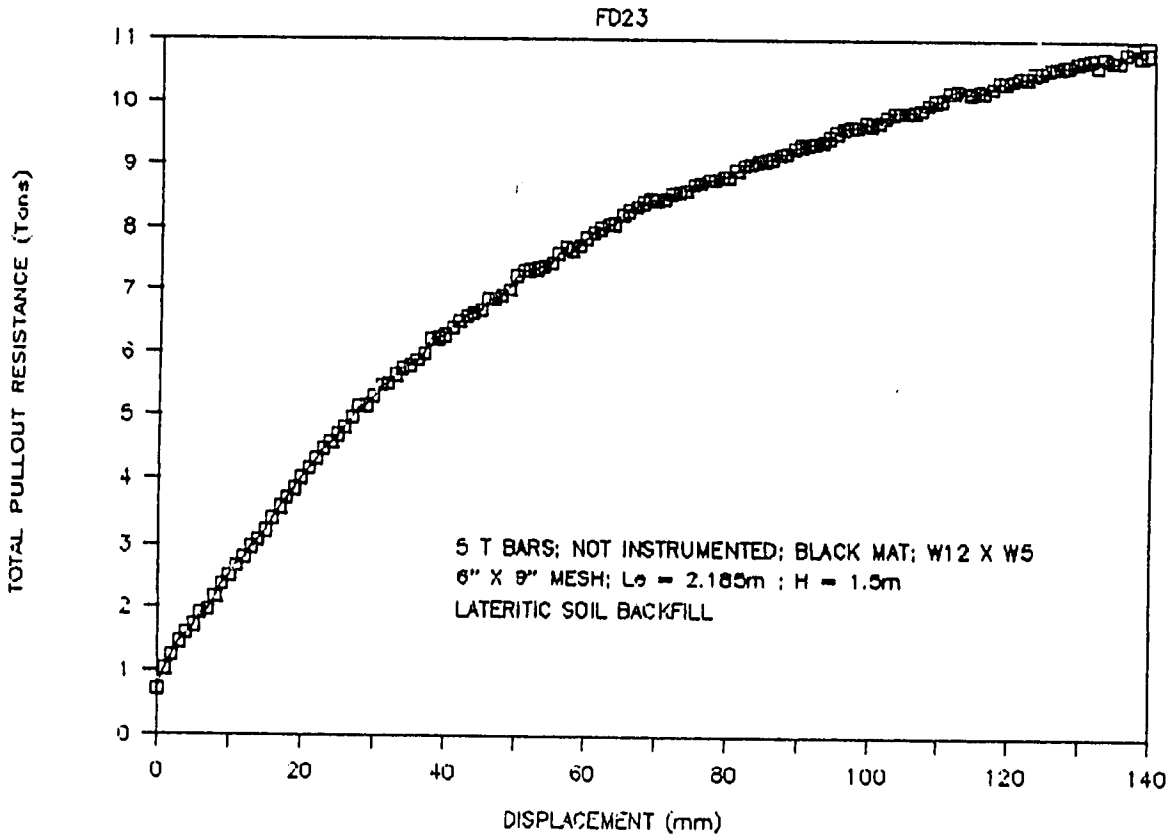

Fig. 74 Field Pullout Resistance of Dummy Bar-mat FD23 in Lateritic Residual Soil.

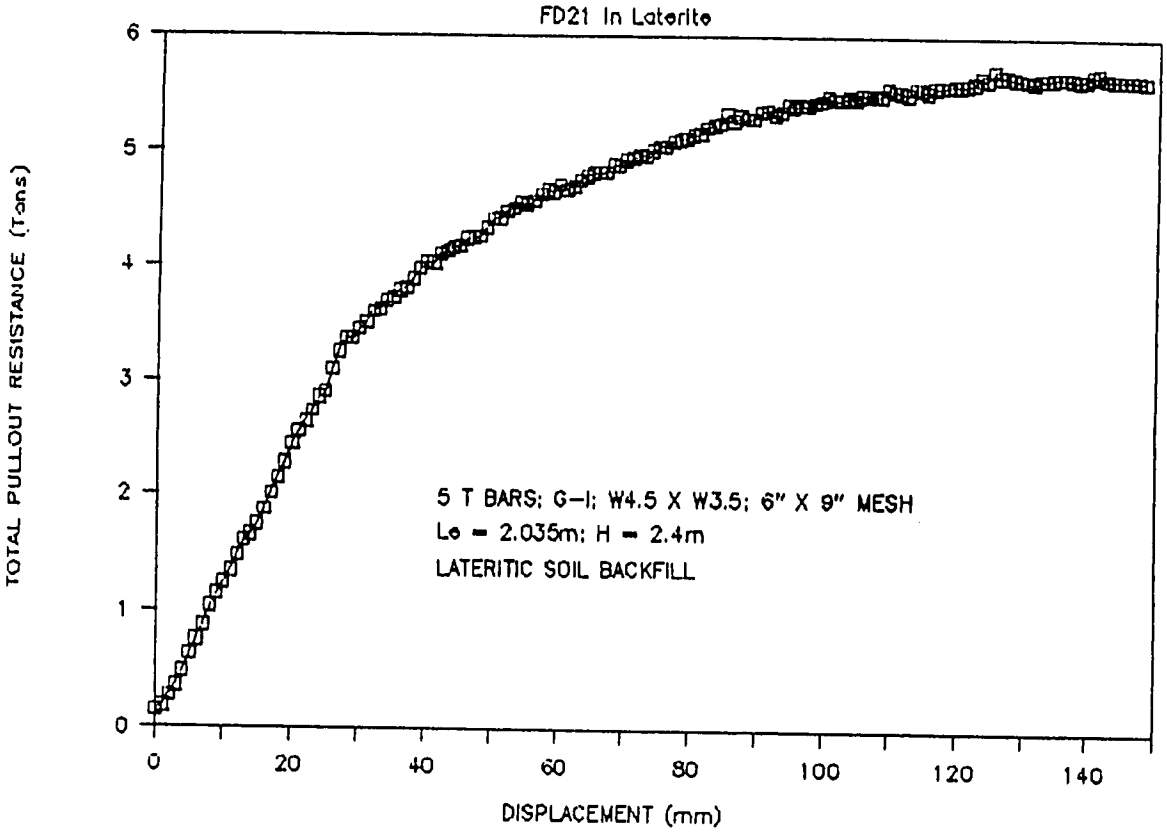

Fig. 75 Field Pullout Resistance of Dummy Bar-mat FD21 in Lateritic Residual Soil.

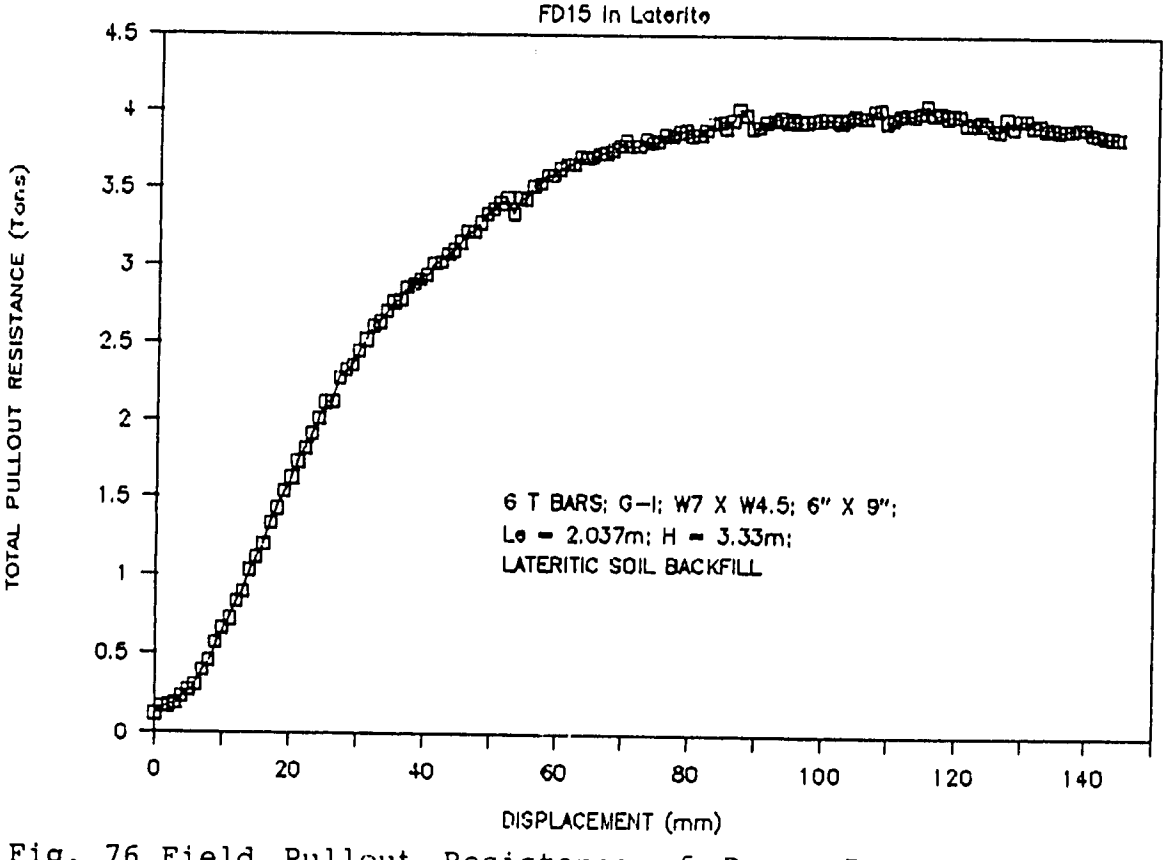

Fig. 76 Field Pullout Resistance of Dummy Bar-mat FD15 in Lateritic Residual Soil.

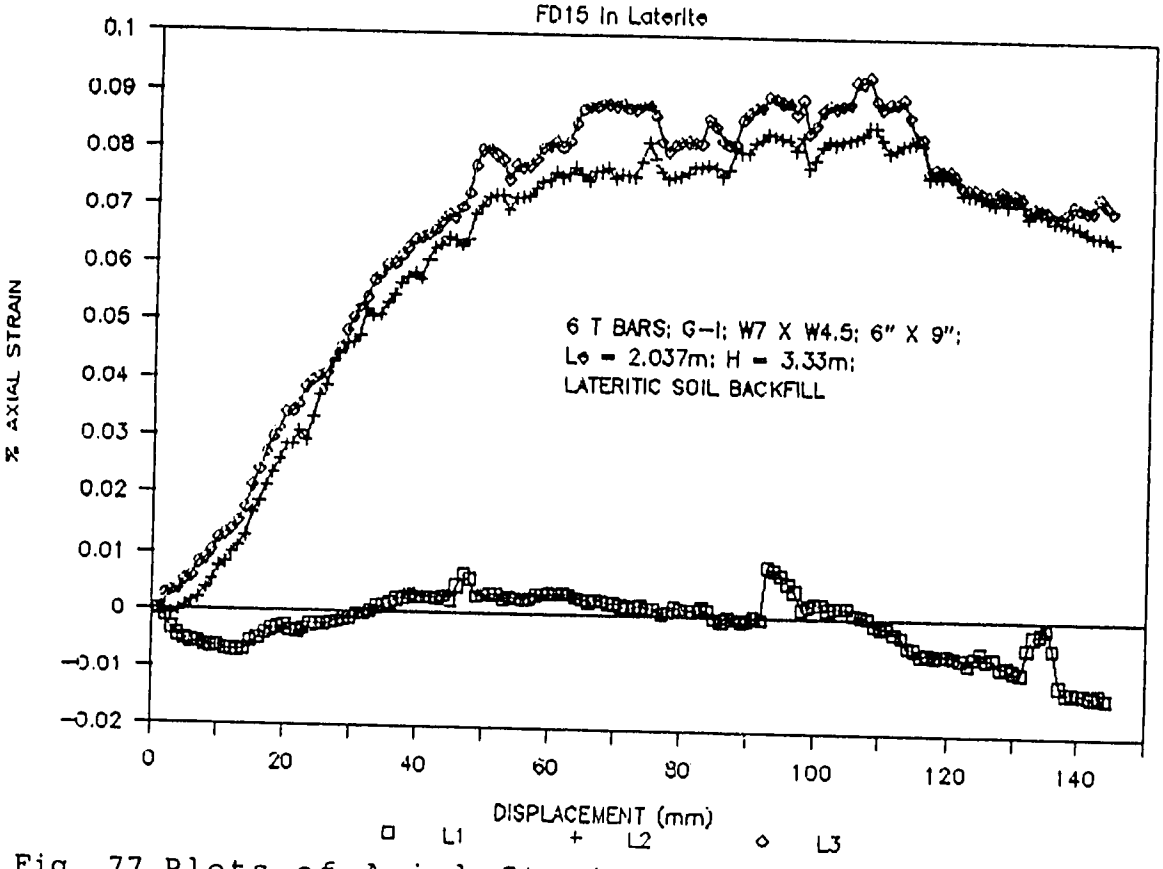

Fig. 77 Plots of Axial Strains Versus Horizontal Mat Displacements for Dummy Bar-mat FD12 in Lateritic Residual Soil.

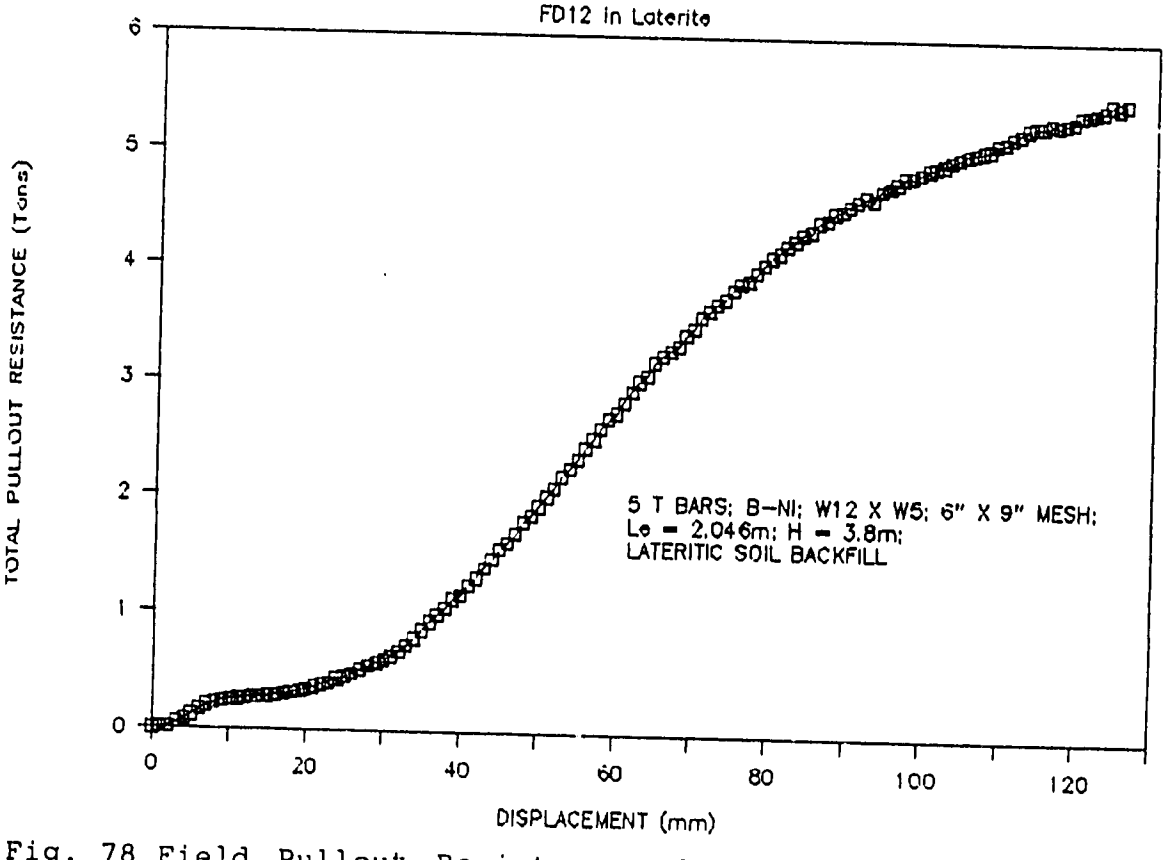

Fig. 78 Field Pullout Resistance of Dummy Bar-mat FD12 in Lateritic Residual Soil.

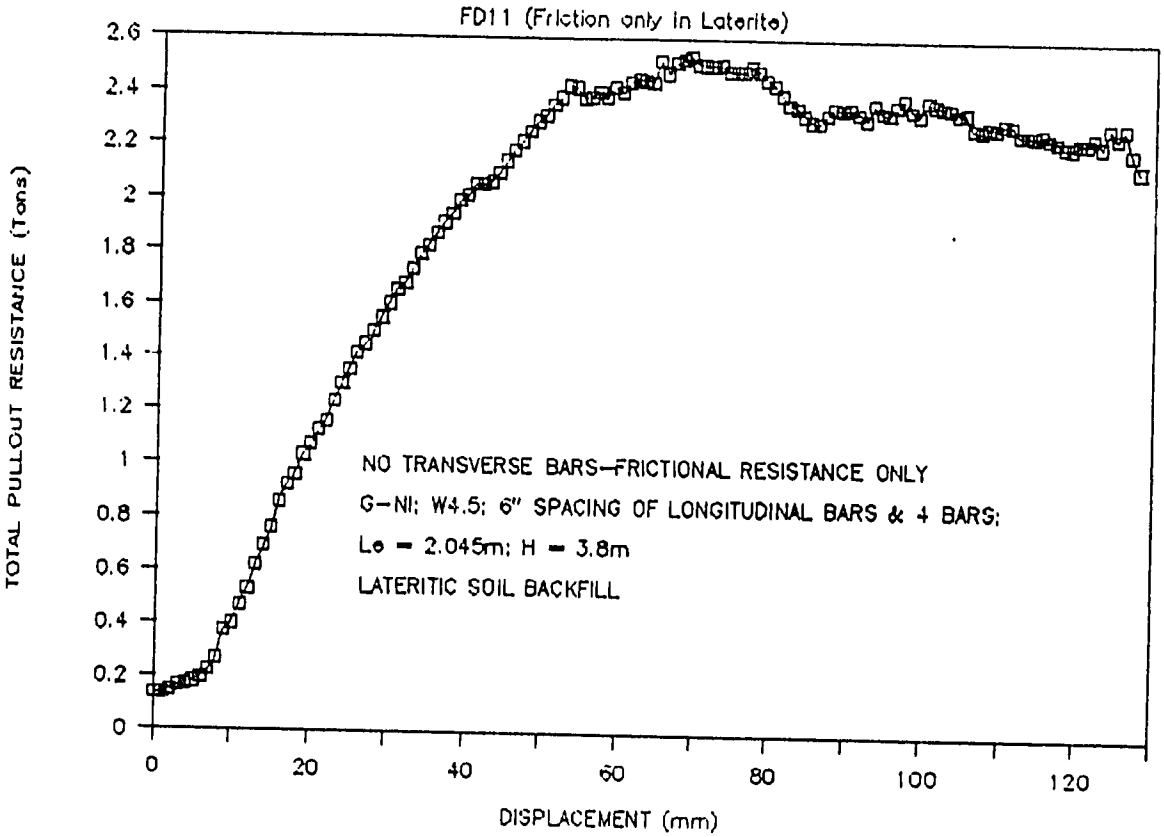

Fig. 79 Field Frictional Resistance of Dummy Bar-mat FD11 in Lateritic Residual Soil.

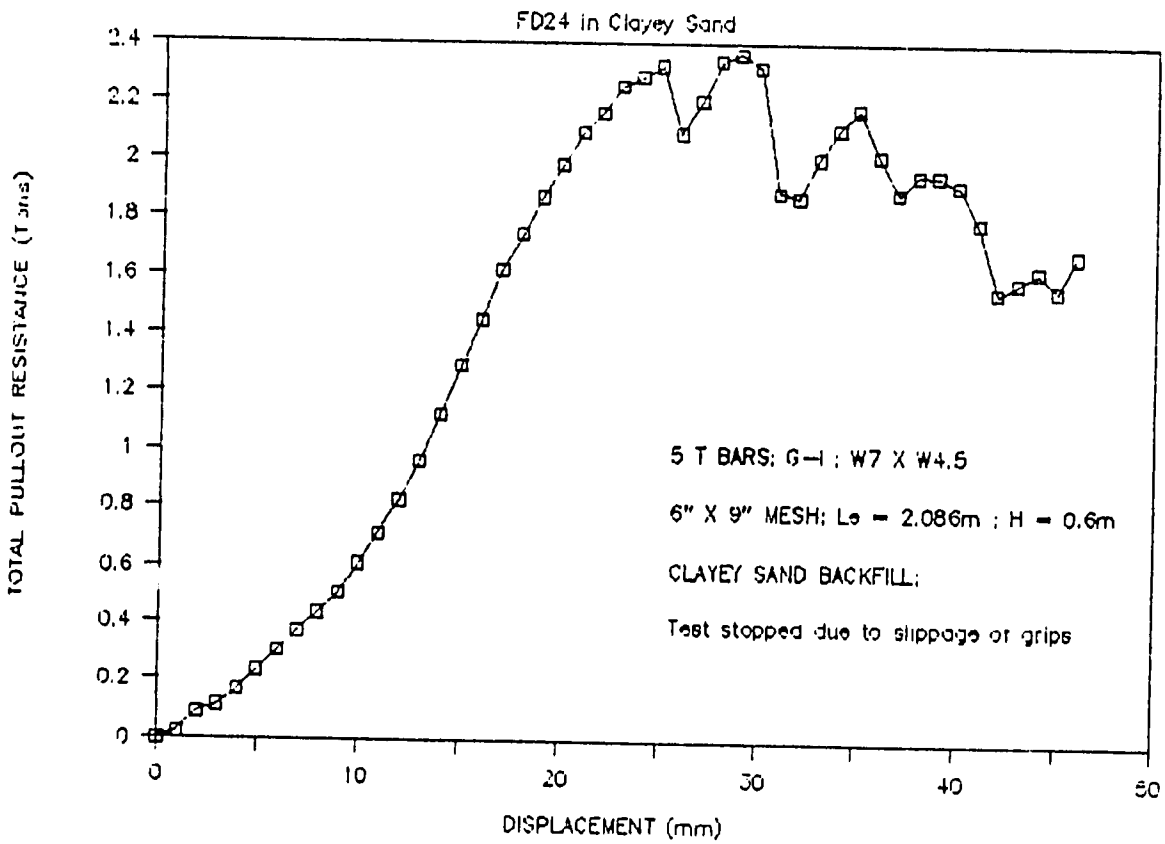

Fig. 80 Field Pullout Resistance of Dummy Bar-mat FD24 in Clayey Sand.

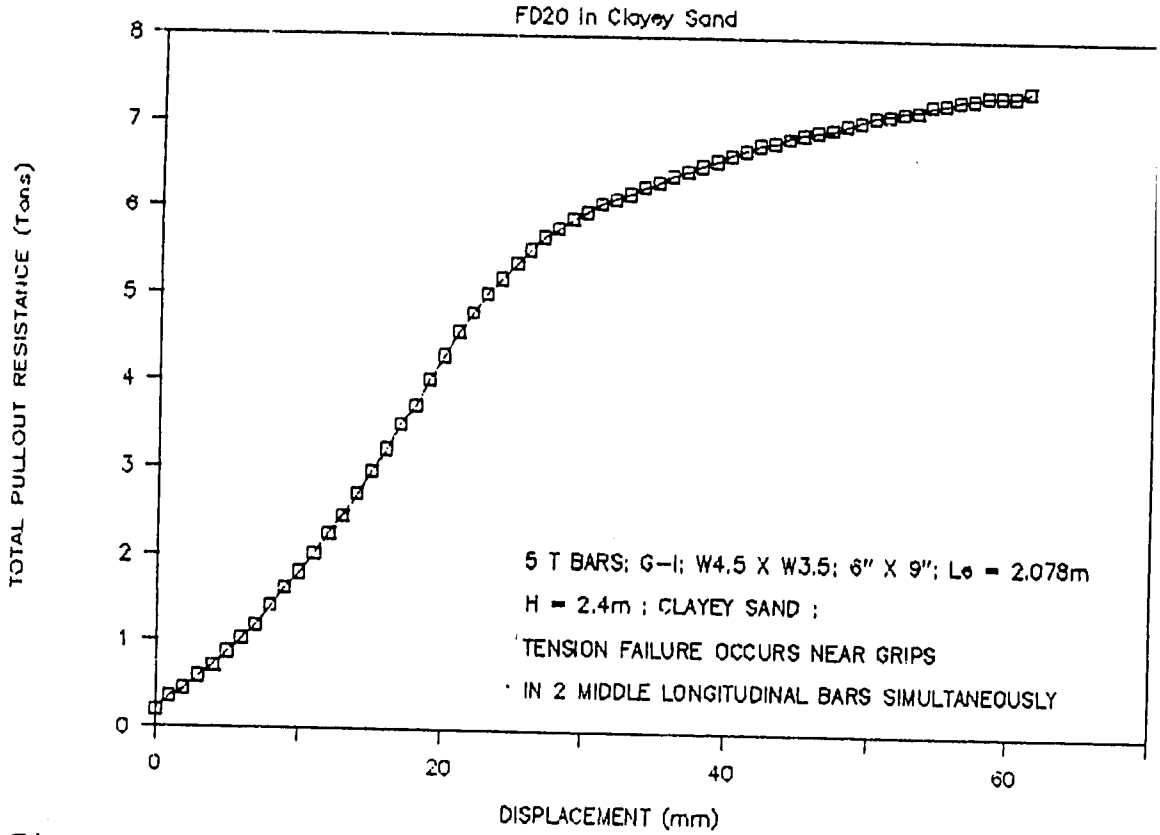

Fig. 81 Field Pullout Resistance of Dummy Bar-mat FD20 in Clayey Sand.

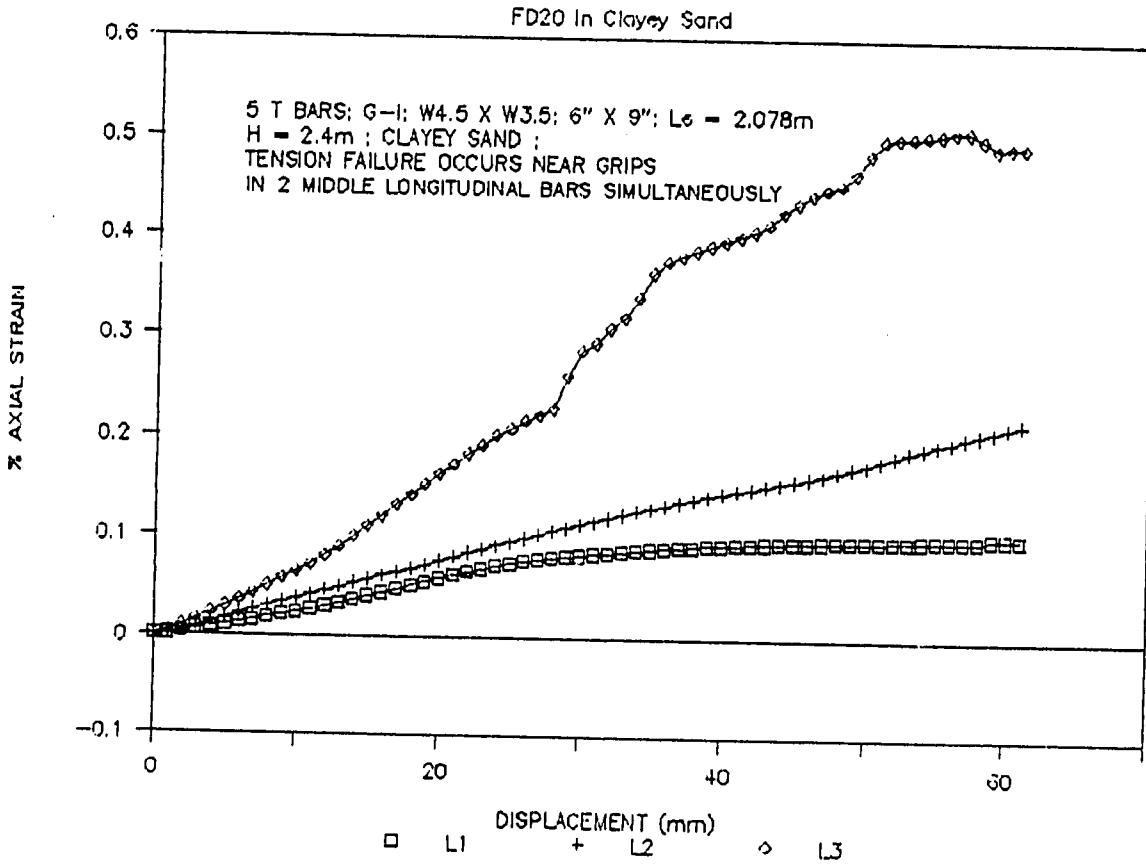

Fig. 82 Plots of Axial Strains Versus Horizontal Mat Displacements for Dummy Bar-mat FD20 in Clayey Sand.

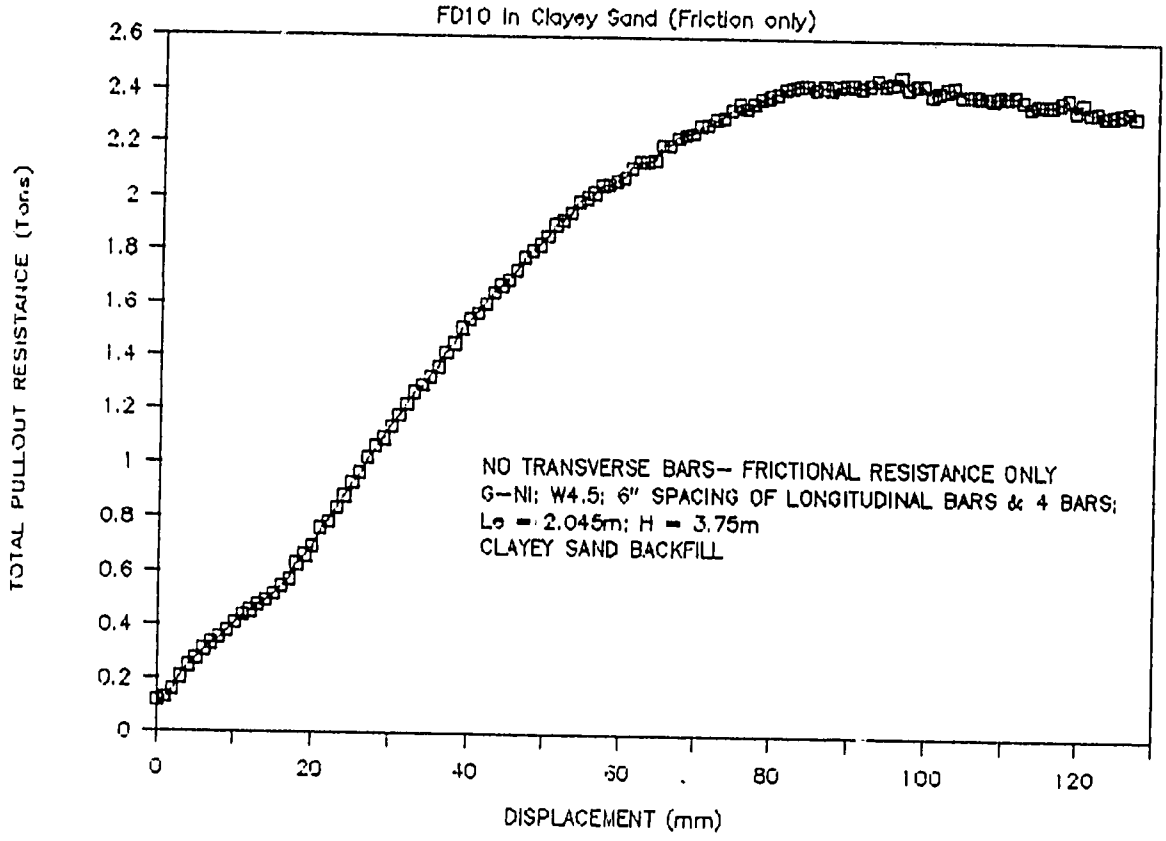

Fig. 83 Field Frictional Resistance of Dummy Bar-mat FD10 in Clayey Sand.

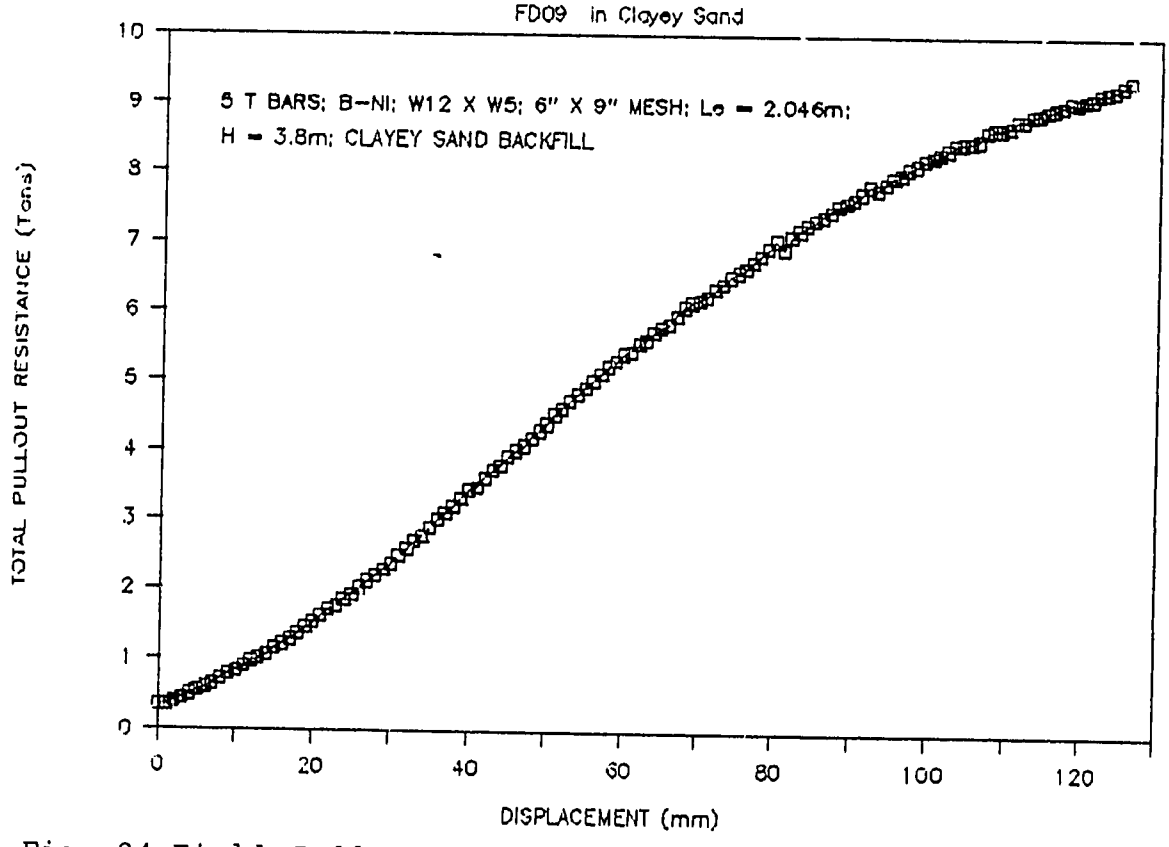

Fig. 84 Field Pullout Resistance of Dummy Bar-mat FD09 in Clayey Sand.

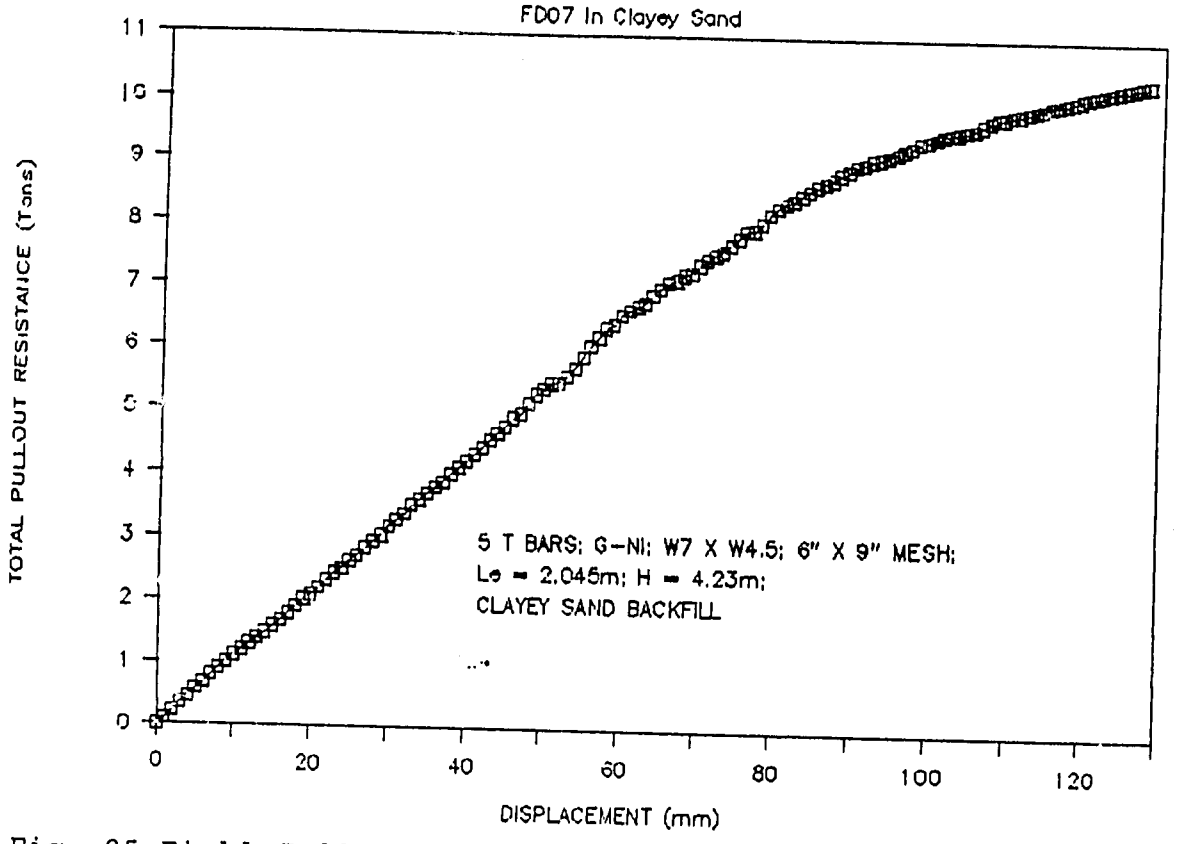

Fig. 85 Field Pullout Resistance of Dummy Bar-mat FD07 in Clayey Sand.

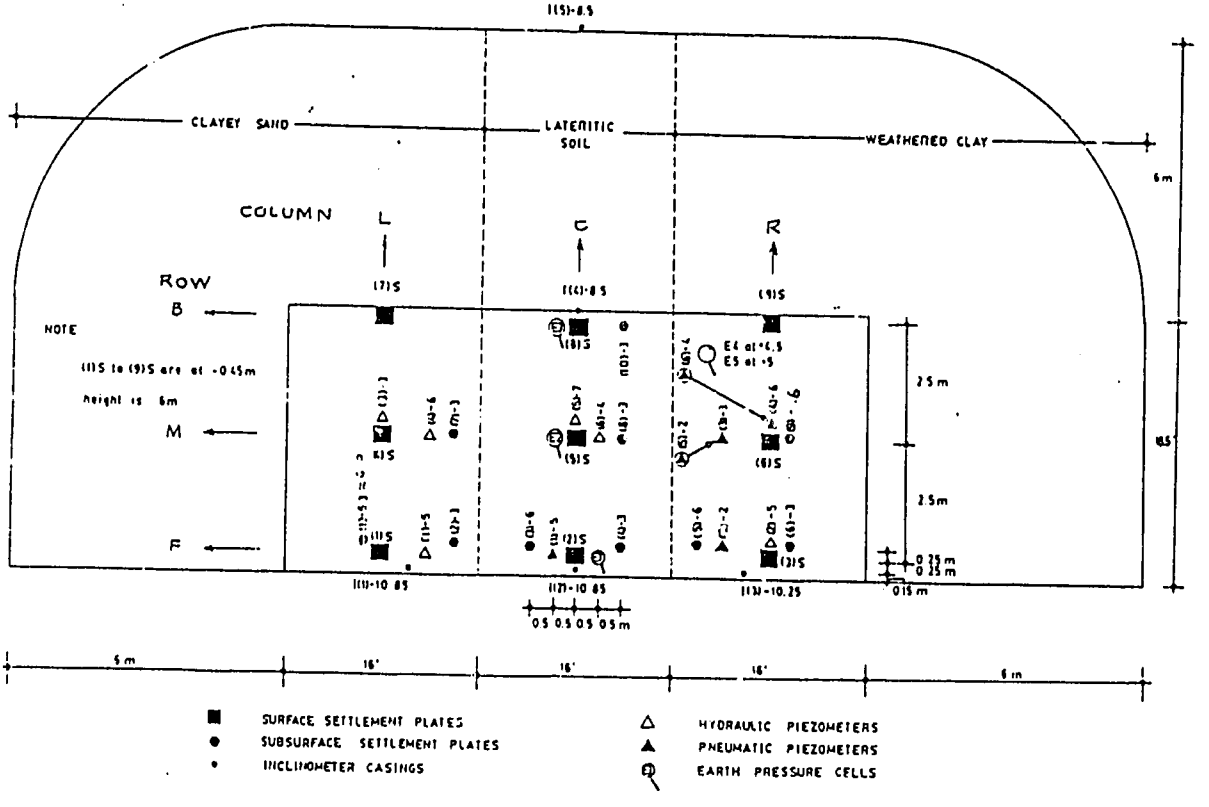

Fig. 86 Schematic Layout of Field Instrumentation for the Welded Wire Wall.

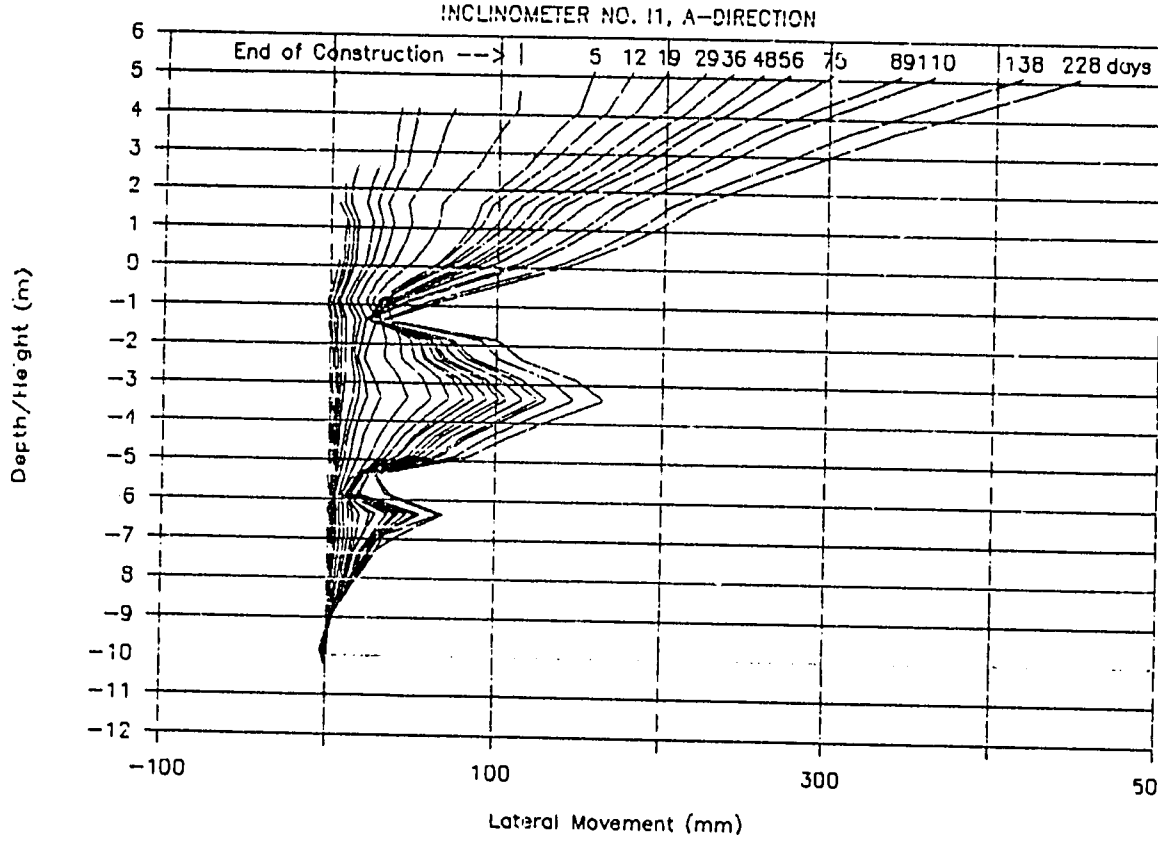

Fig. 87 Plots of Depth/Height Against Lateral Movement for Inclinometer No. 1.

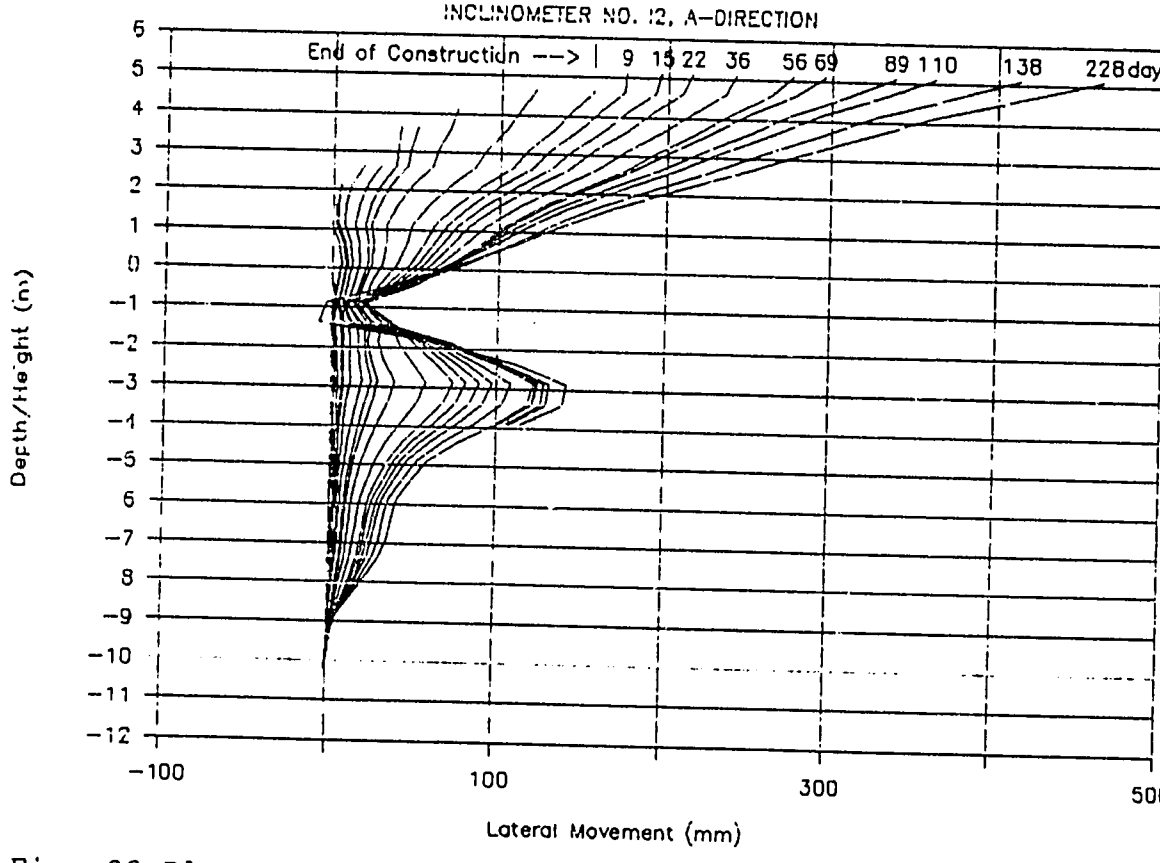

Fig. 88 Plots of Depth/Height Against Lateral Movement for Inclinometer No. 2.

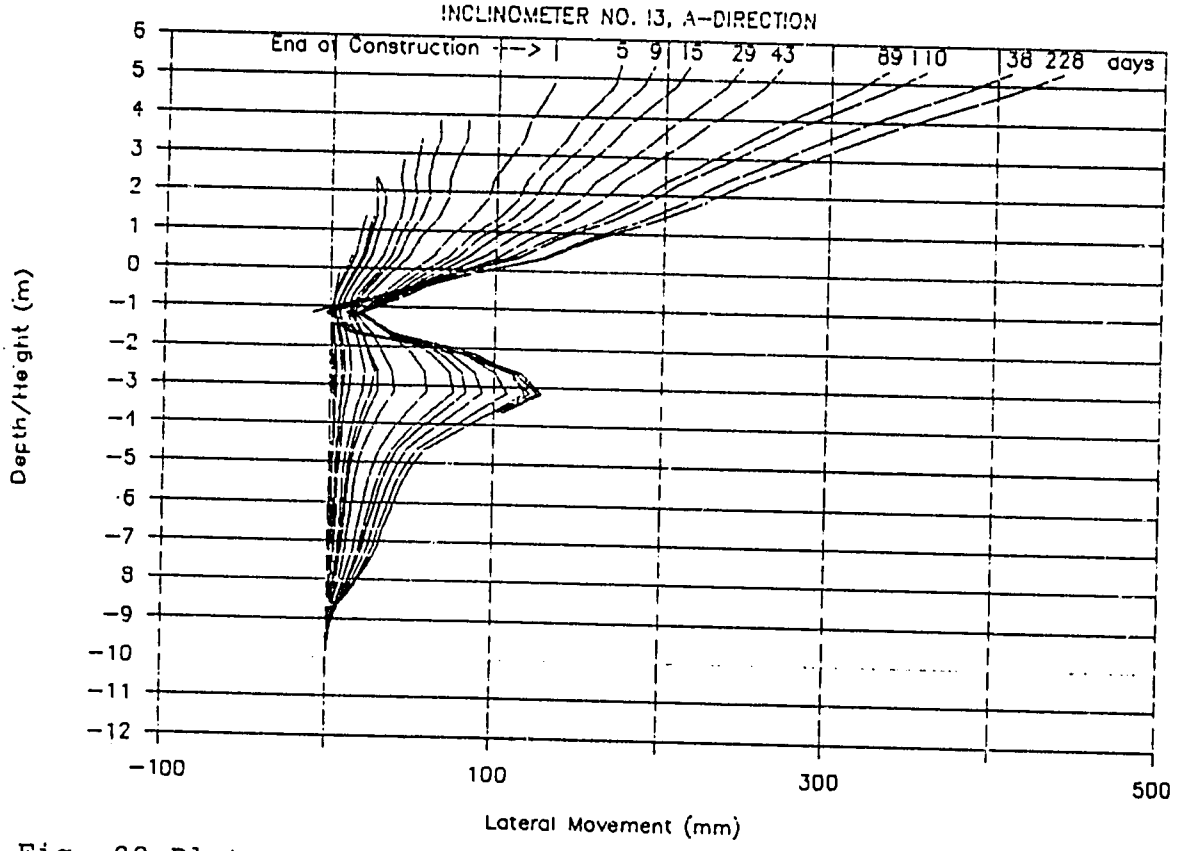

Fig. 89 Plots of Depth/Height Against Lateral Movement for Inclinometer No. 3.

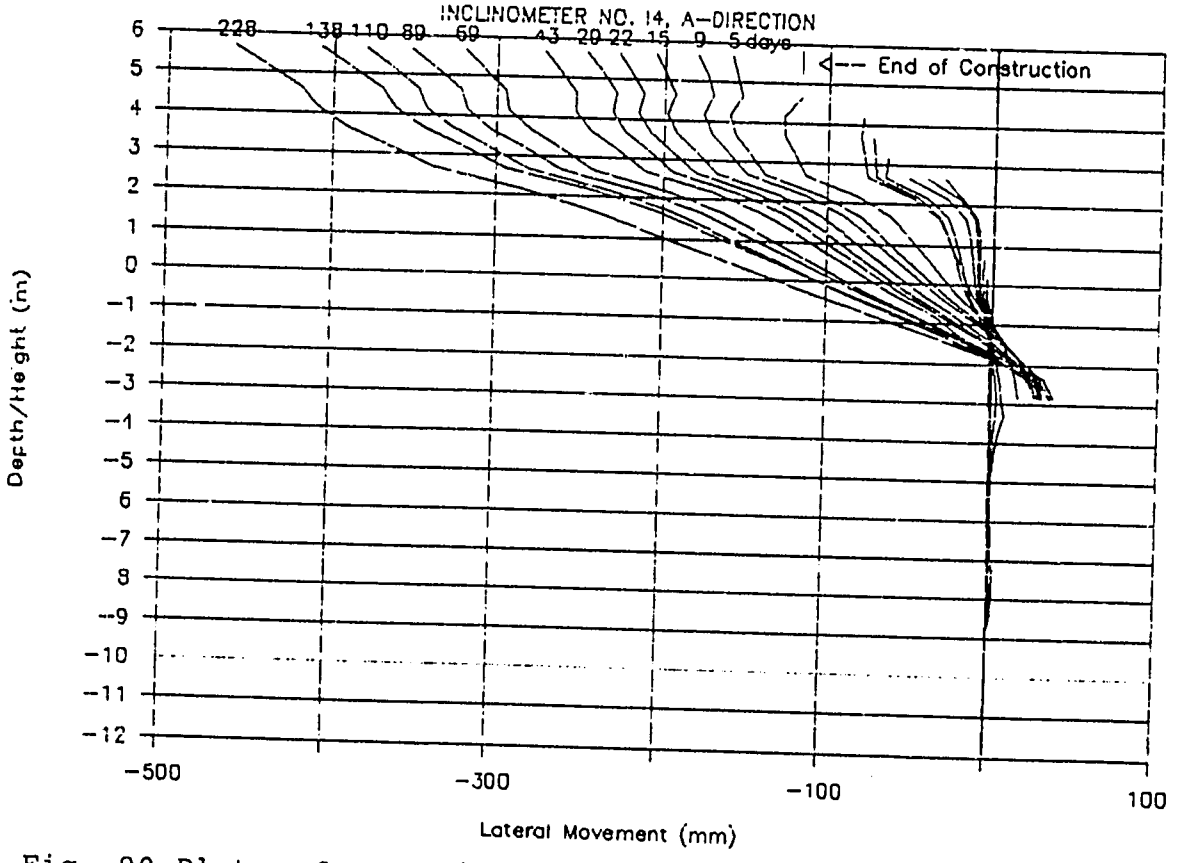

Fig. 90 Plots of Depth/Height Against Lateral Movement for Inclinometer No. 4.

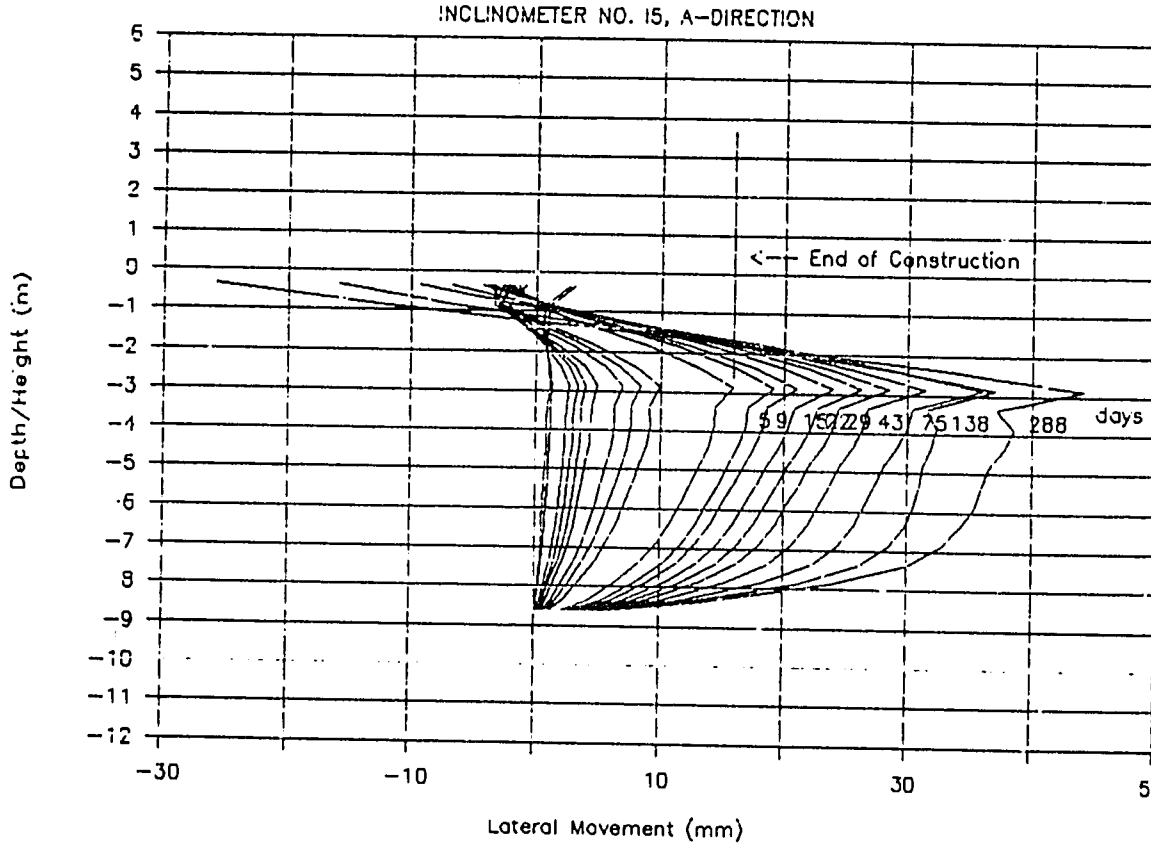

Fig. 91 Plots of Depth/Height Against Lateral Movement for Inclinometer No. 5.

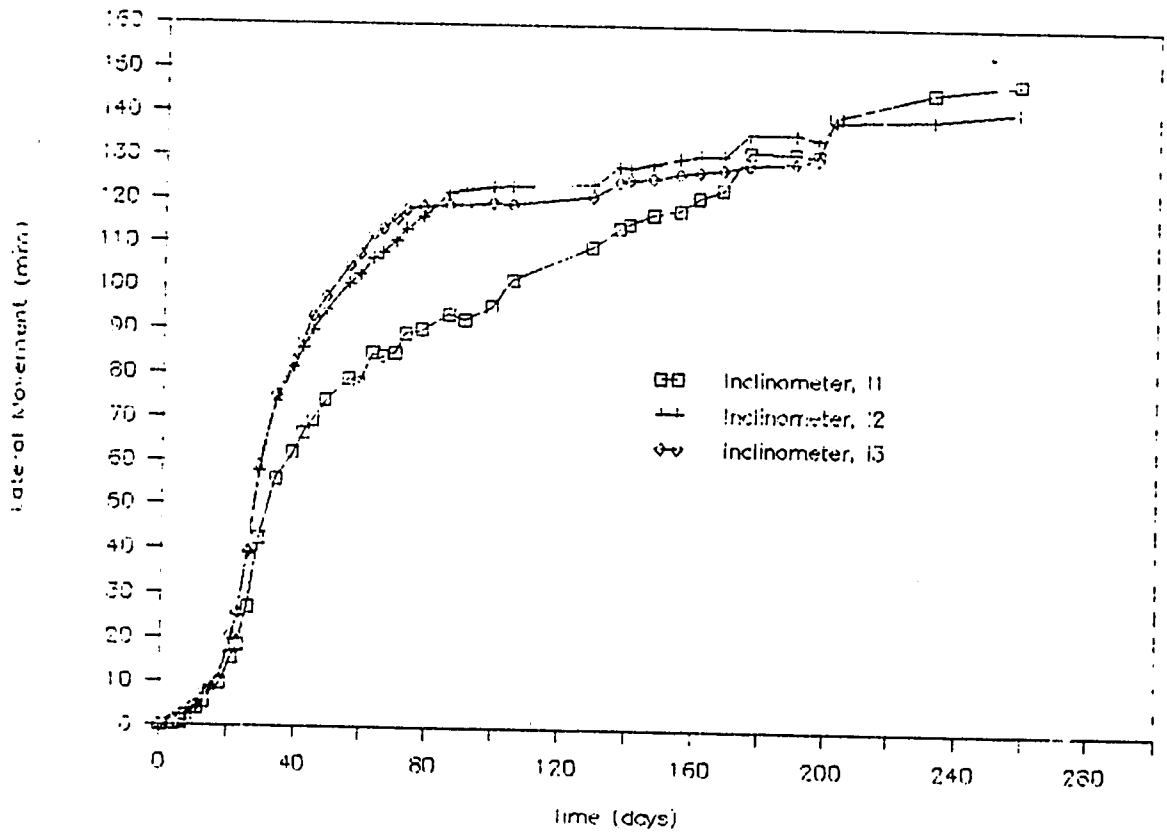

Fig. 92 Maximum Lateral Movement of the Subsoil Plotted Against Time.

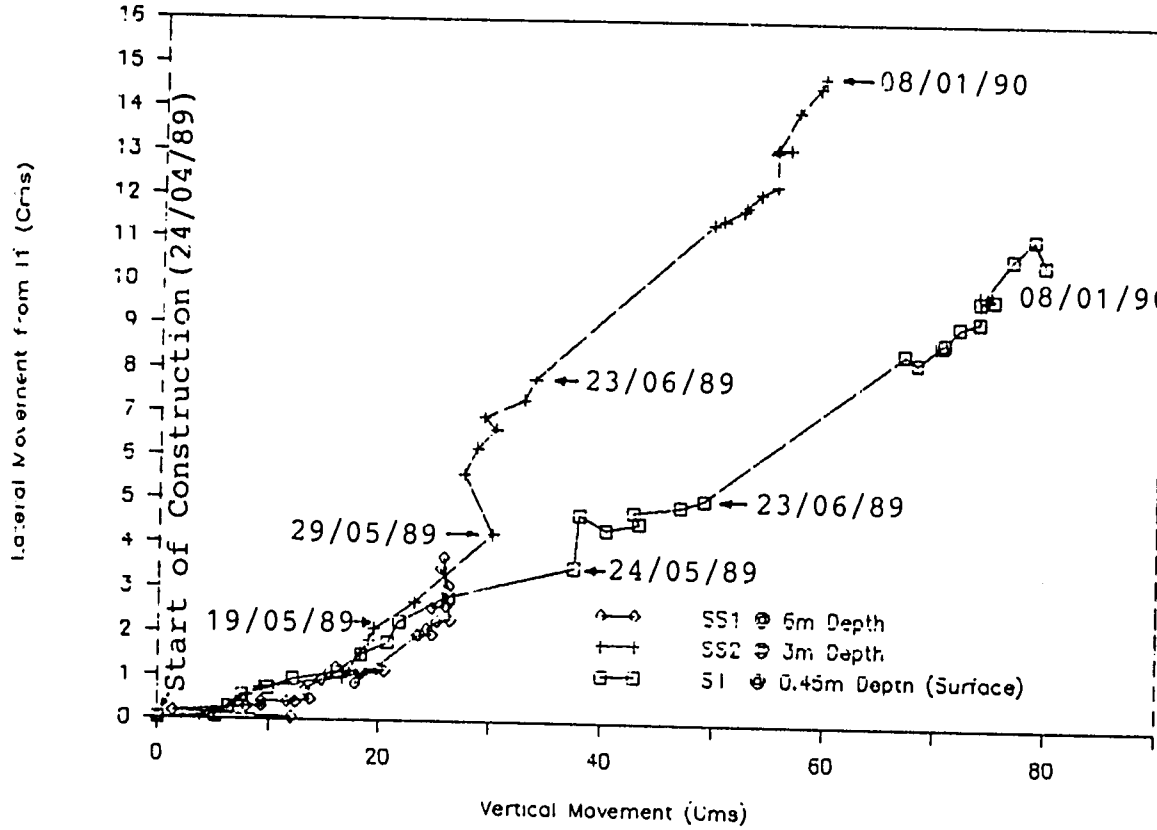

Fig. 93 Maximum Lateral Movement of the Subsoil Plotted Against the Vertical Movement of the Wall (Inclinometer No. 1).

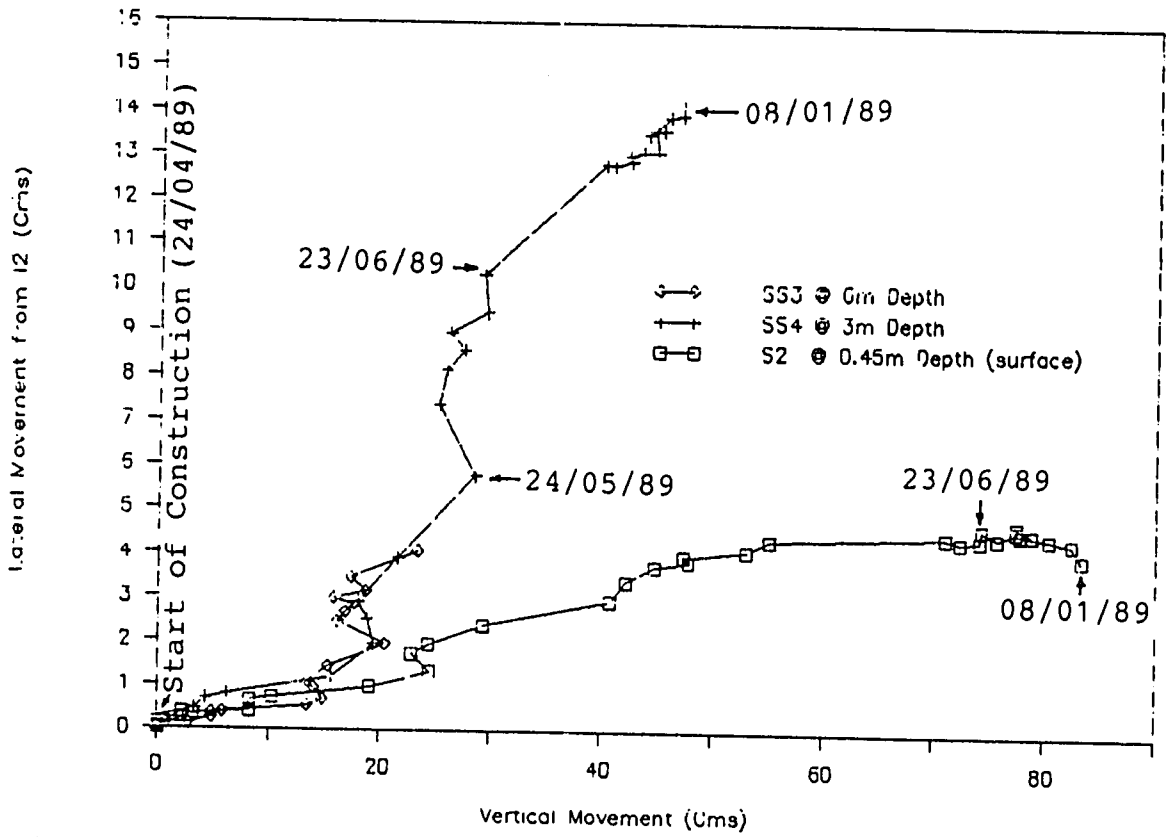

Fig. 94 Maximum Lateral Movement of the Subsoil Plotted Against the Vertical Movement of the Wall (Inclinometer No. 2).

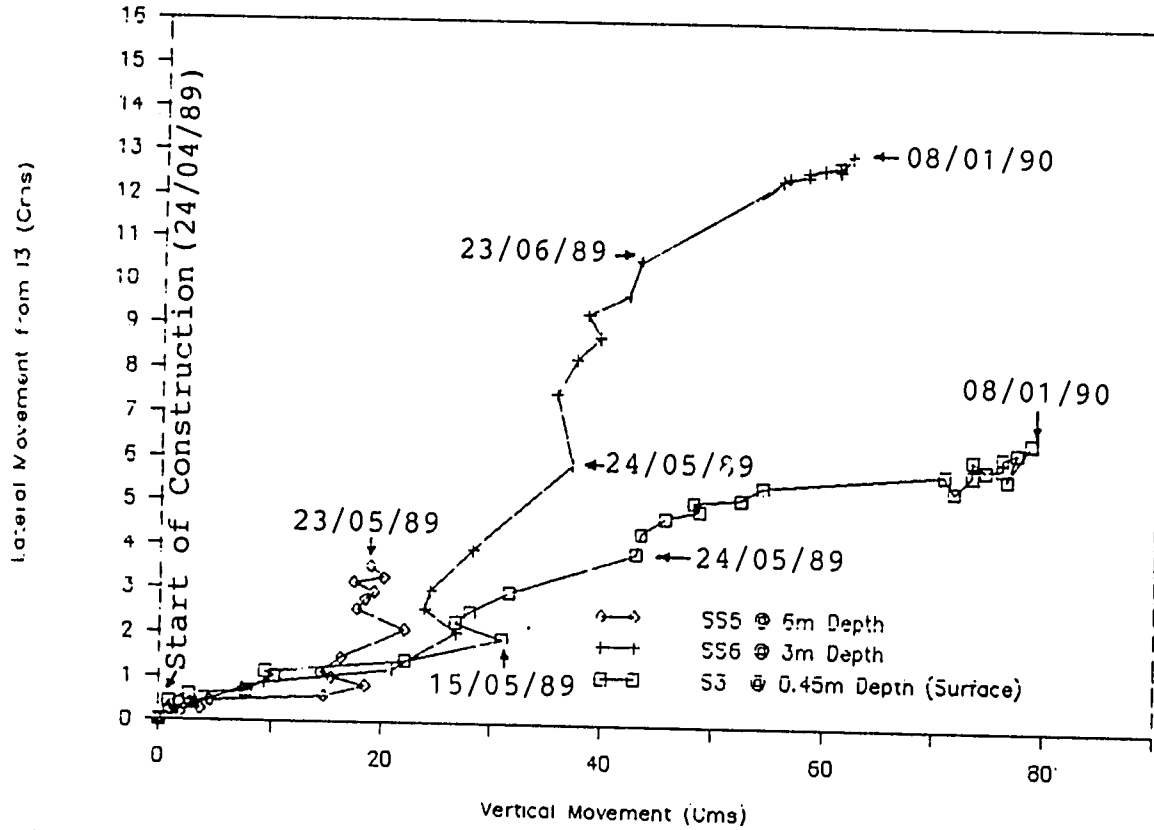

Fig. 95 Maximum Lateral Movement of the Subsoil Plotted Against the Vertical Movement of the Wall (Inclinometer No. 3).

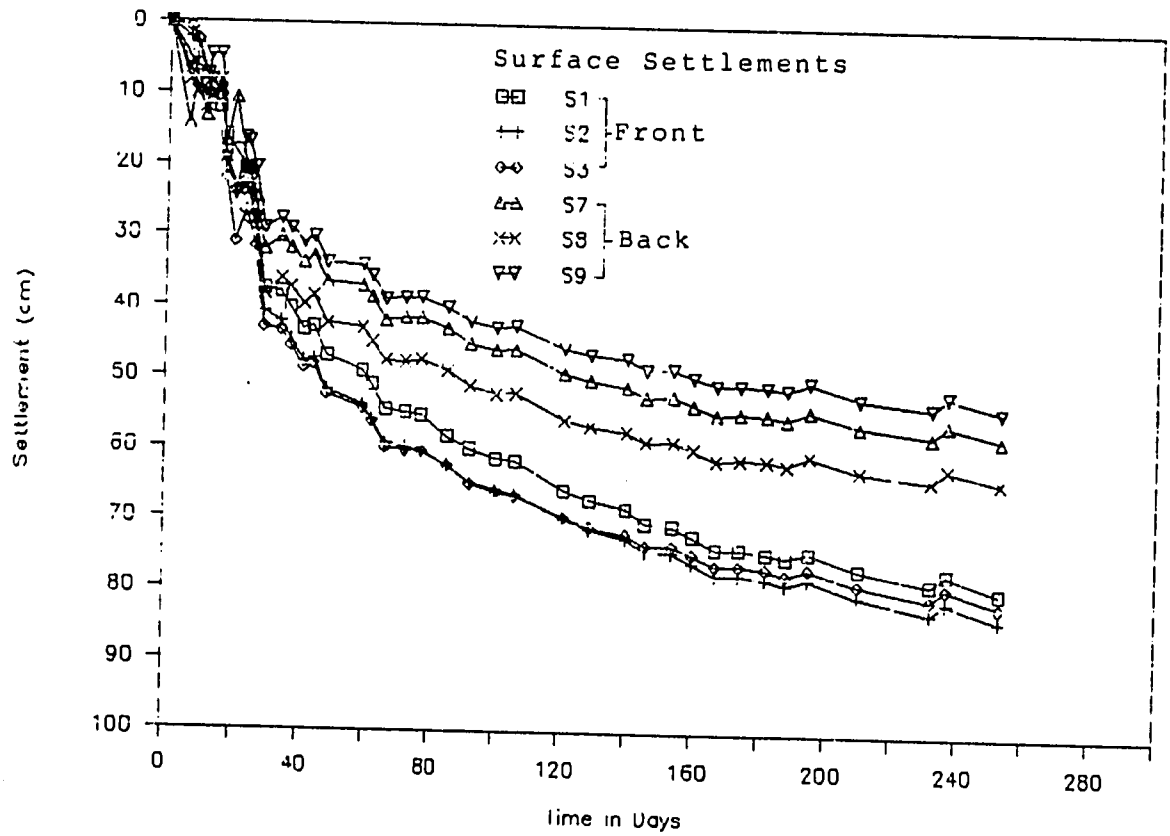

Fig. 96 Observed Surface Settlement-time Relationships of the Front and Back Rows (S1-S2-S3 and S7-S8-S9).

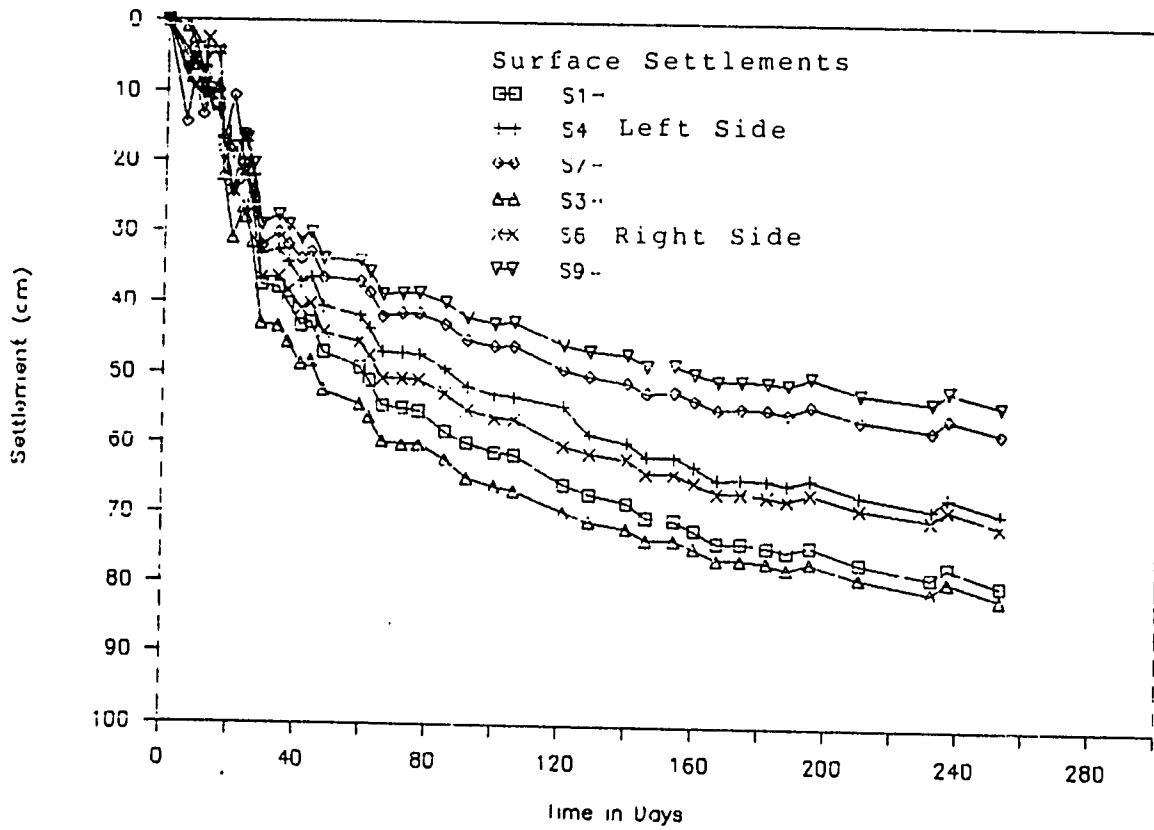

Fig. 97 Observed Surface Settlement-time Relationships of the Left and Right Columns (S1-S2-S3 and S7-S8-S9).

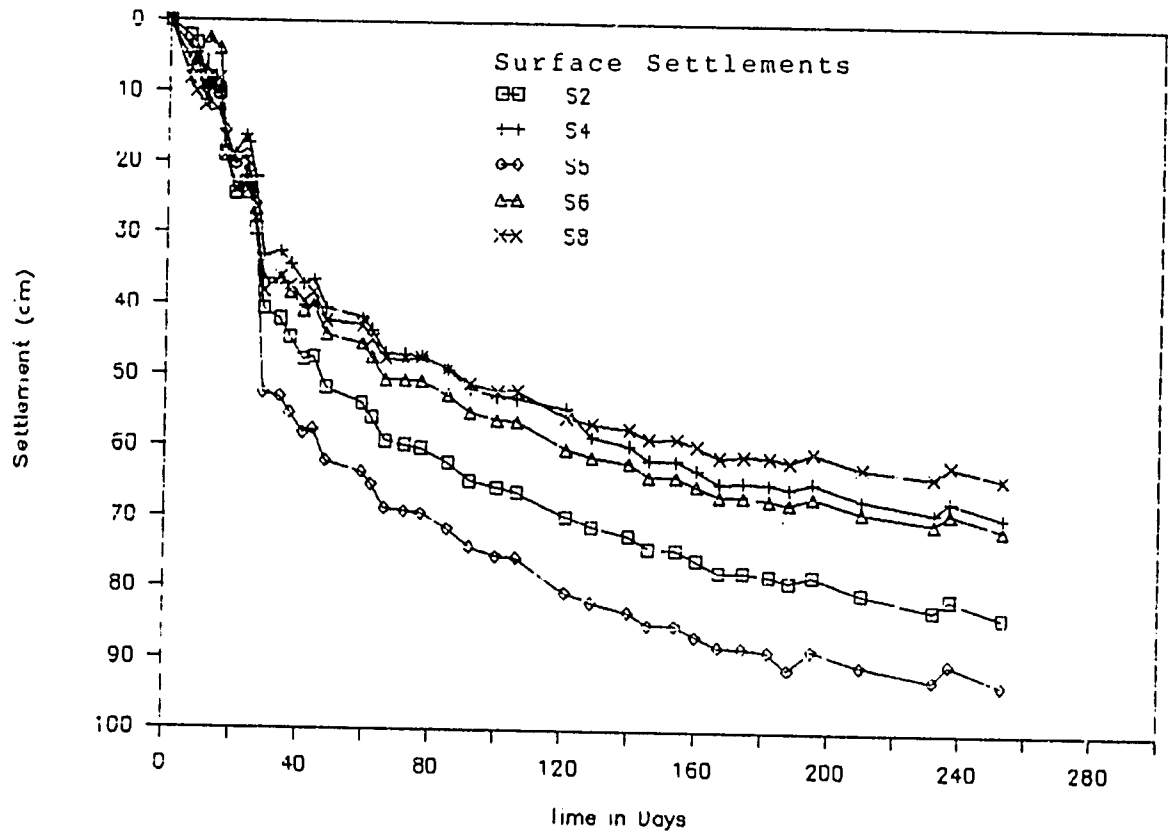

Fig. 98 Observed Surface Settlement-time Relationships of the Center Column and the Middle Row (S1-S2-S3 and S7-S8-S9).

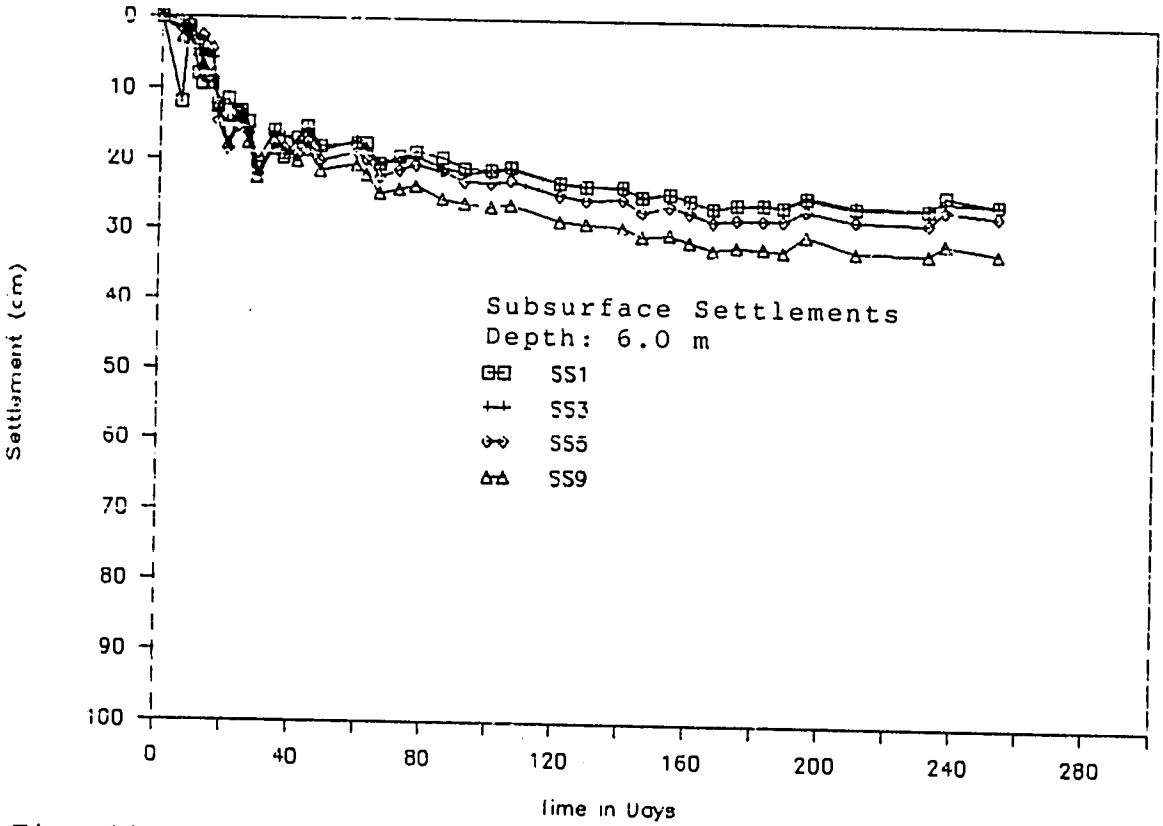

Fig. 99 Observed Subsurface (6.0 m depth) Settlement-time Relationships of the Front and Middle Rows (SS1-SS3-SS5 and SS9).

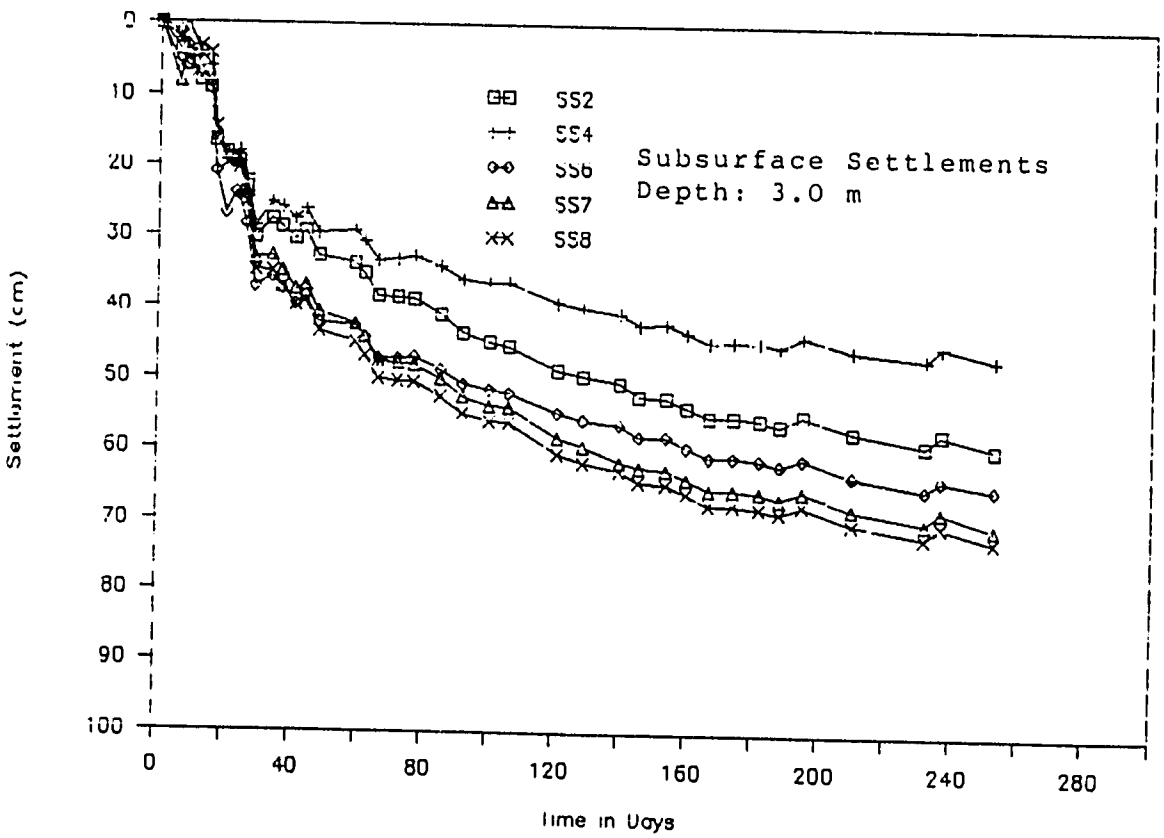

Fig. 100 Observed Subsurface (3.0 m depth) Settlement-time Relationships of the Front and Middle Rows (SS2-SS4-SS6 and SS7-SS8).

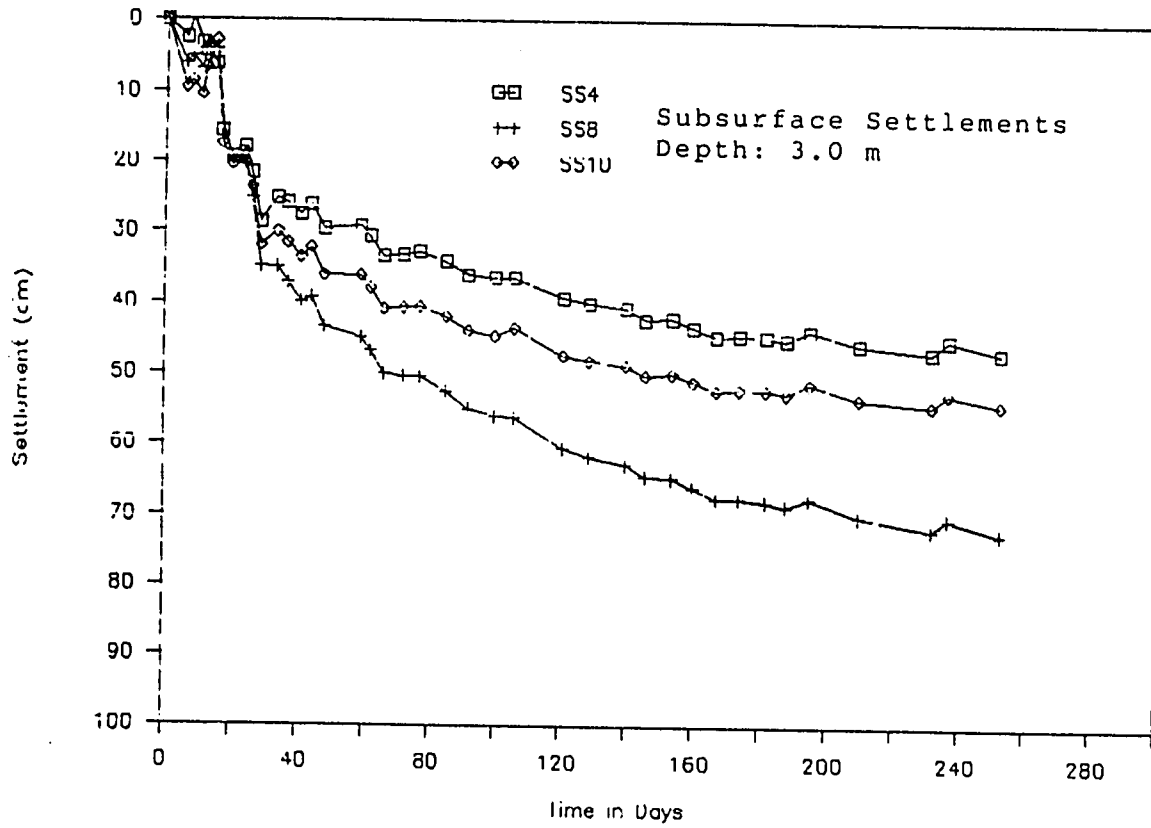

Fig. 101 Observed Subsurface (3.0 m depth) Settlement-time Relationships of the Center Column (SS4-SS8-SS10).

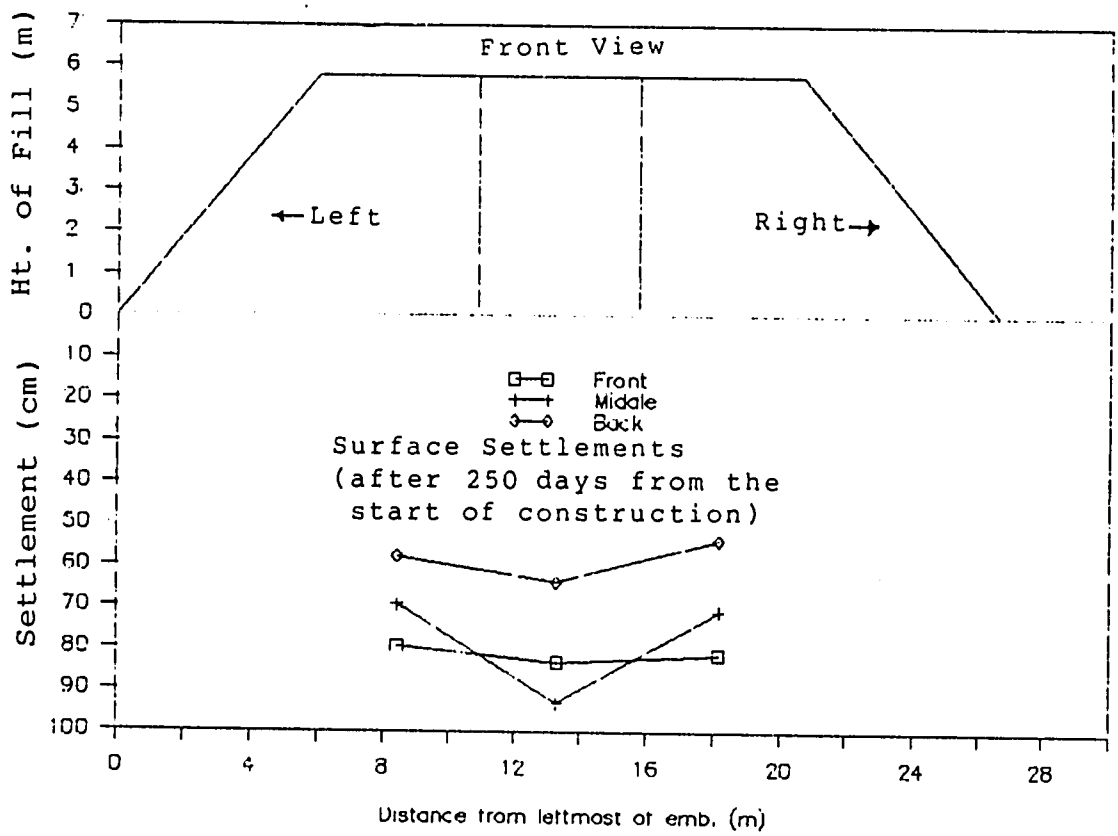

Fig. 102 Surface Settlement Profile along the Longitudinal Section of the Embankment.

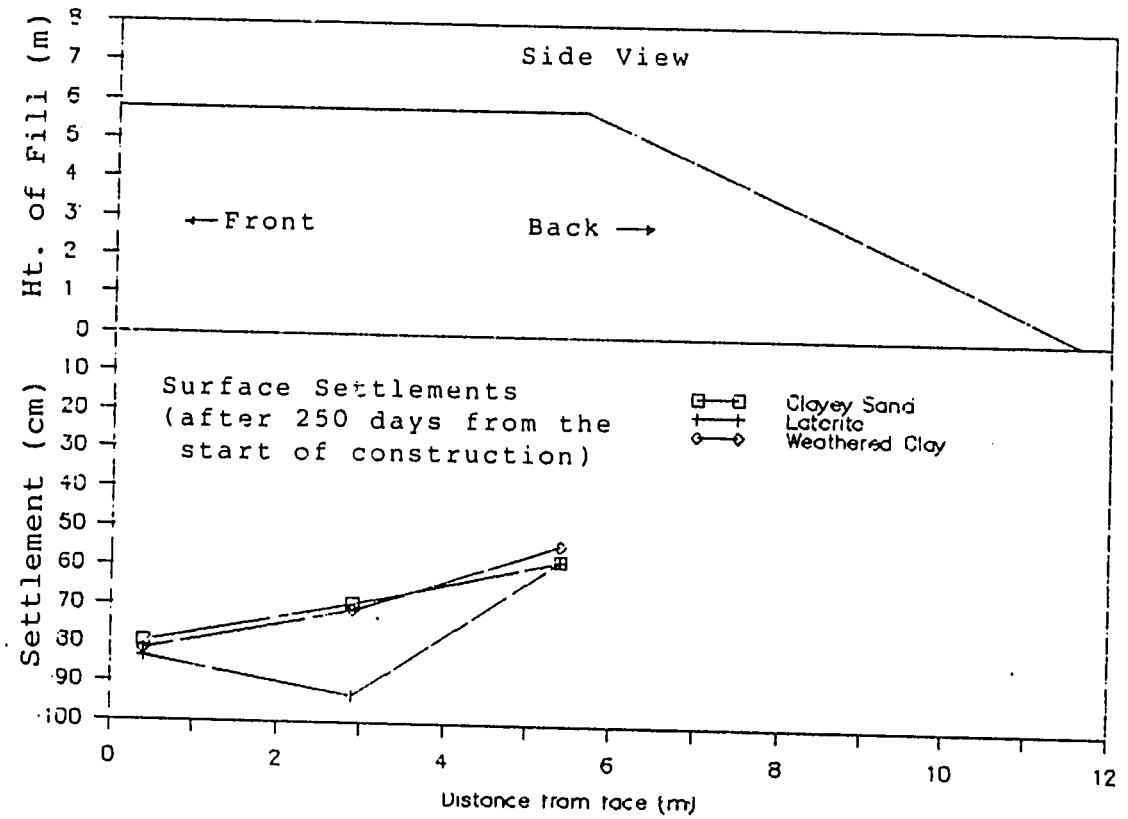

Fig. 103 Surface Settlement Profile Along the Cross-Section of the Embankment.

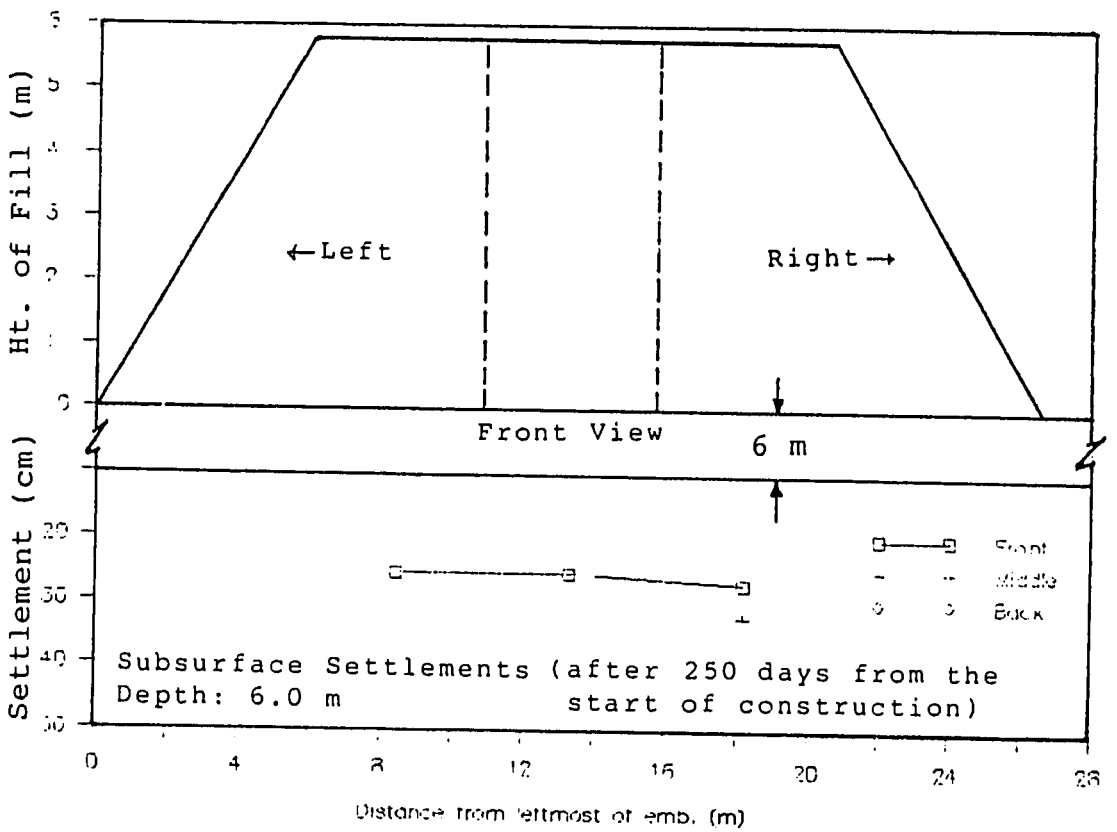

Fig. 104 Subsurface Settlement (6.0 m depth) Profile Along the Longitudinal Section of the Embankment.

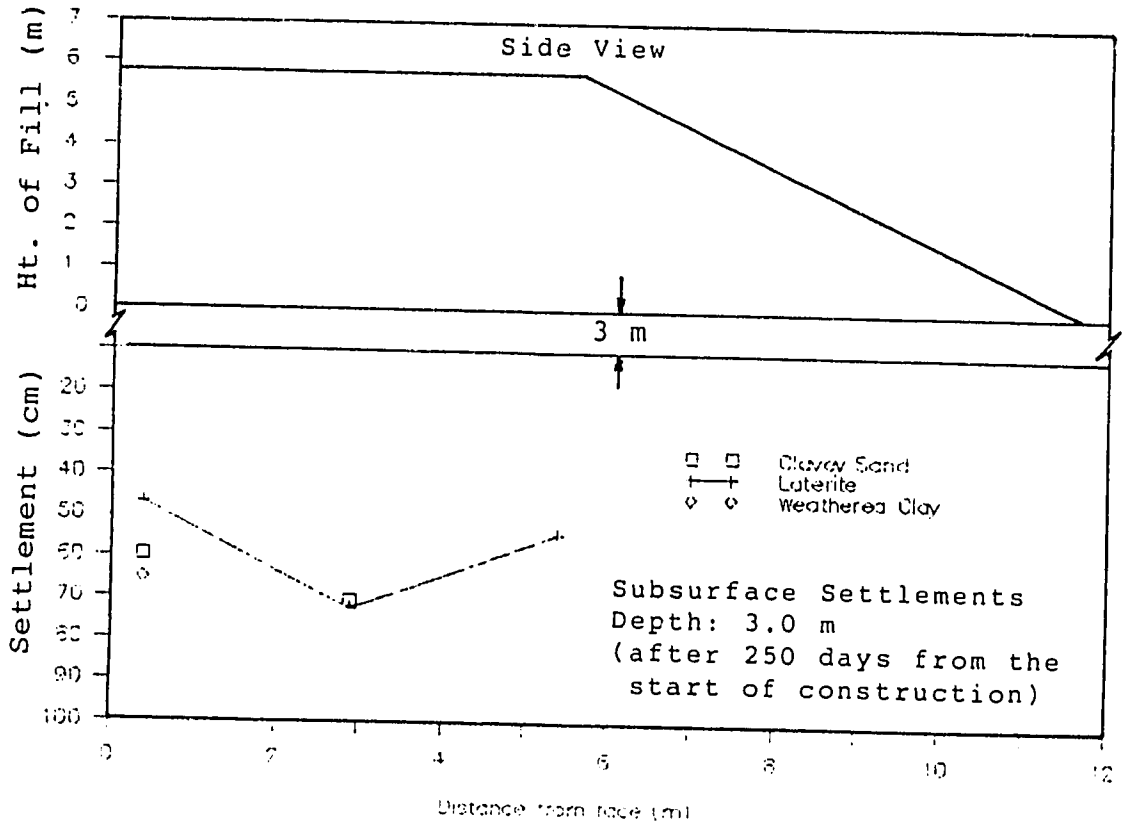

Fig. 105 Subsurface Settlement (6.0 m depth) Profile Along the Cross-Section of the Embankment.

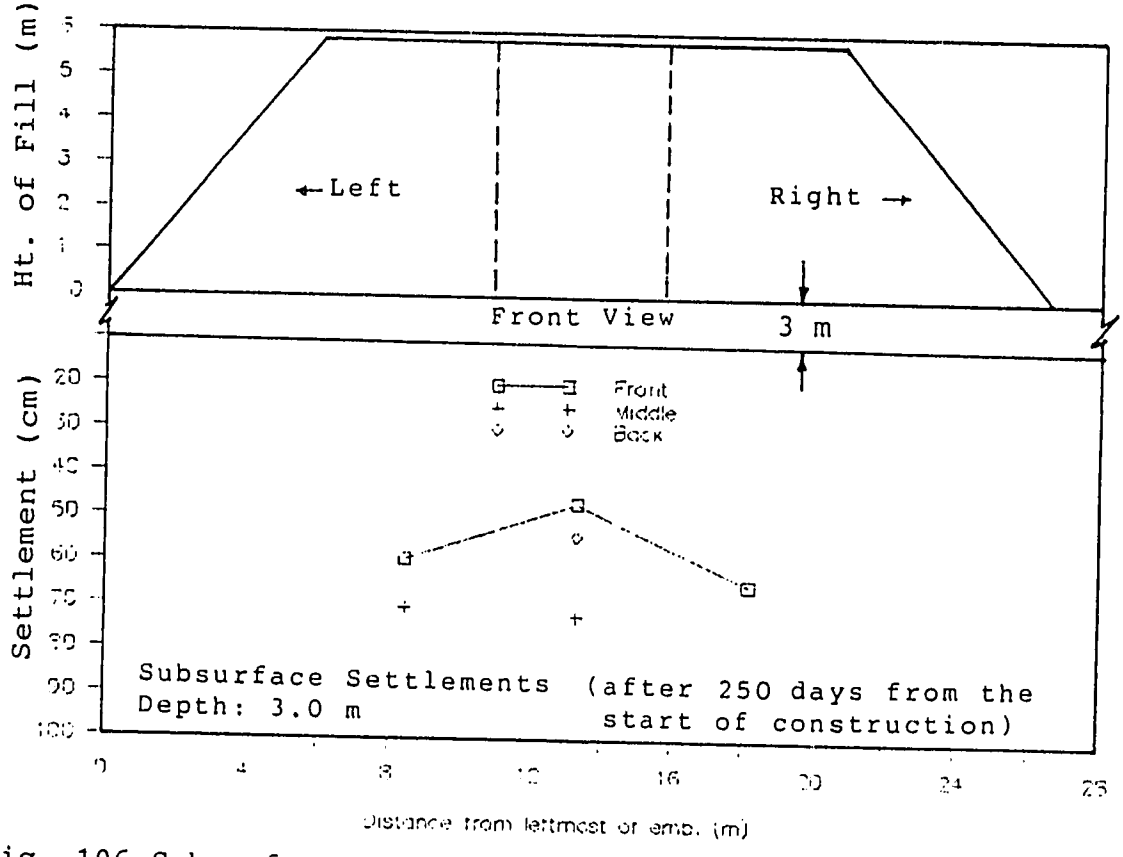

Fig. 106 Subsurface Settlement (3.0 m depth) Profile Along the Longitudinal Section of the Embankment.

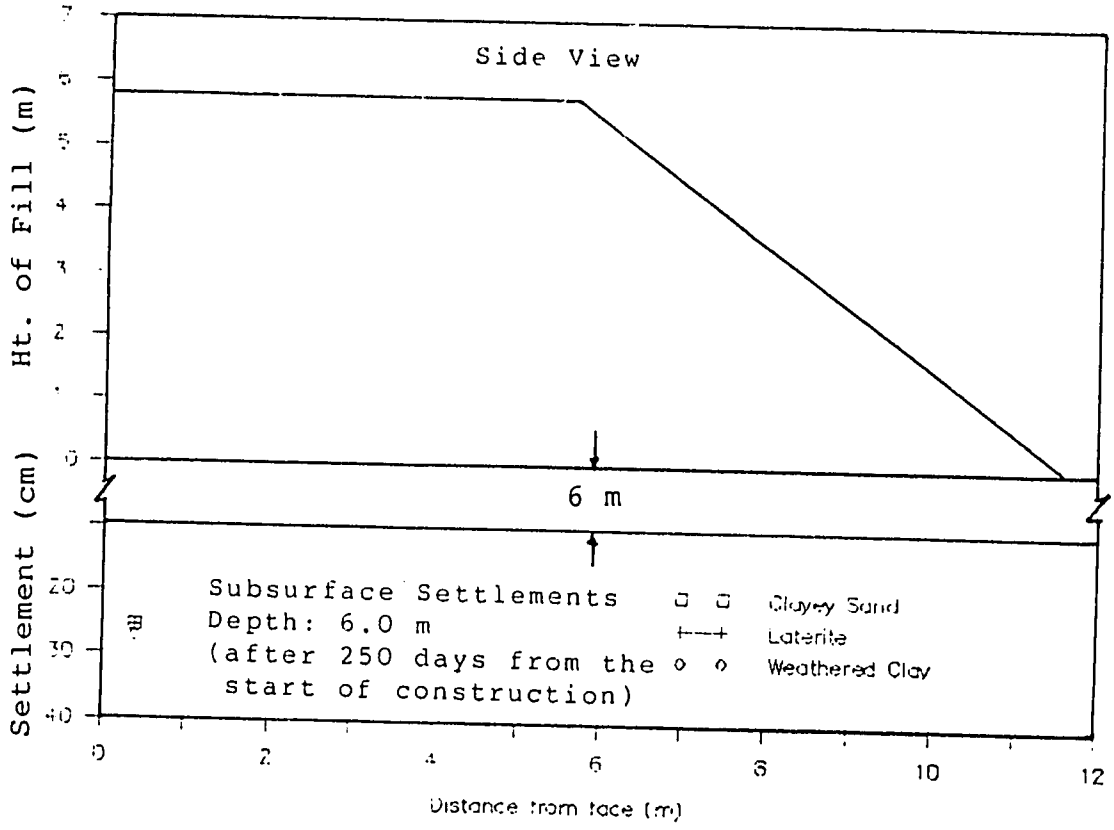

Fig. 107 Subsurface Settlement (3.0 m depth) Profile Along the Cross-Section of the Embankment.

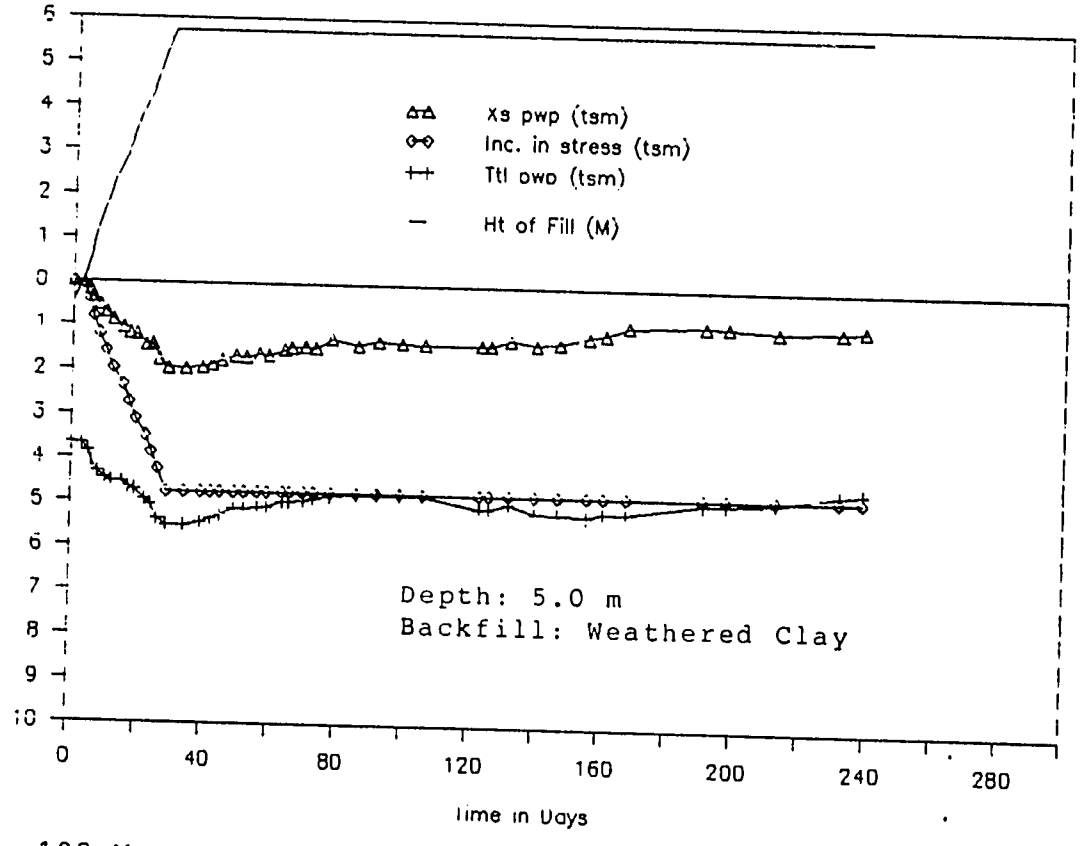

Fig. 108 Measured Excess Porewater Pressure Below the Weathered Clay Backfill at 5.0 m Depth (Hydraulic Piezometer-H2).

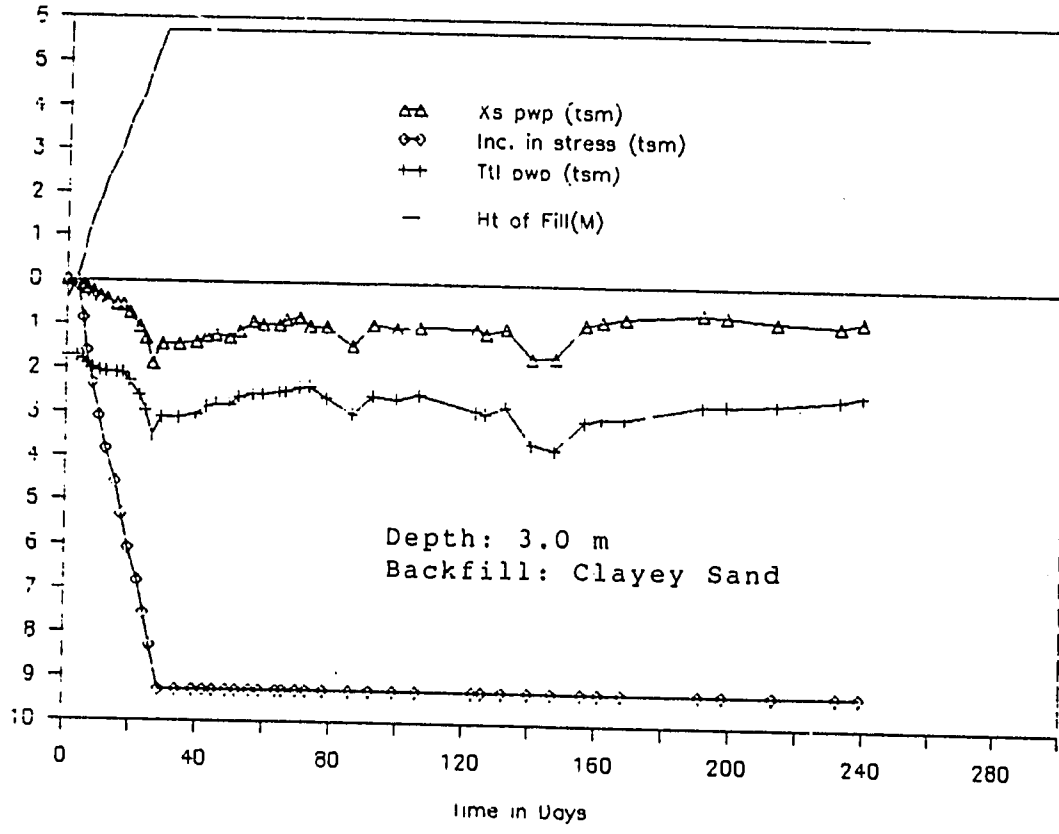

Fig. 109 Measured Excess Porewater Pressure Below the Clayey Sand Backfill at 3.0 m Depth (Hydraulic Piezometer-H3).

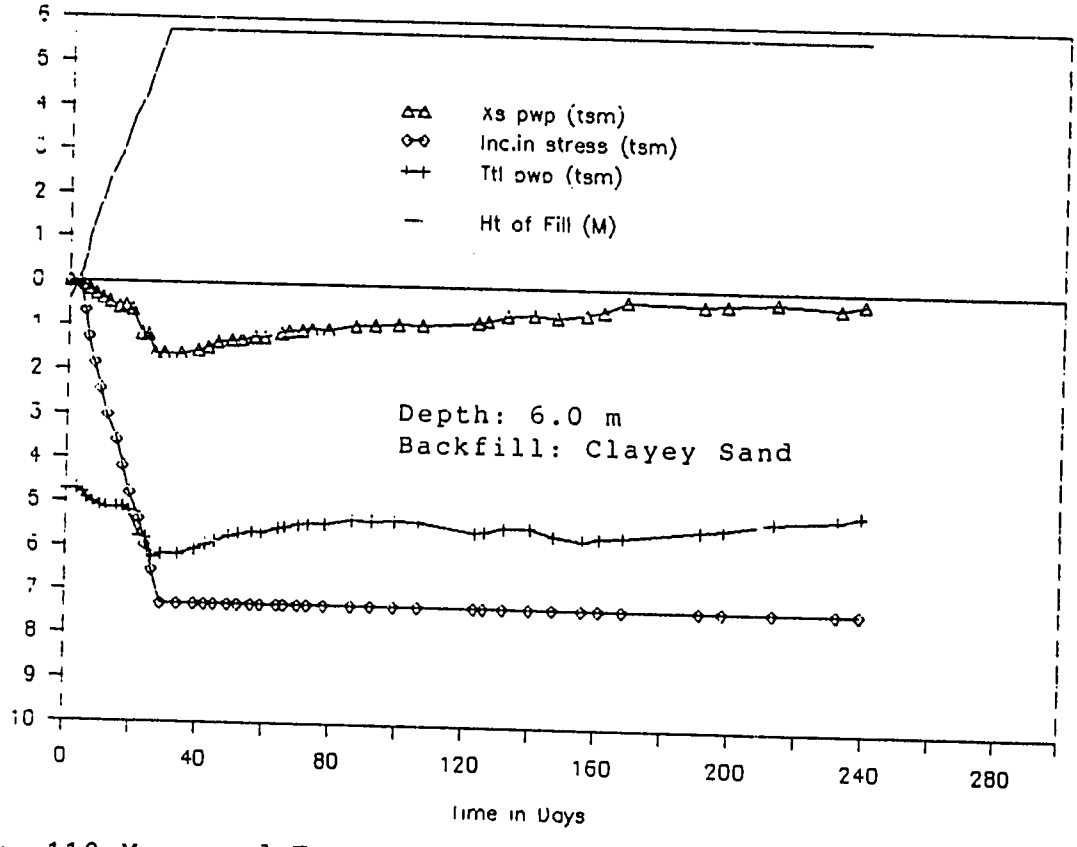

Fig. 110 Measured Excess Porewater Pressure Below the Clayey Sand Backfill at 6.0 m Depth (Hydraulic Piezometer-H4).

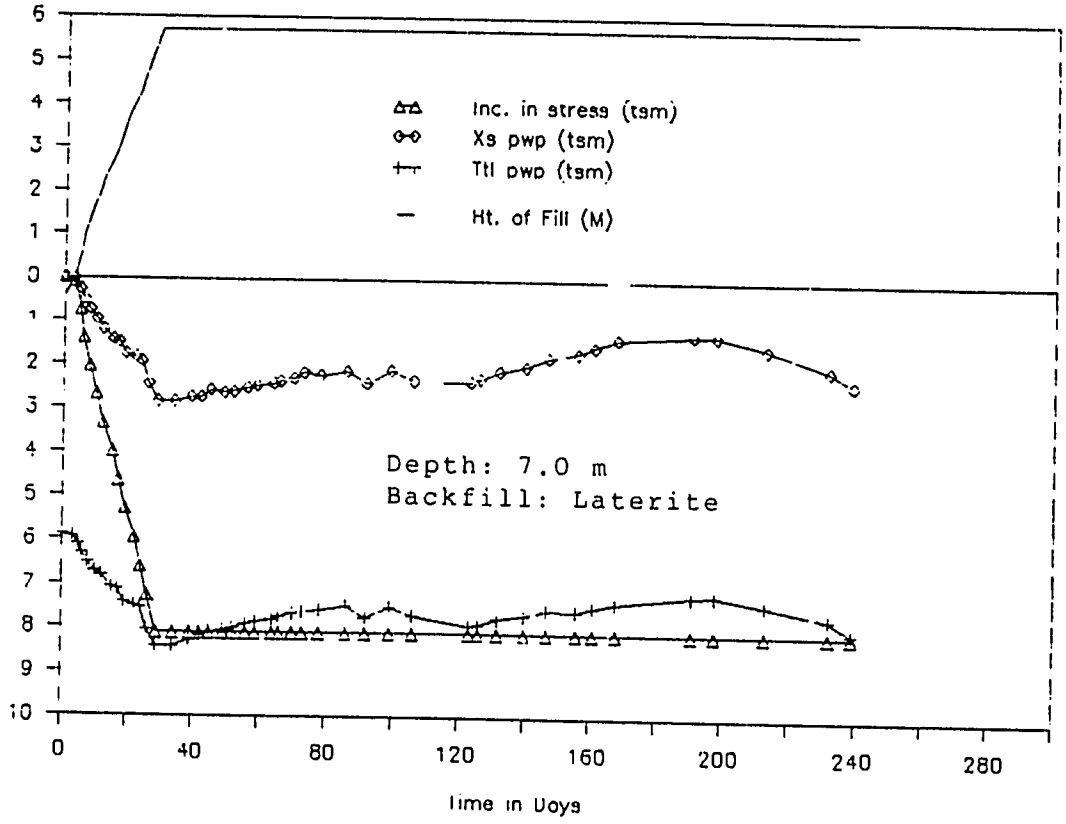

Fig. 111 Measured Excess Porewater Pressure Below the Lateritic Backfill at 7.0 m Depth (Hydraulic Piezometer-H5).

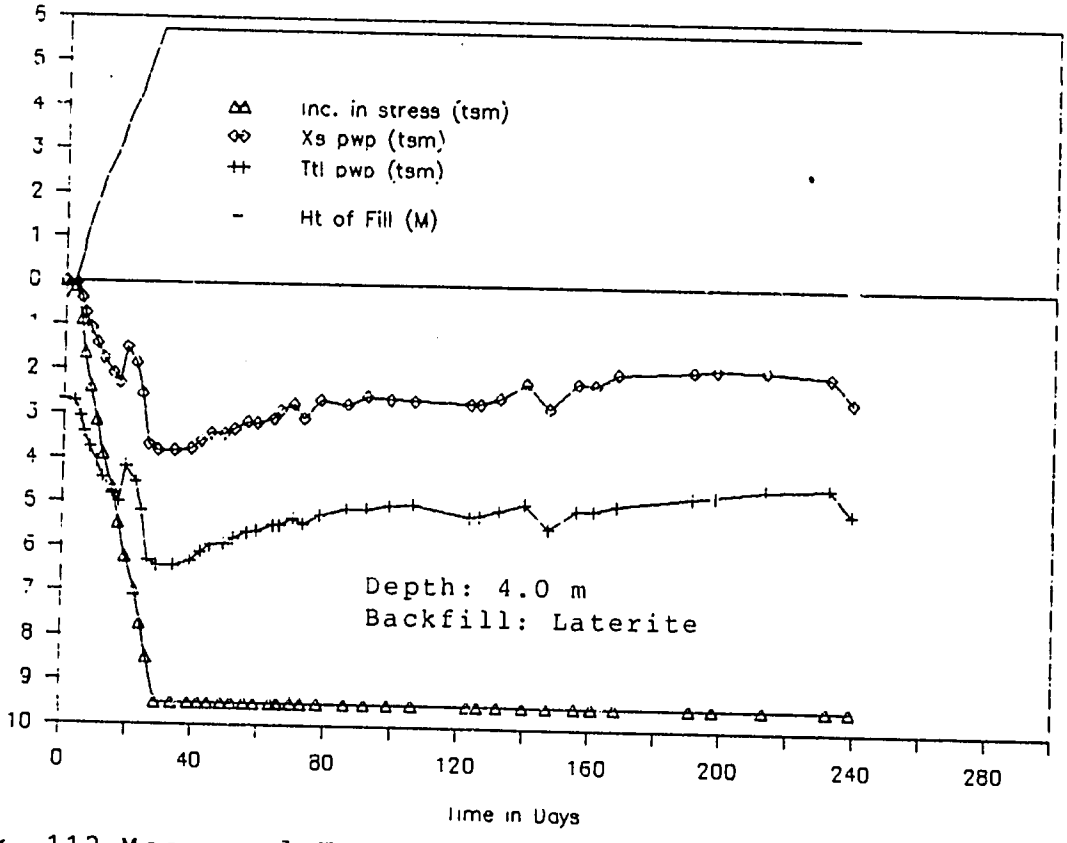

Fig. 112 Measured Excess Porewater Pressure Below the Lateritic Backfill at 4.0 m Depth (Hydraulic Piezometer-H6).

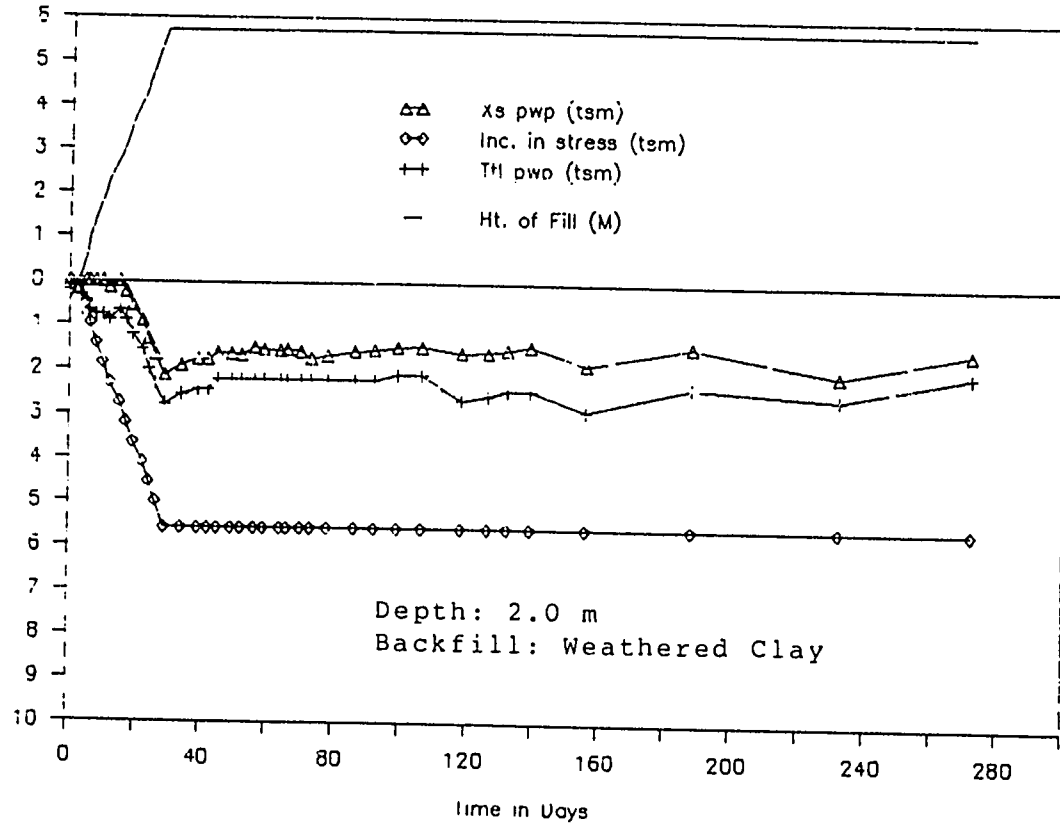

Fig. 113 Measured Excess Porewater Pressure Below the Weathered Clay Backfill at 2.0 m Depth (Pneumatic Piezometer-N2).

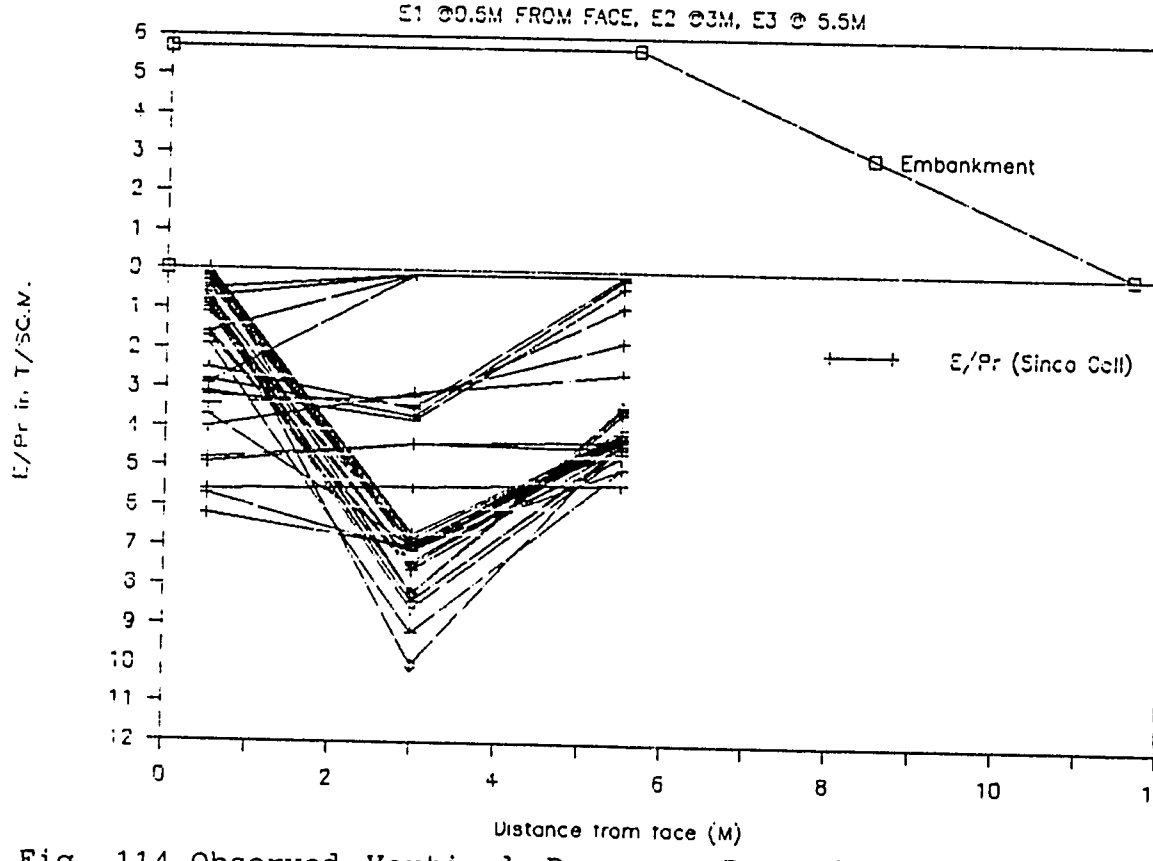

Fig. 114 Observed Vertical Pressure Beneath the Embankment Plotted with Distance from the Face of the Wall.

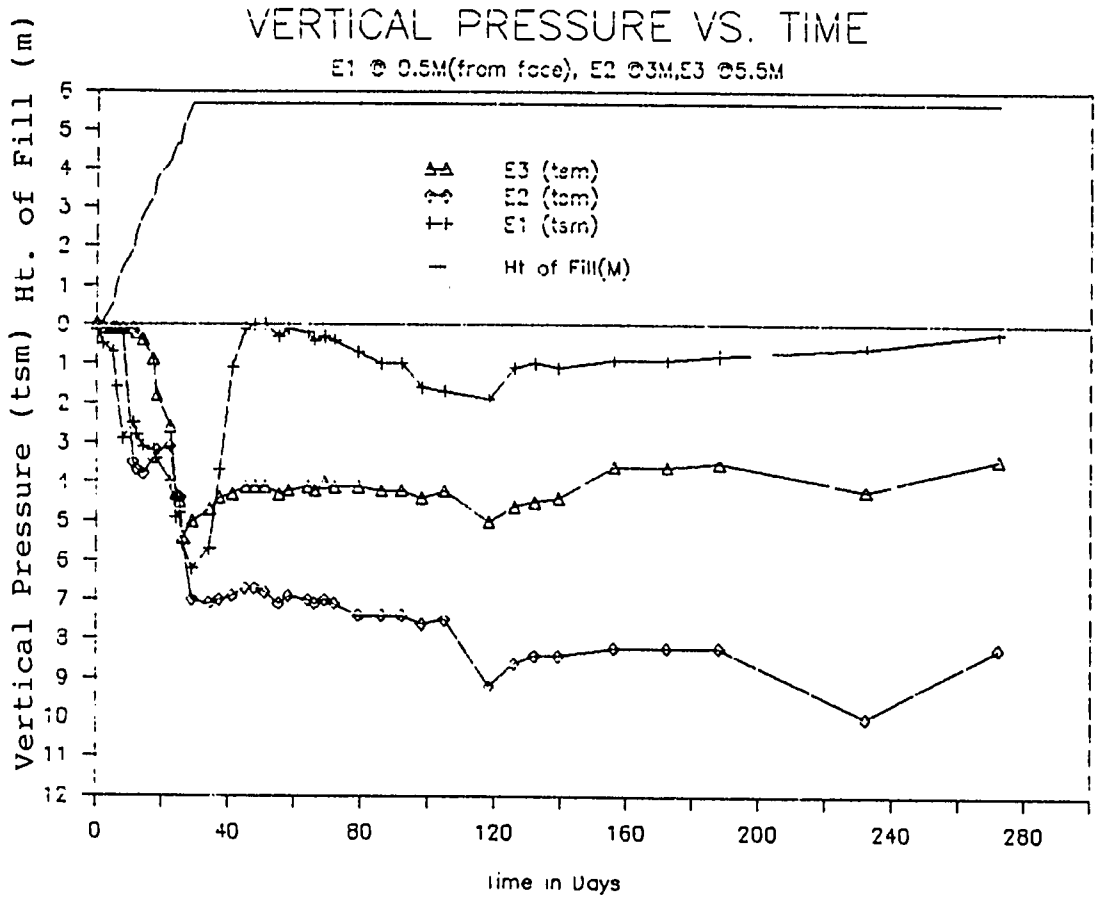

Fig. 115 Plots of Vertical Pressure Beneath the Embankment Against Time.

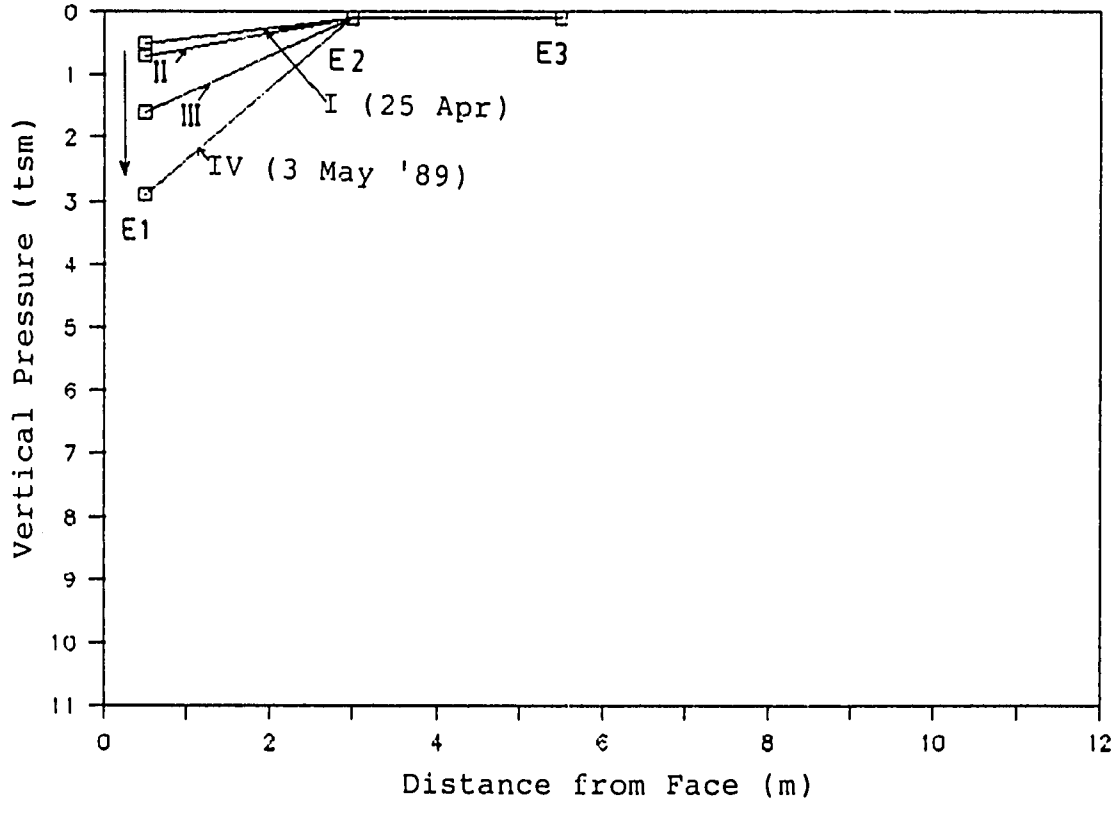

Fig. 116 Vertical Pressure Beneath the Embankment During Construction (Layers I to IV).

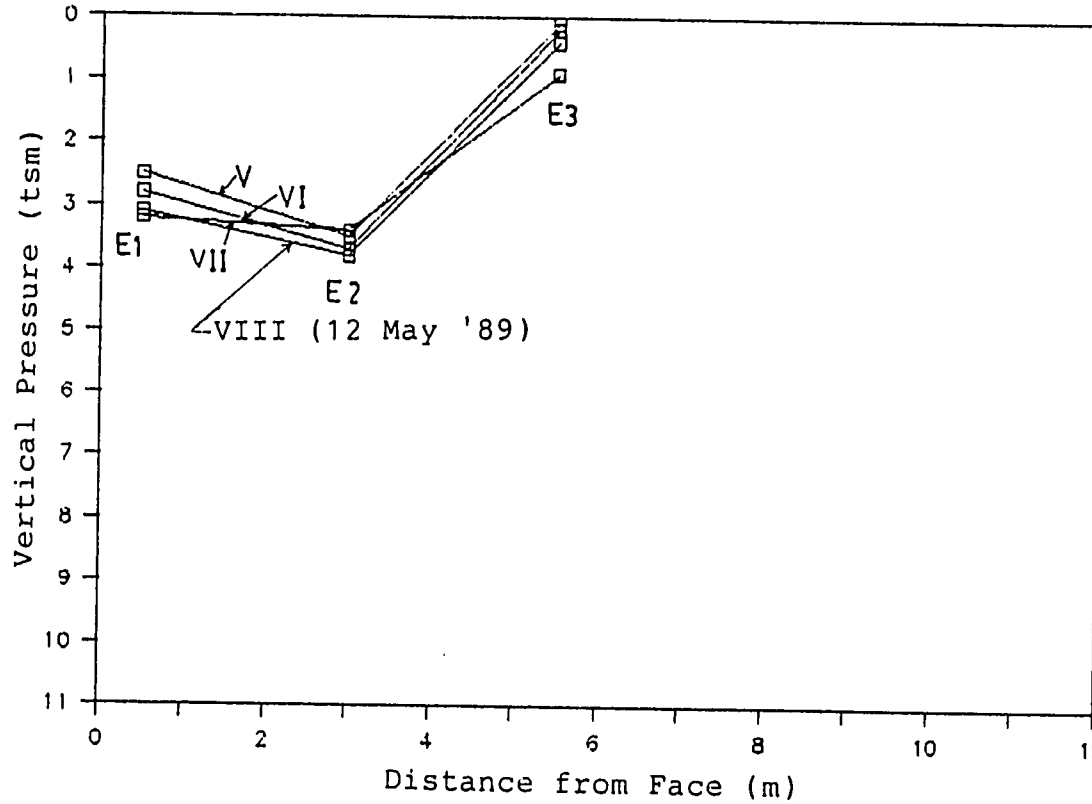

Fig. 117 Vertical Pressure Beneath the Embankment During Construction (Layers V to VIII).

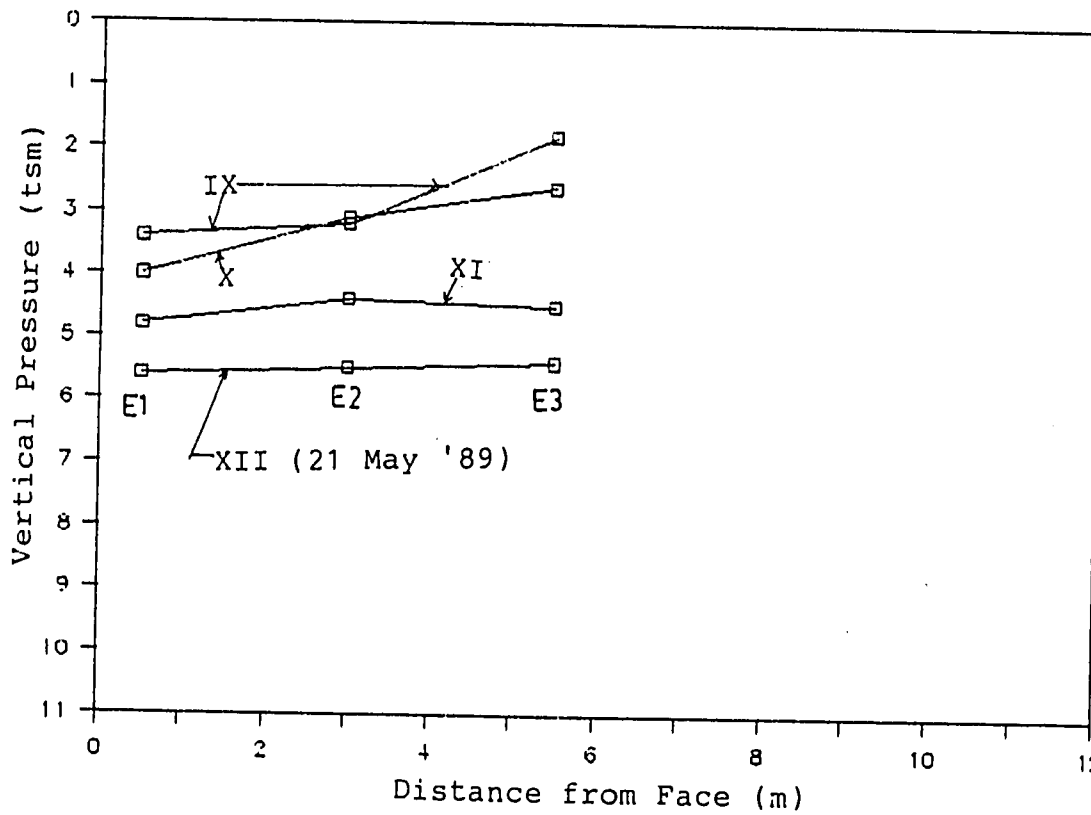

Fig. 118 Vertical Pressure Beneath the Embankment During Construction (Layers IX to XII).

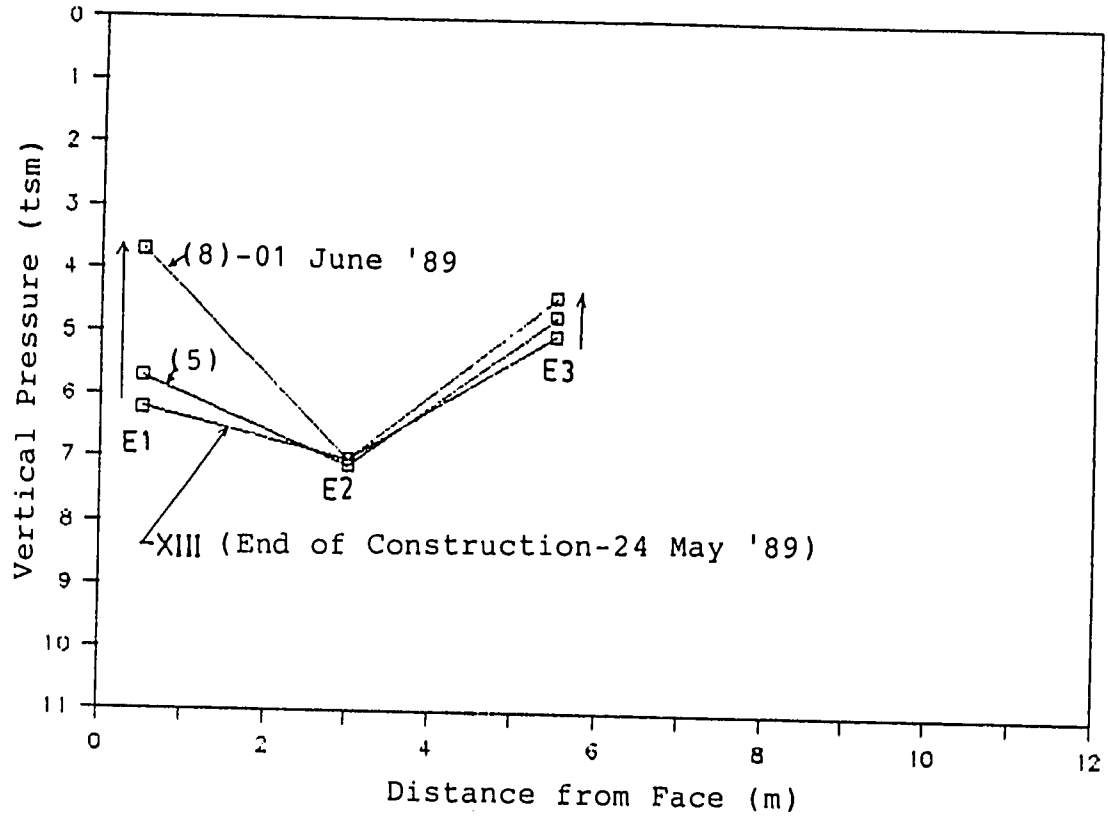

Fig. 119 Vertical Pressure Beneath the Embankment at the End of Construction and 8 Days Later.

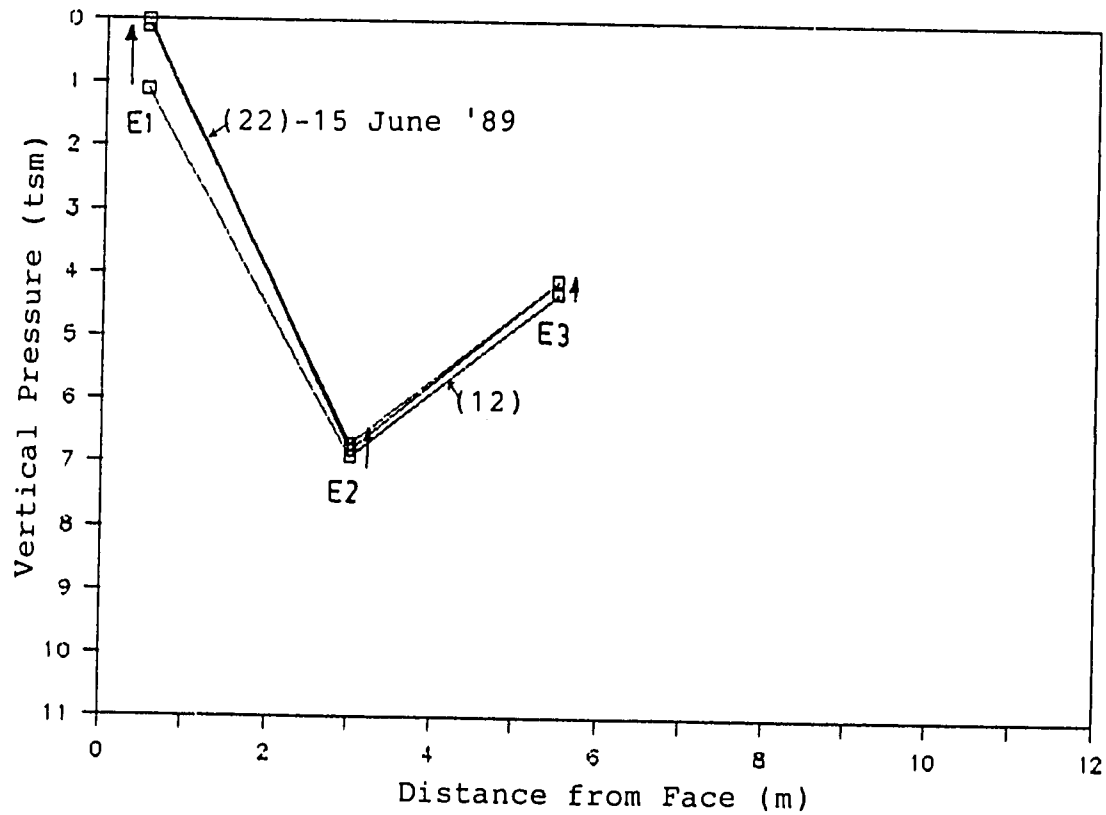

Fig. 120 Vertical Pressure Beneath the Embankment Between 12 and 22 Days After Construction.

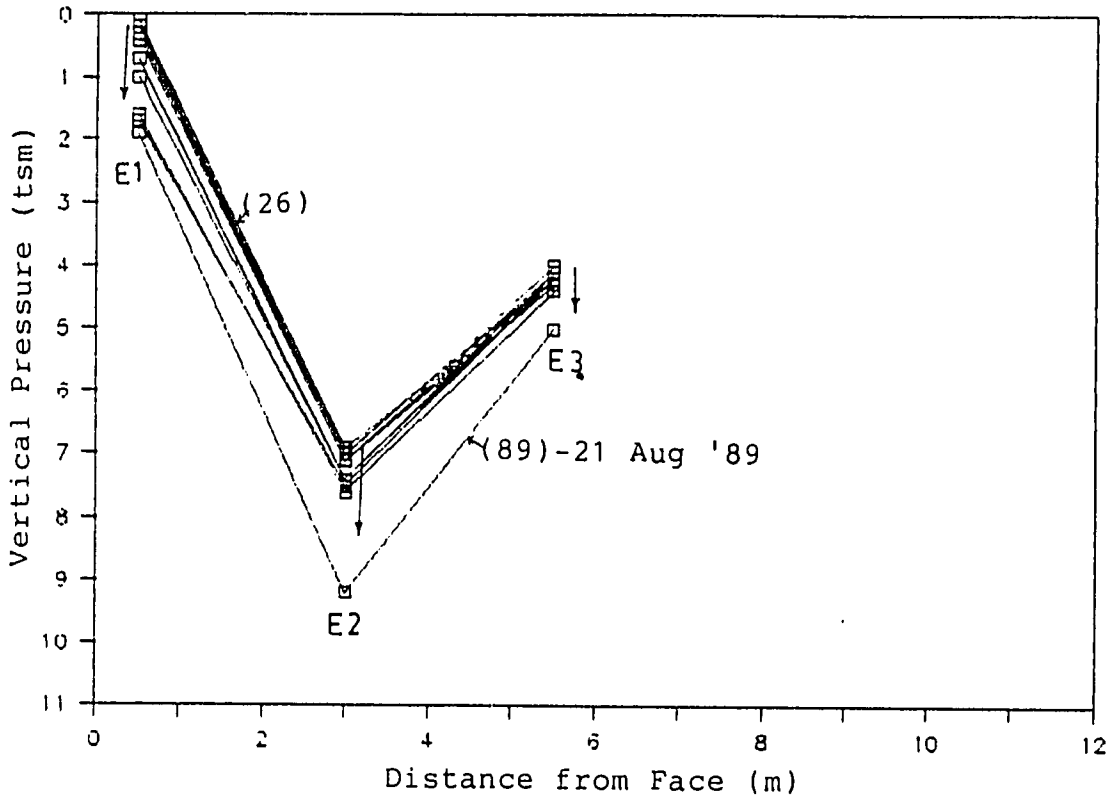

Fig. 121 Vertical Pressure Beneath the Embankment Between 26 and 89 Days After Construction.

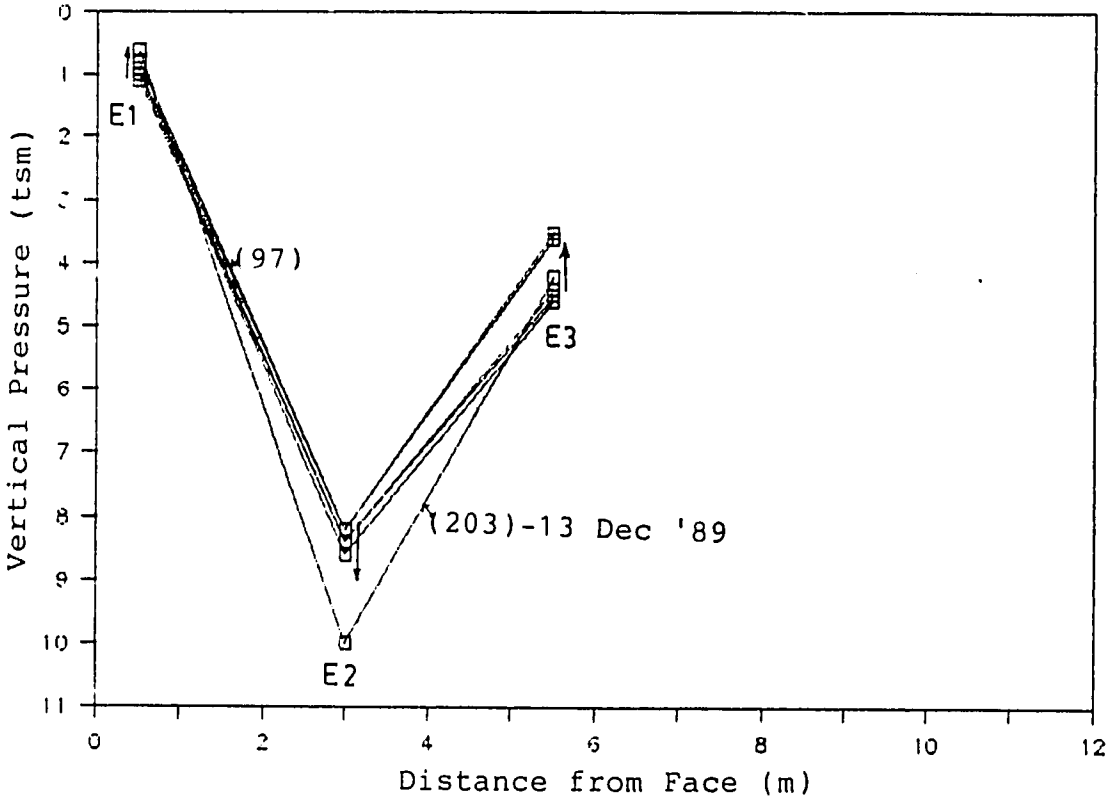

Fig. 122 Vertical Pressure Beneath the Embankment Between 97 and 203 Days After Construction.

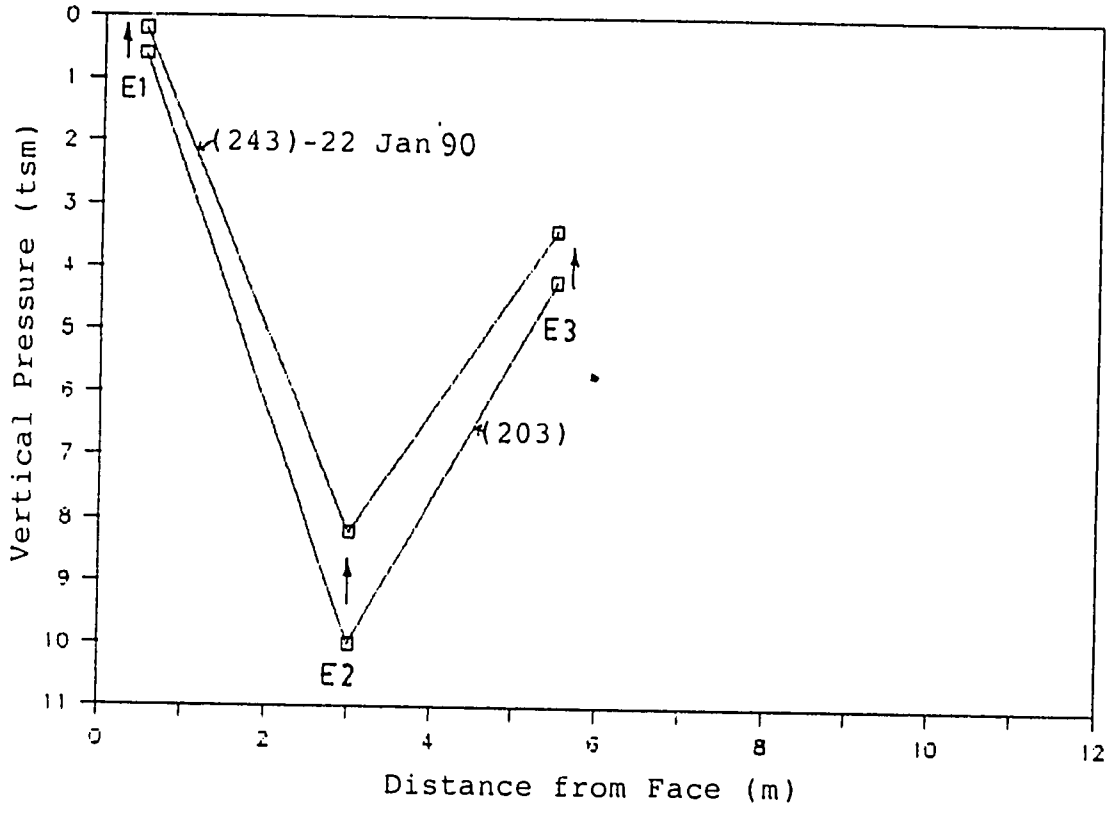

Fig. 123 Vertical Pressure Beneath the Embankment Between 203 and 243 Days After Construction.

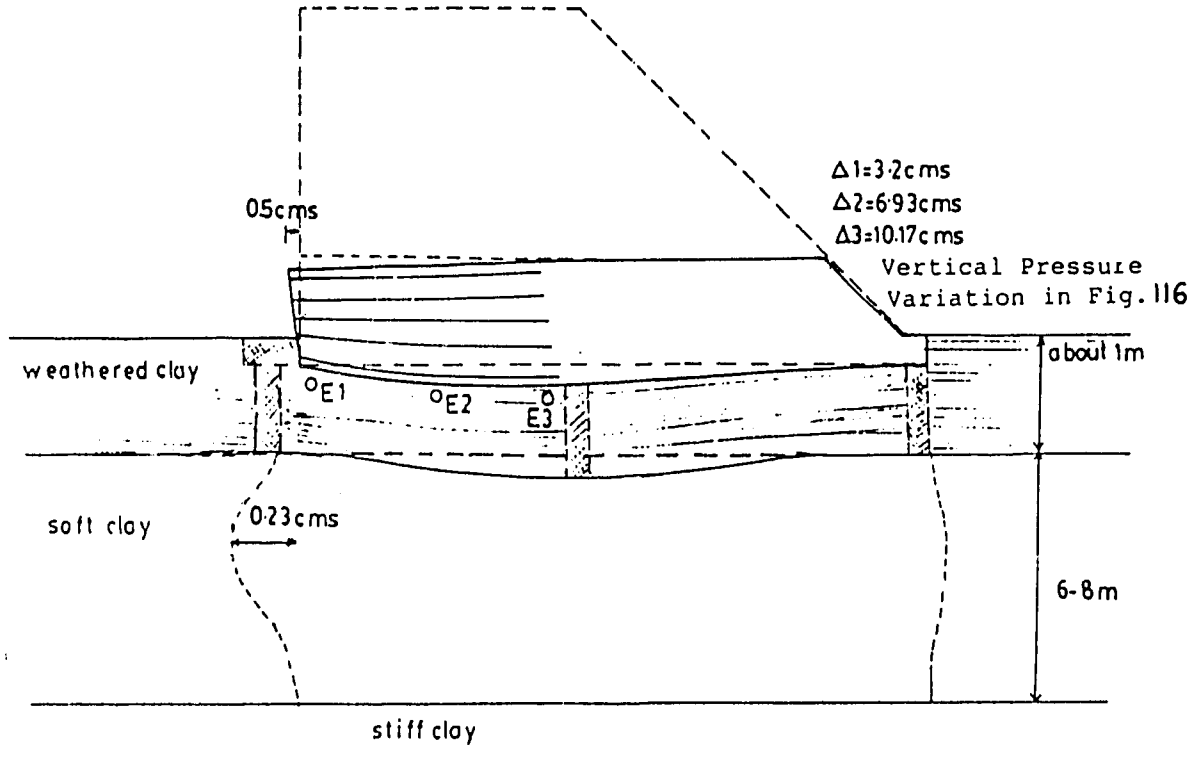

Fig. 124 A Cross-sectional View of Embankment During Construction (after 4 layers).

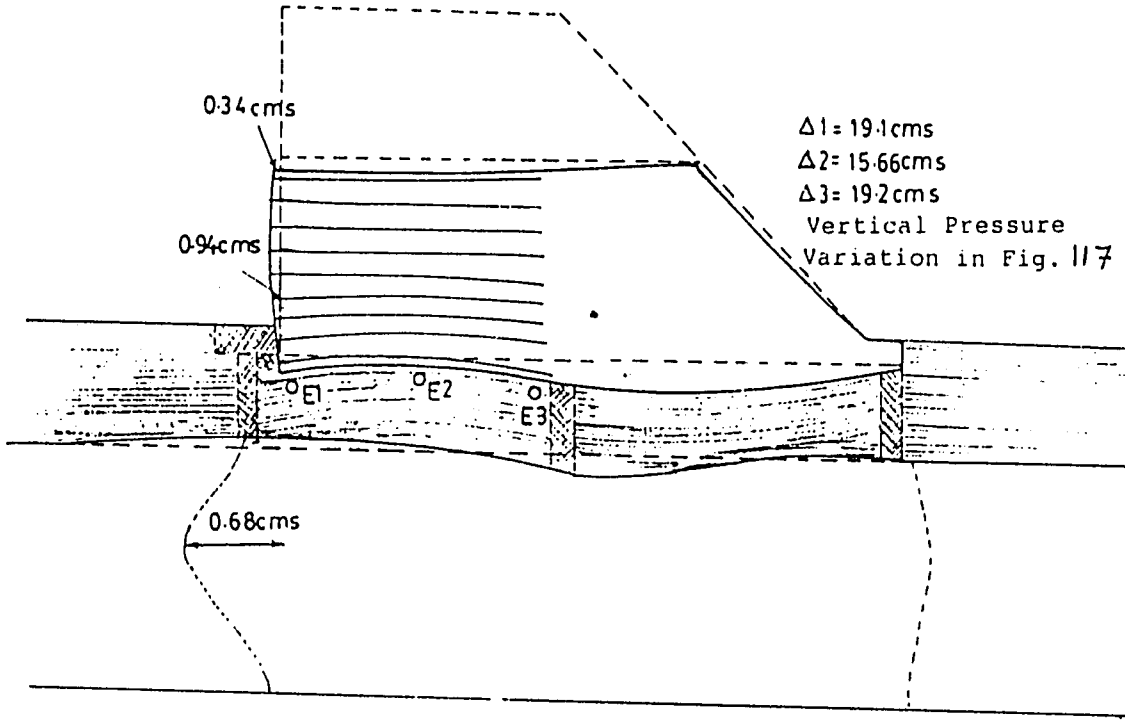

Fig. 125 A Cross-sectional View of Embankment During Construction (after 8 layers).

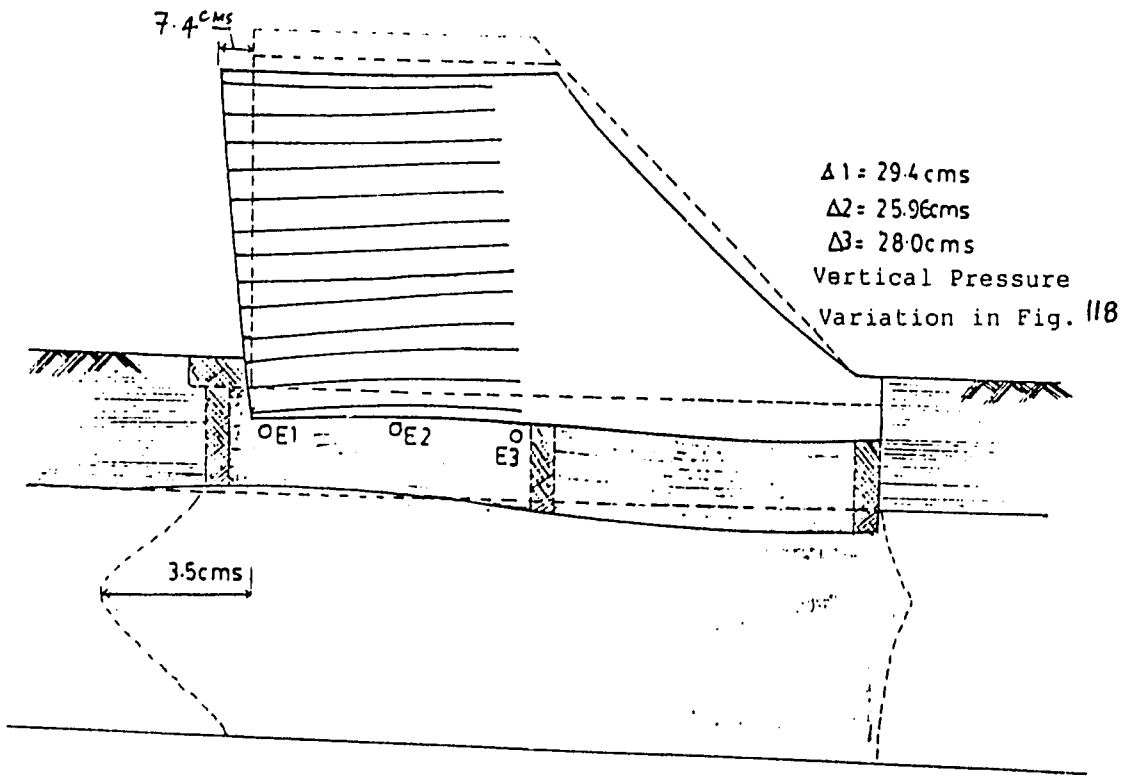

Fig. 126 A Cross-sectional View of Embankment During Construction (after 12 layers).

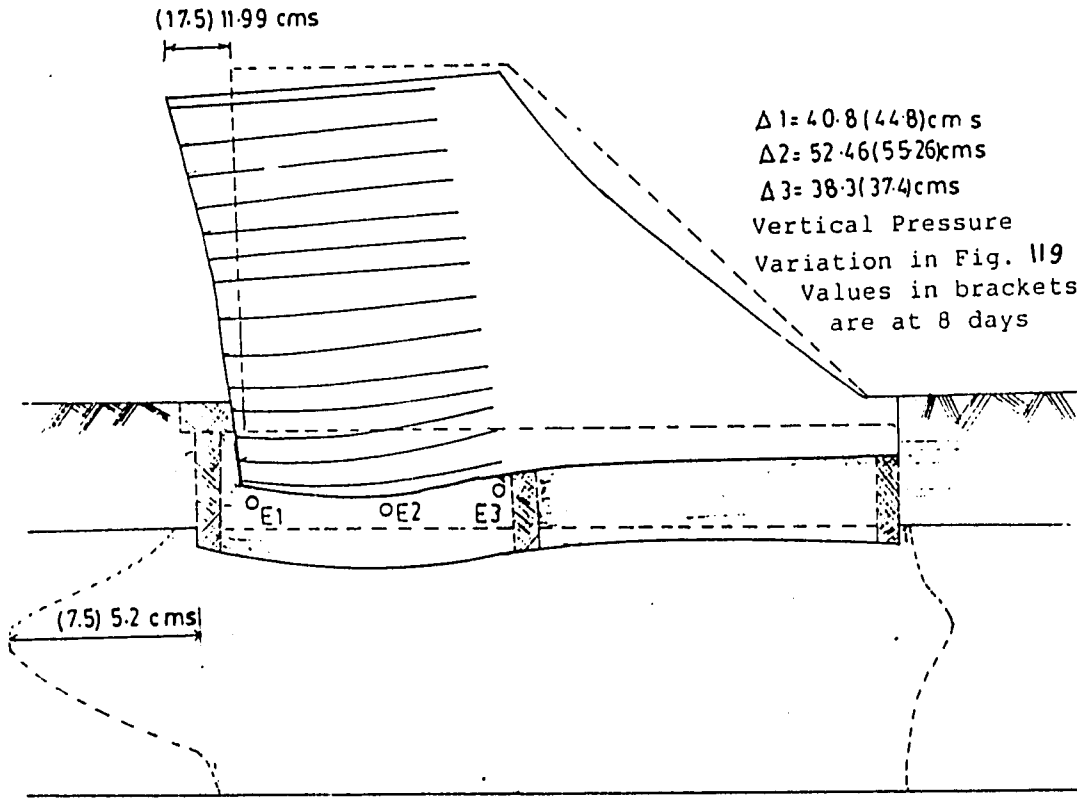

Fig. 127 A Cross-sectional View of Embankment at the End of Construction (13 layers) and 8 Days Later.

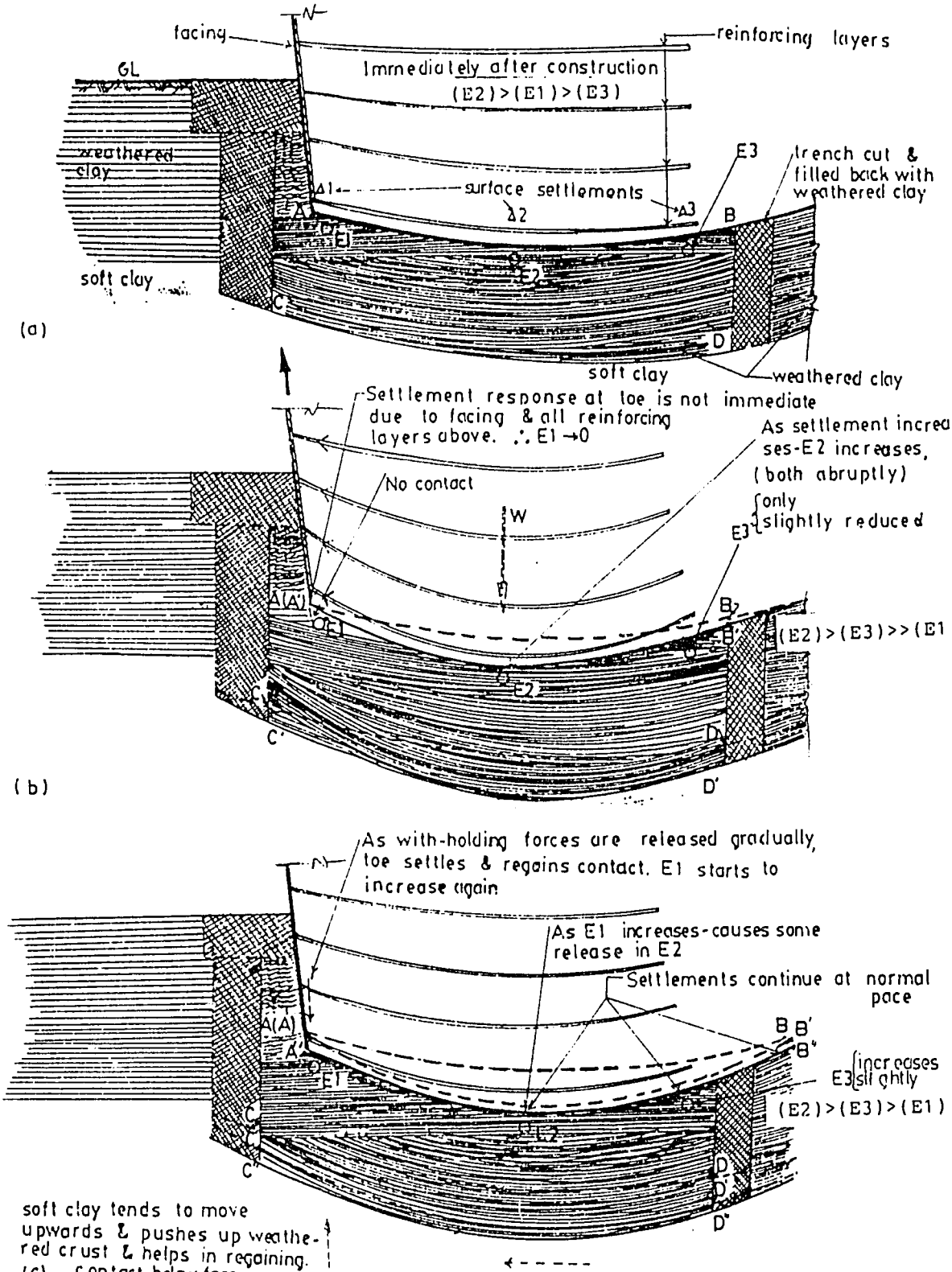

Events in figs (b) & (c) repeat until lateral movement & consolidation of soft clay subsoil ceases

Example:

N	Δ1	Δ2	Δ3	E1	E2	E3	δ_{top}	δ_{-3m}
0	44·8	55·26	38·3	6·2	7·0	5·0	11·99	5·2
22	51·8	62·06	42·4	0·0	6·8	4·1	21·4	9·2
89	69·8	80·56	55·7	1·9	9·2	5·0	35·0	12·0
203	82·5	92·36	63·7	0·6	10·0	4·2	44·9	14·0
243	83·4	93·06	63·9	0·2	8·2	3·4	46·2	14·0

cms. tsm

δ is lateral movement in cms.

N is number of days after constn.

Fig. 128 An Enlarged Cross-sectional View Near the Face of the Wall Showing Mechanism of Cyclic Variation in the Values of the Base Pressure.

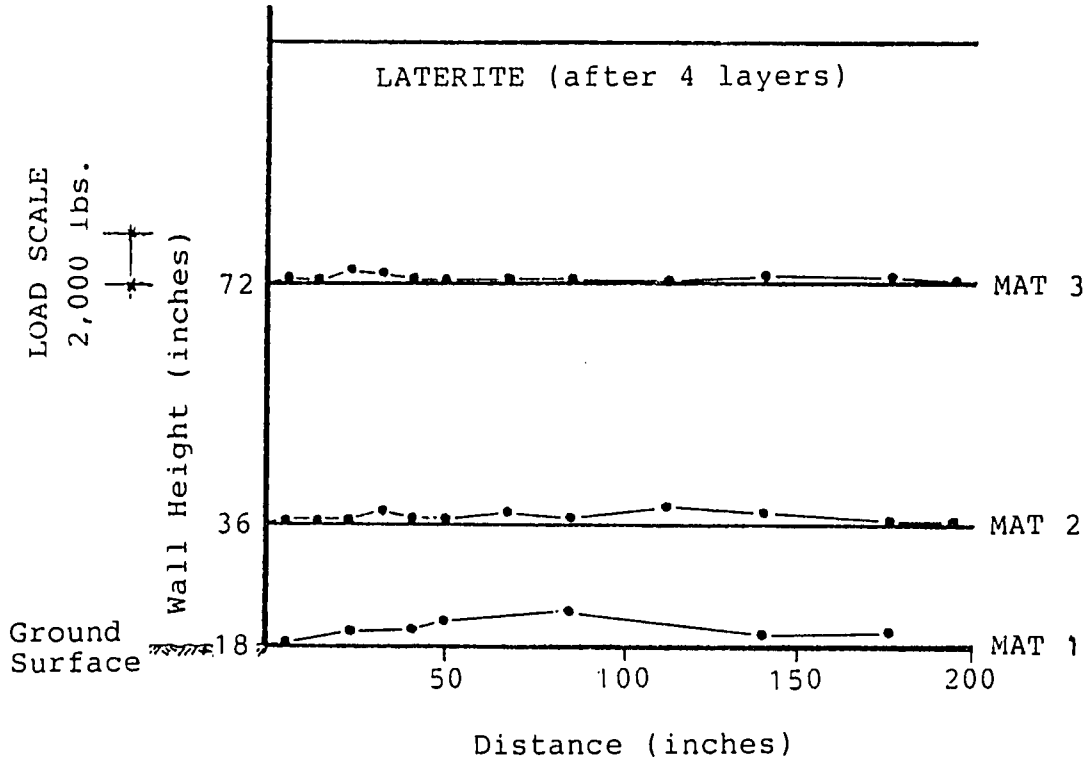

'ig. 129 Measured Axial Tension in the Reinforcing Mats After 4 Layers (Laterite).

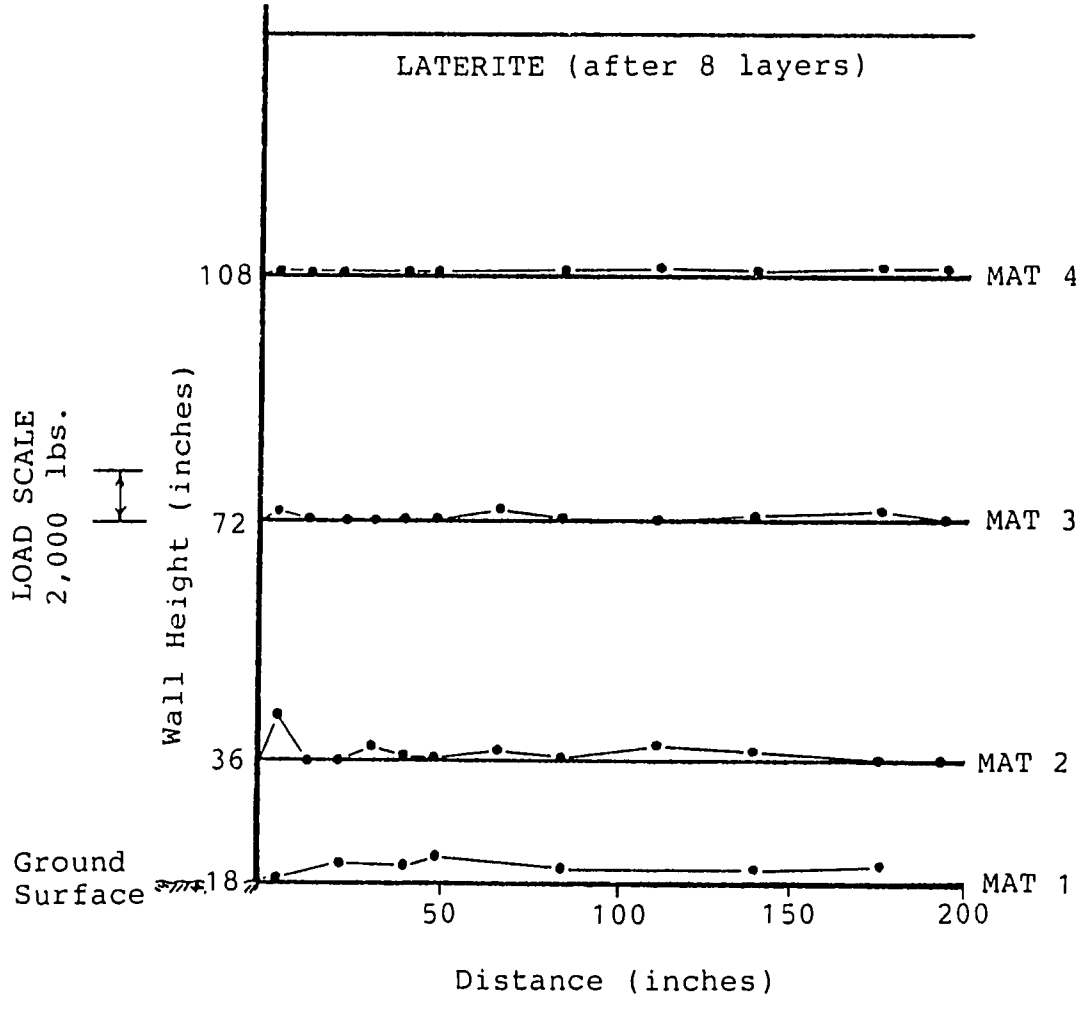

Fig. 130 Measured Axial Tension in the Reinforcing Mats After 8 Layers (Laterite).

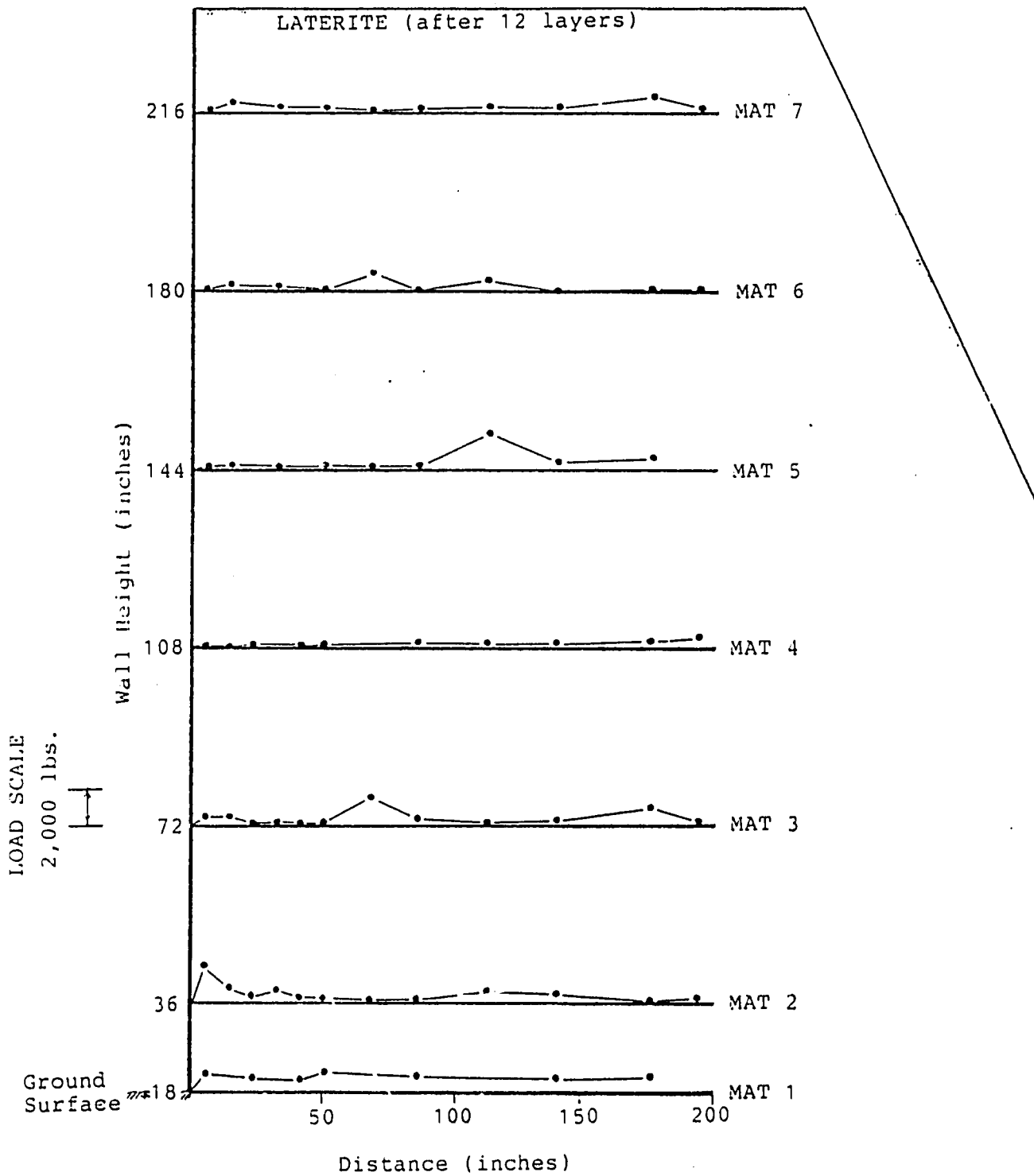

Fig. 131 Measured Axial Tension in the Reinforcing Mats After 12 Layers (Laterite).

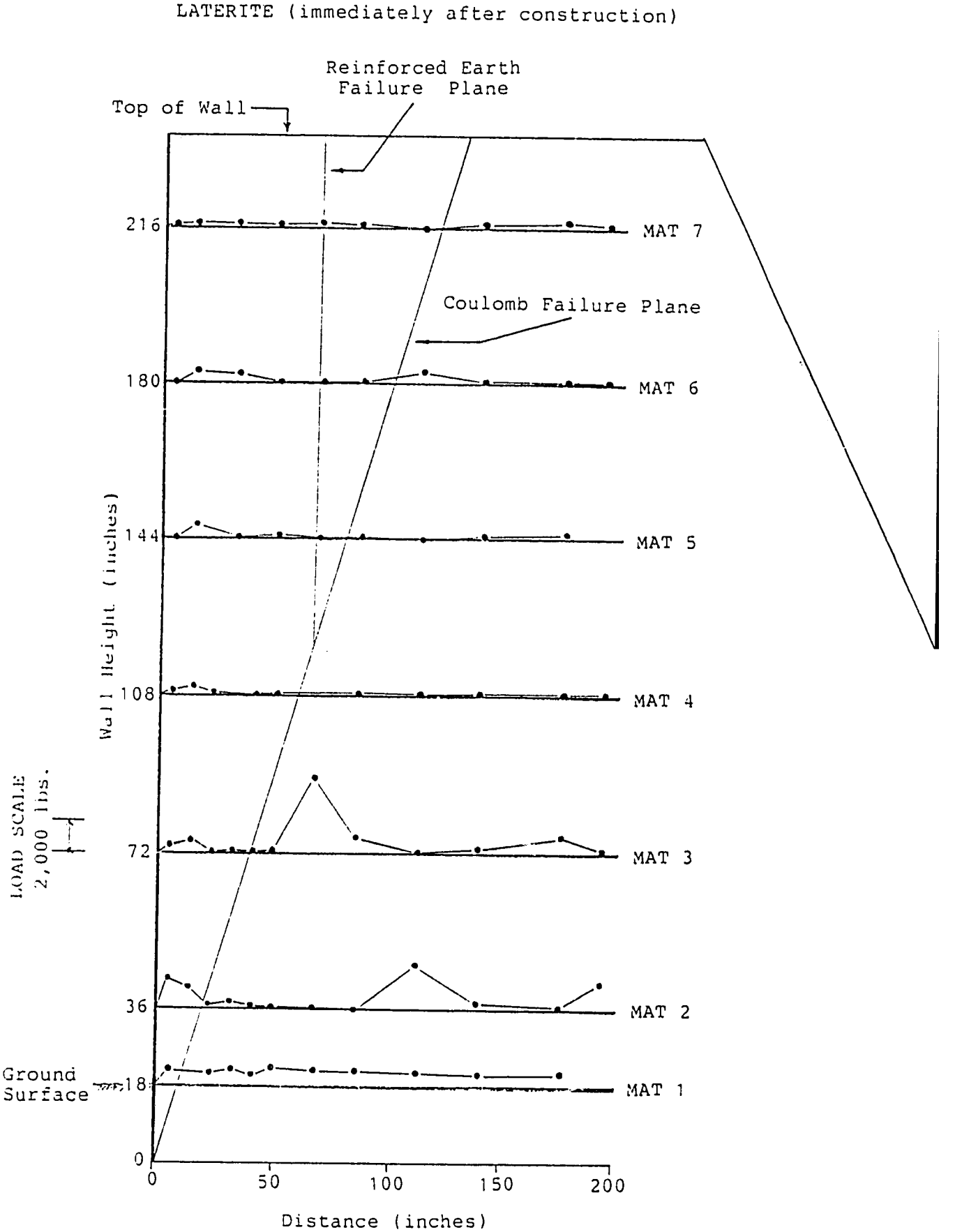

Fig. 132 Measured Axial Tension in the Reinforcing Mats Immediately After Construction (Laterite).

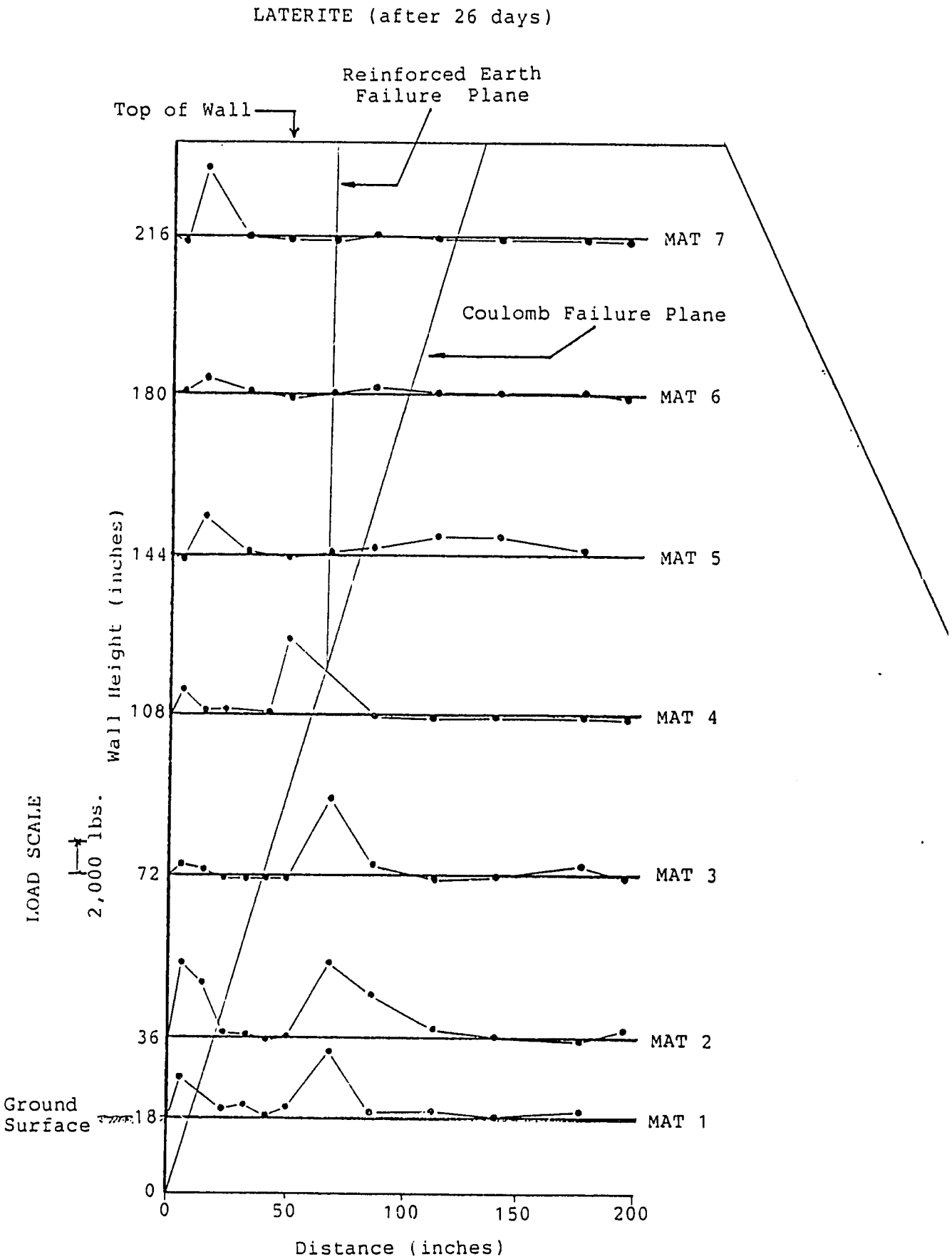

Fig. 133 Measured Axial Tension in the Reinforcing Mats 26 Days After Construction (Laterite).

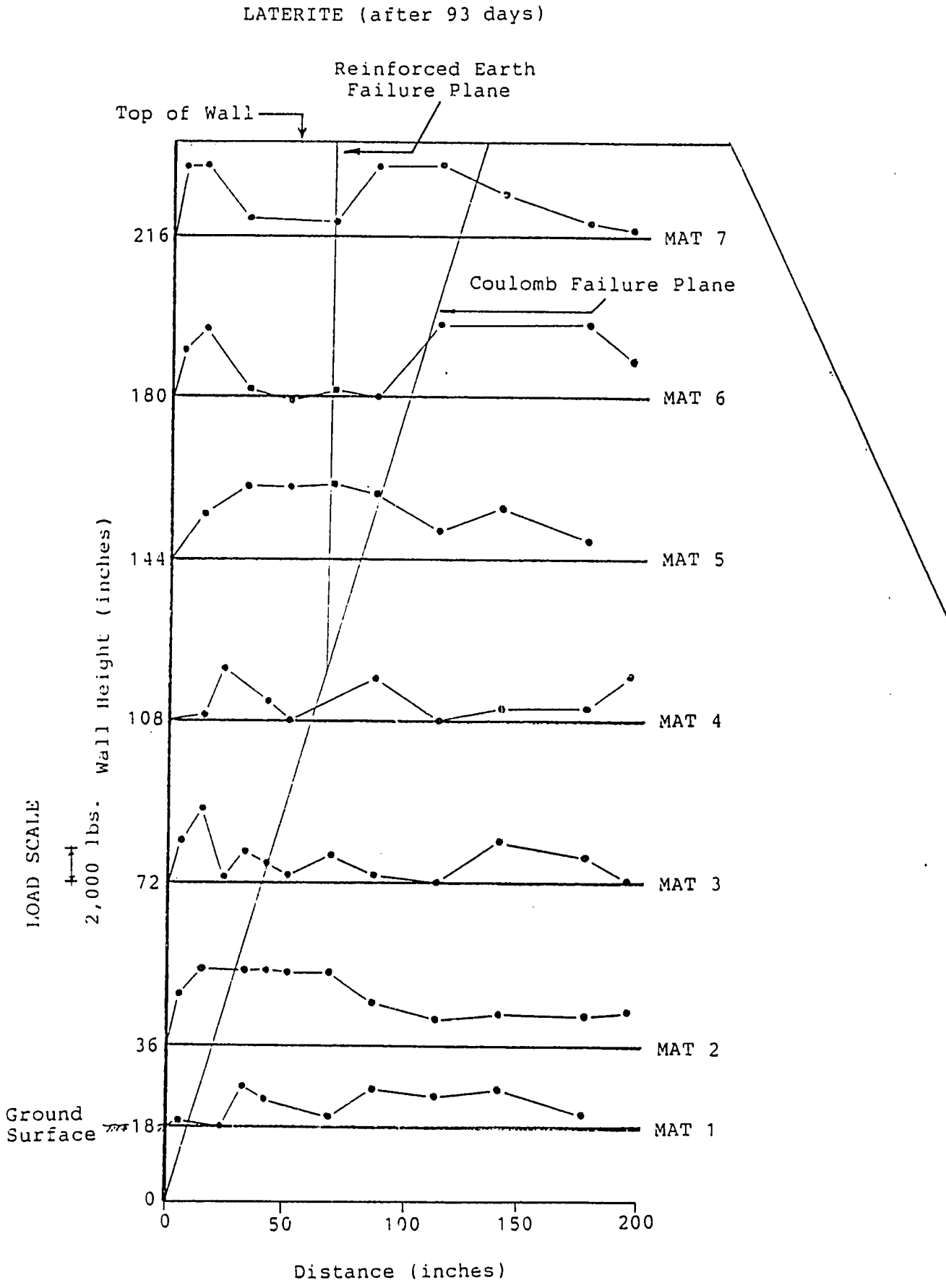

Fig. 134 Measured Axial Tension in the Reinforcing Mats 93 Days After Construction (Laterite).

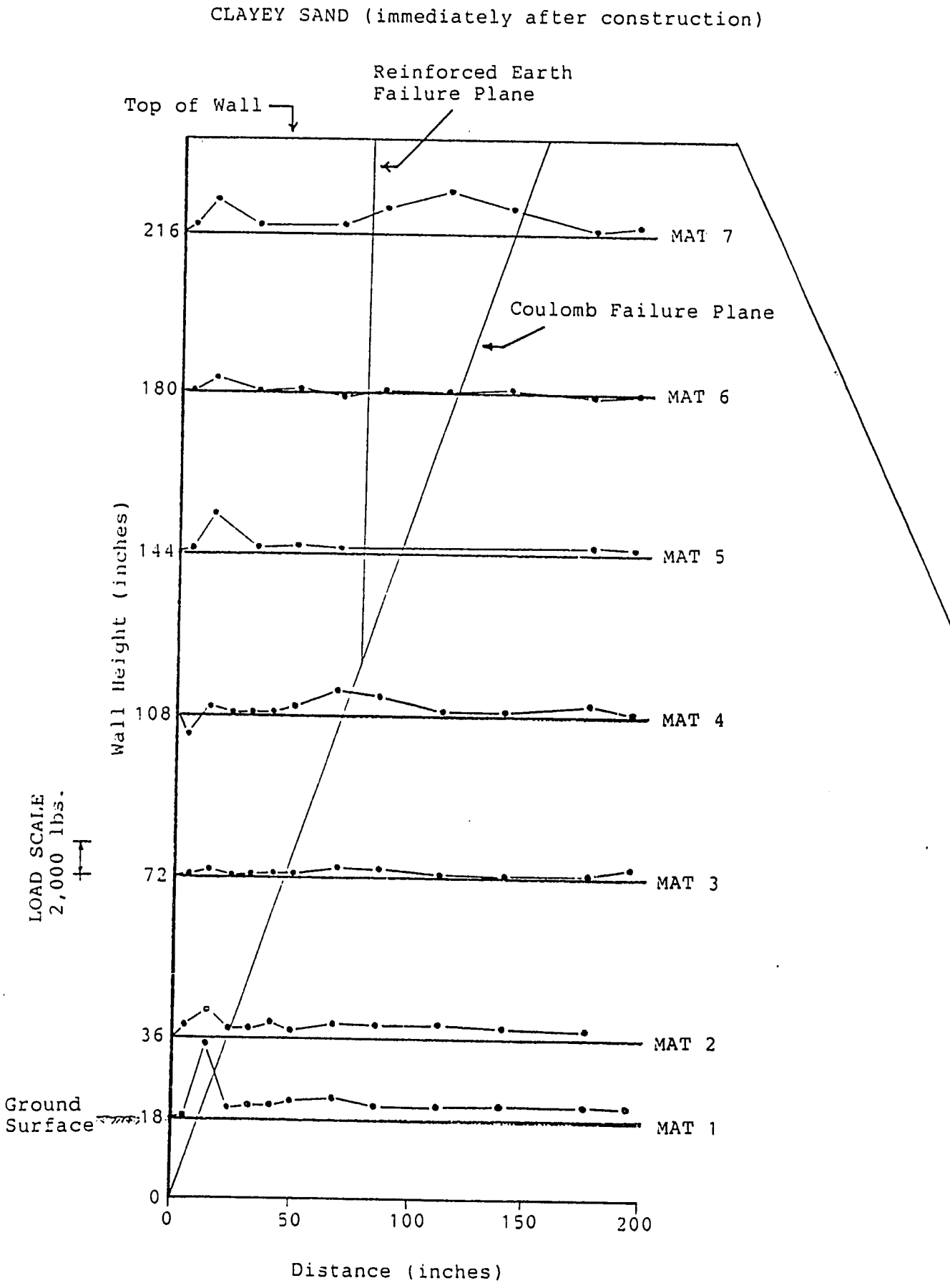

Fig. 135 Measured Axial Tension in the Reinforcing Mats Immediately After Construction (Clayey Sand).

CLAYEY SAND (after 26 days)

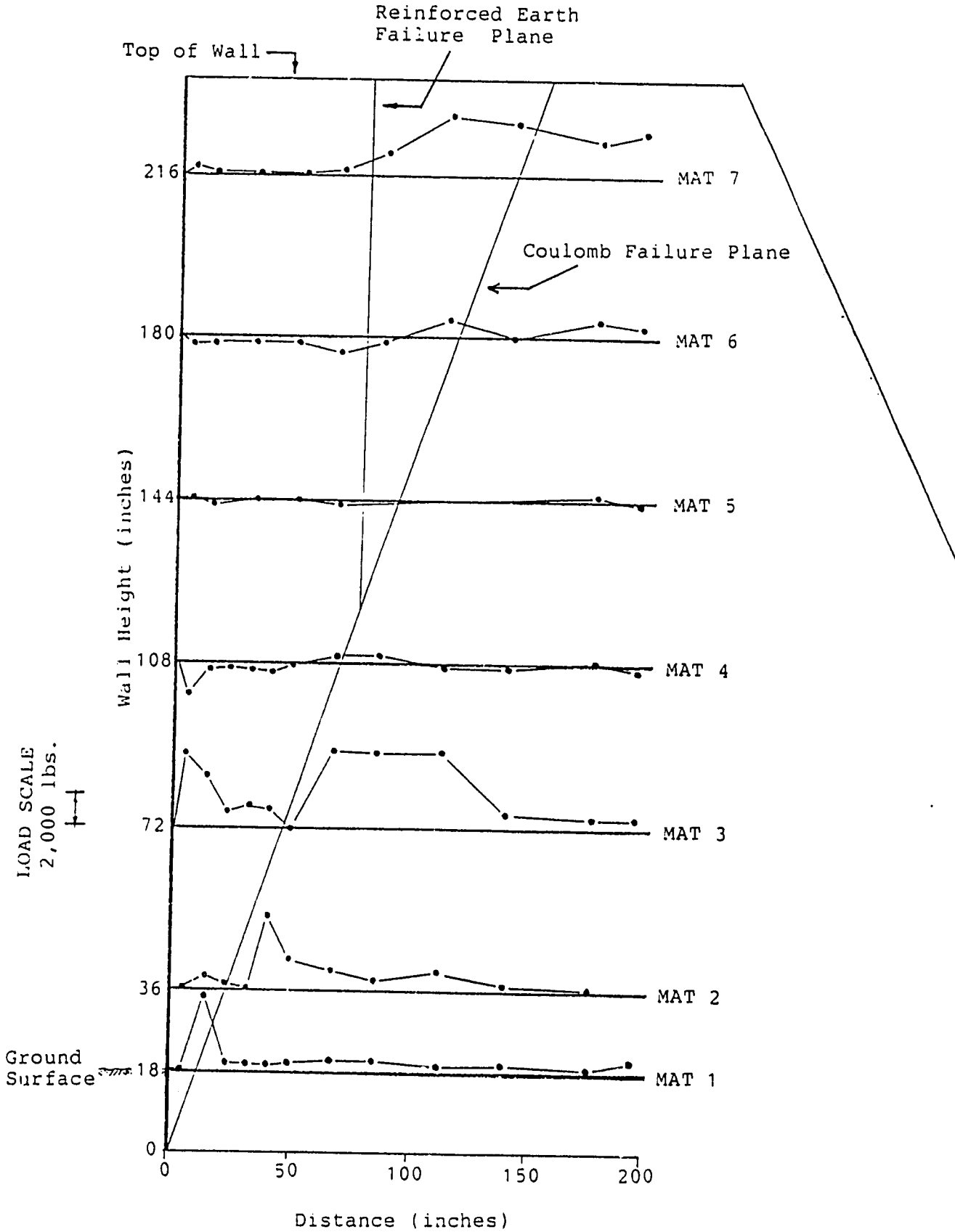

Fig. 136 Measured Axial Tension in the Reinforcing Mats 26 Days After Construction (Clayey Sand).

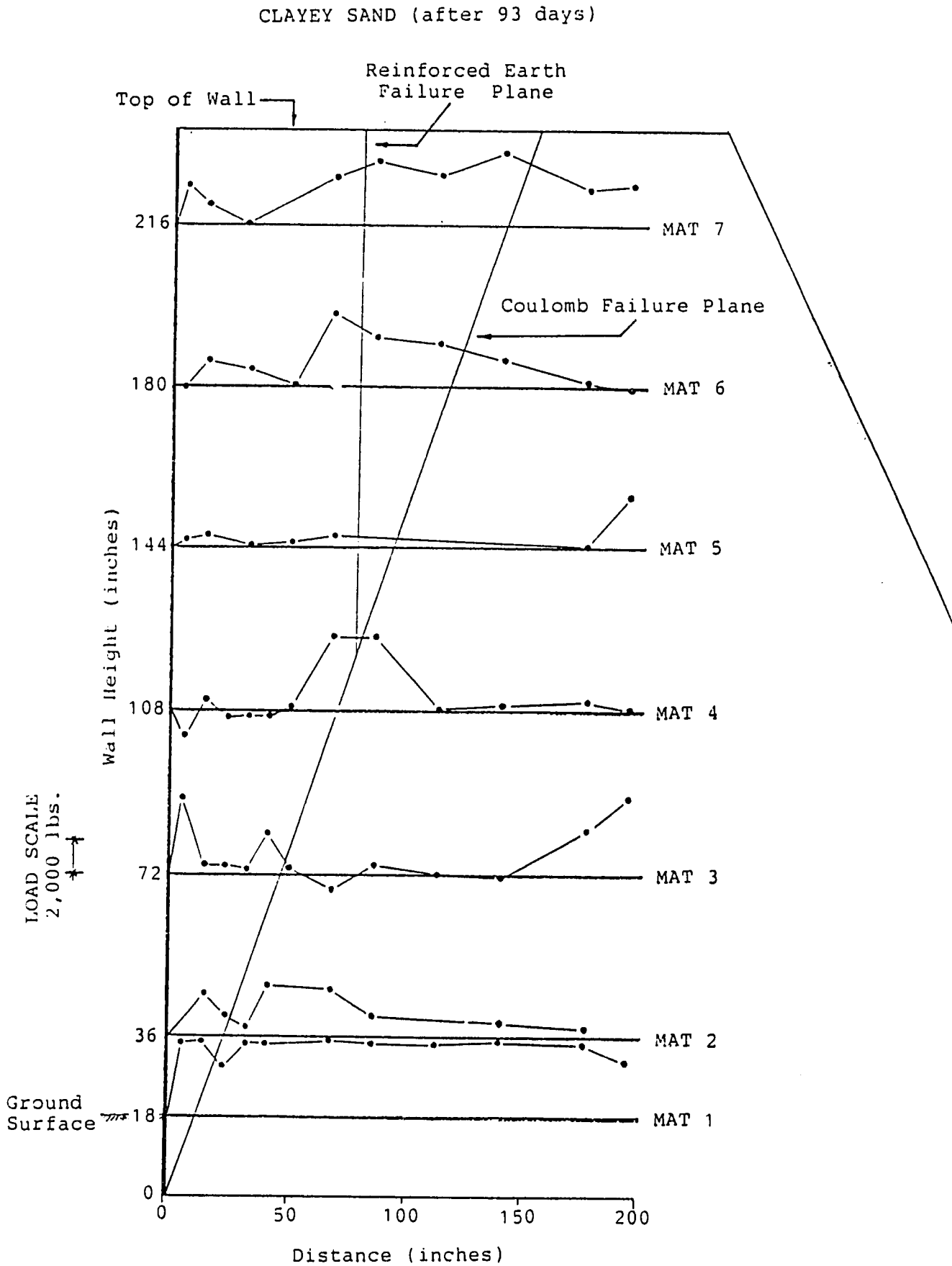

Fig. 137 Measured Axial Tension in the Reinforcing Mats 93 Days After Construction (Clayey Sand).

WEATHERED CLAY (immediately after construction)

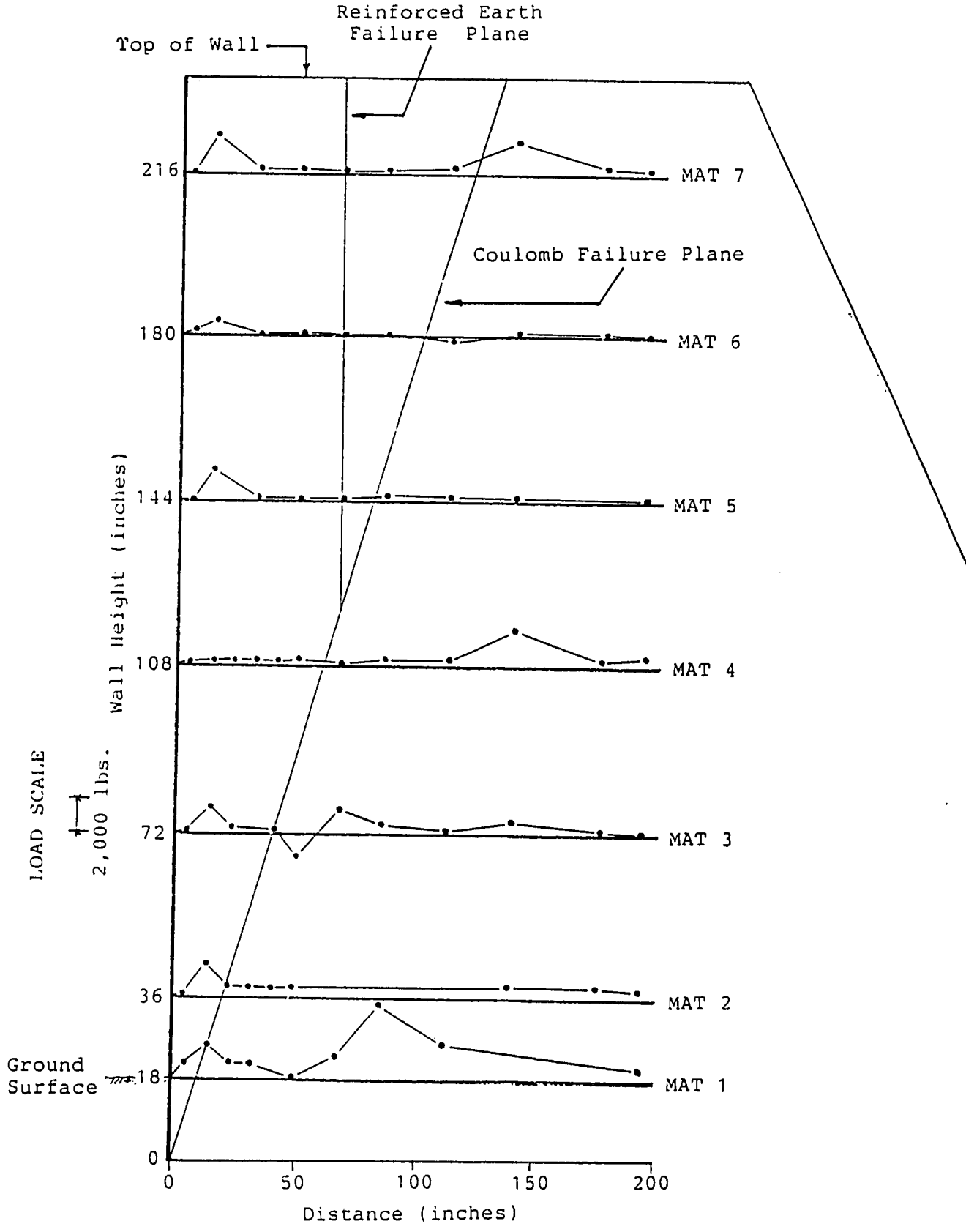

Fig. 138 Measured Axial Tension in the Reinforcing Mats Immediately After Construction (Weathered Clay).

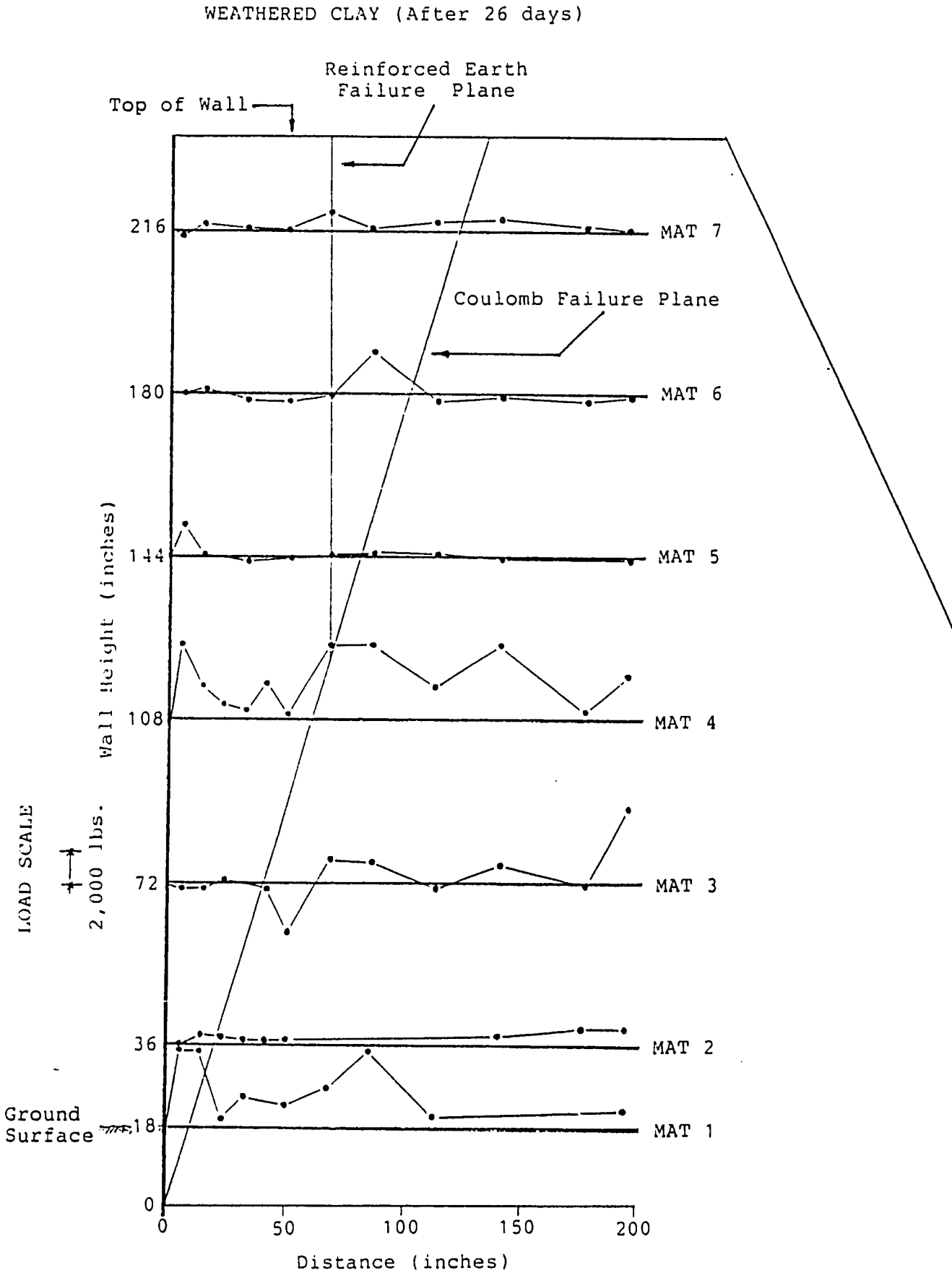

Fig. 139 Measured Axial Tension in the Reinforcing Mats 26 Days After Construction (Weathered Clay).

WEATHERED CLAY (after 93 days)

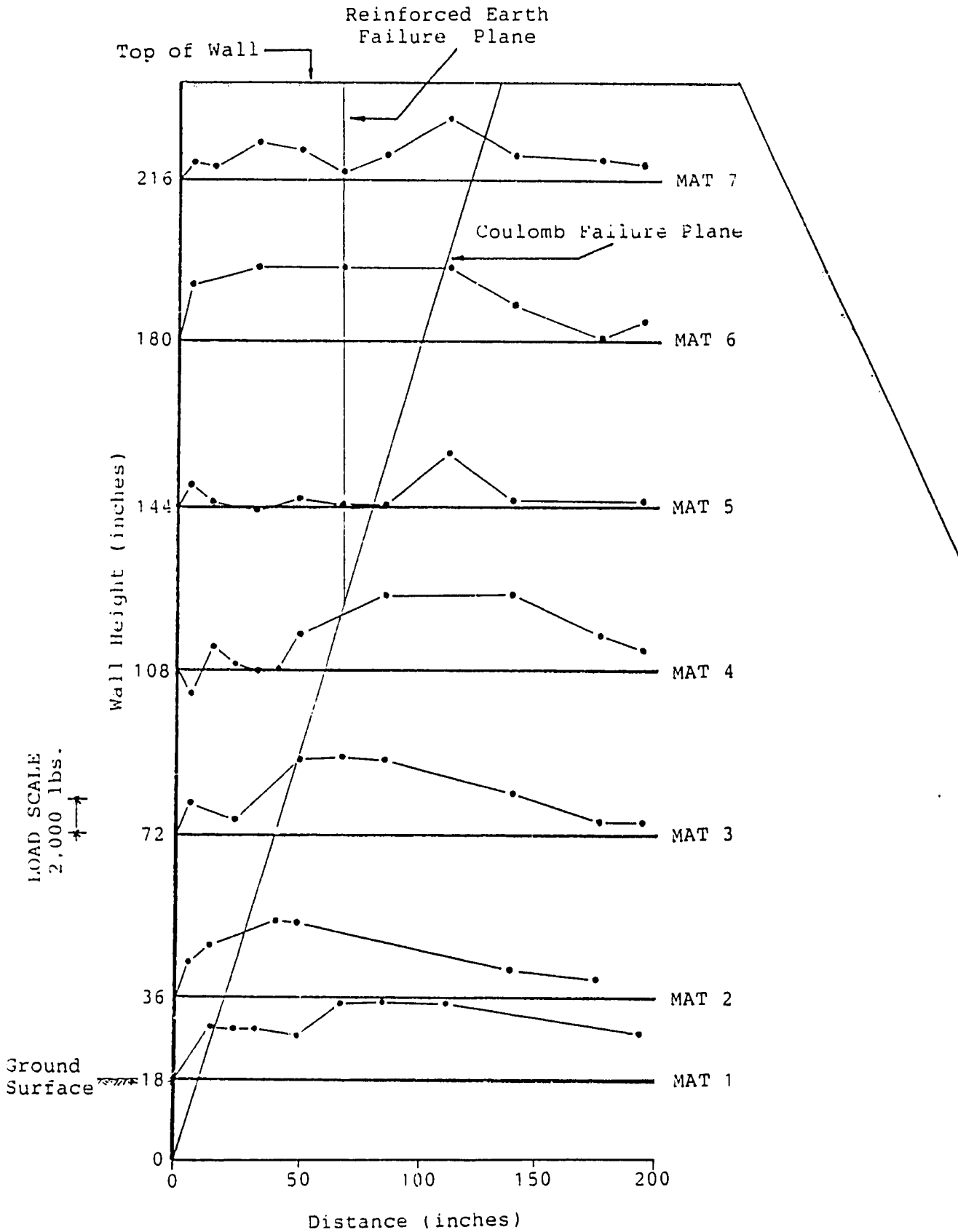

Fig. 140 Measured Axial Tension in the Reinforcing Mats 93 Days After Construction (Weathered Clay).

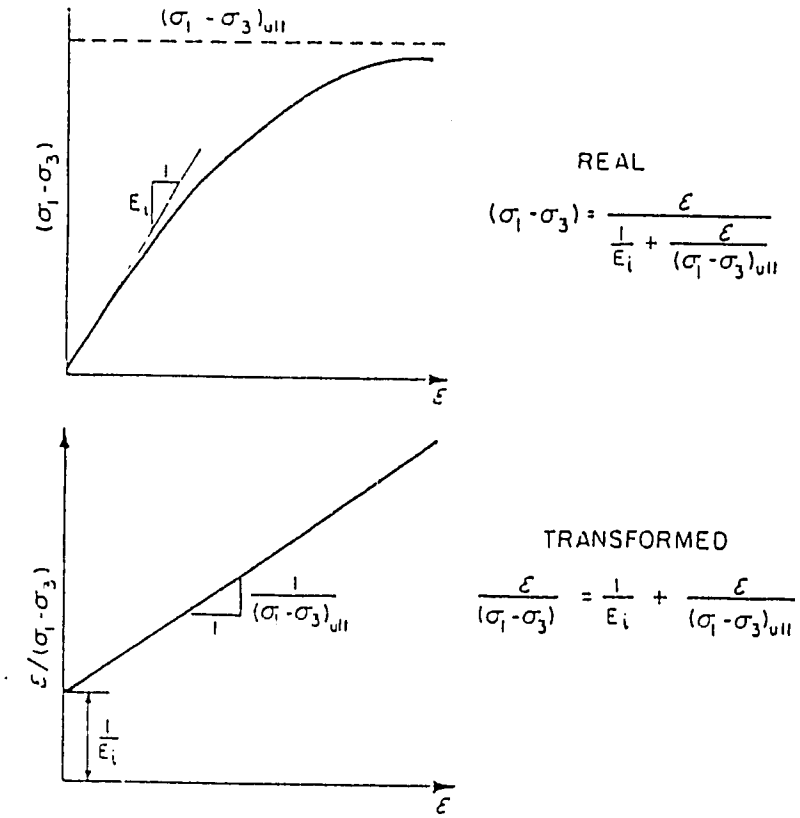

Fig. 141 Hyperbolic Representation of a Stress-strain Curve (after Duncan et al, 1980).

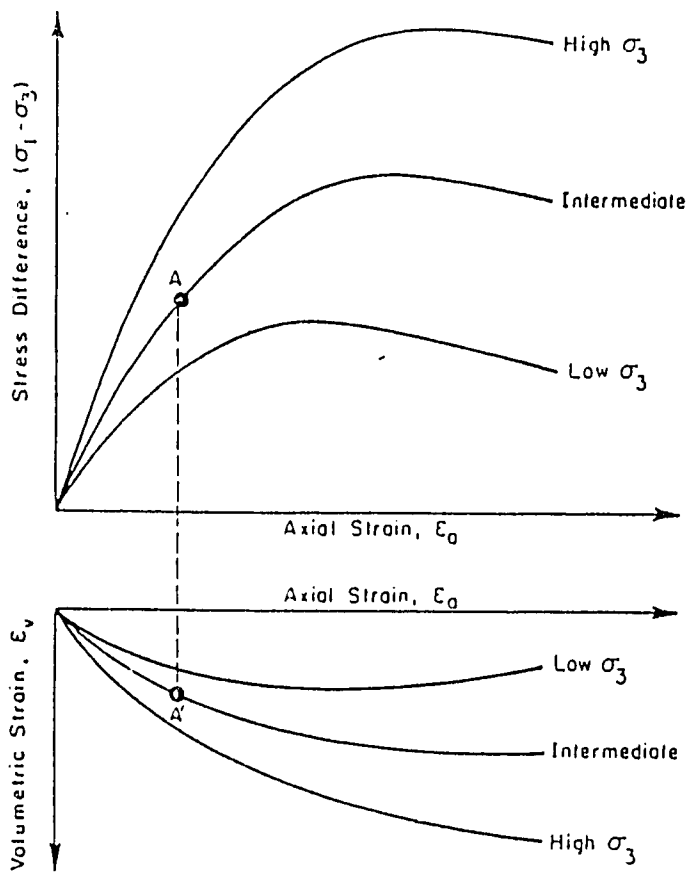

Fig. 142 Nonlinear and Stress-dependent Stress-strain and Volume Change Curves (after Duncan et al, 1980).

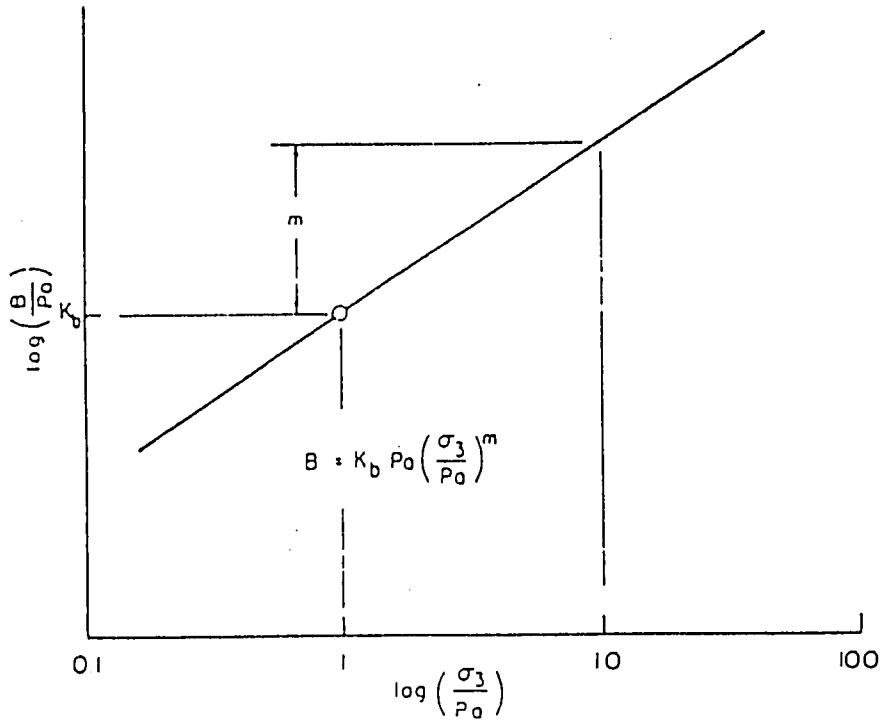

Fig. 143 Variation of Bulk Modulus with Confining Pressure (after Duncan et al, 1980).

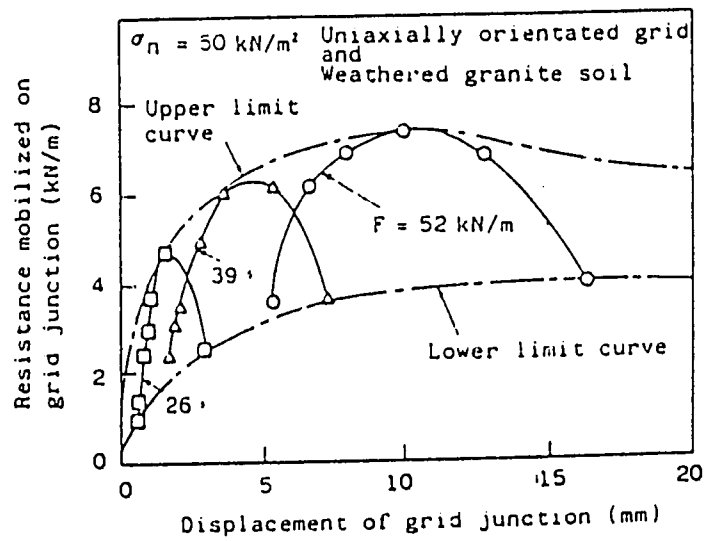

Fig. 144 Distribution of Pullout Resistance Mobilized on Grid Junctions (after Ochiai and Sakai, 1987).

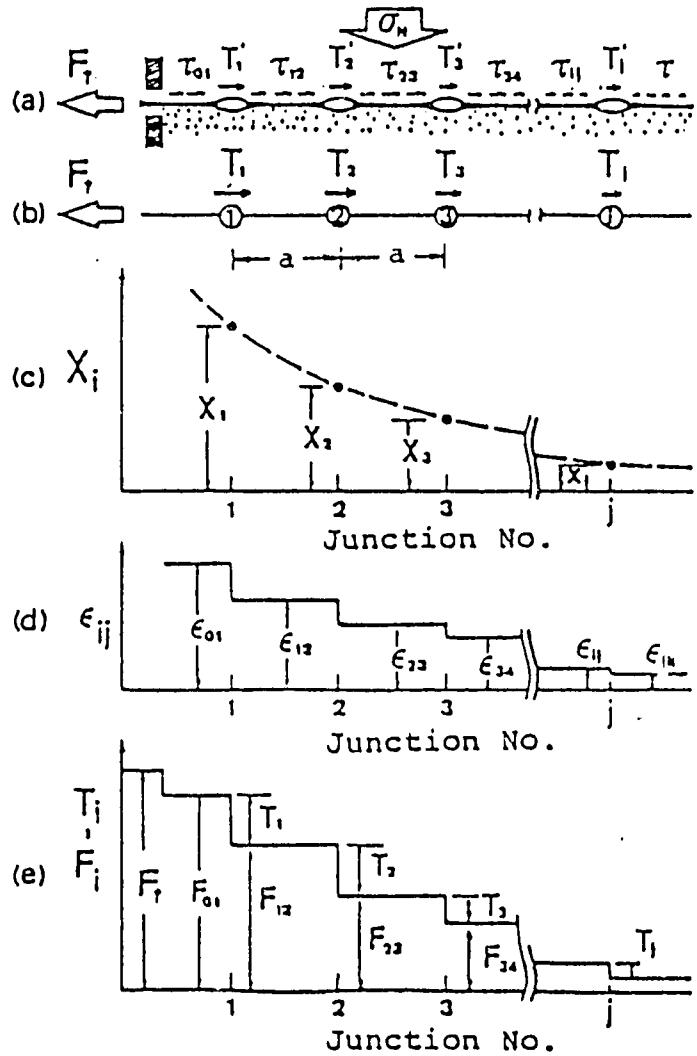

Fig. 145 Analytical Procedure of Results Obtained from Pullout Test (after Ochiai et al, 1988a).

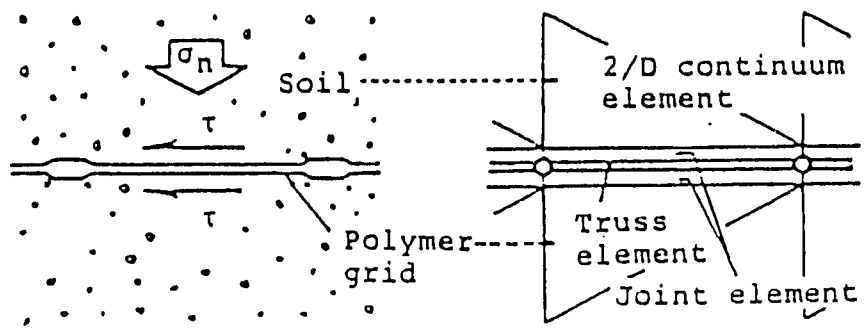

Fig. 146 Finite Element Model for Polymer Grid Reinforced Soil (after Ochiai et al, 1988a).

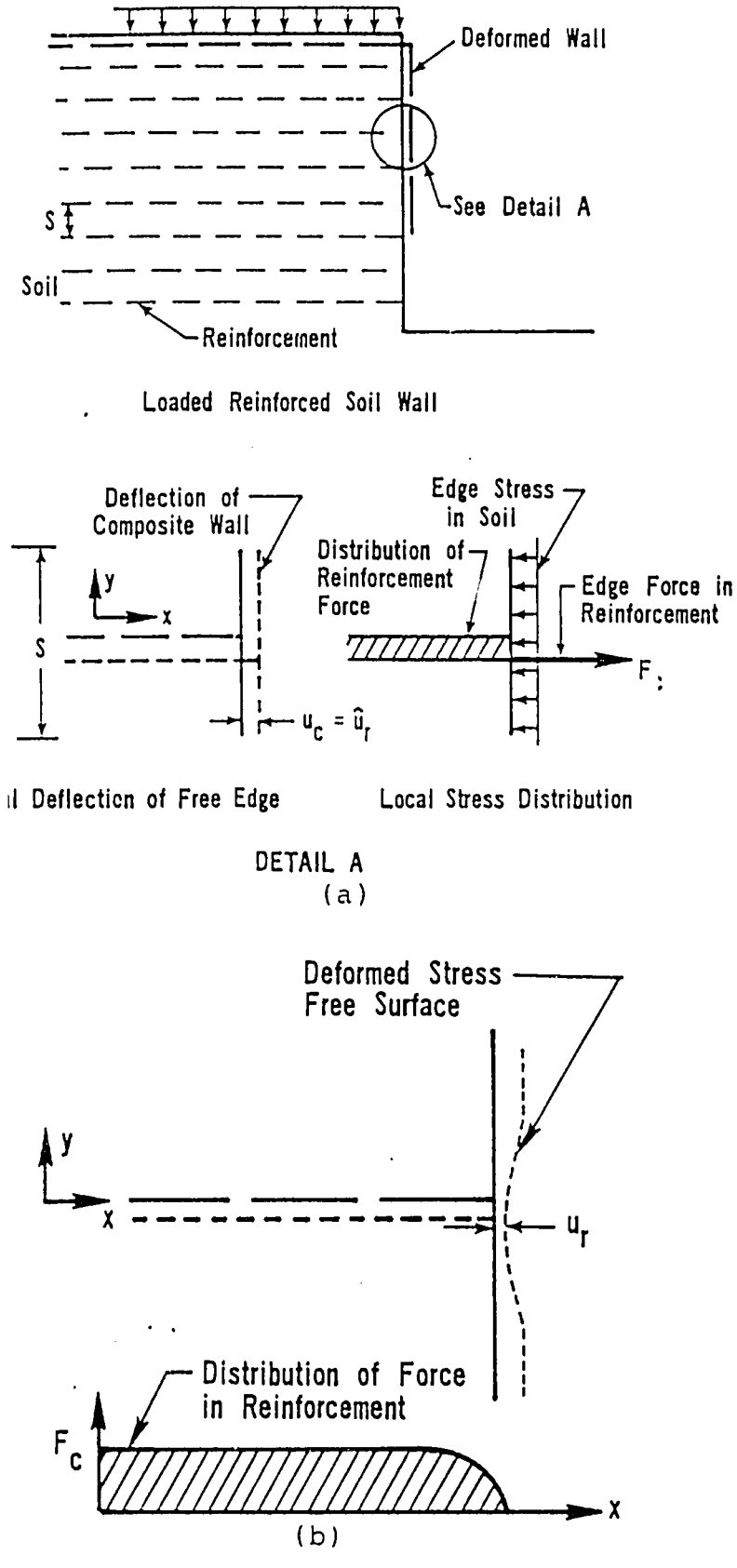

Fig. 147 (a) Composite Model Behaviour of a Loaded Reinforced Soil Wall (after Hermann and Al-Yassin, 1978).
(b) Actual Behavior of Detail A for Loaded Reinforced Soil Wall (after Hermann and Al-Yassin, 1978).

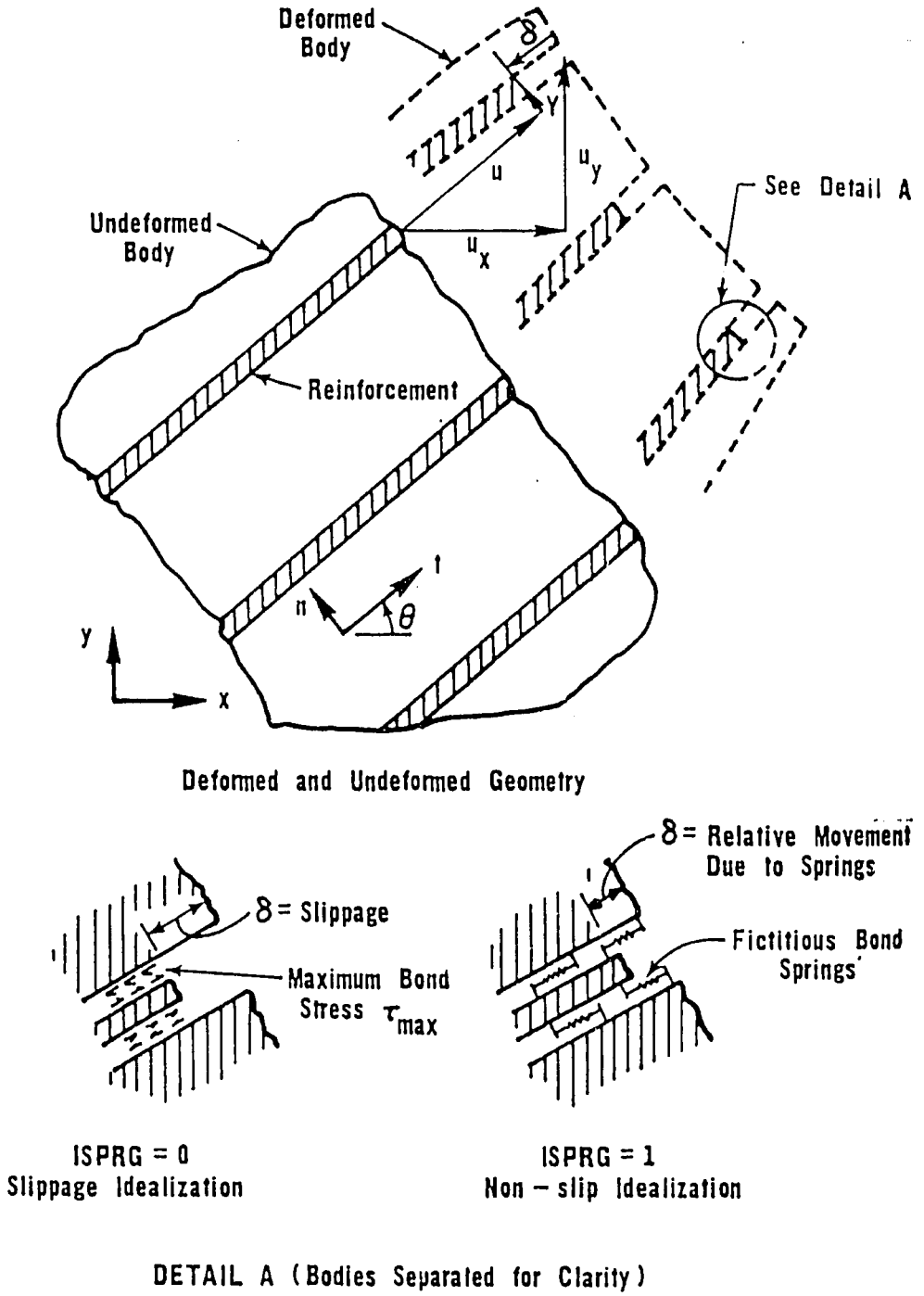

Fig. 148 Idealized Model of Bond Between Reinforcement and Soil (after Hermann and Al-Yassin, 1978).

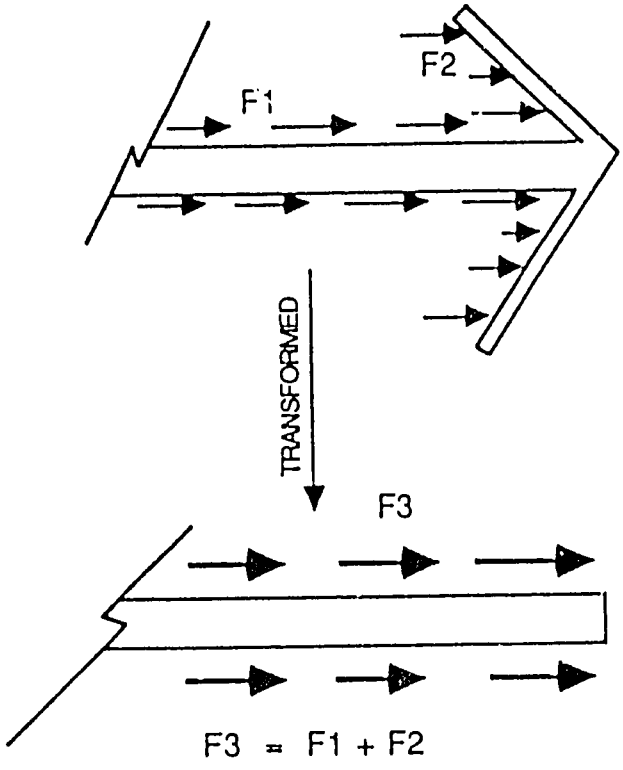

Fig. 149 Tie-back Anchor Wall Transformed to Strip Wall by Applying a High Equivalent Friction Coefficient in Strip Wall (Side View) (after Liu, 1988).

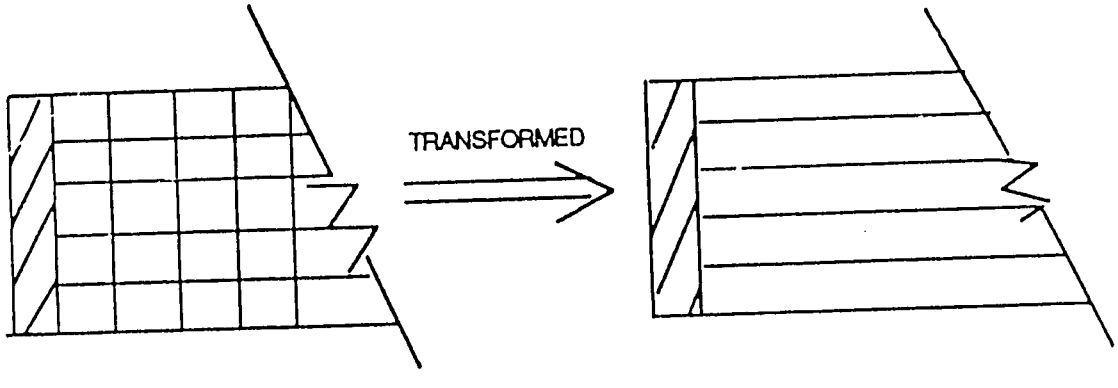

Fig. 150 Welded Wire Wall Transformed to Strip Wall by Applying a High Equivalent Friction Coefficient in Strip Wall (Top View) (after Liu, 1988).